

UNCLASSIFIED

AD NUMBER
AD476617
NEW LIMITATION CHANGE
TO Approved for public release, distribution unlimited
FROM Distribution authorized to U.S. Gov't. agencies and their contractors; Administrative/Operational Use; 24 Nov 1965. Other requests shall be referred to Air Force Rocket Propulsion Laboratory, Edwards AFB, CA.
AUTHORITY
AFRPL ltr, 20 Dec 1971

THIS PAGE IS UNCLASSIFIED

DOWNEY PLANT

RESEARCH DIVISION

LARGE SOLID-PROPELLANT BOOSTERS
EXPLOSIVE HAZARDS STUDY PROGRAM
(PROJECT SOPHY)

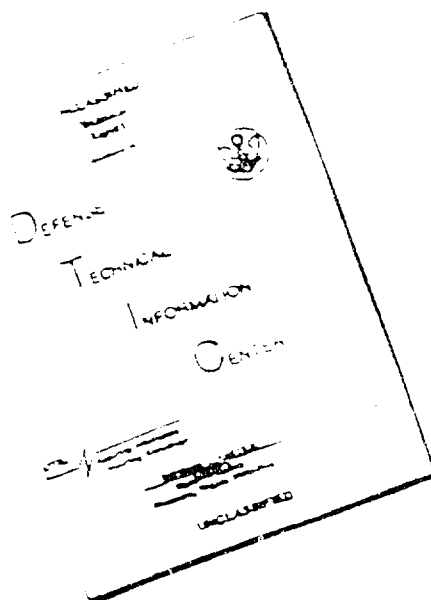
Technical Documentary Report No.
AFRPL-TR-65-211

A Final Report on
Contract AF04(611)-9945

Aerojet Report No. 0866-01(01)FP / November 1965 / Copy 182



DISCLAIMER NOTICE



THIS DOCUMENT IS BEST
QUALITY AVAILABLE. THE COPY
FURNISHED TO DTIC CONTAINED
A SIGNIFICANT NUMBER OF
PAGES WHICH DO NOT
REPRODUCE LEGIBLY.

REPRODUCED FROM
BEST AVAILABLE COPY

AEROJET-GENERAL CORPORATION
Research Division
11711 Woodruff Avenue
Downey, California

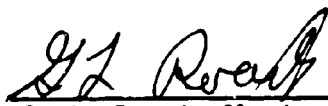
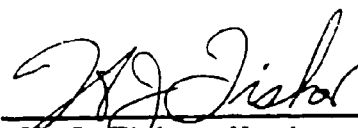
LARGE SOLID-PROPELLANT BOOSTERS
EXPLOSIVE HAZARDS STUDY PROGRAM
(PROJECT SOPHY)

Technical Documentary Report No. AFRPL-TR-65-211

A Final Report on

Contract AF04(611)-9945

Aerojet Report No. 0866-01(01)FP

Prepared by:	<u>O. R. Irwin G. L. Roark P. K. Salzman</u>	Date:	<u>24 November 1965</u>
Reviewed by:	<u> G. L. Roark, Head Explosive Kinetics Dept</u>	No. of Pages:	<u>330</u>
Approved by:	<u> H. J. Fisher, Head Research Division</u>	Classification:	<u>UNCLASSIFIED</u>

FOREWORD

This report was prepared by Aerojet-General Corporation, Downey, California, on Air Force Contract AF 04(611)-9945, which supports the USAF Solid Propellant Hazards Study Program (Project SOPHY).

Project SOPHY was initiated in April 1964 by the Air Force Rocket Propulsion Laboratory, Edwards, California. The AFRPL Program Managers were Mr. Charles R. Cooke for the first three months of the contract and Major Bryan E. Giesler for the remainder of the contract. The Aerojet-General Corporation Program Manager was Mr. G. L. Roark with Dr. O. R. Irwin and P. K. Salzman as Principal Investigators. The SOPHY Program is sponsored by the Air Force Rocket Propulsion Laboratory, the Air Force Eastern Test Range, and the Air Force Space Systems Division.

This report has been reviewed and approved.



BRYAN E. GIESLER

Major, USAF

Solid Propellant Hazards Study Program

Solid Rocket Division

Air Force Rocket Propulsion Laboratory

ABSTRACT

The purpose of this program was to evaluate the detonation characteristics of large rocket motors containing conventional solid-composite Class II propellants. The general approach taken was to first determine the critical diameter of a Class II propellant and then, by means of a critical geometry theory, predict the minimum size of a hollow-cored rocket motor grain of Class II propellant capable of sustaining detonation as well as the effect of donor size, configuration, and location on the initiation of detonation in the grain.

The critical diameter of a typical Class II propellant (AP-PBAN type) was estimated to be about 75 in. based on the results of a combined experimental theoretical study on the effect of RDX adulterant on the critical diameter of the basic AP-PBAN formulation.

The validity of a previously devised theory of critical geometry was tested using an RDX-wax explosive and a PBAN-RDX explosive. The experimentally determined critical dimensions of the various shapes tested were in reasonable agreement with predictions of the theory. The initiation criterion proposed by the critical geometry theory was measured and found to correctly predict the initiation of detonation in a supercritical acceptor charge by an axial, and donor. Supercritical charges could be initiated to detonation by an axial, end donor the diameter of which was only about 40 % of the critical diameter of the acceptor.

CONTENTS

	Page No.
1. INTRODUCTION	1
2. OBJECTIVES	2
3. SUMMARY	2
4. CRITICAL DIAMETER PROGRAM	4
4.1 Introduction	4
4.2 Objective.	5
4.3 Experimental Program	5
4.4 Theoretical Program	48
5. CRITICAL GEOMETRY PROGRAM	73
5.1 Objectives	73
5.2 Theory	73
5.3 Technical Discussion	74
ACKNOWLEDGEMENTS	211
REFERENCES	212
APPENDIX A - The Theory of Critical Geometry . . .	A-1
APPENDIX B - Application of Two Dimensional Com- putations to the Study of Sub-Critical Initiation and Fadeout in a Homogen- eous Explosive	B-1
APPENDIX C - Density and RDX Composition Varia- tions Within a Sample.	C-1

LIST OF ILLUSTRATIONS

Figure No.		Page No.
1.	Particle-Size Analysis of RDX Crystals (Sample 1; Drawn 29 June 1964)	6
2.	Particle-Size Analysis of RDX Crystals (Sample 2; Drawn 13 September 1964)	7
3.	Photomicrographs of AAB-3172 Propellant (3.25 wt % RDX) Showing AP, Al, RDX, and Internal Voids in AP Crystals	9
4.	Photomicrograph of AAB-3188 Propellant (9.0 wt % RDX) Using Phase Contrast, with Dark Field, Showing Distribution of RDX Particles (250X)	11
5.	Typical Steel Chamber Used for Propellant Samples 27 in. in Diameter and Smaller	12
6.	Side View of Casting Chamber for 48-in. -Diameter Propellant Charge	13
7.	Modular Concept of TNT Explosive Donor.	14
8.	Donor Configuration and Handling	15
9.	Typical Cross-Section View of Explosive Mold	17
10.	Schematic of AFRPL 1-36D Solid Hazards Test Facility	19
11.	Typical Critical Diameter Test Setup	20
12.	Test Setup, Critical Diameter Test of 48-in. -Diameter RDX-Adulterated PBAN Propellant Charge	21
13.	Preparation of Unadulterated PBAN Propellant Charge in Second-Stage Minuteman Chamber for Critical Diameter Test	23

LIST OF ILLUSTRATIONS (Continued)

Figure No.	Page No.
14. Test Setup, Critical Diameter Test of Unadulterated PBAN Propellant in Second Stage Minuteman Chamber .	24
15. Scaling of Witness Plate Thickness with Charge Diameter	26
16. Summary of Critical Diameter Test Results	29
17. Detonation Velocity vs Distance Along Charge for 1.0-in. -Diameter AAB-3163 Propellant Charge (16.0 wt % RDX) in Test CD-47	30
18. Detonation Velocity vs Distance Along Charge for 1.0-in. -Diameter AAB-3163 Propellant Charge (16.0 wt % RDX) in Test CD-45	31
19. Detonation Velocity vs Distance Along Charge for 1.29-in. -Diameter AAB-3164 Propellant Charge (12.0 wt % RDX) in Test CD-46	32
20. Detonation Velocity vs Distance Along Charge for 1.53-in. -Diameter AAB-3164 Propellant Charge (12.0 wt % RDX) in Test CD-43	33
21. Detonation Velocity vs Distance Along Charge for 1-3/4-in. -Diameter AAB-3187 Propellant Charge (10 wt % RDX) in Test CD-63	34
22. Detonation Velocity vs Distance Along Charge for 2-1/2-in. -Diameter AAB-3187 Propellant Charge (10 wt % RDX) in Test CD-66	35
23. Detonation Velocity vs Distance Along Charge for 3-in. -Diameter AAB-3188 Propellant Charge (9 wt % RDX) in Test CD-64	36
24. Detonation Velocity vs Distance Along Charge for 4-in. -Diameter AAB-3188 Propellant Charge (9 wt % RDX) in Test CD-61	37

LIST OF ILLUSTRATIONS (Continued)

Figure No.		Page No.
25.	Detonation Velocity vs Distance Along Charge for 6-in. -Diameter AAB-3176 Propellant Charge (6.75 wt % RDX) in Test CD-54	38
26.	Detonation Velocity vs Distance Along Charge for 8-in. -Diameter AAB-3176 Propellant Charge (6.75 wt % RDX) in Test CD-55	39
27.	Detonation Velocity vs Distance Along Charge for 11-in. -Diameter AAB-3191 Propellant Charge (4.75 wt % RDX) in Test CD-79	40
28.	Detonation Velocity vs Distance Along Charge for 12-in. -Diameter AAB-3191 Propellant Charge (4.75 wt % RDX) in Test CD-80	41
29.	Detonation Velocity vs Distance Along Charge for 23.5-in. -Diameter AAB-3204 Propellant Charge (1.8 wt % RDX) in Test CD-85	42
30.	Detonation Velocity vs Distance Along Charge for 23.5-in. -Diameter AAB-3203 Propellant Charge (2.4 wt % RDX) in Test CD-86	43
31.	Detonation Velocity vs Distance Along Charge for 44-in. -Diameter ANB-3105 Propellant Charge (0 wt % RDX) in Test CD-87	44
32.	Detonation Velocity vs Distance Along Charge for 44-in. -Diameter ANB-3105 Propellant Charge (0 wt % RDX) in Test CD-88	45
33.	Detonation Velocity vs Distance Along Charge for 48-in. -Diameter AAB-3205 Propellant Charge (0.73 wt % RDX) in Test CD-89	46
34.	Detonation Velocity vs Distance Along Charge for 48-in. -Diameter AAB-3215 Propellant Charge (0.25 wt % RDX) in Test CD-92	47

LIST OF ILLUSTRATIONS (Continued)

Figure No.		Page No.
35.	Physical Model of RDX-Adulterated AP-Al-PBAN Propellant	56
36.	Correlation of Critical Diameter Data Using Simple Model (Equation 14)	59
37.	Correlation of Critical Diameter Data Using Refined Model (Equation 17)	61
38.	Average Detonation Velocity vs Charge Diameter for RDX-Adulterated PBAN Propellants ($0.0073 \leq \text{RDX wt Fraction, } f \leq 0.16$)	64
39.	Estimated Critical Detonation Velocity vs RDX Content for RDX-Adulterated PBAN Propellants	65
40.	Comparison of Predictions of Theoretical Model with Experimental Critical Diameter Data	72
41.	Critical Dimensions of Various Shapes - Nonperforated Grains	75
42.	Critical Dimensions of Various Shapes - Perforated Grains	76
43.	Witness Plate Test Result Classification.	79
44.	Critical Dimensions of Various Shapes from Critical Geometry Theory	80
45.	Test Setup - Critical Diameter Tests.	82
46.	Analysis of Critical Diameter Tests - RDX-Wax.	84
47.	Test Setup - Critical Square Tests	86
48.	Analysis of Critical Square Tests - RDX-Wax	87
49.	Test Setup - Critical Rectangle Tests	89

LIST OF ILLUSTRATIONS (Continued)

Figure No.		Page No.
50.	Analysis of Critical Rectangle Tests - RDX-Wax	90
51.	Test Setup - Critical Equilateral Triangle Tests	93
52.	Analysis of Critical Equilateral Triangular Tests - RDX-Wax	94
53.	Test Setup - Critical Circular Core Cylinder Tests.	96
54.	Analysis of Critical Circular Core Cylinder Tests - RDX-Wax	97
55.	Analysis of Critical Diameter Tests - PBAN-RDX	101
56.	Analysis of Critical Equilateral Triangle Tests - PBAN-RDX	102
57.	Test Setup - Critical Circular Core Cylinder Tests (PBAN-RDX)	105
58.	Analysis of Critical Circular-Core Cylinder Tests - PBAN-RDX	106
59.	Analysis of Critical Cross-Core Cylinder Tests - PBAN-RDX	108
60.	Test Setup Used to Determine Initial Pressure in Plexiglas	114
61.	Determination of Initial Shock Velocity in Plexiglas.	116
62.	Test Setup Used to Determine Shock Attenuation in Plexiglas	117
63.	Shock Attenuation in Plexiglas, 3-in. -Diameter Column	119
64.	Shock Attenuation in Plexiglas, 3-1/2-in. -Diameter Column	120

LIST OF ILLUSTRATIONS (Continued)

Figure No.	Page No.
65. Shock Attenuation in Plexiglas, 4-in. -Diameter Column	121
66. Shock Attenuation in Plexiglas, 5-in. -Diameter Column	122
67. Shock Attenuation in Plexiglas, 6-in -Diameter Column	123
68. Shock Attenuation in Plexiglas, U vs X, Column Dia- meters of 3, 3-1/2, 4, 5, and 6 in	124
69. Shock Attenuation in Plexiglas, P vs X, Column Dia- meters of 3, 3-1/2, 4, 5, and 6 in	126
70. Shock Attenuation in Plexiglas, P/P_0 vs x/d	127
71. Test Setup - Hugoniot of PBAN-RDX Propellant	128
72. Streak Record-Hugoniot of PBAN-RDX Explosive - Test No. 2	130
73. Streak Record-Hugoniot of PBAN-RDX Explosive - Test No. 3	131
74. Streak Record-Hugoniot of PBAN-RDX Explosive - Test No. 6	132
75. Streak Record-Hugoniot of PBAN-RDX Explosive - Test No. 7	133
76. Determination of PBAN-RDX Hugoniot - Test No. 2	134
77. Determination of PBAN-RDX Hugoniot - Test No. 3	135
78. Determination of PBAN-RDX Hugoniot - Test No. 6	136
79. Determination of PBAN-RDX Hugoniot - Test No. 7	137

LIST OF ILLUSTRATIONS (Continued)

Figure No.		Page No.
80.	Hugoniot of PBAN-RDX Explosive	138
81.	Test Setup - Initiation Criterion Tests.	140
82.	Pressure Entering PBAN-RDX Explosive - Hugoniot Reflection Method	142
83.	P_R vs d for PBAN-RDX Explosive.	143
84.	Initiation Criterion of PBAN-RDX Explosive - P^+ vs d	144
85.	Initiation Criterion of PBAN-RDX Explosive - P^+ vs A	146
86.	Axial End Donor Test Setup for Nonperforated Acceptor	148
87.	Axial, End Donor Test - Test No. B.4.2.1.1.1 (Time Increment = 2.76 μ sec/frame)	149
88.	Axial, End Donor Test B.4.2.1.1.1, Distance vs Time Data 1.0-in. -Diameter Booster	150
89.	Axial, End Donor Test B.4.2.1.1.2, Distance vs Time Data 2.0-in. -Diameter Booster	151
90.	Axial, End Donor Test B.4.2.1.1.3, Distance vs Time Data 1.50-in. -Diameter Booster	152
91.	Axial, End Donor Test B.4.2.1.1.5 - Distance-Time Data 1.75-in. -Diameter Booster.	153
92.	Wave Profiles - Test No. B.4.2.1.1.1	155
93.	Wave Profiles - Test No. B.4.2.1.1.2	156
94.	Wave Profiles - Test No. B.4.2.1.1.3	157
95.	Wave Profiles - Test No. B.4.2.1.1.5	158

LIST OF ILLUSTRATIONS (Continued)

Figure No.		Page No.
96.	Side Donor Attenuation Test Setup for Nonperforated Acceptor	164
97.	Side Donor Test - Test No. B.4.2.1.3.1 (Time Increment = 2.76 μ sec/frame).	165
98.	Side Donor Test - Test No. B.4.2.1.3.2 (Time Increment = 2.76 μ sec/frame)	166
99.	Nonaxial End Donor Attenuation Test Setup for Perforated Acceptor	168
100.	Nonaxial, End Donor Test - Hollow Core Acceptor - Test No. B.4.2.2.2.1 (Time Increment = 8.4 μ sec/frame)	169
101.	Nonaxial, End Donor Test - Hollow Core Acceptor - Test No. B.4.2.2.2.2 (Time Increment = 8.4 μ sec/frame)	170
102.	Side Donor Test - Hollow Core Acceptor - Test No. B.4.2.2.3.2 (Time Increment = 8.4 μ sec/frame)	171
103.	Test of Initiation Criterion	173
104.	Test of Initiation Criterion	174
105.	Detonation of Composition B Charge - Test No. B.1.a.2 (Time Increment = 1.4 μ sec/frame).	184
106.	Detonation of RDX-Wax Charge - Test No. B.1.a.5 (Time Increment = 1.4 μ sec/frame).	185
107.	Detonation of RDX-Wax Charge - Test No. B.1.a.9 (Time Increment = 1.4 μ sec/frame).	186

LIST OF ILLUSTRATIONS (Continued)

Figure No.		Page No.
108.	Detonation of RDX-Wax Charge - Test No. B.1.a.13 (Time Increment = 1.4 μ sec/frame)	187
109.	Pure Wax Sample - Test No. B.1.a.12 (Time Increment = 1.4 μ sec/frame).	188
110.	Circular-Core Composition B Booster - Test Without Rod. (Time Increment = 2.76 μ sec/frame)	197
111.	Circular-Core Composition B Booster Test With Rod (Time Increment = 2.76 μ sec/frame)	198
112.	Side Donor Test - Composition B Charge (Time Increment = 2.76 μ sec/frame)	199
113.	Estimation of Correct RDX Content to Give a Critical Diameter of 3 in.	206
114.	Voids in PBAN-RDX Batch 1.	207
115.	Typical X-Rays of Samples from PBAN-RDX Batch 1.	208
116.	X-Ray of Turned Down Sample from PBAN-RDX Batch 1	209
117.	Photomicrograph of PBAN-RDX Sample Containing 9.2% RDX.	210

LIST OF TABLES

Table No.		Page No.
1.	Critical Diameter Test Plan	16
2.	Summary of Test Results of Critical Diameter Program	27
3.	Summary of AFRPL Blast Data	49
4.	Evaluation of $g(f)$ for RDX Contents Between 0.375 and 16 wt %	67
5.	Calculated Values of the Critical Diameter of RDX-Adulterated PBAN Propellant of $0 \leq f \leq 0.16$, Using Refined Model	70
6.	Experimental Program Outline	77
7.	Critical Diameter Tests - RDX-Wax	81
8.	Critical Square Tests - RDX-Wax	85
9.	Critical Rectangle Tests - RDX-Wax	88
10.	Critical Equilateral Triangle Tests - RDX-Wax	92
11.	Critical Circular Core Cylinder Tests - RDX-Wax	95
12.	Critical Diameter Tests - PBAN-RDX	99
13.	Critical Equilateral Triangle Tests - PBAN-RDX	100
14.	Circular Core Cylinder Tests - PBAN-RDX	104
15.	Cross Core Cylinder Tests - PBAN-RDX	107
16.	Summary of Critical Geometry Tests - RDX-Wax	110

LIST OF TABLES (Continued)

Table No.		Page No.
17.	Summary of Critical Geometry Tests - PBAN-RDX	111
18.	Shock Velocity in Plexiglas.	115
19.	Densities of Plexiglas Columns and Composi- tion B Boosters Prepared for Attenuation Tests. .	118
20.	Hugoniot of PBAN-RDX Explosive	129
21.	Initiation Criterion Tests.	141
22.	Axial, End Donor Tests	147
23.	Wave Diameter, Area and Shock Pressure	160
24.	Demonstration Tests	163
25.	Theoretical Program Outline.	176
26.	Detonation Velocity vs Dimension - RDX-Wax. . .	177
27.	Detonation Velocity vs Dimension - PBAN-RDX. .	178
28.	Critical Detonation Velocities	179
29.	Preliminary Tests - RDX-Wax.	183
30.	Summary of Dent Data from Preliminary Tests. .	190
31.	Development of Propellant Casting.	203

1. INTRODUCTION

The United States is developing and testing large solid-propellant rocket motors for use in national defense and space exploration. Because of the large quantities of energetic propellant involved, the catastrophic failure of such a motor is potentially capable of causing vast destruction. A catastrophic failure could be initiated by such mishaps as involvement in fire, impact from some sort of projectile, fall-back during a launch, or exposure to shock resulting from an explosion.

Relatively little has been accomplished in the systematic investigation of the hazards associated with large solid rocket motors, yet these hazards are of grave concern from both cost and personnel-safety viewpoints, especially since an increase in the size and frequency of use of these motors is anticipated in the future. It is necessary that techniques be developed to accurately analyze and predict the hazards and damage capabilities of large solid rocket motors.

In the past, explosive-hazard evaluation tests were conducted to gain information on particular propellant formulations and applications. When the formulations or applications were altered, it was necessary to conduct new tests. The answers to many questions about the hazards associated with solid motors were not known, and when doubts existed they were resolved in favor of more conservative safety criteria. With the advent of the larger solid motors, the cost of "more safety" has become prohibitive.

The Hazards Analysis Branch of the Air Force Rocket Propulsion Laboratory, Edwards Air Force Base, California, is conducting a solid-propellant hazards study program, Project SOPHY, to analyze the potential explosive hazards of handling, transporting, testing, and launching large solid-propellant systems. As an initial effort under Project SOPHY, Aerojet has conducted a combined experimental and theoretical study to answer some of the questions of one aspect of the hazards problem: the hazard created by the detonation of a large motor containing a Class II solid-composite propellant. This is the final report on the initial SOPHY studies.

Existing detonation theories cannot be applied directly to the analysis of the detonability of conventional solid-propellant motor grains, because they consider the propagation of a steady-state detonation only in solid cylindrical charges, while solid-rocket-motor grains are normally in the form of cylinders with various shapes of internal perforations. To assess the detonation hazards of real motors, the approach taken in the present

program has been to first determine the minimum diameter (i.e., the critical diameter) of a solid cylindrical grain that will sustain detonation, and then, by a concurrently developed theory of critical geometry, to relate the critical diameter of the solid cylindrical grain to the critical or minimum size of a given grain geometry that will sustain detonation.

2. OBJECTIVES

The long-range objective of these studies is to enable prediction of the hazards associated with handling, transporting, and launching solid-propellant rocket motors.

The specific objectives of this program are: (1) to determine the critical diameter of typical Class II propellants, and (2) to extend the critical-diameter concept to other grain configurations and to determine the donor intensity, configuration, and location at which partial or complete detonation can occur.

For technical direction and definition, the program was divided into two separate tasks: (1) critical-diameter studies, and (2) critical-geometry studies. These tasks are reported in Sections 4 and 5.

3. SUMMARY

Eighty-one instrumented critical-diameter tests were performed on RDX-adulterated AP-PBAN propellant samples in which the RDX content was decreased from 16 wt % to 0.25 wt % as the sample diameters increased from 1 to 48 in. The experimental data (critical diameter vs RDX content) were used in conjunction with an existing theoretical detonation model to develop an improved model, consistent with the data, for predicting the critical diameter of unadulterated AP-PBAN propellant.

The final form of the model, which is in excellent agreement with all critical-diameter data for RDX weight fractions $f \leq 0.10$, is

$$d_c = 15.3 \left(\frac{1}{f + 0.003} \right)^{1/3} - 30.4 \text{ in.}$$

where:

d_c = critical diameter (in.)

f = weight fraction (wt %/100)

The model predicts a critical diameter of 75.6 in. for unadulterated AP-PBAN propellant.

The current theory of critical geometry evaluates the detonability of a given system by developing criteria to determine (1) the critical dimensions for sustainment of detonation of any configuration in terms of the critical diameter of that material and (2) the level of shock stimulus from a donor necessary to initiate detonation.

A very useful estimation of the validity of the theory of sustainment was found from the results of the experimental program using RDX-wax explosive. It was found that the predicted critical dimensions of various shapes were somewhat higher than the data obtained. This was confirmed by the results of testing with PBAN-RDX explosive where the difference amounted to a range of about 3-20%.

It was found that the results obtained could be correlated by using a concept of "equivalent diameter" (based on the equations of the original theory and the critical dimensions found) which, for the PBAN-RDX explosive, was found to be accurate within about 5%. It was also indicated that for circular-core cylinders, the critical web thickness was only about one-half of the critical diameter of the material, for both explosive compositions.

For PBAN-RDX explosive, an initiation criterion was measured and found to be correct in predicting the detonation of a supercritical acceptor charge with an axial end donor when this criterion was plotted as shock pressure required for initiation of detonation vs wave diameter. It was tentatively concluded that the critical geometry theory of initiation of detonation can be used to correctly predict if initiation will take place for the system geometry considered. It was also shown that for initiation of supercritical charges by axial end donors, the critical donor diameter was considerably less than (about 60%) the critical diameter of the acceptor.

4. CRITICAL DIAMETER PROGRAM

4.1 INTRODUCTION

Although the critical diameter of conventional Class II solid-composite propellants (i. e., propellants containing ammonium perchlorate oxidizer, aluminum, and an oxygen-lean binder such as polyurethane or PBAN) has never been determined experimentally, information available at the inception of the program suggested that it was very large. In the Beauregard Tests, solid cylindrical charges of Class II propellant 19 in. and 22 in. in diameter did not sustain a detonation when initiated on one end by a large high-explosive booster. Results of Aerojet theoretical studies conducted prior to Contract AF 04(611)-9945 were consistent with these experiments in that they indicated that the critical diameter of an ammonium perchlorate-polyurethane propellant was very large (approximately 660 in.).

Since the critical diameter of Class II solid-composite propellants was apparently so large as to economically preclude its direct measurement by full-scale tests, a method was required by which the critical diameter could be predicted from the results of small scale experiments. One approach is to modify the propellant so as to reduce the critical diameter to an economically practical level. There are several possible methods that might be used to accomplish this. For example, previous Aerojet studies have indicated that the critical diameter for porous AP composite propellants decreases as the pore content increases, and approaches the critical diameter of pure low-density ammonium perchlorate ($d_c \approx 1$ to 2 in.) for sufficiently large, homogeneously distributed pore contents. The critical diameter of a nonporous solid-composite propellant might then be estimated by extrapolation of the curve for critical diameter vs percent porosity back to zero porosity.

The approach adopted by Aerojet in the present program was to determine the critical diameters of composite propellant samples that had been adulterated with various percentages of a high explosive (RDX). The experimentally determined curve for critical diameter vs adulterant content was used as a guide in the development of a theoretical detonation model to predict the critical diameter of unadulterated Class II propellant.

As a subtask of the critical-diameter program, the usefulness of another technique for estimating the critical diameter of a propellant by sub-scale (subcritical size) testing was evaluated. This technique studies the decay rate of a detonation wave induced in a subcritical cylindrical

sample by an explosive booster and correlates this with the degree of subcriticality. A detailed quantitative understanding of the detonation process in the subcritical (nonsteady state) region was required. The analytical work associated with this approach was subcontracted to Shock Hydrodynamics, Inc. This work is reported in Appendix B.

4.2 OBJECTIVE

The objective of the critical-diameter program was to reliably predict the minimum (critical) diameter of a cylindrical sample of a typical Class II propellant that is capable of sustained detonation. This objective was accomplished as follows:

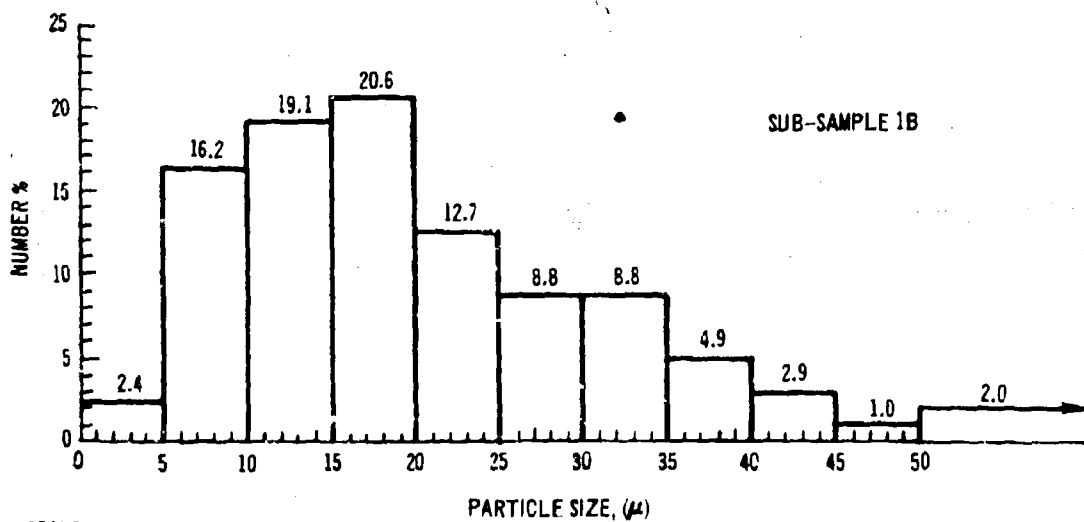
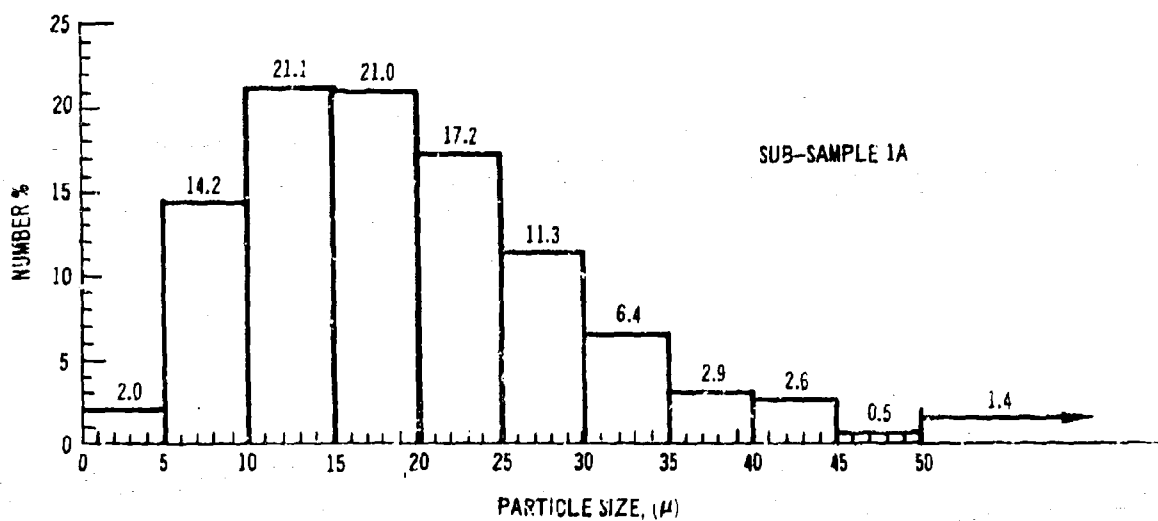
- a. The critical diameter of RDX-adulterated Class II propellant was determined as a function of RDX content.
- b. A theoretical detonation model, consistent with the experimental data for critical diameter vs RDX content was developed by modifying and refining a previously developed Aerojet detonation model for porous Class II propellants.
- c. The refined theoretical model was extrapolated to zero percent RDX to predict the critical diameter of the unadulterated Class II propellant.

4.3 EXPERIMENTAL PROGRAM

4.3.1 Propellant Processing

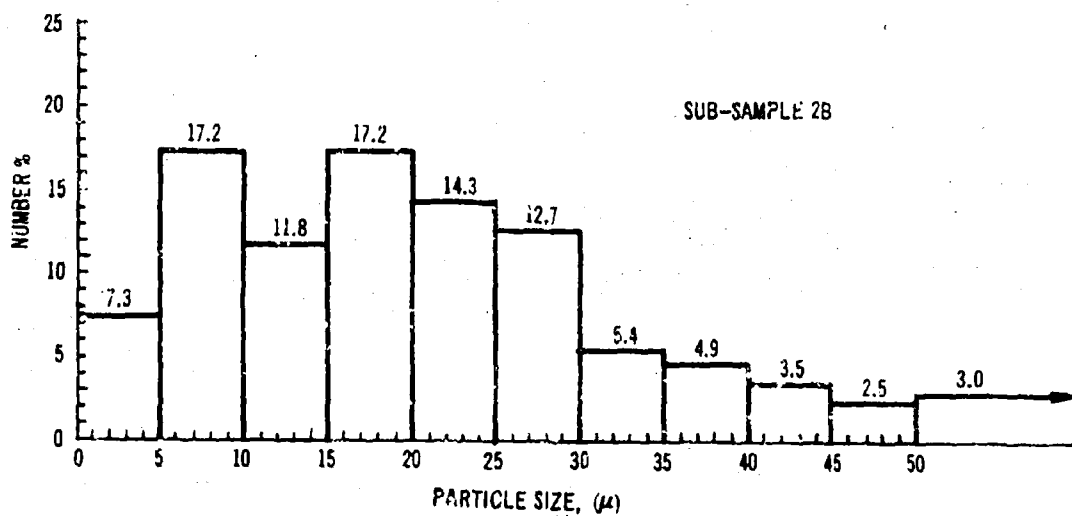
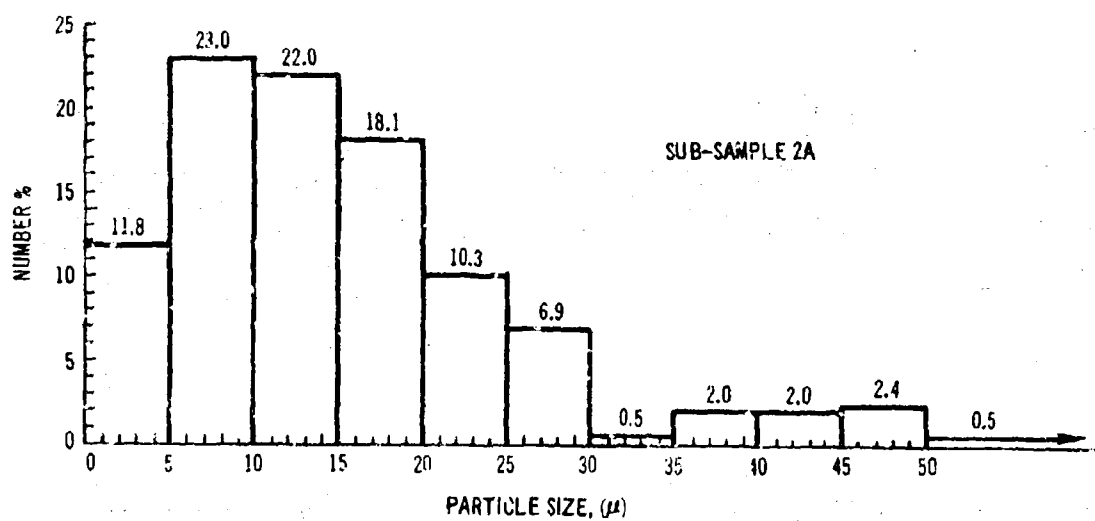
The AP-PBAN composite propellants (basic formulation: ANB-3105 CD) containing various percentages of explosive adulterant (RDX) used in all critical-diameter tests were mixed and cast according to previously developed manufacturing techniques that were known to yield good-quality propellant.

A single lot of Class-E (a small particle-size grade) RDX, obtained from the Holston Defense Corporation, Kingsport, Tennessee, was used to prepare all RDX-adulterated propellant batches. A particle-size analysis of this lot of RDX is presented in Figures 1 and 2.



2844-2

Figure 1. Particle-Size Analysis of RDX Crystals
(Sample 1; Drawn 29 June 1964).



2844-2

Figure 2. Particle-Size Analysis of RDX Crystals
(Sample 2; Drawn 13 September 1964).

4.3.2 Propellant Quality Control

Because of the known strong influence of porosity on critical diameter, it was essential that the porosity content of all RDX-adulterated propellant samples used in this program be consistently held to the lowest level attainable with present processing techniques.

Two methods were used to monitor the void content of RDX-adulterated propellants. They were: (1) comparison of density measurement on uncured (liquid) and cured (solid) samples from each batch of propellant, and (2) X-ray examination of the test articles. In the first method, the uncured propellant was used as the reference material and was assumed to have no porosity. Development of voids during curing would presumably be indicated if the density of the cured propellant is lower than the density of the liquid propellant. Since the density of the propellant always increases slightly during curing, there was some question as to the ability of this method to detect low concentrations of uniformly distributed small voids, i. e., the cured propellant could be slightly porous and still have a density equal to or slightly above that of the uncured liquid "reference" propellant. X-ray examination of the test articles was useful only for detection of gross flaws such as entrapped gas bubbles in the propellant.

A promising technique for detecting low concentrations of uniformly distributed small voids involves the microscopic examination of thin sections of the propellant under various types of lighting, using procedures previously developed at Aerojet's Solid Rocket Operations (SRO). In the previous studies it was found that all propellant constituents as well as any internal flaws in the oxidizer or separations between fuel and oxidizer, could be easily located on the photomicrographs. The photomicrographs of AAB-3172 propellant, containing 3.25 wt % RDX (Figure 3), demonstrated excellent wetting of all solid constituents by the binder. No interstitial voids were detected. However, a few internal defects were present in the oxidizer particles. It may be expected that such voids will have a significant effect upon the critical diameter if present in sufficiently high concentration.

It can be seen in these photomicrographs that the propellant sample is essentially free of voids. This was not unexpected, since past experience indicated that the large gas bubbles entrapped during mixing were easily removed during vacuum casting and that small voids (i. e., uniformly distributed porosity) were not observed unless gas formation occurred as the propellant reached the gel point during cure. Unlike polyurethane, the PBAN binder was not susceptible to such gas-forming reactions.

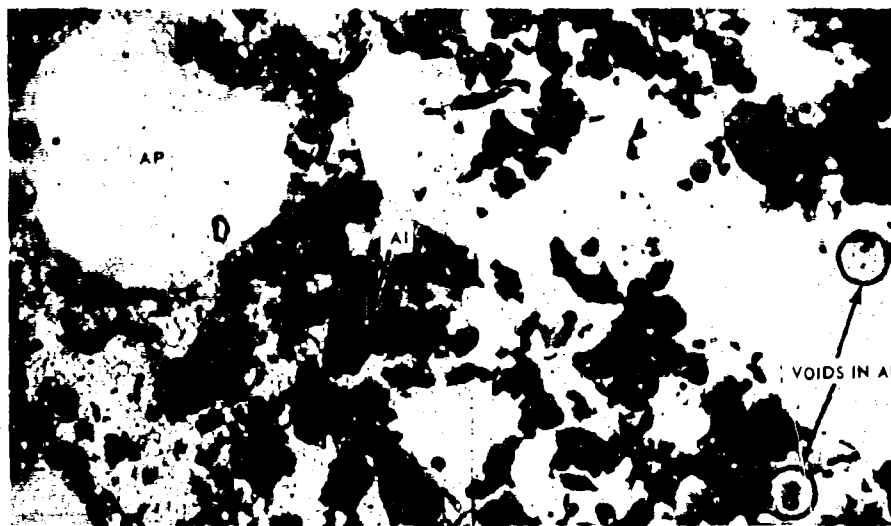
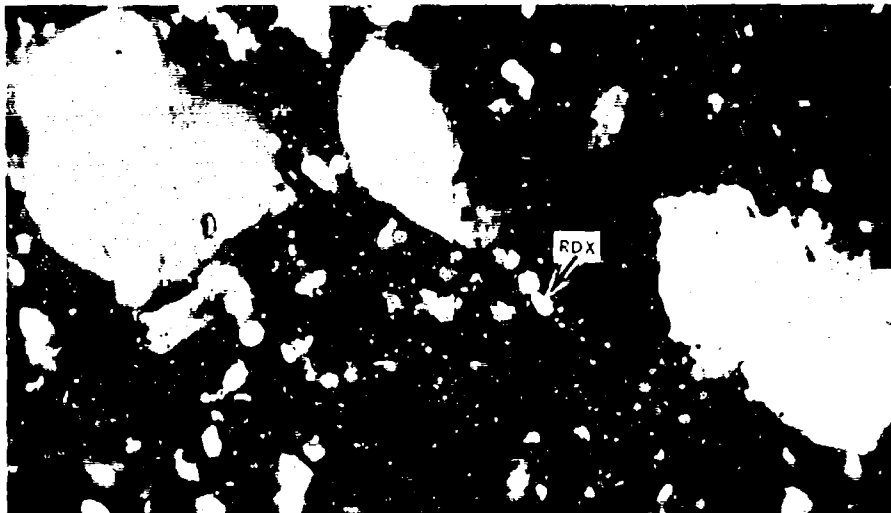


Figure 3. Photomicrographs of AAB-3172 Propellant (3.25 wt % RDX)
Showing AP, Al, RDX, and Internal Voids in AP Crystals.

Individual RDX crystals in an AAB-3188 propellant sample (9.0 wt % RDX) can be clearly identified by the use of phase-contrast dark-field microphotography (Figure 4). It is apparent that there was considerable agglomeration of the smaller RDX particles. In one case (see Figure 4) two aggregates of small RDX particles, that were nearly touching had an overall width of approximately 60 μ . It is probable that such a region would be essentially as effective as a single 60 μ . RDX particle with respect to its ability to initiate an adjacent AP grain.

4.3.3 Propellant Mold Design

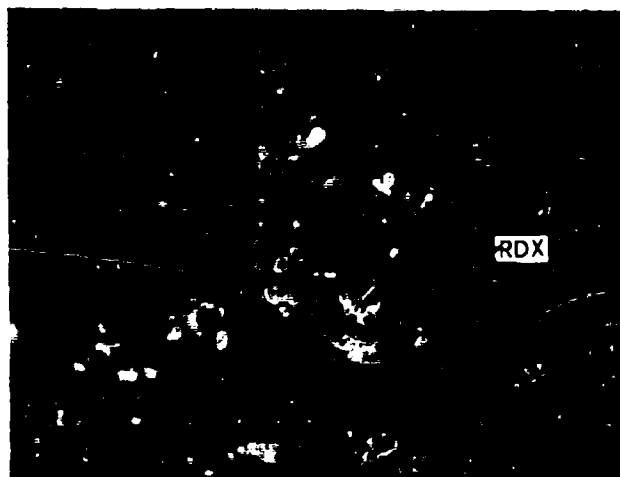
While it is desirable to conduct critical diameter tests with bare charges to avoid the unknown effects of confinement, the original test plan provided for steel confinement of the samples, with the case thickness increasing as the charge diameter increased, since it was believed that the larger charges would deform excessively under their own weight plus the weight of the booster if unconfined.

Stress calculations, based on the physical properties of unadulterated PBAN propellant, and measurements of the load that samples of RDX-adulterated propellant could sustain without gross deformation, indicated that even the largest critical-diameter samples to be tested in the program (48-in. diameter by 192 in. length, 22,000 lb) could be tested unconfined without significant deformation, even under the added load of a 5000-lb explosive booster. It was therefore decided to test all samples without confinement. This permitted simplification of the original design for the steel casting chambers (Figure 5) by elimination of the holes for insertion of pin-probes and viewing of the propellant by a streak camera. A modified chamber is shown in Figure 6. The inside walls of all chambers were coated with mold release to facilitate removal of the cured propellant samples.

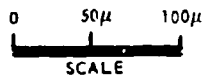
4.3.4 TNT Booster Preparation

4.3.4.1 Booster Mold Design

The booster molds were designed as modular segments to facilitate casting, handling, and shipping. Each module was designed to approximate a 3:1 cone by stacking cylinders with a 4-in. change in diameter/foot of length since the purely conical shape was more expensive to fabricate. The cylindrical shape also provided greater mechanical strength for the charge when the base plate used in casting was removed at the test site. Figures 7 and 8 illustrate the donor design and the assembly to the propellant charge.



PHASE CONTRAST, DARK FIELD SHOWS RDX



**Figure 4. Photomicrograph of AAB-3188 Propellant (9.0 wt % RDX)
Using Phase Contrast, with Dark Field, Showing Distribu-
tion of RDX Particles (250X).**

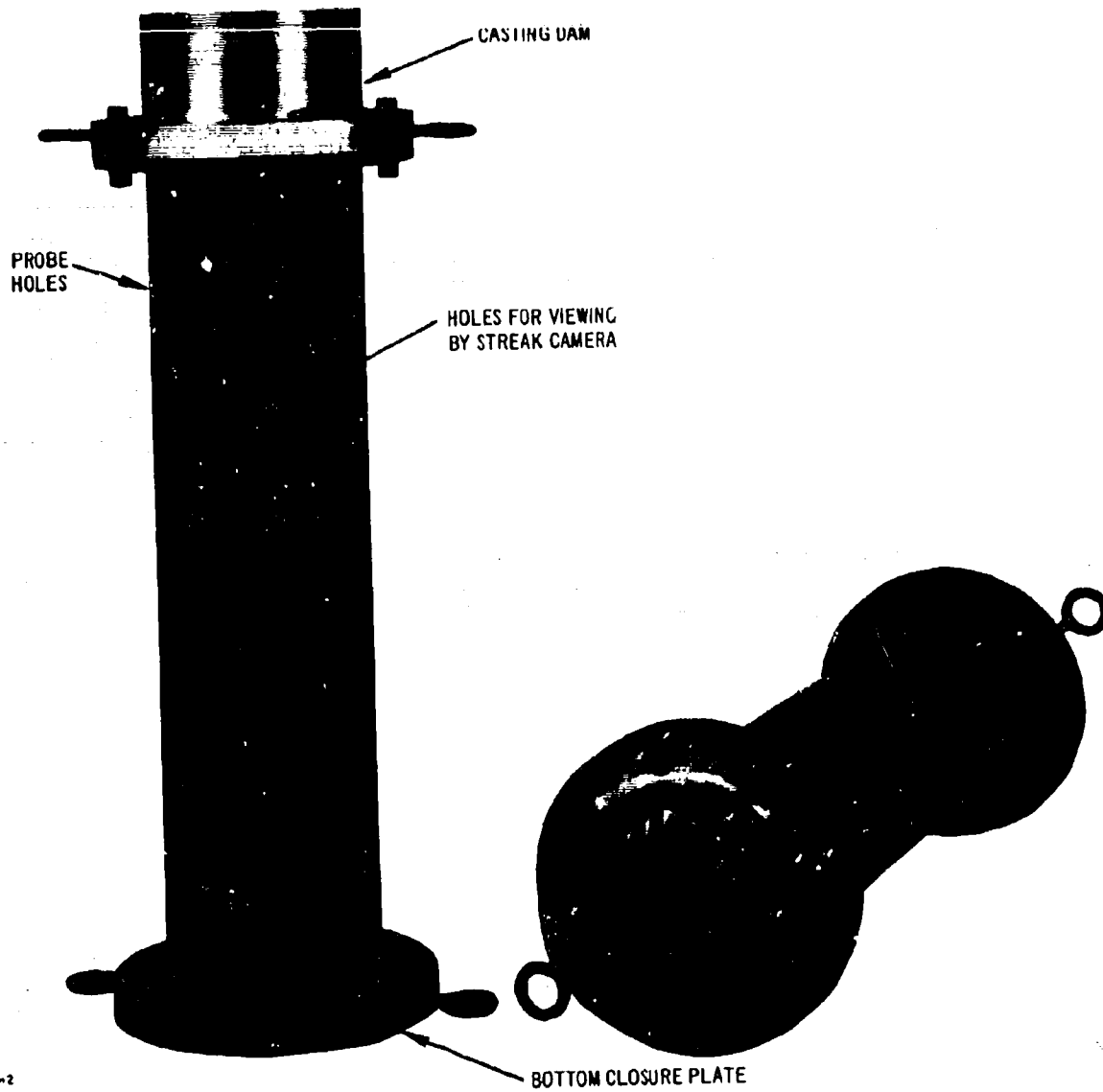


Figure 5. Typical Steel Chamber Used for Propellant Samples
27 in. in Diameter and Smaller.

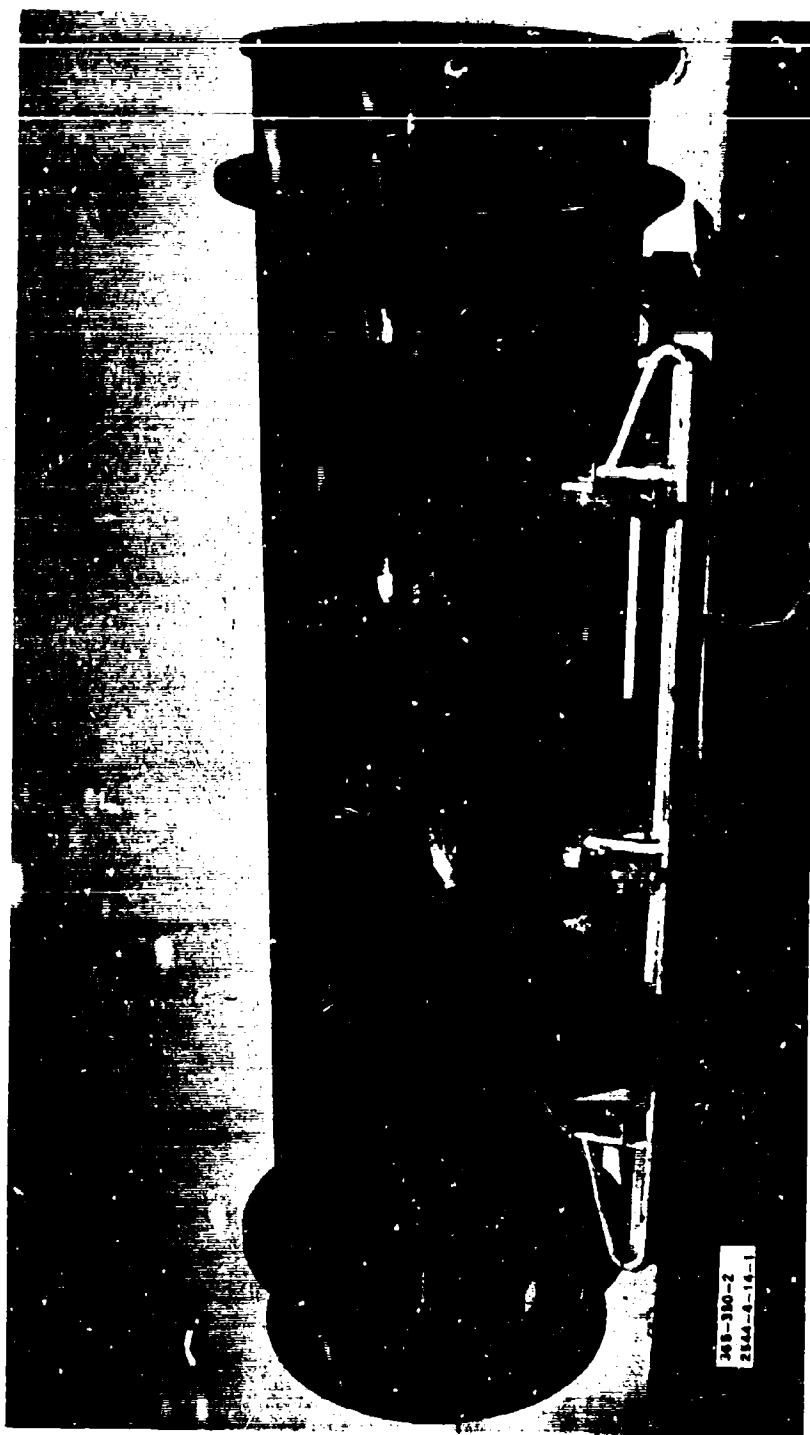


Figure 6. Side View of Casting Chamber for 48-in.-Diameter Propellant Charge.

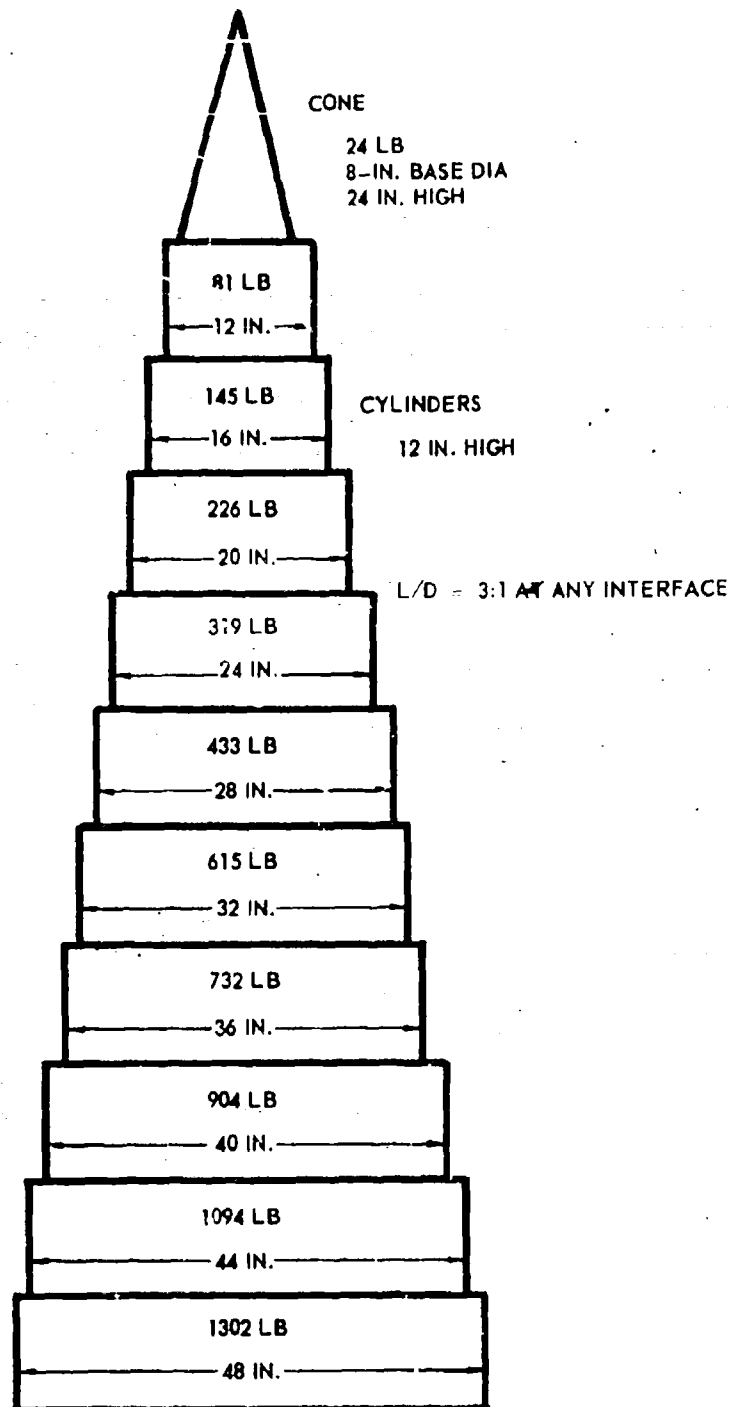


Figure 7. Modular Concept of TNT Explosive Donor.

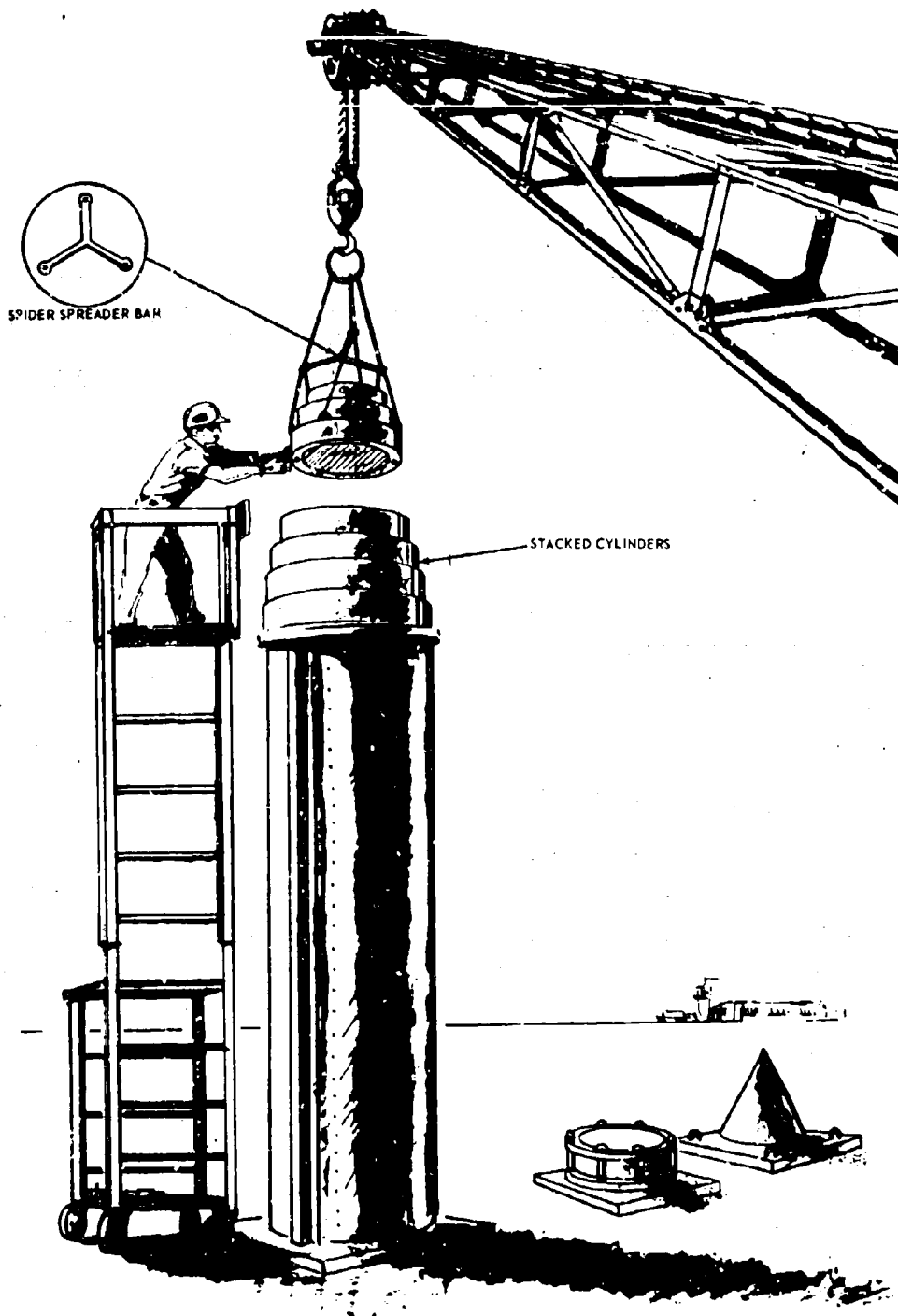


Figure 8. Donor Configuration and Handling.

Each mold consisted of a series of cylindrical castings stiffened by plywood rings. A retainer ring inside each cylinder supported the casting and prevented the explosive from falling out when the bottom plate was removed from the charge. Provisions for handling the charge assembly were provided by six lifting lugs around the lower segment of each module. Figure 9 is a typical cross-section of the mold.

4.3.4.2 Booster Casting Technique

A slurry casting technique was used for casting the booster segments to minimize shrinkage problems resulting from the large contraction that occurs during the solidification of TNT. This technique, which consists of alternately introducing TNT chips (previously prepared from vacuum-melted TNT) and molten TNT into the mold, permits the solid TNT chips to act as a heat sink for the molten TNT, thus minimizing shrinkage. A molten-to-solid TNT ratio of approximately 1:1 was used.

4.3.5 Test Plan

The basic test plan consisted of determining the critical diameters of AP-PBAN composite propellant formulations in which decreasing levels of RDX adulterant have replaced equal weights of AP. The results of each group of tests, together with a concurrently developed theoretical model, were used to select the adulterant level that would bring the critical diameter within the diameter range of the next group of samples. Six test groups with nominal diameters of 1-1/2, 3, 6, 12, 24, and 48 in. were chosen to provide experimental data over a considerable range of diameters and RDX contents. The original test plan, with the anticipated RDX levels for each group is shown in Table 1.

Table 1. Critical Diameter Test Plan.

<u>Test Group</u>	<u>Sample Diameter</u>	<u>Number of Samples</u>	<u>Anticipated RDX Level</u>
1	1-1/4 to 2 in.	32	16 wt %
2	2 to 4 in.	16	12 to 16 wt %
3	6 to 9 in.	8	10 to 14 wt %
4	11 to 14 in.	8	8 to 12 wt %
5	18 to 27 in.	8	6 to 10 wt %
6	48 in.	4	2 to 8 wt %

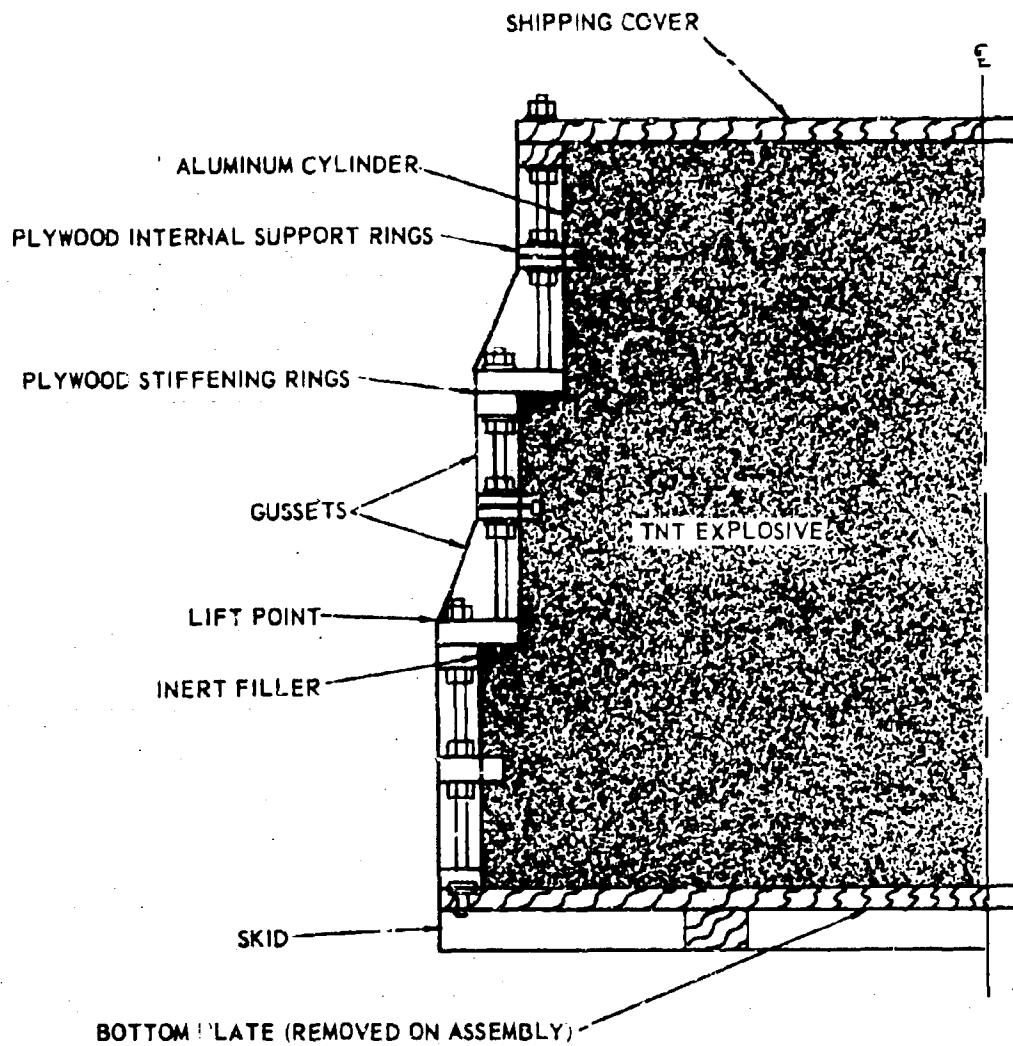


Figure 9. Typical Cross-Section View of Explosive Mold.

In addition to the test groups shown in Table 1, three auxiliary detonability tests were scheduled with unadulterated AP composite propellant cast into Minuteman chambers (two second-stage chambers, 44 in. in diameter and one first-stage chamber, 65 in. in diameter). Also, five additional (subcritical) unadulterated AP-PBAN propellant samples were to be tested for the rate of fading of an induced detonation wave, in support of a subcontractor's (Shock Hydrodynamics, Inc.) theoretical studies; because of problems in fabricating satisfactory probes for monitoring detonation velocity at the center of the subcritical samples, these tests were not performed.

4.3.5.1 Test Procedure

All critical diameter tests were conducted with solid cylindrical propellant samples having a length/diameter ratio of at least 4:1. Detonation was initiated by conical high-explosive boosters (cast TNT) with a height/base ratio of 3:1. The basic test setup consisted of the propellant sample, placed vertically on a steel witness plate (supported above the ground by wooden blocks) with a booster resting on top of the propellant charge. The velocity of the detonation wave induced in the propellant by detonation of the booster was monitored, as it propagated down the test sample, by two rows of pin probes placed along opposite sides of the charge, and by high-speed streak photography. Testing of propellant charges of 100 lb or less (nominally 8 in. in diameter) was conducted at the Aerojet Chino Hills Ordnance Laboratory. Testing of larger propellant charges was conducted at the 1-36D Solid Hazards Test Facility of the Air Force Rocket Propulsion Laboratory.

In the AFRPL tests, side-on blast overpressure was measured at 15 positions, arranged on three radial lines 120° apart (5 positions per line), and face-on overpressure on one radial line (5 positions). The Kistler piezoelectric-transducer and charge-amplifier system was used to monitor all blast data, which was then recorded on a high-speed magnetic tape recorder. The data was played back at a lower speed, to permit an effective time expansion of the data, for recording on a CEC string galvanometer oscillograph. Heat flux and thermocouple data from the thermal radiation emitted in the large tests were recorded directly on the string galvanometer oscillograph. Documentary and high-speed (Fastax) film coverage was provided on all AFRPL tests. The layout of the 1-36D Test Facility is shown in Figure 10.

The test setup used for instrumented critical diameter tests of the samples in Table 1 is illustrated by Figures 11 and 12.

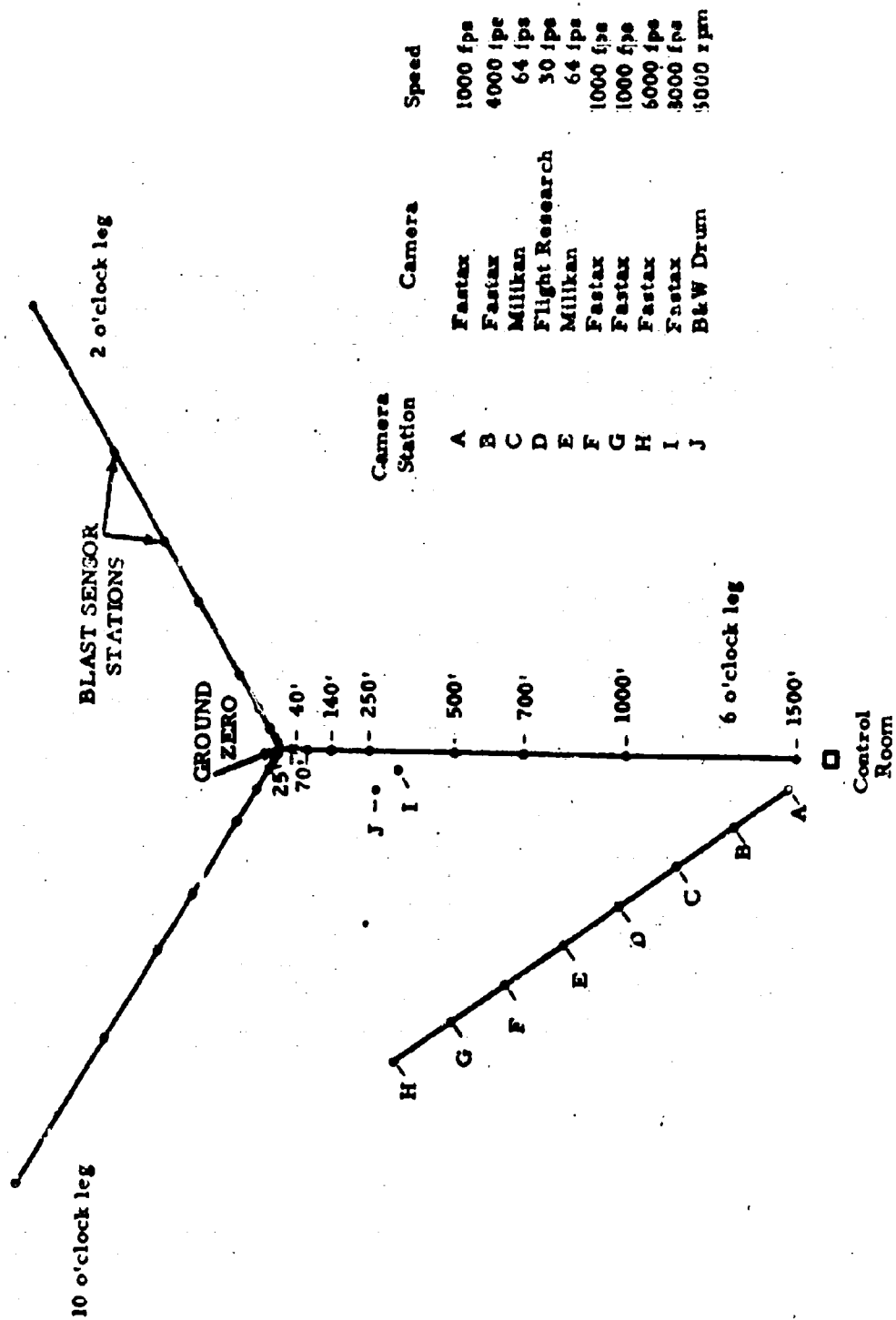


Figure 10. Schematic of AFRPL 1-36D Solid Hazards Test Facility.

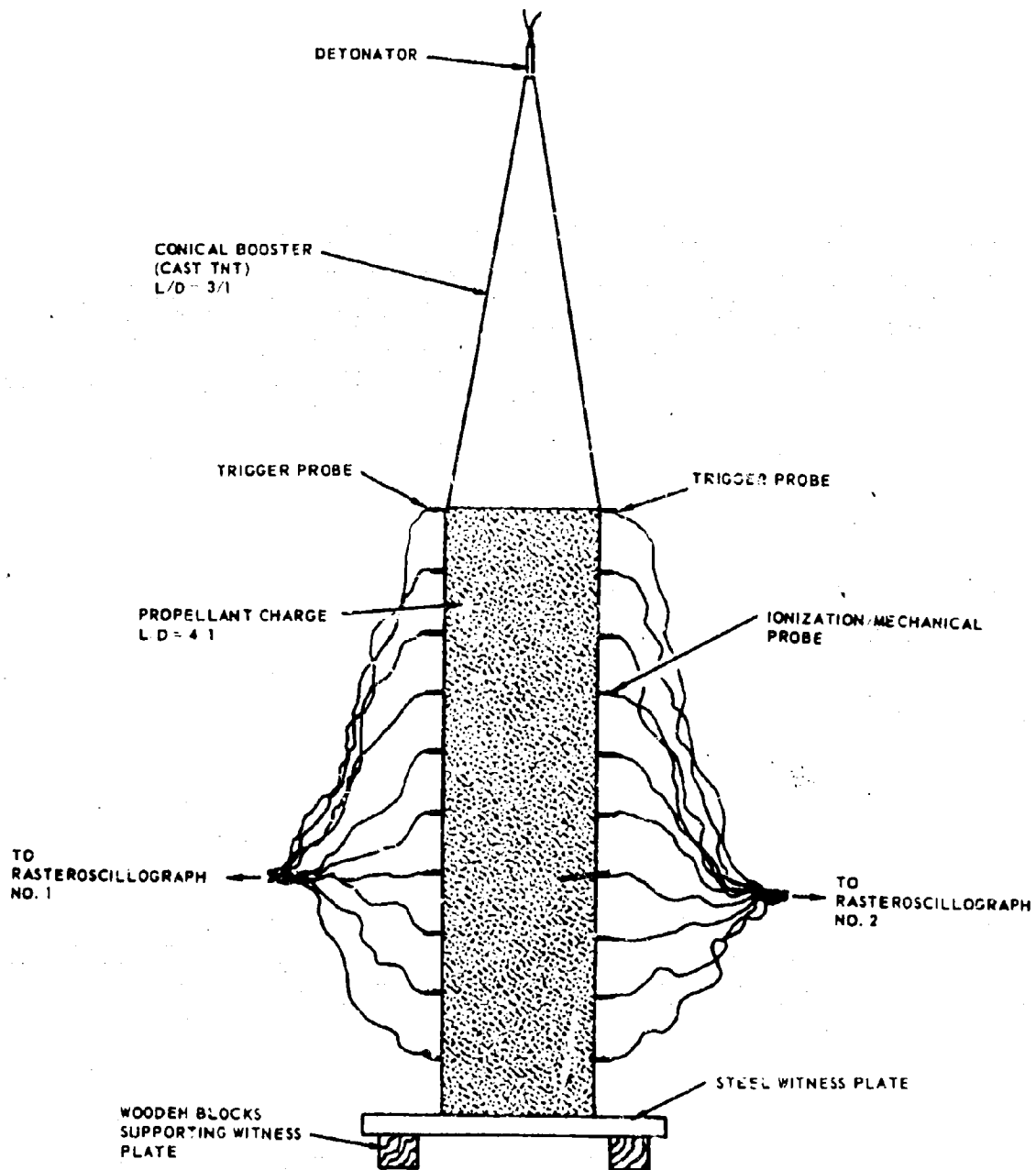


Figure 11. Typical Critical Diameter Test Setup.

ERRATA

1. Page iii. Remove and insert new page iii, attached.
2. Page 55, Equation (6). Add " ℓ " after "distance."
3. Page 62, Equation (20). Add " $+1/3$ " at end of equation.
4. Page 65. Remove and insert new page 65, attached.
5. Page 108. Remove and insert new page 108, attached.
6. Page 161. Remove and insert new page 161, attached.
7. Page 201, 4th paragraph. Delete and substitute:

"The best results were obtained with Class E (MIL-R-3980, 95% minimum 325 mesh) RDX. The study also showed the feasibility of casting into molds of various shapes without any special problems in curing or in releasing the samples."

ABSTRACT

The purpose of this program was to evaluate the detonation characteristics of large rocket motors containing conventional solid-composite Class II propellants. The general approach taken was to first determine the critical diameter of a Class II propellant and then, by means of a critical geometry theory, predict the minimum size of a hollow-cored rocket motor grain of Class II propellant capable of sustaining detonation as well as the effect of donor size, configuration, and location on the initiation of detonation in the grain.

The critical diameter of a typical Class II propellant (AP-PBAN type) was estimated to be about 75 in. based on the results of a combined experimental and theoretical study on the effect of RDX adulterant on the critical diameter of the basic AP-PBAN formulation.

The validity of a previously devised theory of critical geometry was tested using an RDX-wax explosive and a PBAN-RDX explosive. The experimentally determined critical dimensions of the various shapes tested were in reasonable agreement with predictions of the theory. The initiation criterion proposed by the critical geometry theory was measured and found to correctly predict the initiation of detonation in a supercritical acceptor charge by an axial, end donor. Supercritical charges could be initiated to detonation by an axial, end donor the diameter of which was only about 40 % of the critical diameter of the acceptor.

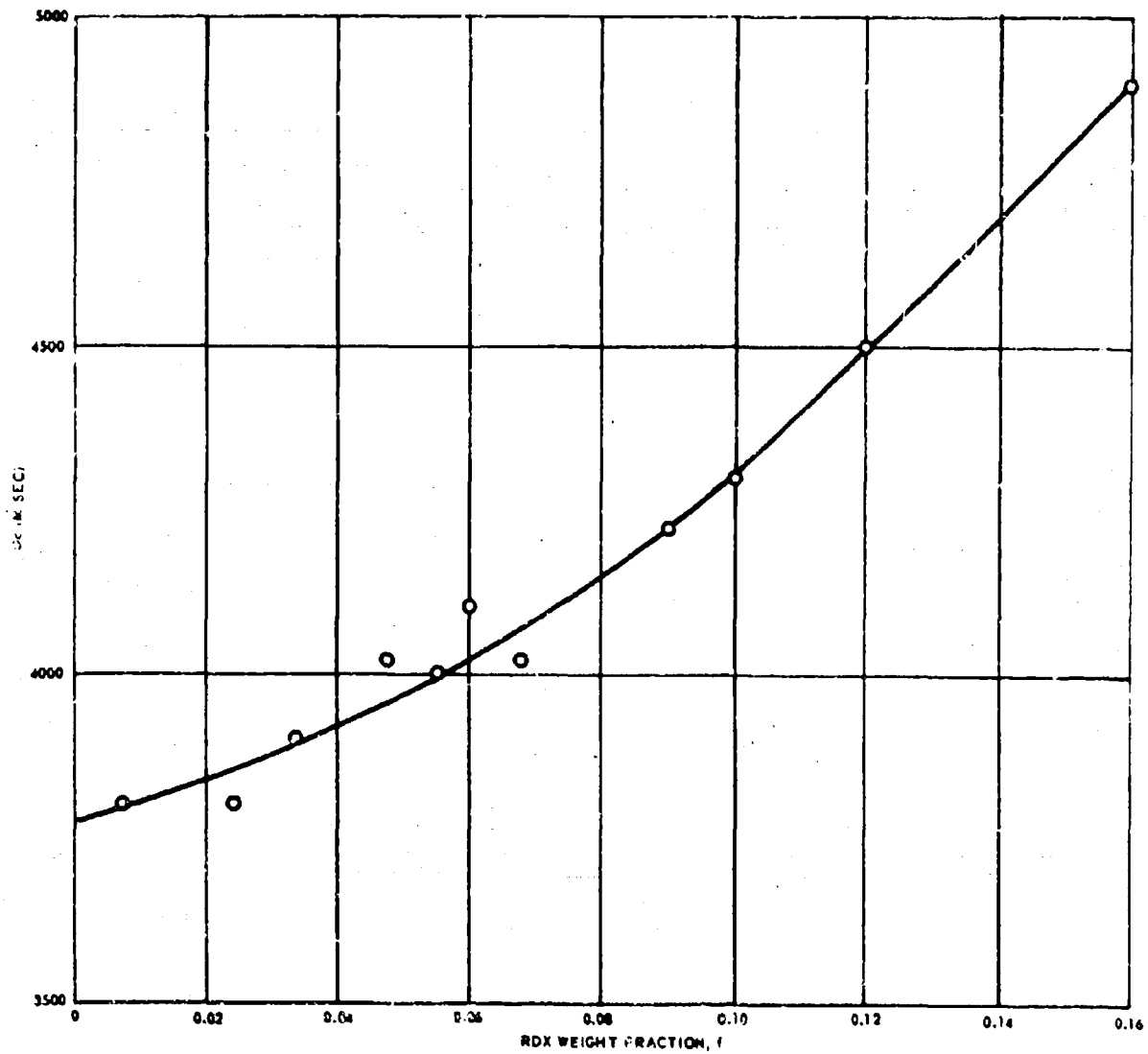


Figure 39. Estimated Critical Detonation Velocity vs RDX Content
for RDX-Adulterated PBAN Propellants.

$$d_{oc} = \frac{d_c}{2} \left[1 + \sqrt{1 + \frac{16\lambda}{\pi d_c} \left(5 \frac{\lambda}{d_c} + 3 \right)} \right]$$

$$\lambda = 0.475 \text{ IN.}$$

$$d_c = 2.66 - 2.80 \text{ IN.}$$

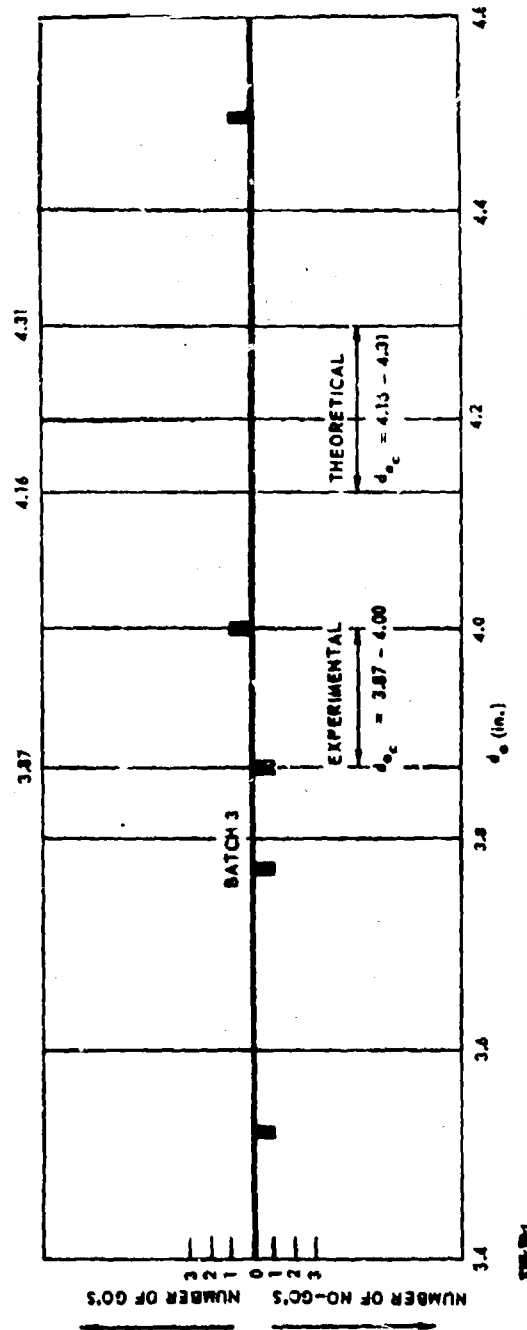
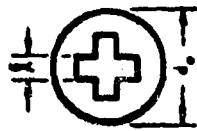


Figure 59. Analysis of Critical Cross-Core
Cylinder Tests - PBAN-RDX.

where the integration is made over the entire wave surface. Knowing that the equation of the circles being considered is

$$(x + h)^2 + y^2 = r^2$$

it is easy to show that

$$dA = 2 \pi r \, dx \text{ and}$$

$$\int_0^A dA = \int_{x_0}^{x_1} 2 \pi r \, dx$$

or

$$A = 2 \pi r (x_1 - x_0)$$

Substituting above gives

$$\bar{P} = 1/(x_1 - x_0) \int_{x_0}^{x_1} P \, dx$$

When $r \leq 2$ or if $r > 2$ and $h > \sqrt{r^2 - 4}$ this becomes

$$\bar{P} = 1/(r-h) \int_0^x P \, dx$$

and when $r > 2$ and $h < \sqrt{r^2 - 4}$ this becomes

$$\bar{P} = \frac{1}{r - \sqrt{r^2 - 4}} \int_{x_0}^{x_1} P \, dx$$

The value of the integral, $\int P \, dx$ (which is contained in both expressions) was found by numerically integrating the shock-pressure (vs x) data mentioned above for each wave profile and the average pressure found from the values of r , h , x_0 , and x_1 for that profile. These results are also listed in Table 23.

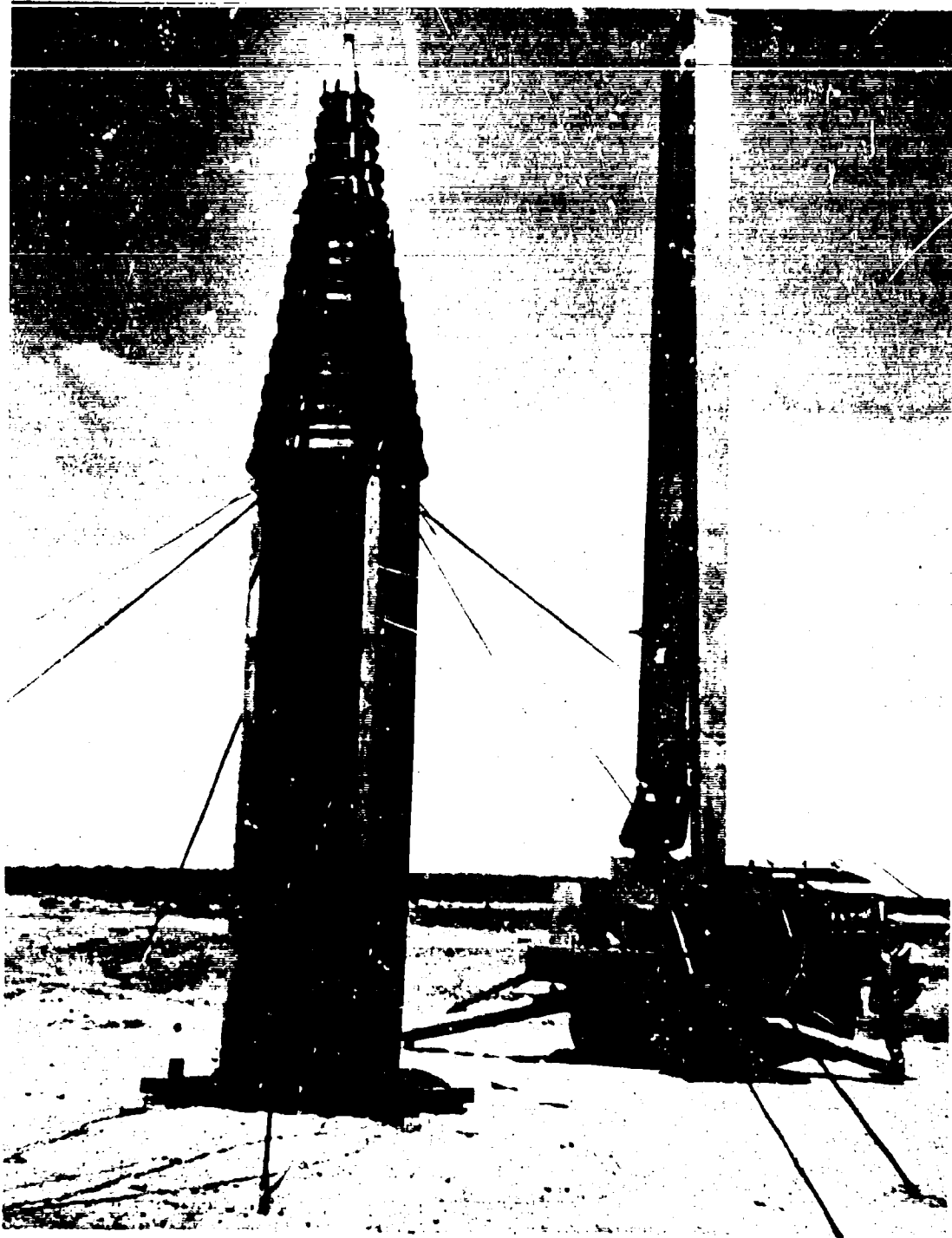


Figure 12. Test Setup, Critical Diameter Test of 48-in. -Diameter
RDX-Adulterated PBAN Propellant Charge.

To permit the propellant samples contained in the first- and second-stage steel Minuteman chambers (see Section 5.1.2.5) to be tested in a configuration approaching that of the conventional critical diameter tests, the following operations were required:

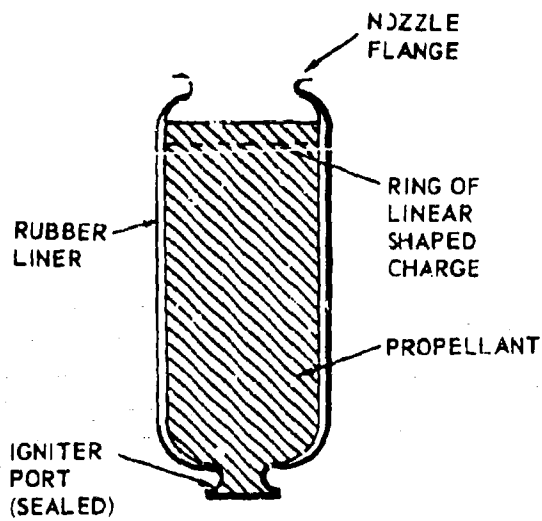
- a. Removal of the steel case above the free surface of the propellant charge by cutting with linear shaped charge.
- b. Inverting of the chamber and placing the exposed propellant surface on a steel witness plate.
- c. Forming a full-diameter, flat top surface, for mating with the TNT booster, by wrapping an aluminum sheet around the chamber, with the top edge of the aluminum level with the igniter port, and packing the resulting annulus with C-4 explosive.
- d. Improvising detonation velocity probes by mounting a vertical row of duPont T-1 targets along the outside of the steel case (with a 1/4-in. gap between the target faces and the case).

These steps are illustrated in Figure 13. The resulting test setup for a modified second-stage Minuteman chamber is shown in Figure 14.

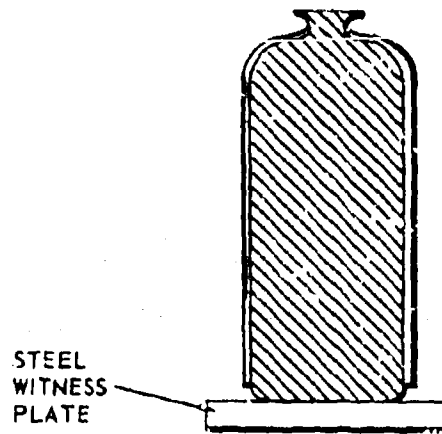
Various combinations of the following types of detonation velocity probes were used in the critical diameter tests. These are: (1) ionization probes, consisting of either coaxial or parallel conductors separated by a thin layer of insulating resin, (2) combined ionization/mechanical probes, in which closure of the electrical circuit was accomplished either by the ionized detonation wave passing across the separated electrical conductors at the end of the probe or by crushing and shorting of the probe by the mechanical action of the wave, and (3) a mechanically actuated shorting switch (duPont T-1 or T-2 targets).

A Beckman and Whitley model 194 streak camera was used in the first 39 tests conducted at the Chino Hills Ordnance Laboratory. A Barr and Stroud model CP-6 streak camera was used in the remaining CHOL tests. An Aerojet-modified Beckman and Whitley Model 224 drum camera was used in the first 16 tests conducted at AFRPL. The remaining six tests were conducted without high-speed streak photography because of deteriorating performance of the drum camera.

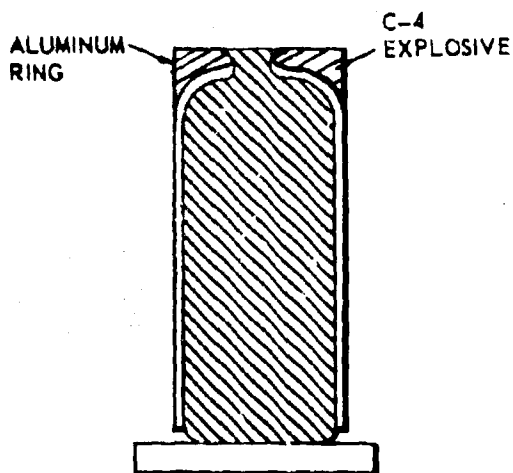
High-speed photographic coverage of the AFRPL tests was provided by a line of eight cameras as shown in Figure 10.



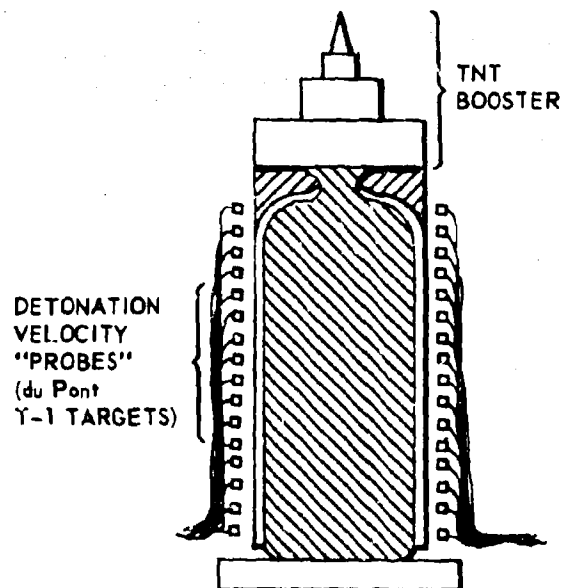
(1) CUTTING OF NOZZLE FLANGE
WITH LINEAR SHAPED CHARGE



(2) PLACING OF INVERTED CHAMBER, WITH
NOZZLE FLANGE REMOVED, ON STEEL
WITNESS PLATE



(3) PACKING OF COMPOSITION C-4
EXPLOSIVE TO PROVIDE FLAT
INTERFACE FOR TNT BOOSTER.



(4) COMPLETED CHARGE, WITH TNT
BOOSTER IN PLACE

Figure 13. Preparation of Unadulterated PBAN Propellant Charge in
Second-Stage Minuteman Chamber for Critical Diameter Test.



Figure 14. Test Setup, Critical Diameter Test of Unadulterated PBAN Propellant in Second Stage Minuteman Chamber.

All witness plates were fabricated from hot-rolled steel stock. The thickness of the plates was scaled approximately linearly with propellant sample diameter for samples up to 27 in. in diameter (see Figure 15). Three 48-in.-diameter samples of RDX-adulterated propellant and two samples of unadulterated AP-PBAN propellant were tested on 4-in.- and 2-in.-thick plates, respectively, instead of the 6- to 7-in.-thick plates required by an extrapolation of the linear scaling used on the smaller samples.

4.3.6 Data Reduction

The rasterscillograph records of the probe data and the streak camera records from each test were converted to distance-time information which was then transformed to average velocity data by a standard numerical differentiation technique (Reference 1). The criterion for sustenance of detonation was the stabilizing of the velocity of the wave at some essentially constant value after the high-velocity detonation wave from the booster had decayed in the first half of the charge. Although minor fluctuations of the successive data points were usually observed in a sustained detonation, there was no difficulty in distinguishing this behavior from the fading detonation wave in a subcritical sample. In all tests the witness plate results confirmed the indications of the probe and streak camera records, i. e., sustained detonations created sharp-edged full-diameter dents or holes in the plates, while the fading waves in the subcritical samples caused only gross bending of the plates.

4.3.7 Experimental Results

The results of the tests performed on the critical diameter program are summarized in Table 2 and Figure 16 (tests CD-1 through CD-12, which were preliminary witness-plate tests to verify the selection of an RDX level of 16 wt % for the first test group, are not included). The variation of detonation velocity with distance along the sample, for the tests that bracket the critical diameter for the propellant formulations presented in Table 2, are shown in Figures 17 through 34. It should be noted that the curves drawn through the data points are eye-fits only, and are presented to indicate the trend of the data.

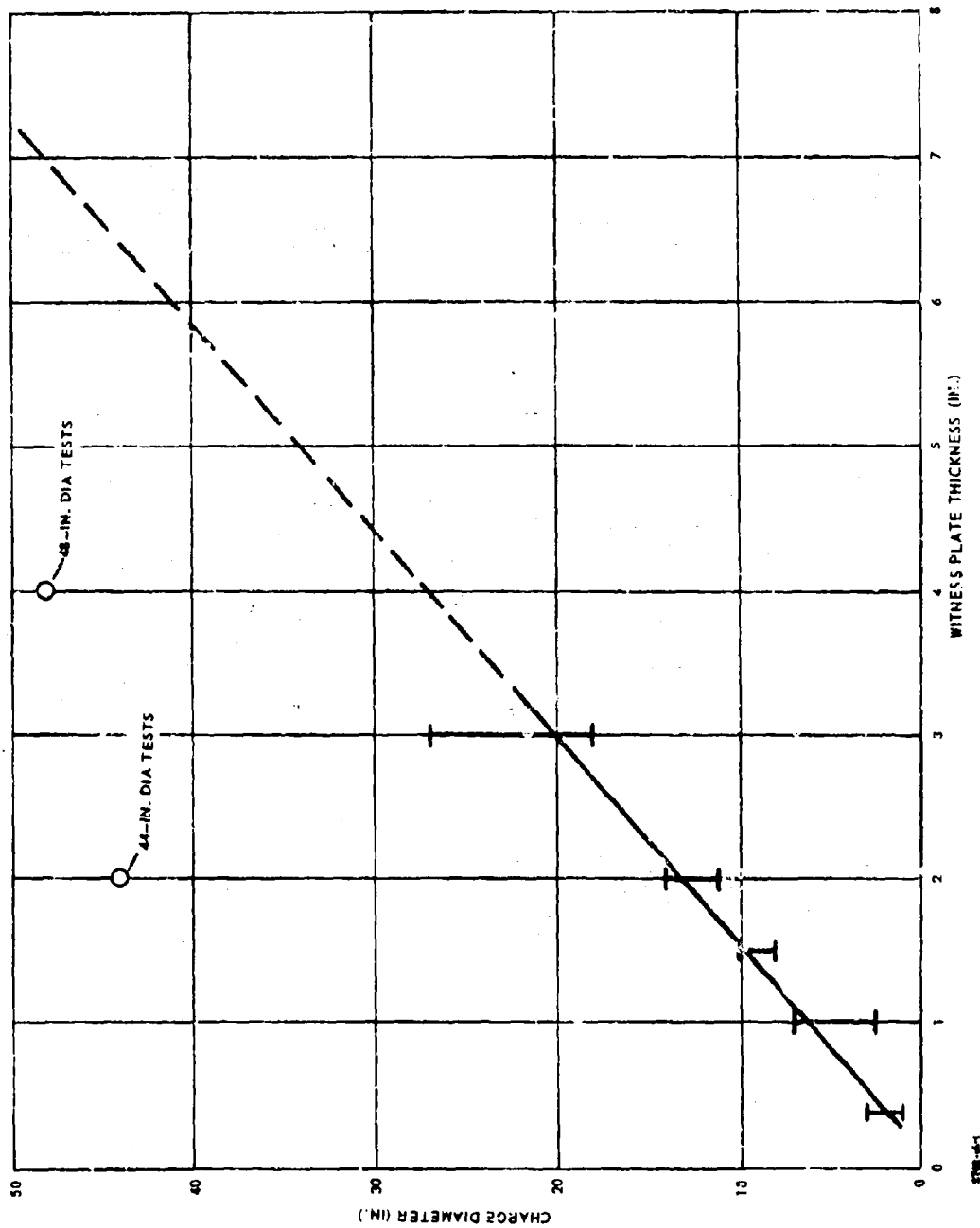


Figure 15. Scaling of Witness Plate Thickness with Charge Diameter.

Table 2. Summary of Test Results of Critical Diameter Program.

Propellant Designation	KDX Content (wt. %)	Nominal Sample Dimensions Dia x Length (in.)	Test No(a)	Test Results*			Average Steady State Detonation Velocity (mm/ μ sec)
				Probe	Streak Camera	Witness Plate	
AAB-3163	16.0	1 x 8	CD-47	-	-	-	--
		1 x 8	CD-45	+	+	+	4.886 (13)
		1.25 x 16 (b)	CD-18	-	No Data	-	--
		1.25 x 12 (c)	CD-29	+	+	+	4.932 (27)
		1.25 x 8	CD-15	+	+	+	5.014 (5)
		1.25 x 8	CD-44	+	+	+	5.063 (6)
		1.5 x 8	CD-13	No Data	+	+	5.187 (1)
		1.5 x 8	CD-14	No Data	+	+	5.054 (1)
		1.5 x 8	CD-19	No Data	+	+	5.384 (11)
		1.5 x 8	CD-20	No Data	+	+	5.245 (5)
		1.5 x 8	CD-27	+	+	+	5.199 (7)
		1.75 x 8	CD-21	(d)	+	+	5.141 (1)
		1.75 x 8	CD-22	(d)	+	+	5.098 (6)
		1.75 x 8	CD-26	+	+	+	5.194 (6)
		1.75 x 8	CD-28	+	+	+	5.362 (10)
		1.75 x 8	CD-31	+	+	+	5.136 (10)
		2 x 8	CD-23	+	+	+	5.125 (5)
		2 x 8	CD-24	+	+	+	5.233 (4)
		2 x 8	CD-25	+	+	+	5.194 (6)
		2 x 8	CD-30	+	+	+	5.220 (11)
AAB-3164	12.0	1.3 x 10	CD-46	-	-	-	--
		1.53 x 8	CD-43	+	+	+	4.574 (5)
		1.63 x 8	CD-42	+	No Data	+	4.620 (4)
		2 x 8	CD-16	+	+	+	4.726 (10)
		2 x 8	CD-17	No Data	No Data	+	--
		2.5 x 10	CD-32	+	+	+	4.831 (12)
		2.5 x 10	CD-33	+	+	+	4.876 (8)
		2.5 x 10	CD-36	+	+	+	4.988 (4)
		3 x 12	CD-34	+	No Data	+	4.957 (6)
		3 x 12	CD-35	+	+	+	4.973 (7)
		3 x 12	CD-41	+	+	+	4.906 (13)
		3 x 12	CD-48	+	No Data	+	4.852 (16)
		3.5 x 14	CD-38	(d)	No Data	+	--
		3.5 x 14	CD-39	(d)	No Data	+	--
		4 x 16	CD-37	+	+	+	4.936 (8)
		4 x 16	CD-40	(d)	+	+	4.070 (4)
		4 x 16	CD-49	+	No Data	+	4.848 (8)

(a) Includes all tests except CD-1 through CD-12, which were preliminary witness plate tests.

(b) Test charge consisted of two 8-in. -long charges placed end-to-end.

(c) Test charge consisted of a 4-in. -long charge placed on top of an 8-in. -long charge.

(d) Streak camera not used.

(e) Tested in 0.023-in. thick steel confinement.

(f) Unadulterated PBAN propellant in second-stage Minuteman chamber.

** = steady-state detonation; - = failing detonation.

Numbers in parentheses indicate number of data points used in computing average detonation velocity.

Table 2 (Continued).

Propellant Designation	RDX Content (wt %)	Nominal Sample Dimensions Dia x Length (in.)	Test No.(a)	Test Results*			
				Probes	Camera	Witness Plate	Average Steady State Detonation Velocity (mm/μsec)
AAB-3187	10.0	1.5 x 6	CD-73	-	No Data	-	--
		1.75 x 7	CD-63	-	-	-	--
		2.5 x 10	CD-62	+	+	+	4.372 (5)
		2.5 x 10	CD-66	+	+	+	4.299 (8)
		3 x 12	CD-59	+	+	+	4.568 (5)
		3 x 12	CD-65	+	+	+	4.463 (11)
		4 x 16	CD-69	+	No Data	+	4.660 (6)
		4 x 16	CD-70	+	No Data	+	4.678 (6)
AAB-3188	9.0	1.75 x 7	CD-72	-	No Data	-	--
		3 x 12	CD-60	-	-	-	--
		3 x 12	CD-64	-	No Data	-	--
		4 x 16	CD-61	No Data	+	+	4.276 (1)
		4 x 16	CD-68	+	+	+	4.368 (11)
		5 x 20	CD-67	+	No Data	+	4.510 (12)
		7 x 28	CD-71	+	No Data	+	4.568 (12)
		6 x 24	CD-54	-	-	-	--
AAB-3176	6.75	8 x 32 (e)	CD-55	+	+	+	4.192 (20)
		10 x 40	CD-53	+	+	+	4.236 (11)
		12 x 48	CD-56	+	+	+	4.381 (5)
		9 x 36	CD-78	+	No Data	+	4.163 (9)
AAB-3192	6.0	13 x 52	CD-93	+	(d)	+	4.408 (16)
AAB-3165	5.5	14 x 56	CD-75	+	No Data	+	4.269 (10)
AAB-3191	4.75	10 x 40	CD-77	-	No Data	-	--
		11 x 44	CD-79	-	No Data	-	--
		12 x 48	CD-80	+	No Data	+	4.119 (8)
		13 x 52	CD-76	+	No Data	+	4.124 (7)
AAB-3198	3.4	18 x 72	CD-81	+	No Data	+	4.000 (14)
		24 x 96	CD-84	+	No Data	+	4.211 (16)
		27 x 108	CD-83	+	No Data	+	4.515 (2)
		7 x 28	CD-50	No Data	-	-	--
AAB-3172	3.25	7 x 28	CD-57	-	(d)	-	--
		7 x 28	CD-58	-	(d)	-	--
		8 x 32	CD-74	-	No Data	-	--
		9 x 36	CD-51	No Data	No Data	-	--
AAB-3199	2.9	24 x 96	CD-82	No Data	No Data	+	--
AAB-3174	2.75	11 x 44	CD-52	-	-	-	--
AAB-3203	2.4	24 x 96	CD-86	+	No Data	+	3.923 (6)
AAB-3204	1.8	24 x 96	CD-85	-	No Data	-	--
AAB-3173	1.75	11 x 44	CD-71	-	(d)	-	--
AAB-3205	0.73	48 x 192	CD-89	+	(d)	+	3.979 (9)
AAB-3213	0.50	48 x 192	CD-90	No Data	(d)	+	--
AAB-3215	0.25	48 x 192	CD-92	-	(d)	-	--
ANB-3105	0	44 x 107 (f)	CD-87	-	(d)	-	--
ANB-3105	0	44 x 107 (f)	CD-88	-	(d)	-	--

(a) Includes all tests except CD-1 through CD-12, which were preliminary witness plate tests.

(b) Test charge consisted of two 8-in.-long charges placed end-to-end.

(c) Test charge consisted of a 4-in.-long charge placed on top of an 8-in.-long charge.

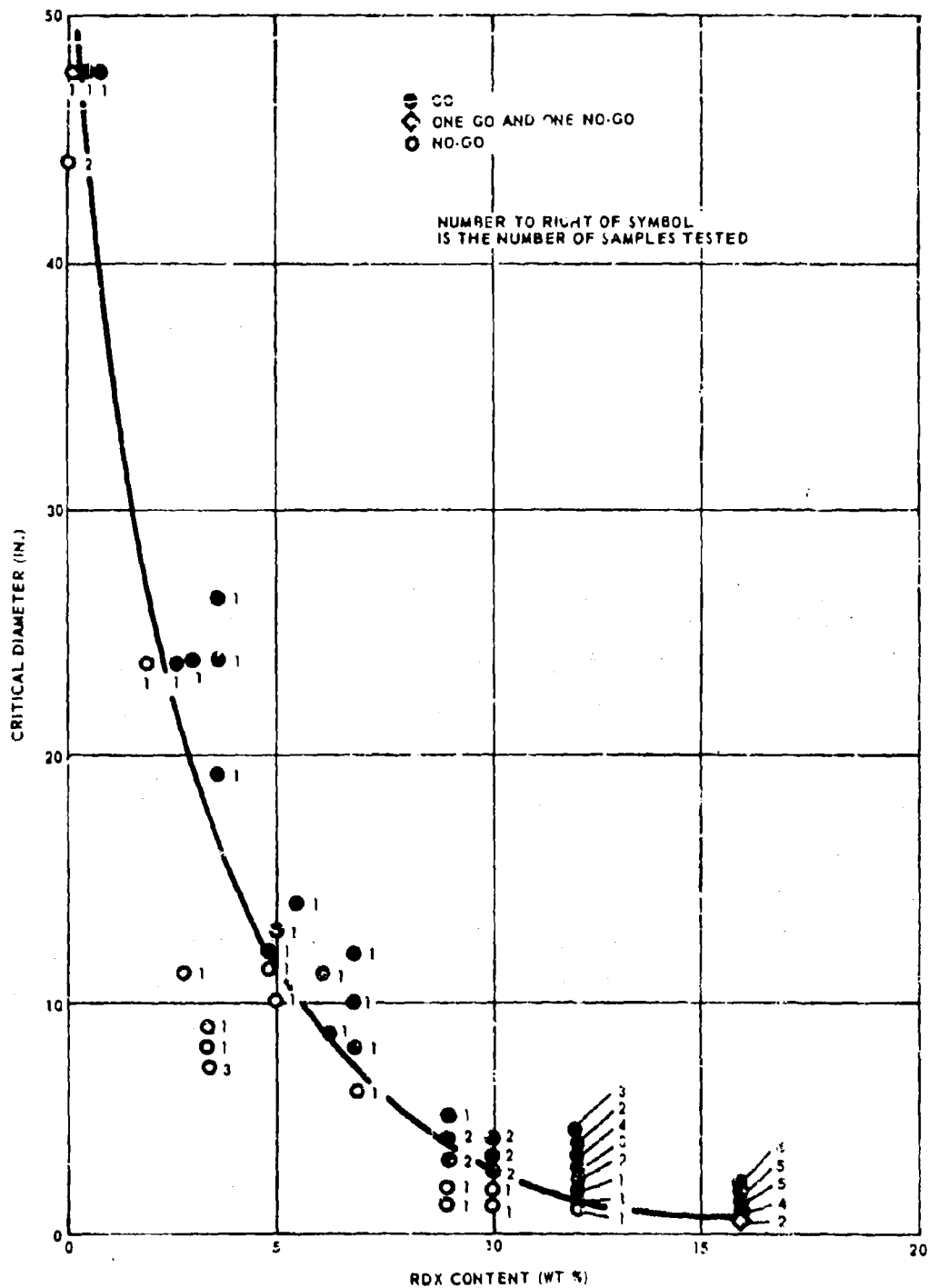
(d) Streak camera not used.

(e) Tested in 0.023-in. thick steel confinement.

(f) Unadulterated PBAN propellant in second-stage Minuteman chamber.

*+ = steady-state detonation; - = failing detonation.

Numbers in parentheses indicate number of data points used in computing average detonation velocity.



2788-16-1

Figure 16. Summary of Critical Diameter Test Results.

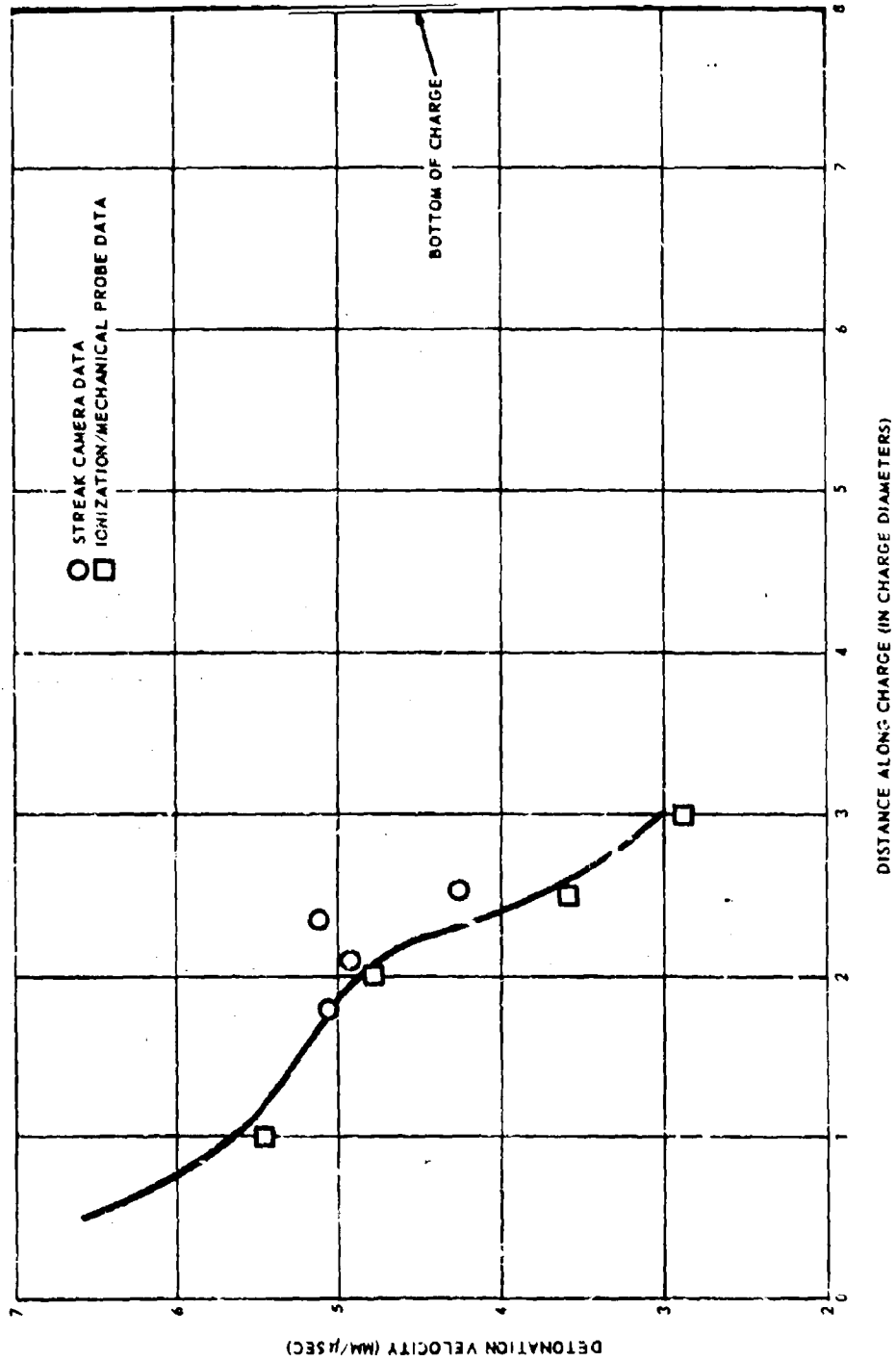


Figure 17. Detonation Velocity vs Distance Along Charge for
1.0-in. -Diameter AAB-3163 Propellant Charge
(16.0 wt % RDX) in Test CD-47.

2783-17-1

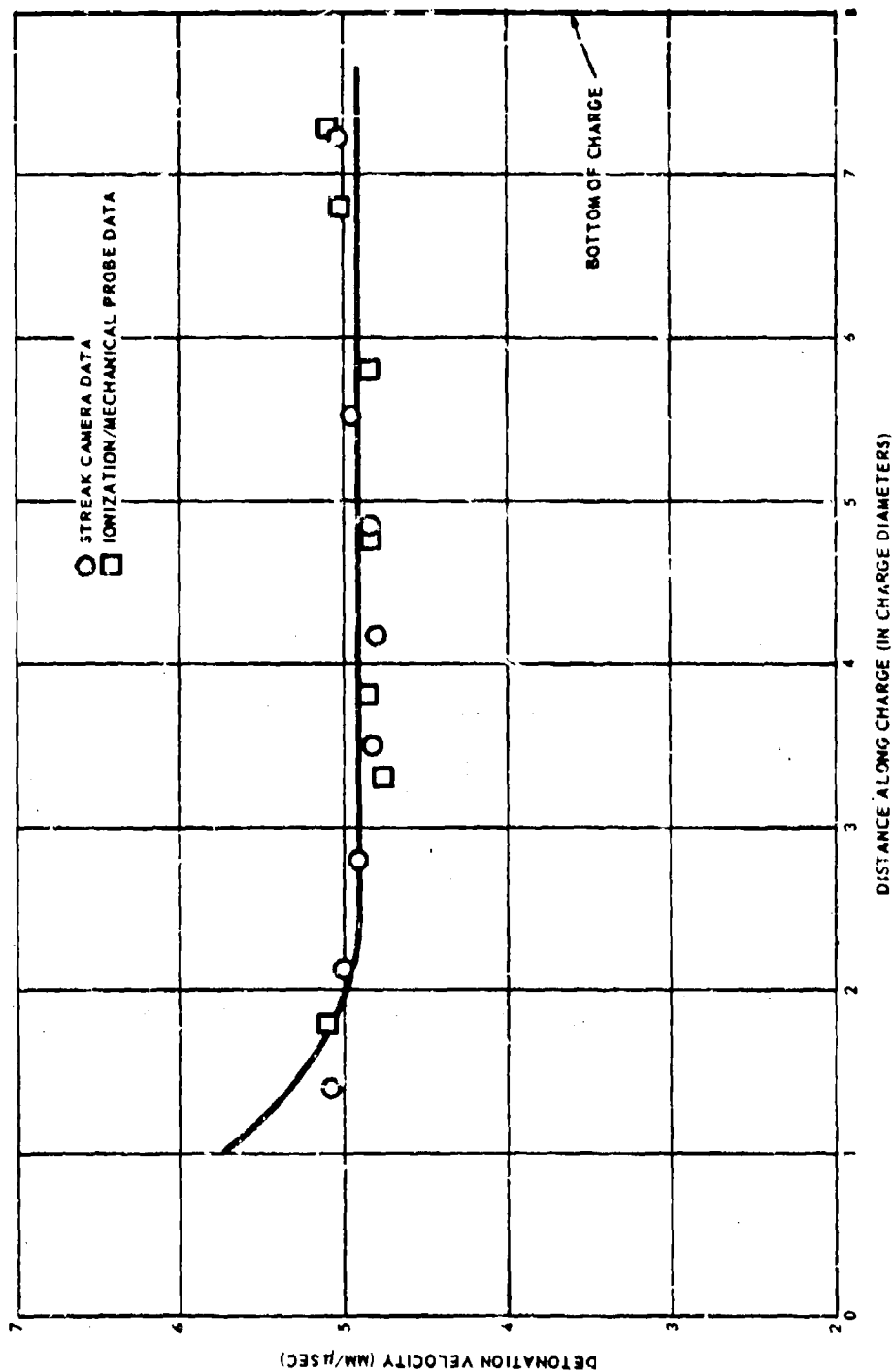


Figure 18. Detonation Velocity vs Distance Along Charge for
 1.0-in. Diameter AAB-3163 Propellant Charge
 (16.0 wt % RDX) in Test CD-45.

2702-10-1

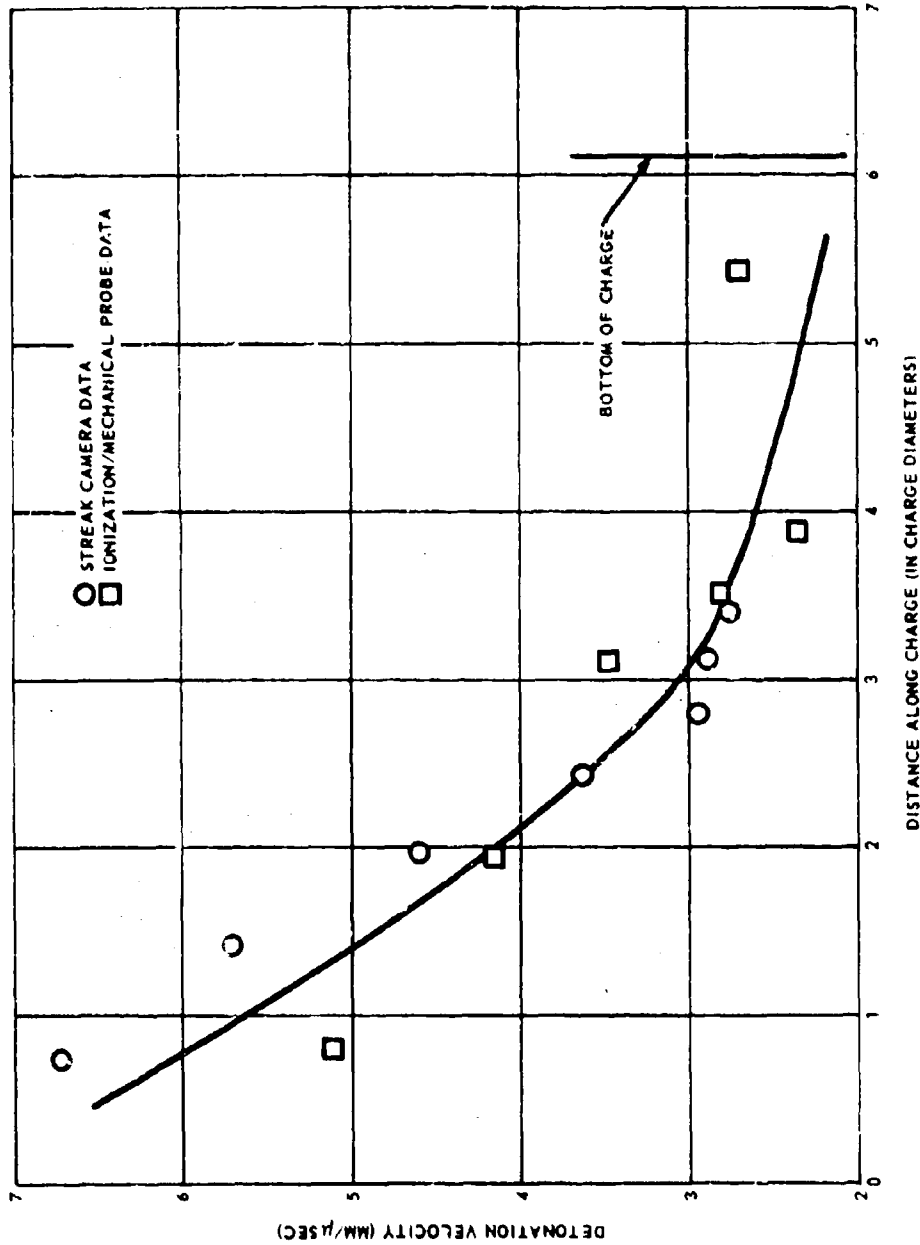


Figure 19. Detonation Velocity vs Distance Along Charge for
 1.29-in. Diameter AAB-3164 Propellant Charge
 (12.0 wt % RDX) in Test CD-46.

2750-15-1

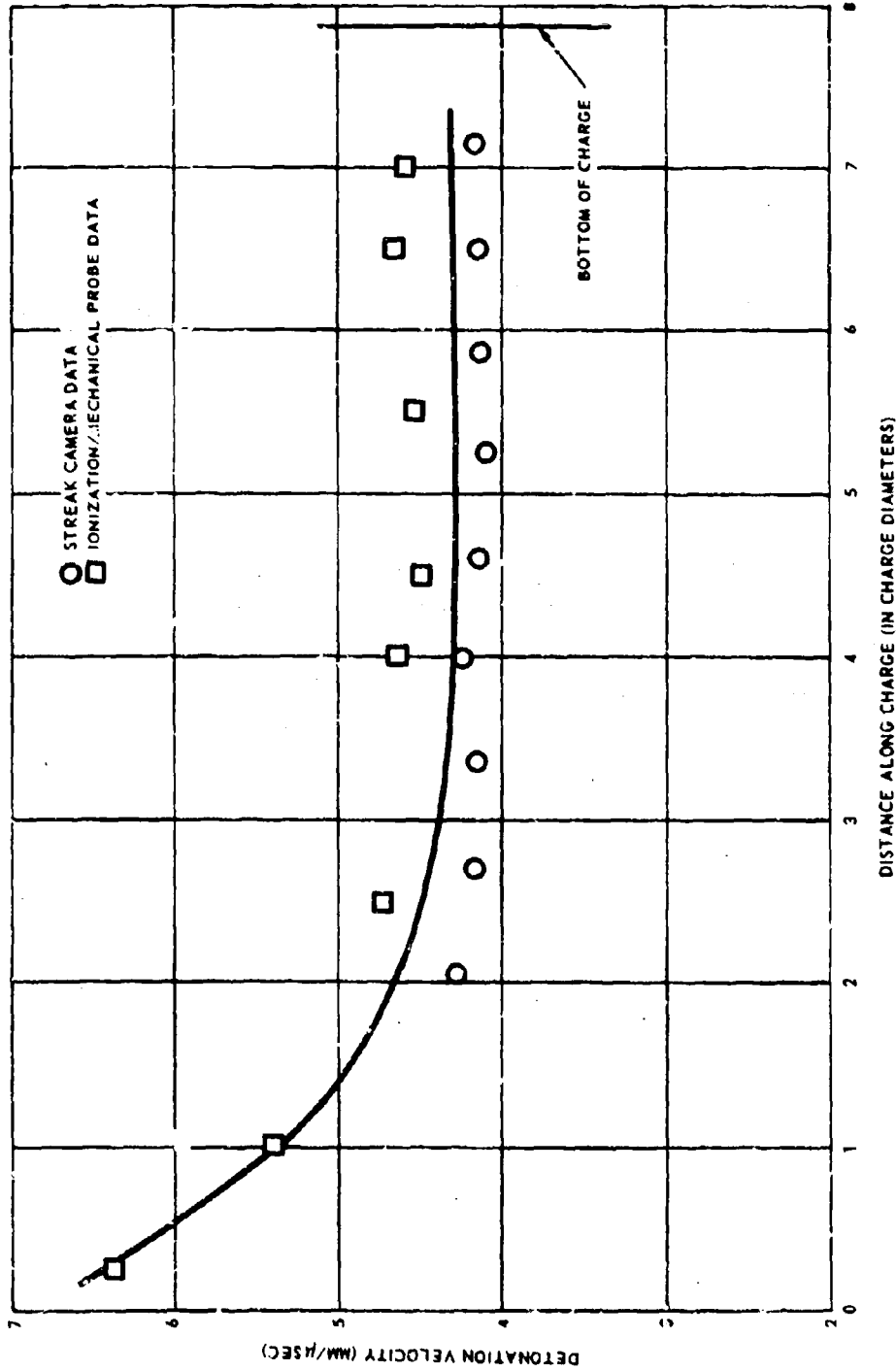


Figure 20. Detonation Velocity vs Distance Along Charge for
1.53-in. Diameter AAB-3164 Propellant Charge
(12.0 wt % RDX) in Test CD-43.

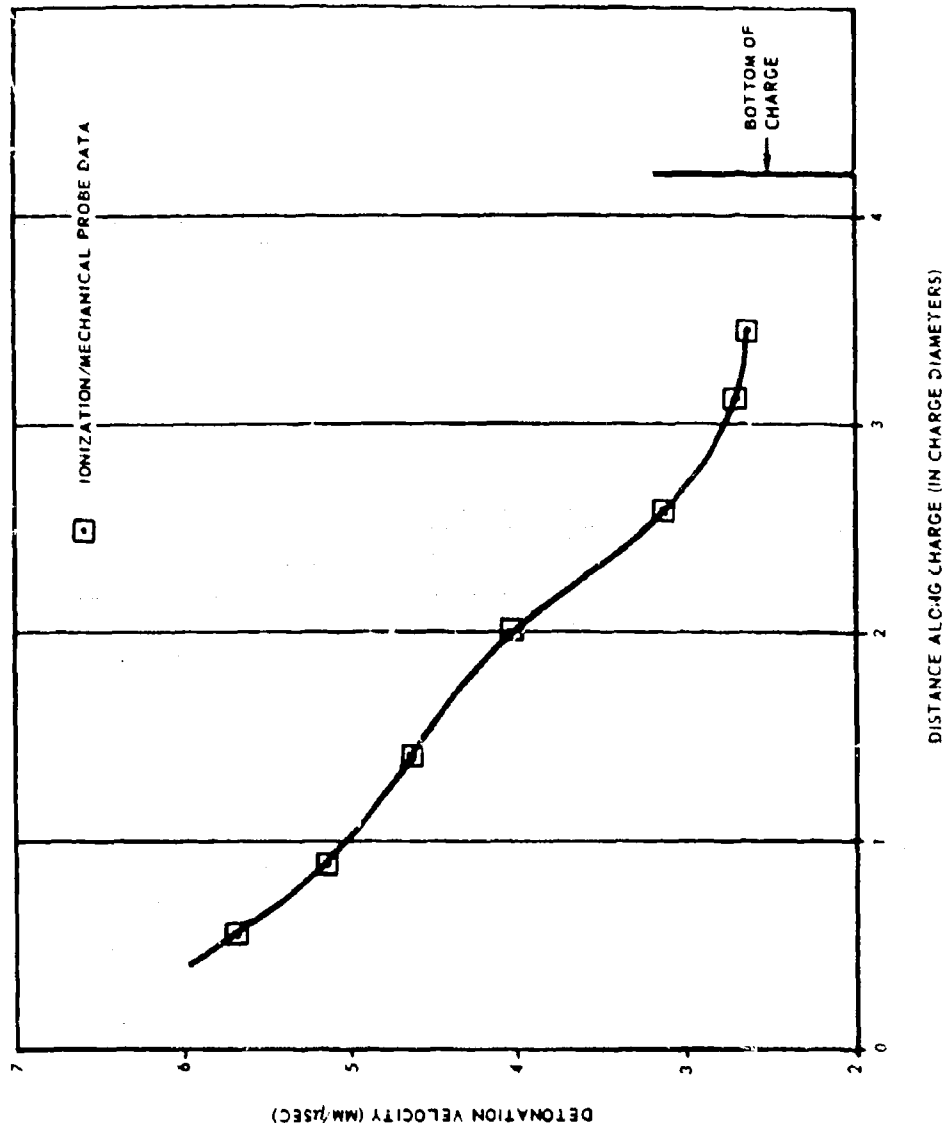


Figure 21. Detonation Velocity vs Distance Along Charge for
1-3/4-in. Diameter AAB-3187 Propellant Charge
(10 wt % RDX, in Test CD-63.

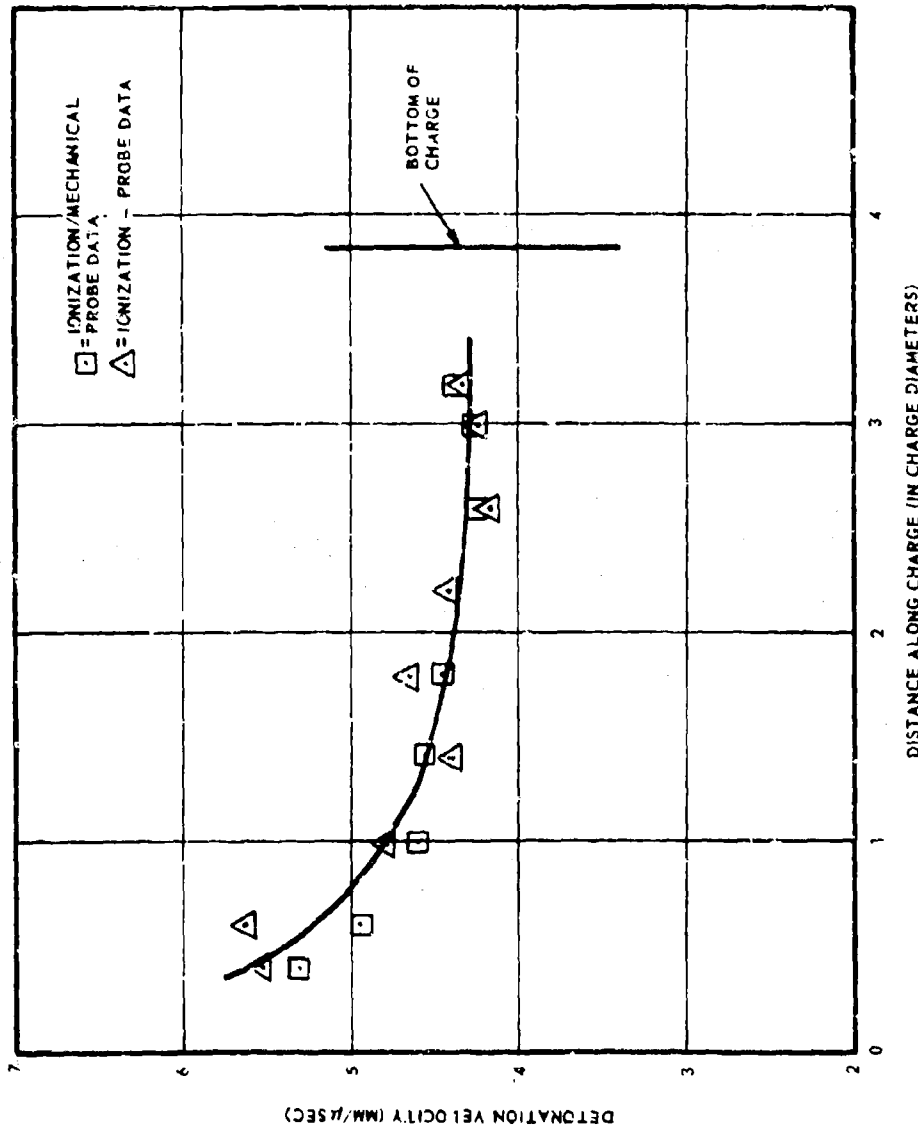


Figure 22. Detonation Velocity vs Distance Along Charge for
2-1/2-in. Diameter AAB-3187 Propellant Charge
(10 wt % RDX) in Test CD-66.

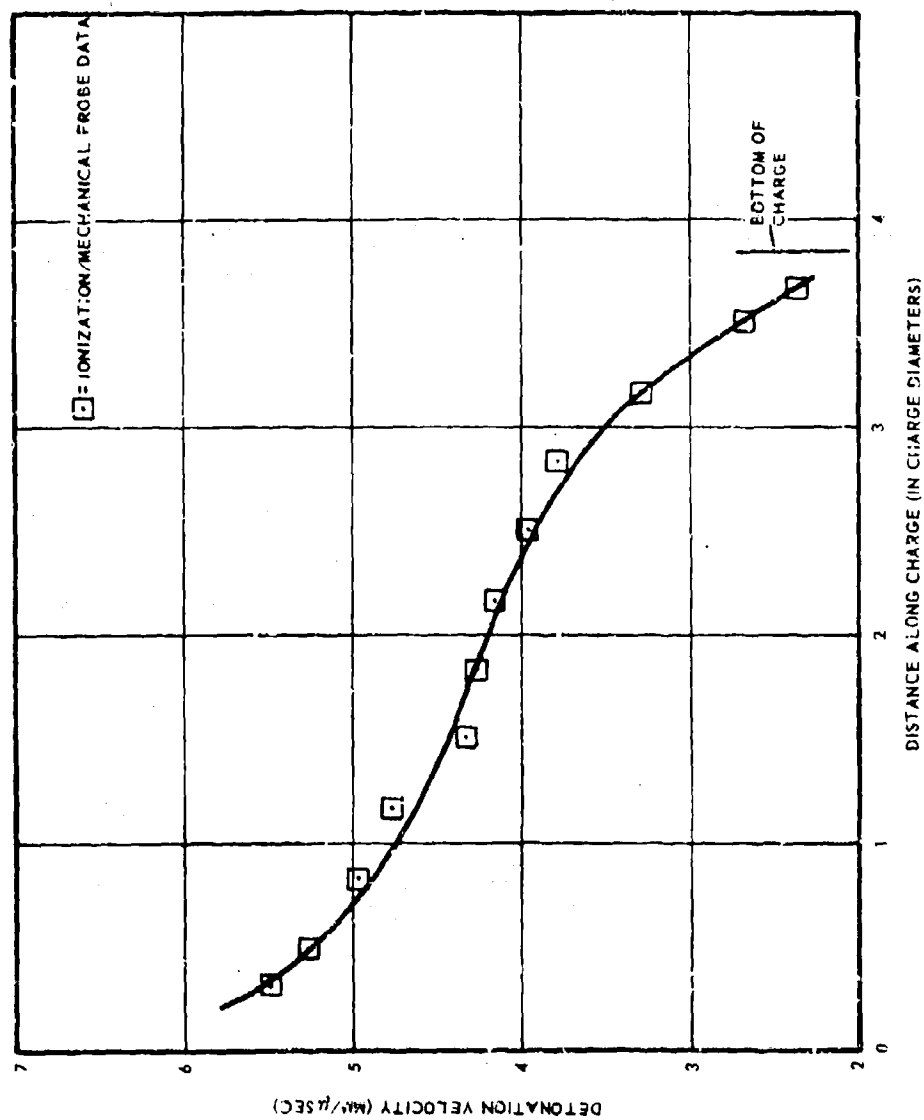


Figure 23. Detonation Velocity vs Distance Along Charge for
3-in. Diameter AAB-3188 Propellant Charge
(9 wt % RDX) in Test CD-64.

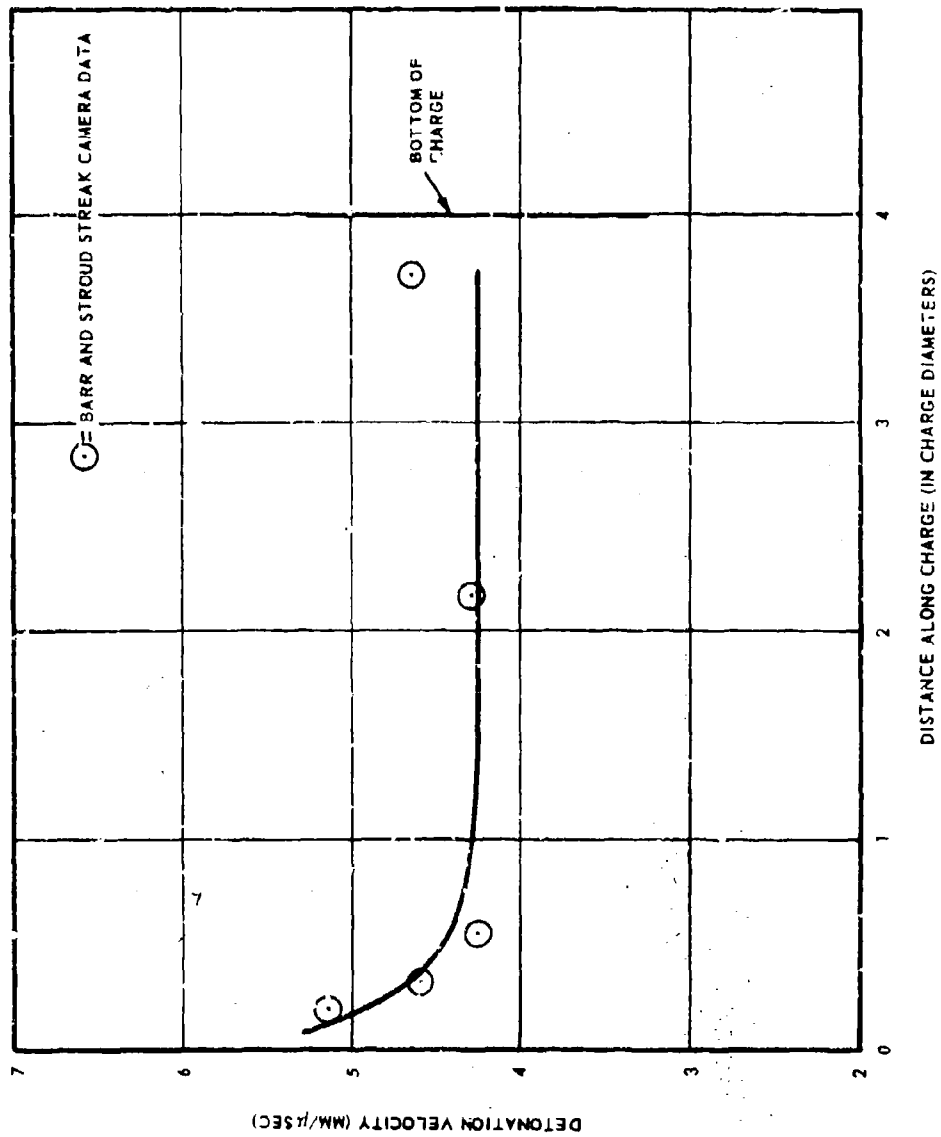


Figure 24. Detonation Velocity vs Distance Along Charge for
4-in. Diameter AAB-3128 Propellant Charge
9 wt % RDX, in Test CD 61.

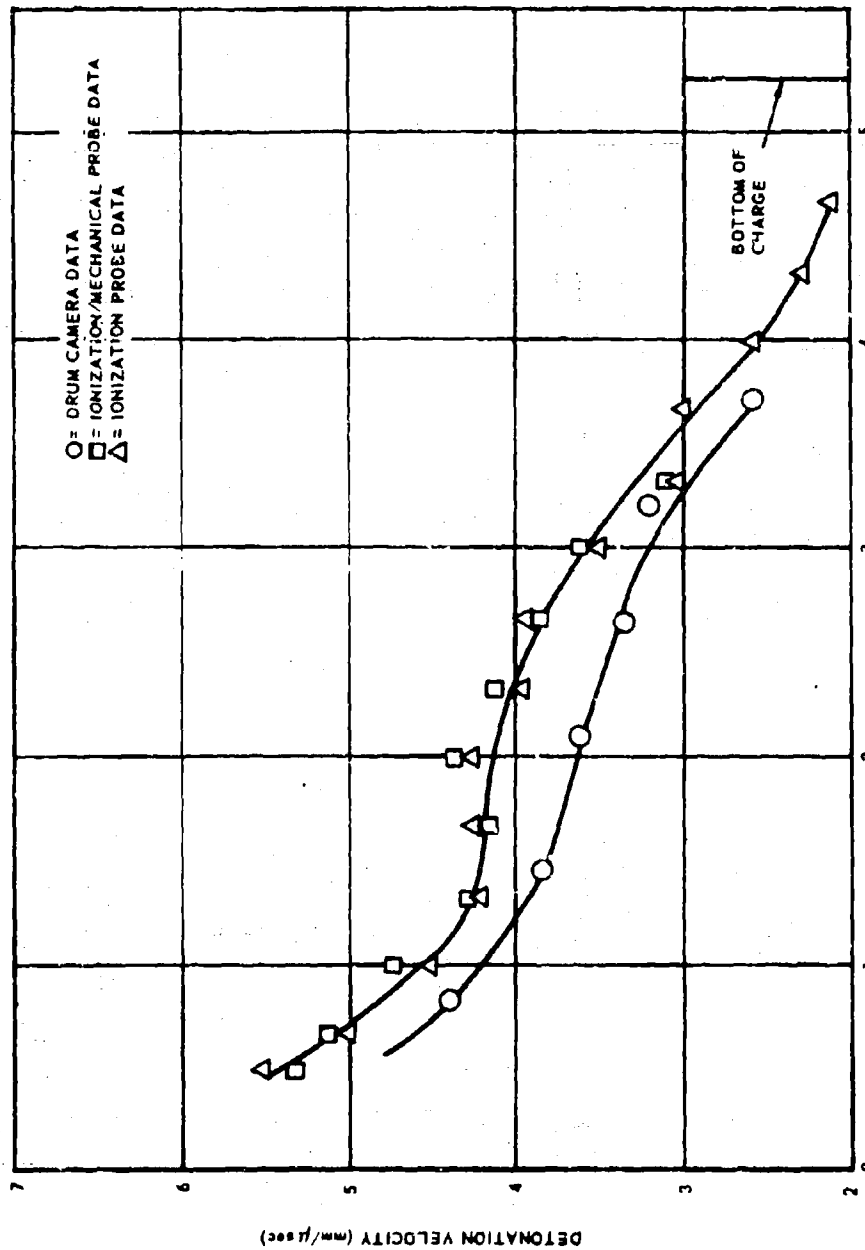


Figure 25. Detonation Velocity vs Distance Along Charge for 6-in. Diameter AAB-3176 Propellant Charge (6.75 wt % RDX) in Test CD-54.

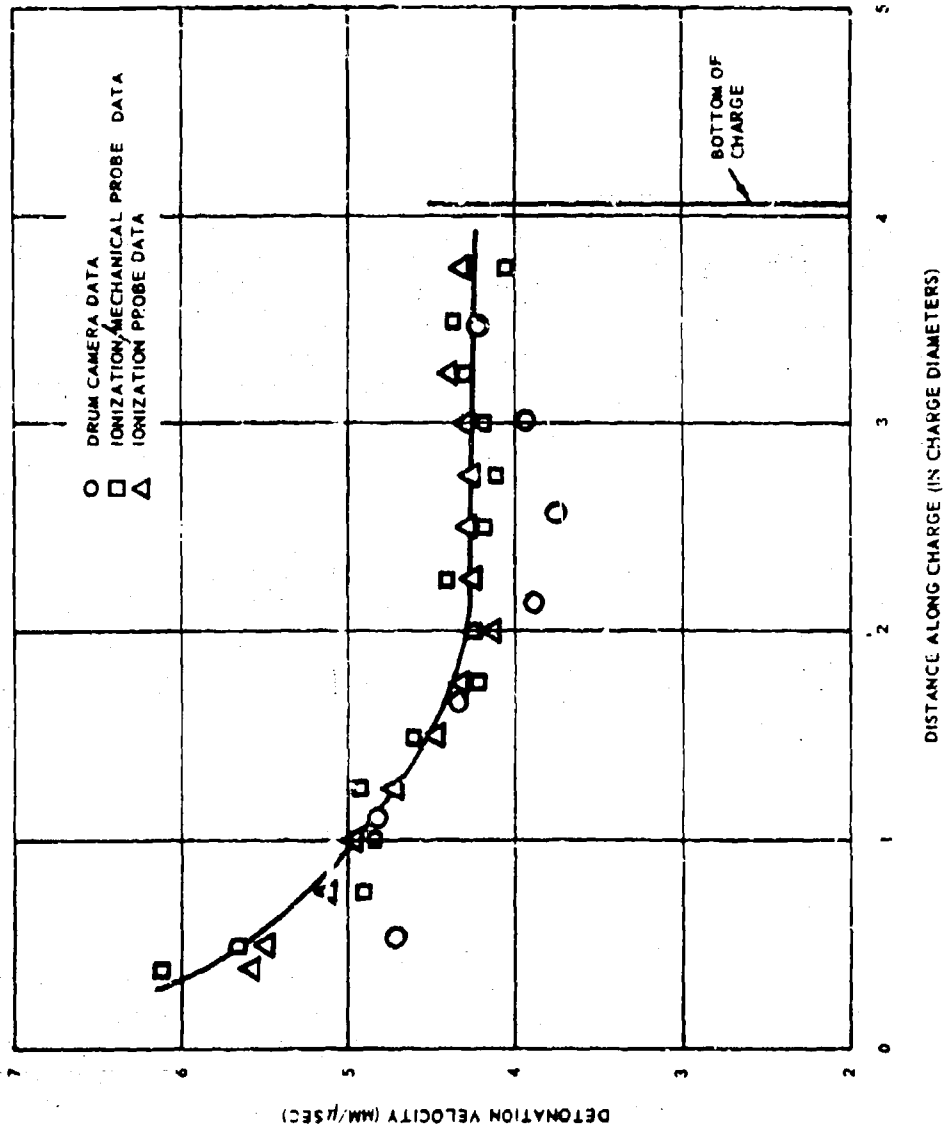


Figure 26. Detonation Velocity vs Distance Along Charge for
8-in. -Diameter AAB-3176 Propellant Charge
(6.75 wt % RDX) in Test CD-55.

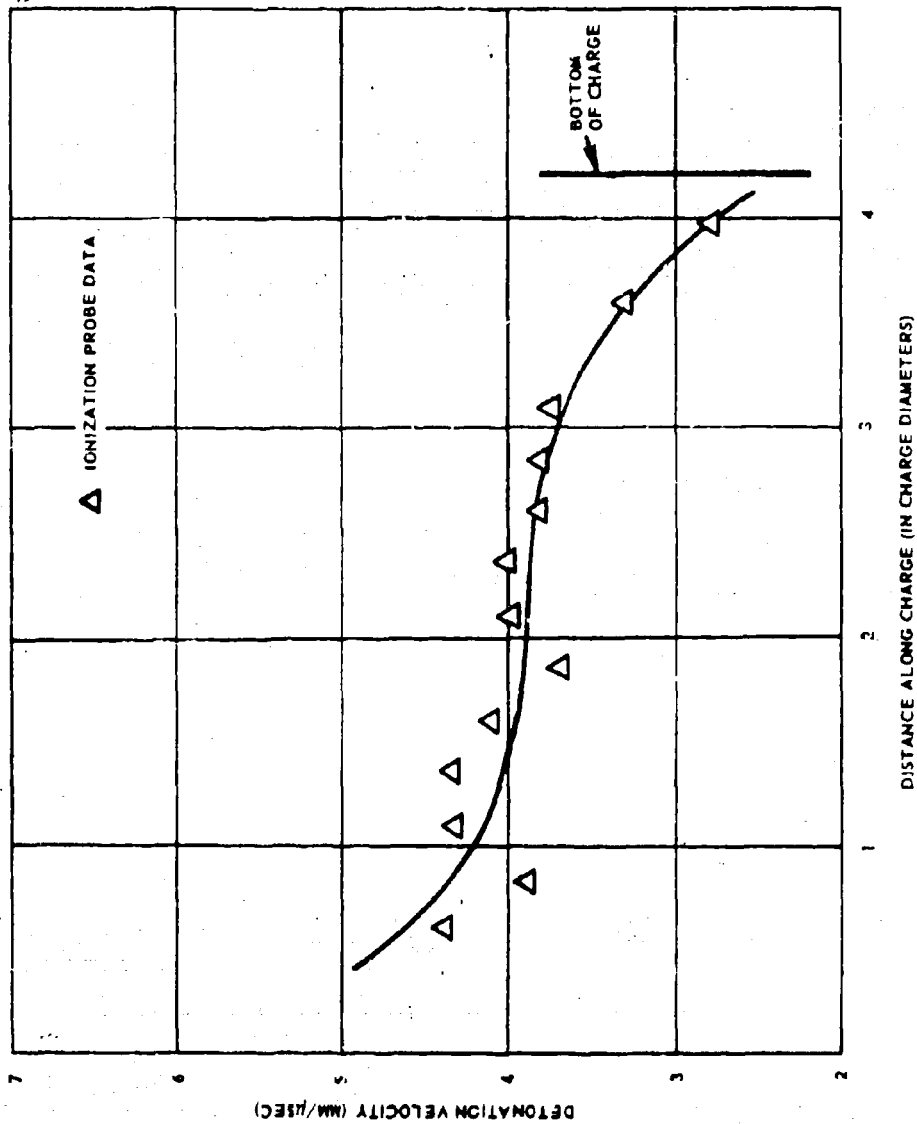


Figure 27. Detonation Velocity vs Distance Along Charge for
11-in. Diameter AAB-3191 Propellant Charge
(4.75 wt % RDX) in Test CD-79.

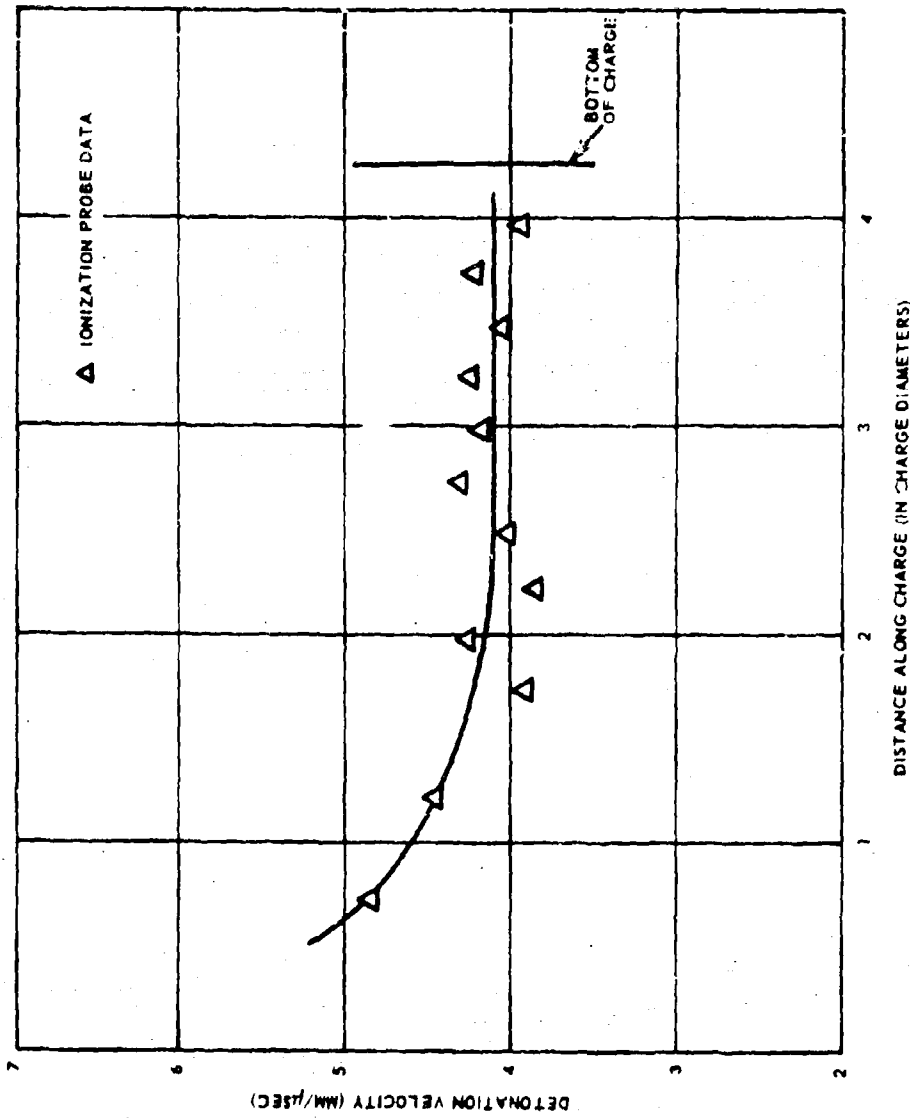


Figure 28. Detonation Velocity vs Distance Along Charge for
12-in. Diameter AAB-3191 Propellant Charge
(4.75 wt % RDX) in Test CD-80.

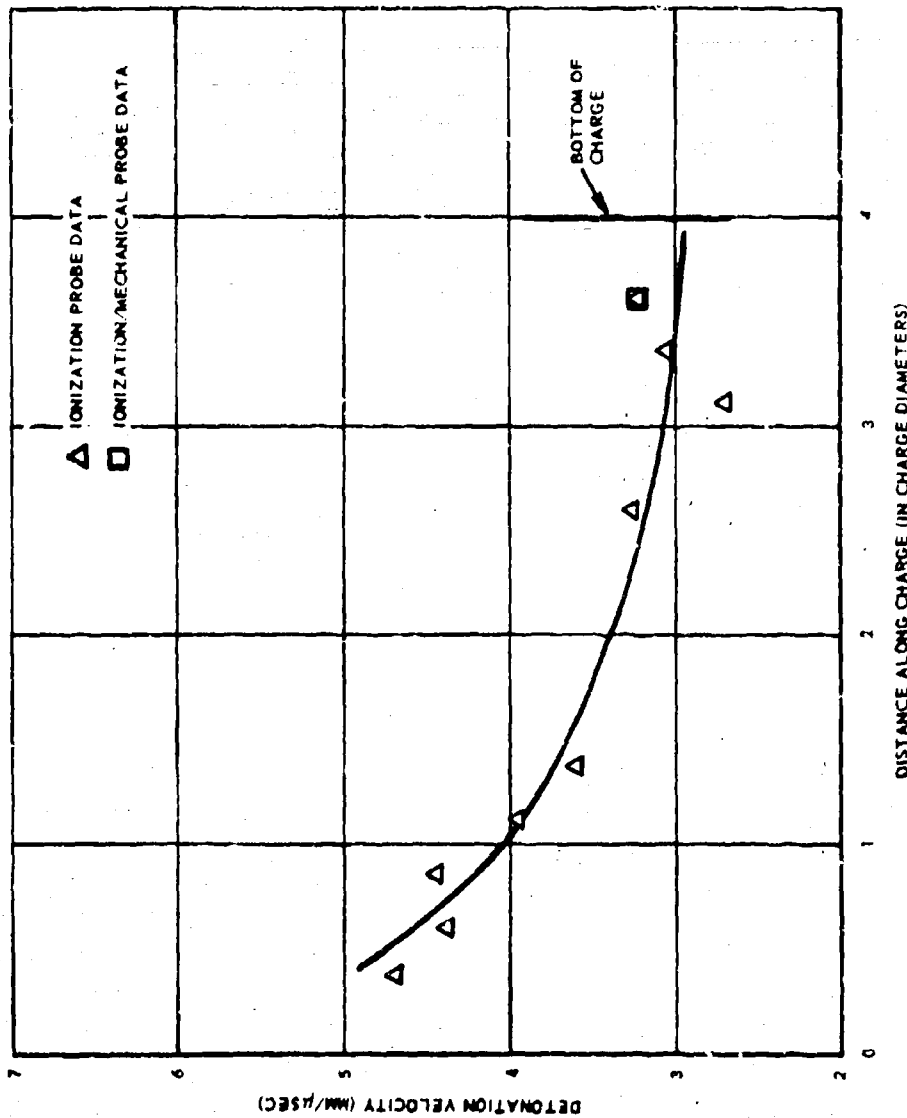


Figure 29. Detonation Velocity vs Distance Along Charge for
23.5mm Diameter AAB-3204 Propellant Charge
(1.8 wt % RDX) in Test CD-85.

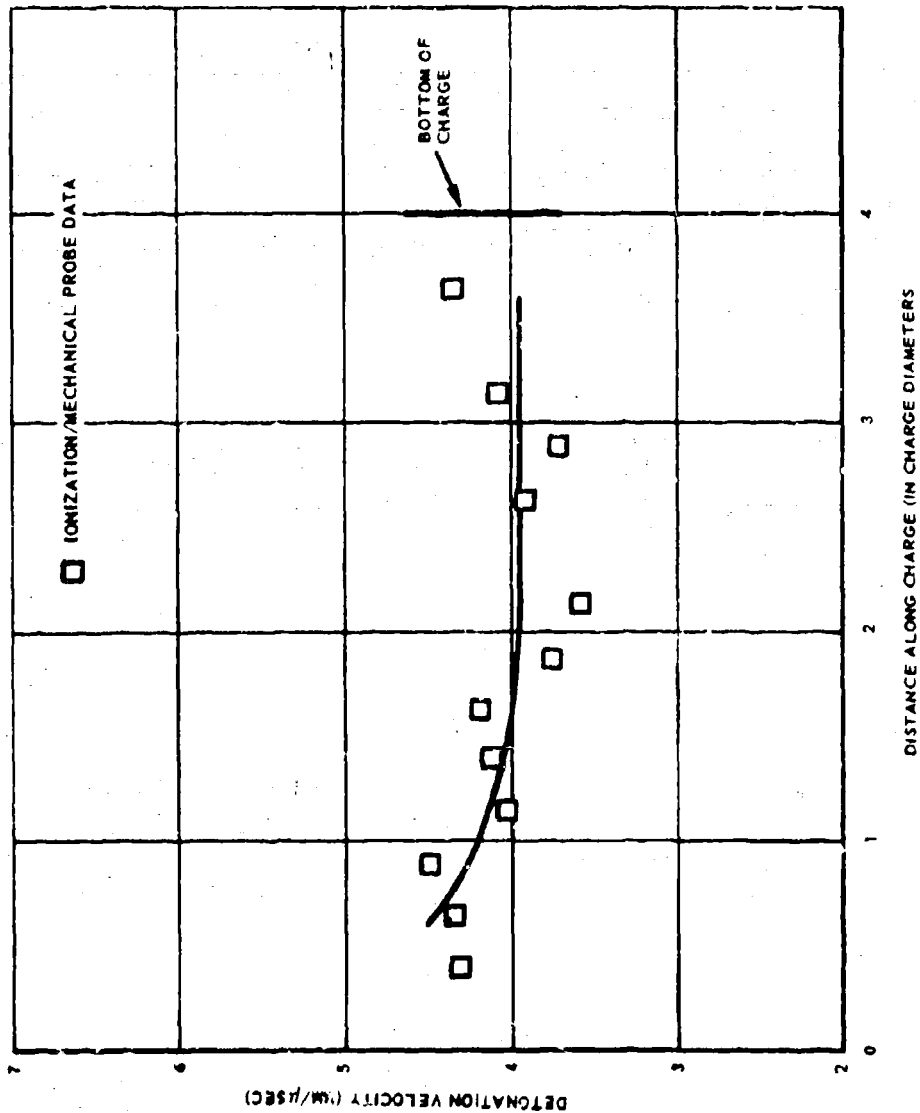


Figure 30. Detonation Velocity vs. Distance Along Charge for
2.4 wt % RDX in Test CD-86.

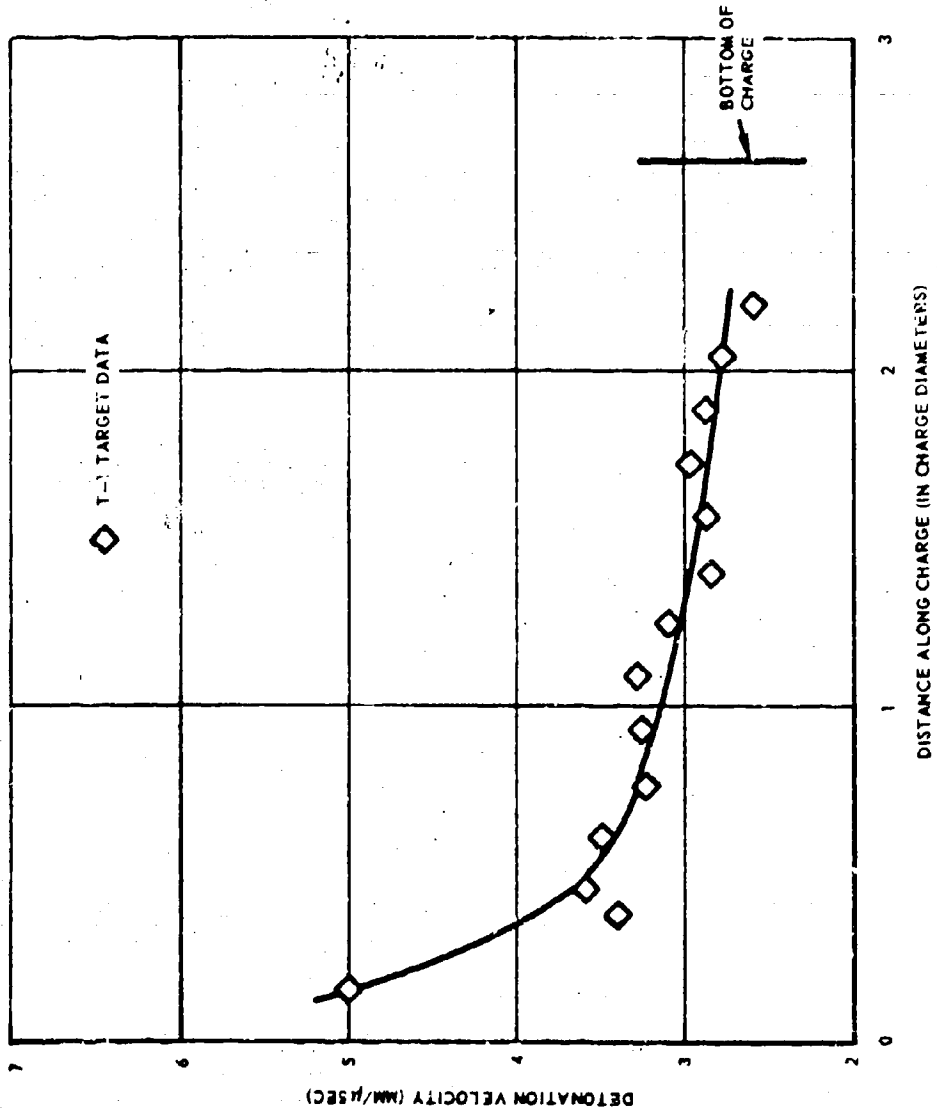


Figure 31. Detonation Velocity vs Distance Along Charge for
44-in. Diameter ANB-3105 Propellant Charge
(0 wt % RDX) in Test CD-87.

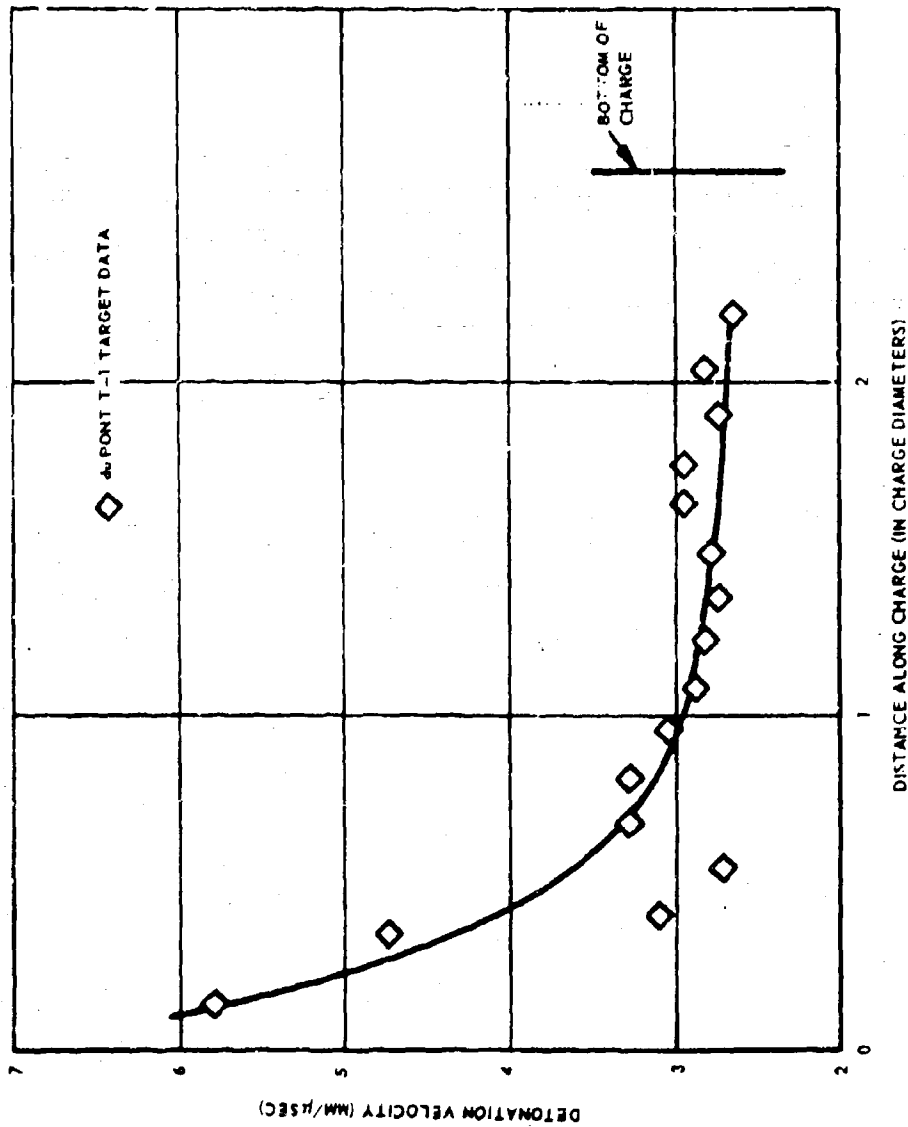


Figure 32. Detonation Velocity vs Distance Along Charge for 44-in. Diameter ANB-3105 Propellant Charge (0 wt % RDX) in Test CD-88.

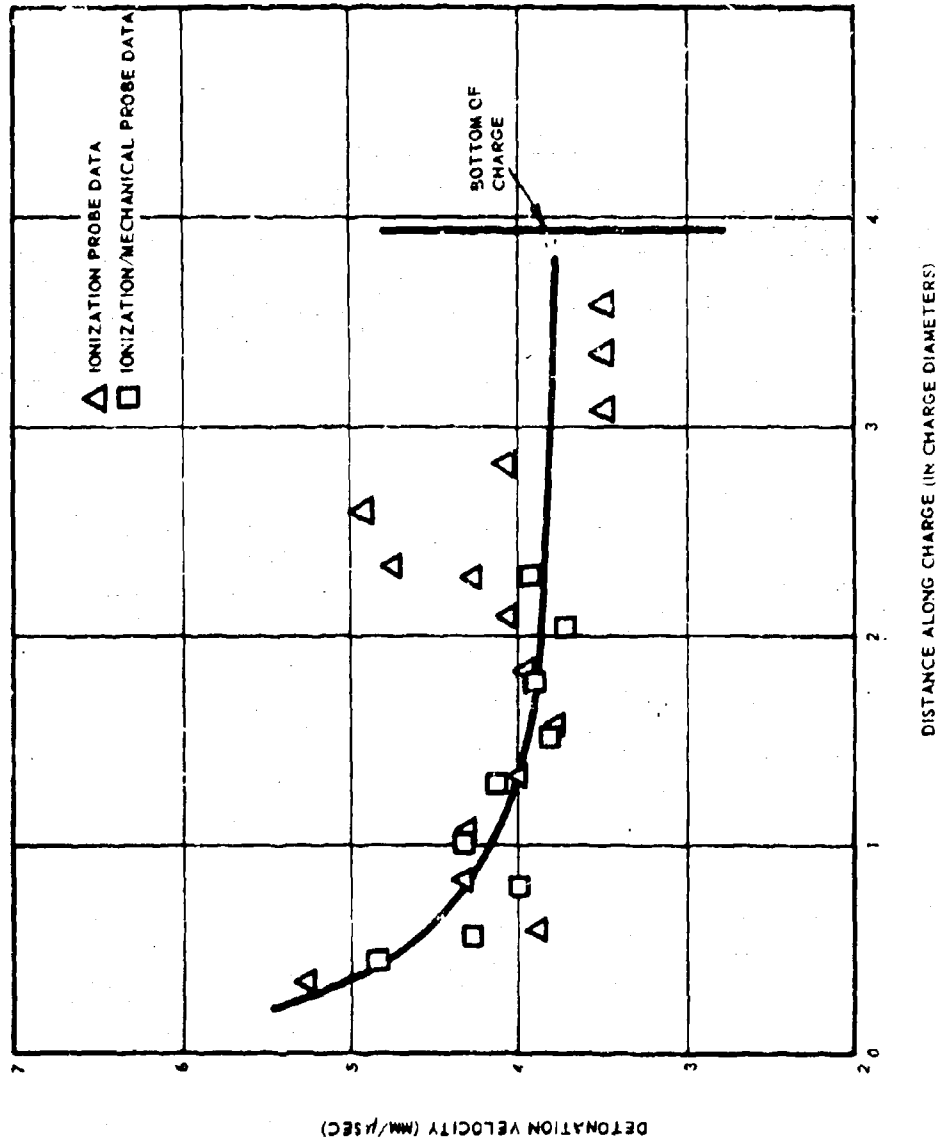
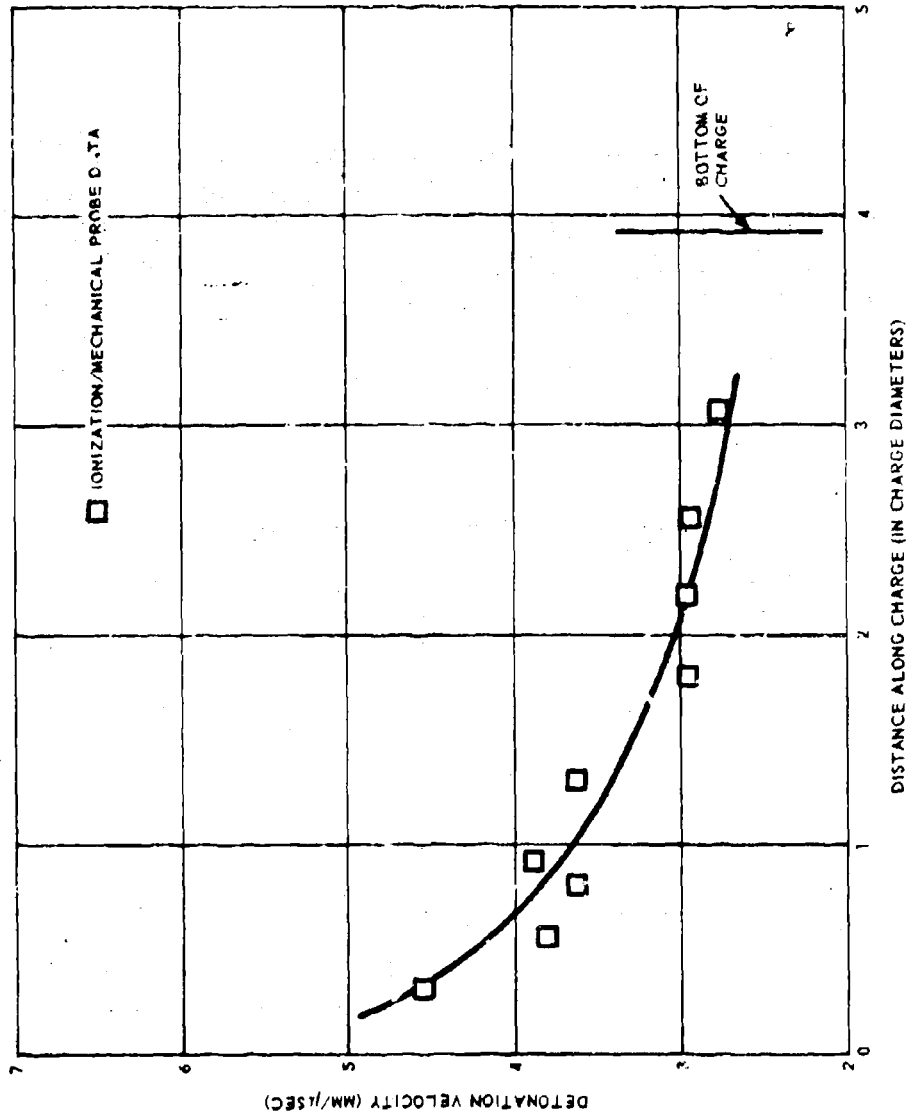


Figure 33. Detonation Velocity vs Distance Along Charge for
48-in. Diameter AAB-3205 Propellant Charge
(0.73 wt % RDX) in Test CD-89.



2768-31-1

Figure 34. Detonation Velocity vs Distance Along Charge for
48-in. Diameter AAB-3215 Propellant Charge
(0.25 wt % RDX) in Test CD-92.

Because unanticipated instrumentation problems followed activation of Test Site 1-36D, very little blast data was obtained from the first AFRPL tests. A summary of the AFRPL blast data is presented in Table 3. It should be emphasized that some of the data reported in these tables (indicated by *) is considered questionable because of some instrumentation malfunction during transfer of the data from magnetic tape to oscillograph records. These magnetic tape records will be re-evaluated during the next fiscal year.

When the first-stage Minuteman chamber, containing Thiokol AP-polysulfide propellant without RDX adulterant (see Section 5.1.2.5), was prepared for testing it was necessary, to remove one end of the steel case (slightly above the propellant surface) with linear shaped charge. However, unlike the second-stage chambers, the first-stage case did not have a rubber liner and was then in almost direct contact with the propellant. The explosive cutting operation was considerably more hazardous than the previous case cutting operations. In spite of the precautionary covering of the surface of the propellant grain with silicone oil, the propellant was inadvertently ignited during the third application of linear shaped charge and it was destroyed by fire. Ignition was probably caused by a hot fragment from the jet of the linear shaped charge or by a spall from the case.

4.4 THEORETICAL PROGRAM

In a previously developed theoretical detonation model (Reference 2), the energy release process considered largely responsible for propagating detonation in porous propellants was the decomposition of the ammonium perchlorate oxidizer via a grain-burning mechanism (Reference 3) following ignition of the AP by the uniformly distributed shock-heated voids (hot spots) in a time that is very short compared to the grain-burning time. It was further assumed that reactions of gasified binder and aluminum with oxidizer decomposition products did not release a significant amount of energy in the detonation reaction zone. Thus, while the total detonation reaction time may, in principle, be considered to be the sum of the times required to complete the essentially consecutive processes of initiation of AP decomposition (t_i), AP grain burning (t_o), binder burning (t_b), and aluminum burning (t_{Al}), i. e.,

$$t = t_i + t_o + t_b + t_{Al} \quad (1)$$

Table 3. Summary of AFRPL Blast Data.

Test No.	RDX Content (%)	Mun Sample Dimensions Dia x Length (in.)	Sample Weight (lb)	TNT Booster Weight (lb)	Test Results	Test Overpressure Data - Charge Radius No. 1				
						Dist (ft)	Side-On Pressure (psi)	End-On Pressure (psi)	Positive Side-On Impulse foot-seconds	Positive Pulse Duration (msec)
CD-79	4.75	11 x 64	278	75	No-Ga	28	1 (1) -- (2) 1 (3)	1 1 1	1 (1) -- (2) 1 (3)	1 -- 1
CD-80	4.75	12 x 48	361	106	Go	15	1 -- 1	1 -- 1	1 -- 1	1 -- 1
CD-81	3.4	18 x 72	1191	360	Go	70	1 36.3 Avg = 14.3	1 1 1	1 133 133	1 11.9 11.9
CD-82	2.9	24 x 96	1769	796	Go	70	1 49.3 Avg = 49.3	1 1 1	1 164 164	1 14.3 14.3
CD-83	3.4	27 x 108	1861	1110	Go	70	90.0 100.0 102.0 Avg = 103.0	00 00 1 00	00 00 00 00	00 00 00 00
CD-84	3.4	24 x 96	1752	796	Go	70	75.0 61.0 1 Avg = 58.0	00 00 1 00	00 00 00 00	00 00 00 00
CD-85	1.8	24 x 96	3107	796	No-Ga	70	115.0 00 00 Avg = 115.0	461.0 00 00 461.0	00 00 00 00	00 00 00 00
CD-86	2.4	24 x 96	3133	796	Go	70	69.0 00 60.0 Avg = 64.5	172.0 00 1 172.0	00 00 00 00	00 00 00 00
CD-87	0	44 x 116	9268	6675	No-Ga	70	100.0 00 133.0 Avg = 139.0	-- 00 1 00	00 00 00 00	00 00 00 00
CD-88	0	44 x 116	9260	6675	No-Ga	70	00 133.0 00 Avg = 133.0	-- -- 1 00	00 00 00 00	00 00 00 00
CD-89	0.73	48 x 192	21,629	5875	Go	160	120.0 119.0 Avg = 123.0	1 507 507	-- -- --	-- -- --
CD-90	0.50	48 x 192	21,999	5875	Go	160	130.0 100.0 97.20 Avg = 114.0	1 160 1 160	673 -- -- --	22.5 -- -- 22.5
CD-91	1.78	11 x 64	278	75	No-Ga	160	2.30 -- 2.77 Avg = 2.50	1 2.73 1 2.73	18.3 -- 21.3 30.0	18.3 -- 27.0 23.2
CD-92	0.25	48 x 192	21,971	5875	No-Ga	160	-- -- --	1 -- 1	-- -- --	-- -- --
CD-93	6.0	13 x 52	635	65	Go	160	5.900 4.55 6.190 Avg = 5.640	1 30.50 1 30.50	-- 45.6 -- 45.6	-- 26.3 -- 26.3
Comp. B Explosive Calibration Test		22 x 80	2003	--		160	11.10 9.650 14.70 Avg = 11.60	1 -- 1 1	96.00 119.0 102.0 100.0	20.60 26.90 19.50 21.30

(1) 2 o'clock leg
(2) 6 o'clock leg
(3) 10 o'clock leg
0 Questionable data
00 Data not reduced
1 Charge not installed
-- No data

Table 3. (Continued).

Peak Overpressure Data - Gauge Station No. 2										
Test No.	RME Content (wt %)	Mum Sample Pkts x Length (in.)	TNT Weight (lb)	TNT Weight (lb)	Test Results	Peak Overpressure Data - Gauge Station No. 2				
						Dist (ft)	Under-Can Pressure (psi)	Pass-On Pressure (psi)	Positive Side-On Impulse (psi-msec)	Positive Pulse Duration (msec)
CD-79	4.75	11 x 64	278	73	No-Ga	60	52.8 52.8 Avg = 52.8	1 1 1	151 121	9.12 9.12
CD-80	4.75	12 x 60	361	106	Go	60	64.6 64.6 Avg = 64.6	1 1 1	60.7 60.7	3.83 3.83
CD-81	3.4	18 x 72	1191	360	Go	160	9.38 9.38 Avg = 9.38	1 1 1	64.2 64.2	26.8 26.8
CD-82	2.9	24 x 96	2749	796	Go	160	13.3 13.3 Avg = 13.3	1 1 1	154 154	24.6 24.6
CD-83	3.4	27 x 108	3061	1110	Go	160	10.00 10.00 10.00 Avg = 10.00	1 1 1	oo oo oo	oo oo oo
CD-84	3.4	24 x 96	2752	796	Go	160	10.00 10.00 10.00 Avg = 10.00	1 1 1	oo oo oo	oo oo oo
CD-85	1.8	24 x 96	3107	796	No-Ga	160	10.00 oo oo Avg = 10.00	1 oo oo	oo oo oo	oo oo oo
CD-86	3.4	24 x 96	3113	796	Go	160	12.00 12.00 12.00 Avg = 12.00	1 1 1	oo oo oo	oo oo oo
CD-87	0	64 x 116	9368	6475	No-Ga	160	29.00 oo 28.00 Avg = 28.00	1 oo 1	oo oo oo	oo oo oo
CD-88	0	64 x 116	9368	6475	No-Ga	160	oo 29.20 oo Avg = 29.20	1 1 1	oo oo oo	oo oo oo
CD-89	0.75	68 x 192	21,829	5875	Go	250	18.10 18.6 19.50 Avg = 18.70	1 1 1	318 318	40.7 40.7
CD-90	0.50	68 x 192	21,959	5875	Go	250	17.3 20.0 14.6 Avg = 17.2	1 1 1	411 360 386	61.2 56.4 58.8
CD-91	1.75	11 x 64	278	73	No-Ga	250	0.89 1.27 1.19 Avg = 1.12	0.93 1.170 1 1.050	8.6 10.0 19.0 11.1	22.6 19.2 27.0 22.9
CD-92	0.25	68 x 192	21,971	5875	No-Ga	250	25.9 19.6 1 Avg = 22.9	22.60 25.5 1	328 328	57.7 57.7
CD-93	6.0	13 x 52	435	145	Go	250	2.65 2.11 1 Avg = 2.07	2.17 1.09 1	26.3 23.6 24.0	39.9 29.8 33.1 30.9
Comp. B Explosive Calibration Test		22 x 88	1200	--	250	4.640 3.280 3.25 Avg = 3.720	6.31 4.14 1 6.21	54.40 59.30 51.8 55.20	62.50 65.50 65.9 66.00	

(1) 2 o'clock leg
(2) 4 o'clock leg
(3) 10 o'clock leg
oo Unrecoverable data
oo Data not reduced
1 Charge not handled
-- No data

Table 3. (Continued).

Test No.	RDX Content (wt %)	Nom Sample Dimensions Dia x Length (in.)	Sample Weight (lb)	TNT Residue Weight (lb)	Test Results	Peak Overpressure Data - Gage Station No. 3				
						Dist (ft)	Side-On Pressure (psi)	Face-On Pressure (psi)	Positive Side-On Impulse (psi-msec)	Positive Pulse Duration (msec)
CD-79	4.75	11 x 44	278	75	No-Gs	70				
CD-80	4.75	12 x 48	361	106	Gs	70				
CD-81	3.4	10 x 72	1191	440	Gs	250	2.94 3.27 Avg = 3.11		36.6 44.6 40.6	11.8 30.5 31.2
CD-82	2.9	24 x 96	1749	796	Gs	250	5.16 4.81 4.90 Avg = 5.02		69.5 72.0 70.8	42.1 36.6 39.4
CD-83	3.4	27 x 100	3061	1110	Gs	250	4.40 3.60 2.50 Avg = 3.37	7.00	oo	oo
CD-84	3.4	26 x 96	2752	796	Gs	250	4.10 3.70 2.93 Avg = 3.24	6.20	oo	oo
CD-85	1.8	24 x 96	3107	796	No-Gs	250	3.70 oo oo Avg = 3.70		oo	oo
CD-86	2.6	24 x 96	3113	796	Gs	250	2.00 2.20 2.00 Avg = 2.07	4.70	oo	oo
CD-87	0	44 x 116	5260	4475	No-Gs	250	8.50 oo 8.90 Avg = 8.75		oo	oo
CD-88	0	44 x 116	5260	4475	No-Gs	250	oo 8.26 oo Avg = 8.26		oo	oo
CD-89	0.75	48 x 192	21,829	5875	Gs	500				
CD-90	0.50	48 x 192	21,959	5875	Gs	500				
CD-91	1.75	11 x 44	278	75	No-Gs	500	0.42 0.54 Avg = 0.48			
CD-92	0.25	48 x 192	21,971	5875	No-Gs	500	3.40 3.19 3.65 Avg = 3.41	4.00	132 150 145	82.2 96.2 68.2
CD-93	6.0	13 x 52	435	145	Gs	500	0.58 0.51 0.49 Avg = 0.59	0.63	12.5 10.5 11.8 11.64	40.8 42.6 35.0 39.5
Comp B Explosive Calibration Test		22 x 86	2000	-	500		0.95 0.60 1.00 Avg = 0.96	1.04	25.2 23.3 24.3	49.9 50.5 50.2

(1) 2 o'clock leg
(2) 6 o'clock leg
(3) 10 o'clock leg
o Observed data
oo Data not reduced
† Gage not installed
-- No data

Table 3. (Continued).

Test No.	RDX Content (wt %)	Mean Sample Dimensions Dia x Length (in.)	Sample Weight (lb)	TNT Residue Weight (lb)	Test Results	Peak Overpressure Data - Capt Station No. 4			
						Dist (ft)	Side-On Pressure (psi)	Face-On Pressure (psi)	Positive Side-On Impulse (psi-msec)
CD-79	4.75	11 x 64	278	75	No-Gc	100	2.90	17.7	6.84
							Avg = 2.90	17.7	6.84
CD-80	4.75	12 x 43	341	104	Gc	100	3.30	32.1	22.3
							Avg = 3.30	32.1	22.3
CD-81	5.4	18 x 72	1197	340	Gc	500	1	1	1
							1	1	1
CD-82	2.9	24 x 90	2749	796	Gc	500	1.63	36.9	58.3
							Avg = 1.63	36.9	58.3
CD-83	3.4	27 x 100	3801	1119	Gc	500	1.900	1.900	1.900
							Avg = 1.900	1.900	1.900
CD-84	3.4	24 x 96	2752	796	Gc	500	1.600	1.650	1.650
							Avg = 1.600	1.650	1.650
CD-85	1.8	24 x 96	2107	796	No-Gc	500	1.000	1	1
							1	1	1
CD-86	2.4	24 x 96	2113	796	Gc	500	1.300	1.300	1.300
							Avg = 1.300	1.300	1.300
CD-87	0	66 x 116	9260	6475	No-Gc	500	1	1	1
							1	1	1
CD-88	0	66 x 116	9260	6475	No-Gc	500	1.950	1	1
							Avg = 2.950	1	1
CD-89	0.73	40 x 192	21,829	5875	Gc	700	2.70	122	99.4
							Avg = 2.920	122	99.4
CD-90	0.50	40 x 190	21,909	5875	Gc	700	3.10	123	99.7
							Avg = 2.920	123	99.7
CD-91	1.79	11 x 64	270	75	No-Gc	700	0.340	3.740	34.1
							Avg = 0.310	3.740	34.1
CD-92	0.25	60 x 92	21,971	5875	No-Gc	700	2.34	99.6	90.0
							Avg = 2.42	99.6	90.0
CD-93	6.0	19 x 52	438	143	Gc	700	0.41	0.54	42.2
							Avg = 0.43	0.54	42.2
Comp. B Explosive Calibration Test		22 x 100	2000	-	700	0.50	12.3	60.5	30.3
							Avg = 0.50	12.3	60.5

(1) 2 o'clock log
(2) 4 o'clock log
(3) 10 o'clock log
• Questionable data
oo Data not reduced
1 Charge not installed
-- No data

Table 3. (Continued).

Test No.	RMC Content (%)	Nom Sample Dimensions Dia x Length (in.)	Sample Weight (lb)	TWT Resistor Weight (lb)	Test Resistor	Peak Overpressure Data - Gage Station No. 6			
						Side-On Pressure (psi)	Face-On Pressure (psi)	Positive Side-On Impulse (psi-sec)	Vibrato Pulse Duration (sec)
CD-75	4.75	11 x 64	271	75	No-Ga	150	1	16.8	9.55
						1.18	1	16.8	9.55
						Avg = 1.18			
CD-80	4.75	12 x 68	341	104	Ga	150	1	20.9	27.7
						1.42	1	20.9	27.7
						Avg = 1.42		20.9	27.7
CD-81	3.4	18 x 72	1191	140	Ga	700	1	1	1
						1	1	1	1
						1	1	1	1
CD-82	3.4	24 x 96	2709	794	Ga	700	1	1	1
						1.95	1	29.5	52.5
						Avg = 1.95		29.5	52.5
CD-83	3.4	27 x 100	3041	1118	Ga	700	1	00	00
						1.62	1	00	00
						1.18	1	00	00
						1.12	1	00	00
						Avg = 1.18			
CD-84	3.4	24 x 96	2752	794	Ga	700	0.90	00	00
						0.90	1	00	00
						00	1	00	00
						Avg = 0.90			
CD-85	1.8	24 x 96	2107	794	No-Ga	100	1.19	00	00
						00	1	00	00
						00	1	00	00
						Avg = 1.19			
CD-86	2.4	24 x 96	3113	794	Ga	700	1.00	00	00
						1.00	1	00	00
						1.00	1	00	00
						Avg = 1.00			
CD-87	0	44 x 116	9540	4475	No-Ga	700	1.15	00	00
						1.49	1	00	00
						1.00	1	00	00
						Avg = 1.15			
CD-88	0	44 x 116	9540	4475	No-Ga	700	00	00	00
						1.77	1	00	00
						00	1	00	00
						Avg = 1.77			
CD-89	0.75	44 x 132	21,824	5075	Ga	1000	1.42	87.0	114.0
						1.59	1	86.9	114.3
						1.43	1	85.4	113.2
						Avg = 1.41		86.6	113.4
CD-90	0.50	44 x 132	21,909	5075	Ga	1000	1.47	84.3	114.9
						1.48	1	82.3	113.3
						2.82	1	79.0	107.5
						Avg = 1.78		86.2	119.2
CD-91	1.75	11 x 64	278	75	No-Ga	1000	0.16	2.82	34.9
						0.16	1	2.77	25.6
						0.19	1	2.64	18.9
						Avg = 0.16		2.80	29.8
CD-92	0.25	44 x 132	21,971	5075	No-Ga	1000	1.41	73.2	117.9
						1.39	1	81.6	114.1
						1.78	1	73.3	109.1
						Avg = 1.50		76.0	117.0
CD-93	4.0	13 x 52	435	145	Ga	1000	0.33	7.21	46.0
						0.39	1	7.28	41.3
						0.33	1	6.93	42.2
						Avg = 0.35		7.11	43.2
Comp. B Explosive Calibration Test		22 x 68	1000	-	1000	0.50	1	13.7	54.5
						0.49	1	13.6	54.1
						0.53	1	11.2	46.6
						Avg = 0.51		12.6	53.1

(1) 2 o'clock lag
(2) 4 o'clock lag
(3) 10 o'clock lag
00 Unrecoverable data
- Data not returned
! Gage not installed
- No data

the effective total reaction time for porous AP propellant is considered to be essentially just the AP grain-burning time,

$$t = t_o = R_e / B \quad (2)$$

where R_e , the effective grain radius, is one-half the distance between hot-spot initiation sites (i. e., the shock-heated voids) and B is the Arrhenius-type rate expression for the linear pyrolysis kinetics of AP (References 2 and 3),

$$B = 0.21 T_s \exp \left(\frac{-21,500}{R T_s} \right), \text{ m/sec} \quad (3)$$

where T_s is the surface temperature of the regressing AP particles. The critical diameter of porous AP propellant was then calculated by solving Equation 2 in conjunction with an expression derived from the Jones equation for nonideal detonation (Reference 4), which relates the detonation velocity D of a charge of diameter d to the ideal (maximum) detonation velocity D_i for a charge of infinite diameter, and to the detonation reaction time, t :

$$d = \frac{k D t}{\left[1 - (D/D_i)^2 \right]^{1/2}} \quad (4)$$

4. 4. 1 Detonation Model for RDX-Adulterated Propellant

As in the previous model for porous propellant, the model developed in this program to describe the nonideal detonation behavior of RDX-adulterated AP-PBAN propellant considers that the energy-release process for propagating detonation is grain-burning decomposition of the AP oxidizer, and that the grain-burning process is initiated by uniformly distributed hot-spots in a time that is short compared with the grain-burning time. In the present case, the hot spots are provided by the detonating RDX particles. The RDX reaction time is assumed to be negligible compared to the AP decomposition time. The total detonation reaction time is again given by Equation 2, where the effective grain radius can be related, from geometric considerations and the fixed binder, aluminum, and total oxidizer content (i. e., AP + RDX) of the propellants used in this program, to the RDX weight fraction and average RDX particle diameter d_{RDX} , as follows:

Consider a 1 cc cube of AP-RDX-Al-PBAN propellant in which RDX particles of diameter d_{RDX} and volume v_{RDX} are uniformly distributed throughout the propellant (see Figure 35). Let v be the volume fraction of RDX (and in this case, also the total volume of RDX per cc).

The number of particles of volume v_{RDX} per cc is then

$$\frac{v}{v_{RDX}} = \frac{v}{(4\pi/3)(d_{RDX}/2)^3} \quad (5)$$

and the distance between the centers of the RDX particles is

$$l = \frac{1}{\left[\frac{v}{(4\pi/3)(d_{RDX}/2)^3} \right]^{1/3}} \quad (6)$$

The effective AP grain radius is therefore

$$R_e = \frac{d_{RDX}}{2} \left[\left(\frac{\pi/6}{v} \right)^{1/3} - 1 \right] \quad (7)$$

Thus, R_e , and hence the detonation reaction time for RDX-adulterated AP propellant, is defined in terms of the RDX particle size and the volume fraction of RDX. In practice, the concentrations of the various propellant constituents are normally expressed as weight fractions. Using the relationship between the volume fraction v_i of the i th constituent of density ρ_i and the corresponding weight fraction f_i ,

$$v_i = f_i \left(\frac{\rho}{\rho_i} \right) \quad (8)$$

where ρ is the propellant density, Equation 7 becomes

$$R_e = \frac{d_{RDX}}{2} \left\{ \left[\frac{(\pi/6)(\rho_{RDX}/\rho)}{f} \right]^{1/3} - 1 \right\} \quad (9)$$

where $1/\rho$ for a propellant of n constituents is given by

$$\frac{1}{\rho} = \sum (f_n / \rho_n) \quad (10)$$

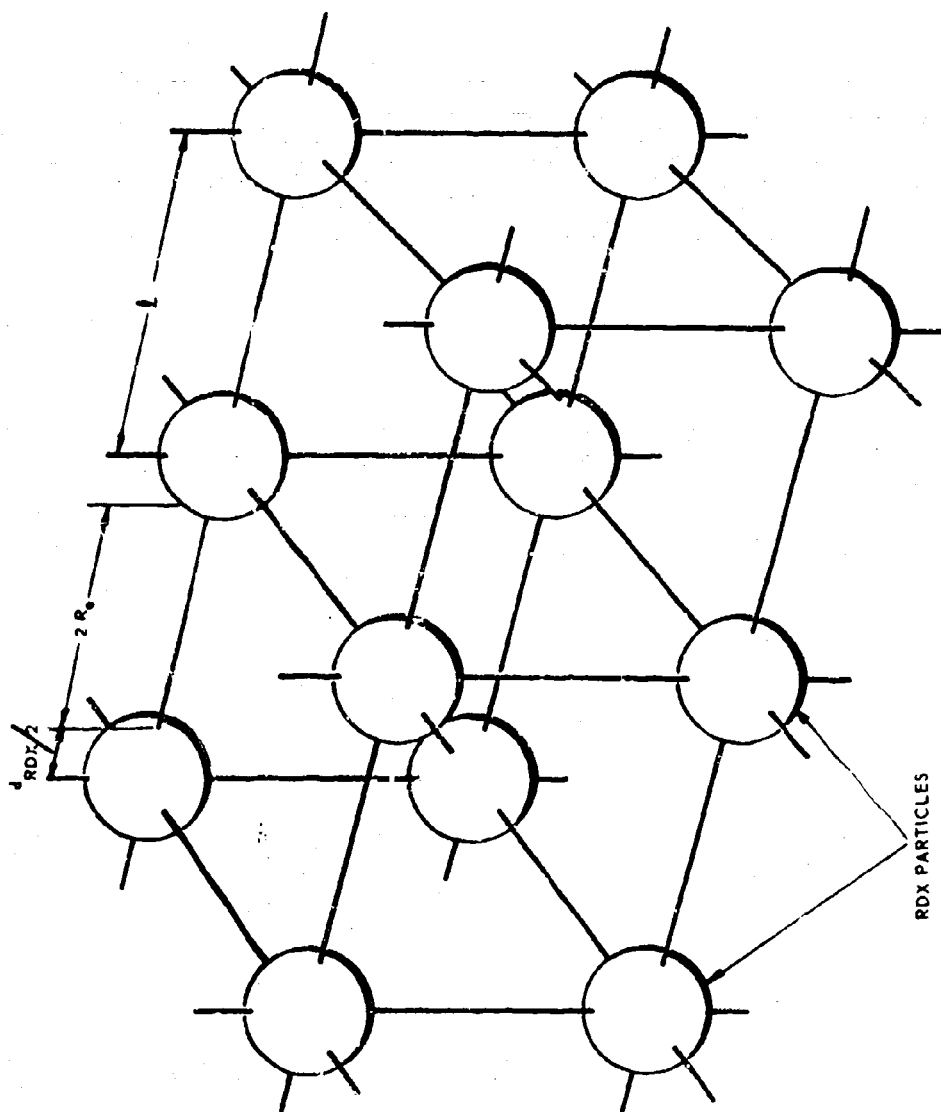


Figure 35. Physical Model of RDX-Adulterated AP-Al-PBAN Propellant.

In the RDX-adulterated AP-Al-PBAN systems considered in this program, the total oxidizer weight fraction is held constant as the RDX content is varied, with constant weight fractions of aluminum and PBAN binder in all cases. For purposes of the model the following composition is assumed:

<u>Constituent</u>	<u>Density</u>	<u>Weight Fraction</u>
RDX	1.8	f
AP	1.95	0.7 - f
Al	2.7	0.15
PBAN	1.0	0.15

Since $1/\rho$ is a function only of f for the above general formulation, Equation 9 becomes

$$R_e = \frac{d_{RDX}}{2} \left(0.0404 + \frac{0.534}{f} \right)^{1/3} - 1 \quad (11)$$

The factor 0.0404 in Equation 11 changes the value of R_e by less than one percent for values of $f \leq 0.10$ (the range of interest in the present study). Therefore the following essentially equivalent simplified expression for R_e will be used in further calculations

$$R_e = \frac{d_{RDX}}{2} \left[\left(\frac{0.534}{f} \right)^{1/3} - 1 \right] \quad (12)$$

By combining Equations 12 and 2 with Equation 4 an expression relating the effect of RDX weight fraction and particle size on the nonideal detonation behavior of RDX-adulterated propellant is obtained. At the critical diameter d_c this becomes

$$d_c = \frac{k D_c \left(\frac{d_{RDX}}{2} \right) \left[\left(\frac{0.534}{f} \right)^{1/3} - 1 \right]}{B_c \left[1 - (D_c / D_i)^2 \right]^{1/2}} \quad (13)$$

4.4.2 Test of Validity of Initial Detonation Model

To adequately test the validity of Equation 13 for predicting the critical diameter of RDX-adulterated propellant as a function of RDX weight fraction, the nature of the variations of D_i , D_c , and B_c with f must be known.

If, as a first approximation, it is assumed that D_i and D_c (and therefore B_c , which is a function of D_c) are independent of RDX concentration in the range of RDX weight fractions of interest (i. e., $f \leq 0.10$) then Equation 13 reduces to

$$d_c = k_1 \left(\frac{1}{f} \right)^{1/3} + k_2 \quad (14)$$

where k_1 and k_2 are constants.

Equation 14 predicts that the critical diameter of RDX-adulterated propellant should vary as the reciprocal of the cube root of the RDX content. In Figure 36, the critical diameter data have been plotted in this manner. While it is apparent that at very low RDX weight fractions the linear relation of Equation 14 is not followed, straight lines of the form of Equation 14 can be drawn between the "Go" and "No-Go" data for $0.10 \geq f \geq 0.018$. The equation of one such line is

$$d_c = 15.3 \left(\frac{1}{f} \right)^{1/3} - 30.9 \quad (15)$$

4.4.3 Refined Theoretical Model

The fact that the critical diameter data do not obey an equation of the form of Equation 14 at very low RDX contents is not surprising since this equation implies that the initiation sites are supplied only by the RDX particles. However, conventionally manufactured good-quality propellants may be expected to contain some small but finite concentration of minute voids. Also, it is well known that large AP grains usually contain many internal flaws and voids. Equation 14 must therefore be modified to include such additional initiation sites. As a first approximation, the additional sites may be considered simply as an additional (constant) weight fraction c of RDX particles.

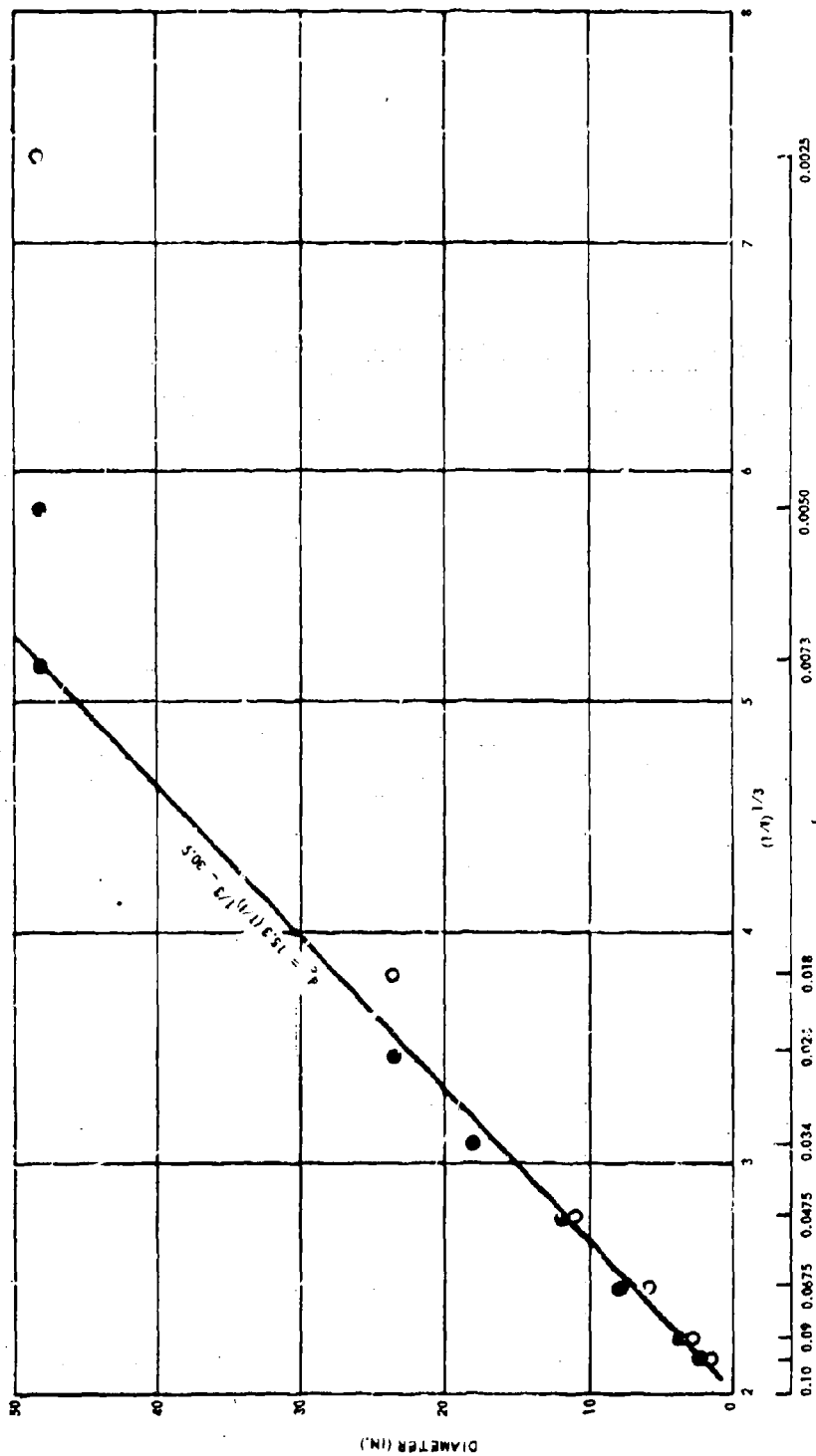


Figure 36. Correlation of Critical Diameter Data Using Simple Model (Equation 15).

Equation 14 then becomes

$$d_c = k_3 \left(\frac{1}{f+c} \right)^{1/3} + k_4 \quad (16)$$

where the constants k_3 and k_4 may not be identical with the corresponding constants of Equation 14. A combination of these constants that makes Equation 16 consistent with all the critical diameter data for propellants with $f \leq 0.10$ was found by trial and error. The resulting expression is

$$d_c = 15.3 \left(\frac{1}{f+0.003} \right)^{1/3} - 30.4 \quad (17)$$

The agreement of Equation 17 with the critical diameter data is illustrated in Figure 37.

4.4.4 Evaluation of Parameters of Refined Model

While Equation 17 is consistent with critical diameter data for $f \leq 0.10$, it too is based on the assumption that D_i , D_c , and B_c are independent of f in this range of RDX weight fractions. To determine if the theoretical expression of Equation 13, as modified by inclusion of the factor 0.003 to account for initiation sites other than RDX particles, i.e.,

$$d_c = \frac{k D_c \left(\frac{d_{RDX}}{2} \right) \left[\left(\frac{0.534}{f+0.003} \right)^{1/3} - 1 \right]}{B_c \left[1 - \left(D_c / D_i \right)^2 \right]^{1/2}} \quad (18)$$

will describe the detonation characteristics of RDX-adulterated propellants when D_i , D_c , and B_c are functions of f , an attempt was made to estimate these functions.

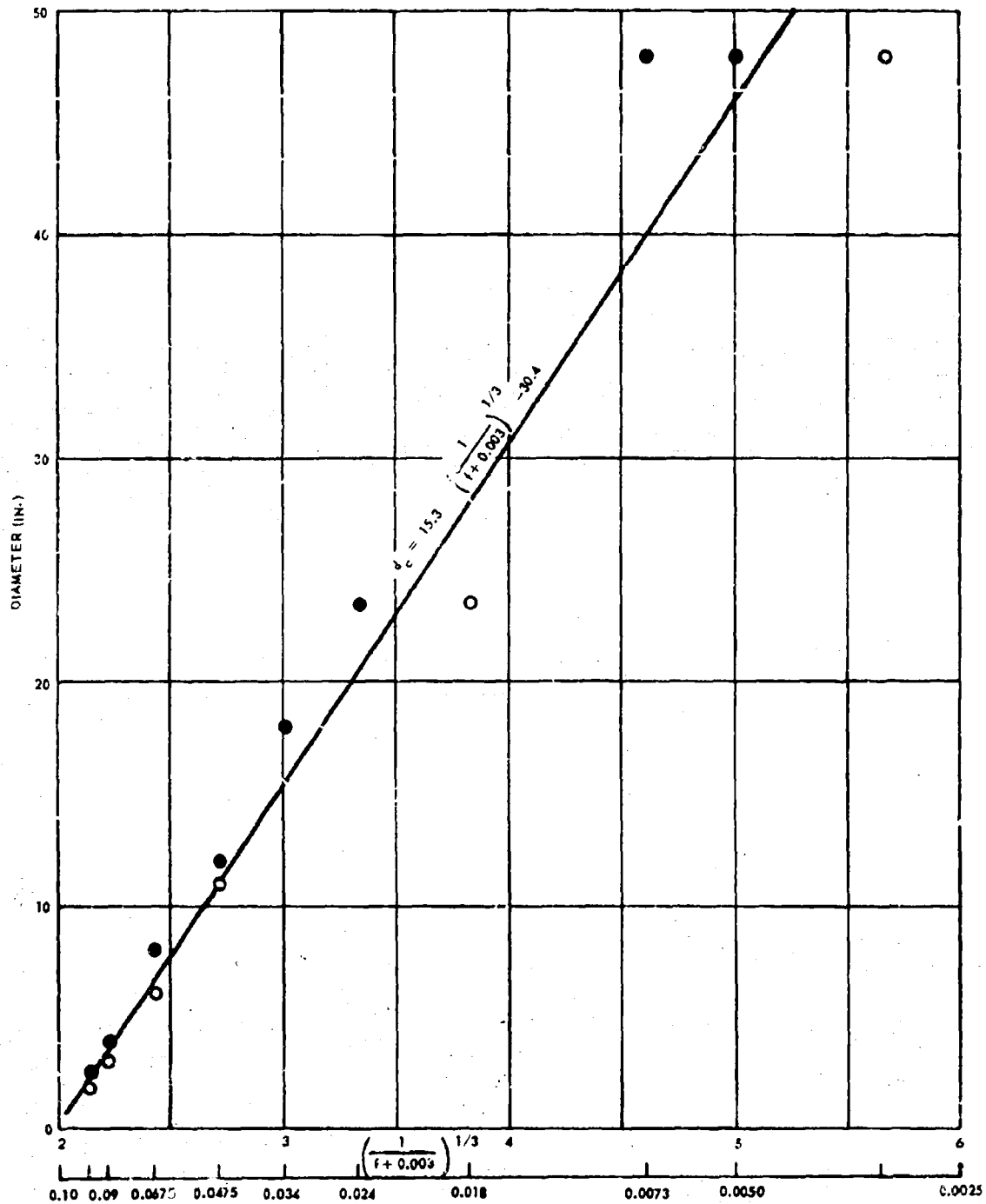


Figure 37. Correlation of Critical Diameter Data Using Refined Model (Equation 17).

4.4.4.1 Ideal Detonation Velocity

D_i can be calculated using the expression of Andersen and Parlin (Reference 5):

$$D_i^2 = 8.368 \times 10^3 \gamma_g (\gamma_g + 2) Q \quad (19)$$

where γ_g is the Gruneisen parameter and Q is the heat of detonation. The Gruneisen parameter is calculated by the expression of Miller (Reference 6):

$$\gamma_g = \frac{\sum [n_i (a \cdot r_e)_i]}{2 \sum n_i} \quad (20)$$

where n_i is the number of atoms of the i th kind and $(a \cdot r_e)_i$ are the Morse potential parameters for the various atoms. The heat of detonation is considered to be the sum of the heats of explosion of RDX and AP and the heat of combustion of the binder in the oxygen furnished by decomposition of the AP. D_i was found to vary essentially linearly with RDX weight fraction. The following best-fit relationship of the calculated values represents the variation of D_i with RDX weight fraction for values of f between 0 and 0.7 with a maximum deviation of 40 m/sec:

$$D_i = 6700 - 500 f, \text{ m/sec; } 0 \leq f \leq 0.7 \quad (21)$$

Equation 21 is in opposition to the intuitively expected increase in D_i with increasing RDX content. This results from the fact that, since the total oxidizer (AP + RDX) is maintained constant as f is varied, the amount of oxygen available for binder burning decreases as the RDX content increases. The net value of Q , and therefore of D_i , decreases with increasing f .

4.4.4.2 Critical Detonation Velocity

Certain features of the test program prevent the accurate determination of D_c as a function of f . These are:

- a. With the exception of the tests with propellant containing 16 wt % RDX, an appreciable gap in diameter existed between the largest subcritical and the smallest supercritical samples of each formulation (in some cases only one test was performed with a given propellant composition).

- b. The considerable scatter noted in the data even for a given diameter of one propellant formulation indicated that the detonation velocity vs diameter curve could not be assumed to necessarily pass through any of the limited number of data points obtained for the propellants of low RDX content.

Because of these uncertainties, the average detonation velocity D_c at the critical diameter of each of the formulations tested was estimated as follows:

- a. All of the average steady state detonation velocity vs diameter data of Table 2 was plotted on a single graph (Figure 38).
- b. The lower limit of each detonation velocity vs diameter curve is shown on the graph by either a solid vertical line (the largest subcritical sample tested with the particular formulation) or by a dashed vertical line (the value of the critical diameter calculated by means of Equation 17).
- c. Eye-fit curves for the variation of detonation velocity with charge diameter were drawn through the field of data points for each formulation. Since inspection of all the plotted data points indicated that the general slope of the collection of data points was steepest for the propellant containing the largest amount of RDX ($f = 0.16$) and decreased with decreasing f , this observation was used as a guide in positioning the curves.
- d. The intersection of the average detonation velocity vs diameter curves with the dashed vertical lines representing the calculated values of the critical diameter for $f \leq 0.10$ or with the solid vertical lines representing the largest subcritical sample tested for $f = 0.12$ and 0.16 was considered to be D_c for the particular formulation.

By plotting the estimated values of D_c for each value of f and drawing an eye-fit curve through the points, a graphical function for D_c vs f is obtained. The resulting curve is shown in Figure 39.

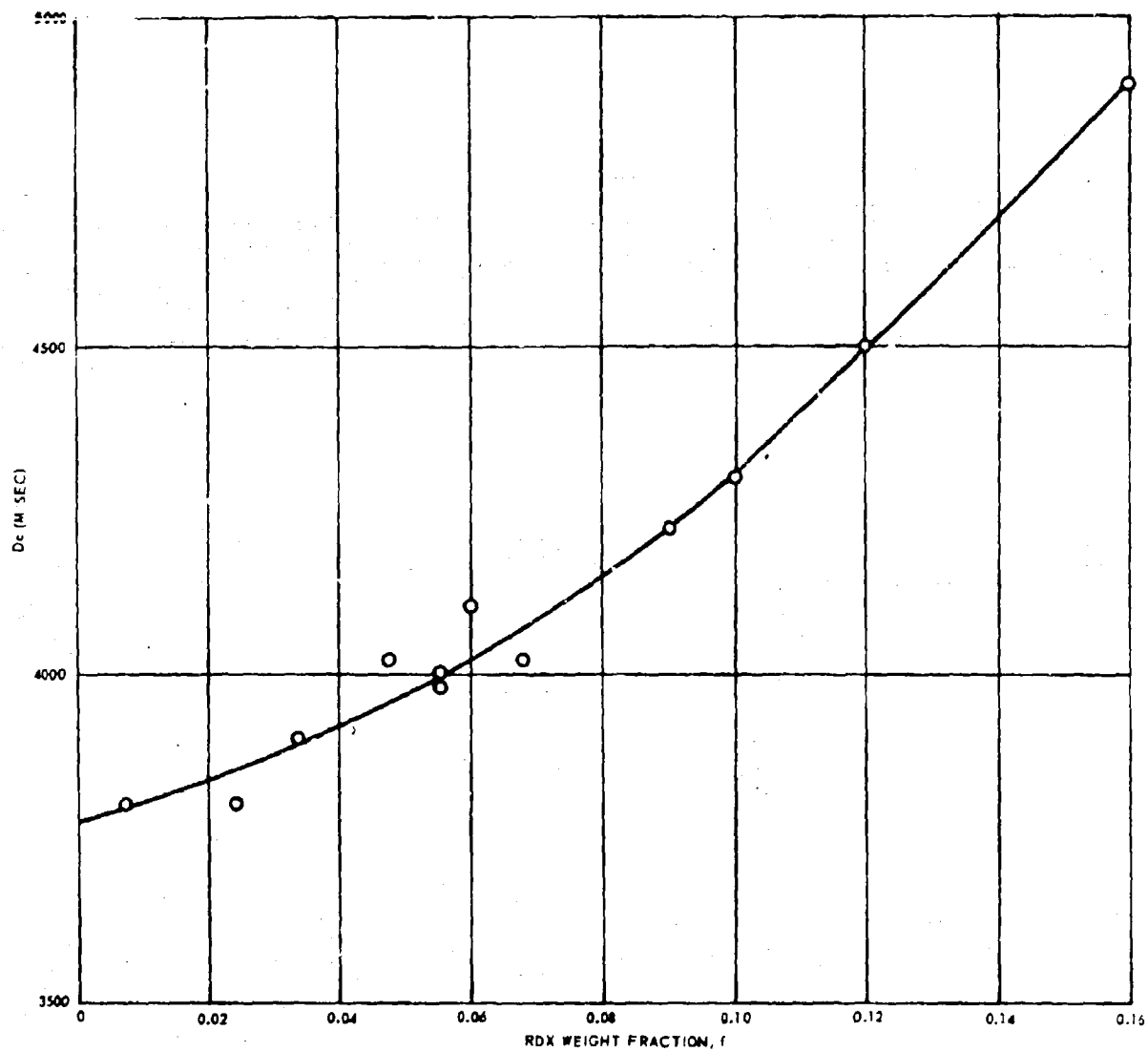


Figure 39. Estimated Critical Detonation Velocity vs RDX Content
for RDX-Adulterated PBAN Propellants.

4.4.4.3 Critical AP Linear Regression Rate

By combining a previously developed relation (Reference 2) between T_g and D

$$T_g = 1824 + 18.4 \rho_o D_c^2 - 0.137 \rho_o^2 D_c^4, \text{ } ^\circ\text{K} \quad (22)$$

with Equation 3, B_c can be related to D_c and hence to f through the graphical function for D_c vs f .

4.4.5 Test of Validity of Refined Detonation Model (Variable D_i , D_c , and B_c)

Equation 18, derived largely from theoretical considerations, may be rewritten as

$$d_c = \left[A \left(\frac{1}{f+0.003} \right)^{1/3} - C \right] \frac{D_c}{B_c [1-(D_c/D_i)^2]^{1/2}} \quad (23)$$

where

$$A = k \left(\frac{d_{RDX}}{2} \right)^{1/3} (0.534) \quad (24)$$

and

$$C = k \left(\frac{d_{RDX}}{2} \right) \quad (25)$$

Let

$$\frac{D_c}{B_c [1-(D_i/D_i)^2]^{1/2}} = g(f) \quad (26)$$

Now Equation 23 will be of the form of Equation 17, which has been shown to be consistent with all critical diameter data for $f \leq 0.10$, only if the function $g(f)$, containing the estimated functions D_i vs f , (Equation 18), D_c vs f (Figure 39), and B_c vs f (Equations 3 and 22, together with Figure 39) is a constant. In Table 4, the calculated values of $g(f)$ for values of f between 0.16 and 0.00375 are presented. It is seen that for $f \leq 0.10$, $g(f)$ is essentially a constant, with the maximum

Table 4. Evaluation of $g(f)$ for RDX Contents Between 0.375 and 16 wt %.

RDX Weight Fraction f	Propellant Density ρ_0 (g/cc)	Critical Detonation Velocity D_c (m/sec)	Surface Temperature of Grain- Burning AP T_s (°K)	Critical Linear Regression Rate B_c (m/sec)	Ideal Detonation Velocity D_i (m/sec)	g (f)
0.16	1.751	4900	2355	4.995	6620	1460
0.12	1.757	4500	2305	4.405	6640	1389
0.10	1.759	4300	2277	4.112	6650	1370
0.09	1.760	4220	2266	4.045	6655	1350
0.0675	1.764	4065	2244	3.817	6666	1344
0.0475	1.766	3955	2228	3.649	6676	1346
0.04	1.767	3920	2223	3.595	6680	1346
0.02	1.770	3840	2211	3.482	6690	1346
0.01	1.771	3805	2206	3.428	6695	1350
0.00375	1.772	3300	2205	3.427	6698	1346

and minimum values differing by less than 2%. Since, with constant $g(f)$ Equation 23 becomes essentially identical with the experimentally consistent Equation 17, it too will be valid for f -values between 0.10 and 0.00375 (the mid-value of f for the subcritical and supercritical 48-in. diameter samples with f -values of 0.0025 and 0.0050 respectively).

Having established the essential constancy of $g(f)$, the correctness of the geometrical factor $(0.534)^{1/3}$ in Equation 18 may also be determined.

From Equations 24 and 25,

$$\frac{A}{C} = (0.534)^{1/3} \quad (27)$$

but, from Equations 17 and 23

$$A g(f) = 15.3 \quad (28)$$

and

$$C g(f) = 30.4 \quad (29)$$

so that

$$\frac{A}{C} = 0.5033 = (0.1275)^{1/3} \quad (30)$$

Since Equations 28 and 29 are consistent with the experimental critical diameter data for $f \leq 0.10$, it is concluded that the correct value of the geometrical factor to be used in Equation 18 is $(0.1275)^{1/3}$. The final form of the theoretical detonation model is therefore

$$d_c = \frac{k \left(\frac{d_{RDX}}{2} \right) D_c \left[\left(\frac{0.1275}{f+0.003} \right)^{1/3} - 1 \right]}{B_c \left[1 - \left(D_c / D_i \right)^2 \right]^{1/2}} \quad (31)$$

which is identical with Equation 17, i. e.,

$$d_c = 15.3 \left(\frac{1}{f+0.003} \right)^{1/3} - 30.4$$

when $C = k(d_{\text{RDX}}/2) = 2.252 \times 10^{-2}$ (see Equations 25 and 29) and when D_i , D_c , and B_c either assume their estimated functional forms or where the combined function $g(f) = 1350$ ($f \leq 0.10$).

4.4.6 Predictions of the Refined Theoretical Model

Equation 31 or its equivalent, Equation 17, may now be used to estimate the critical diameter of RDX-adulterated AP-PBAN propellant as a function of f , as well as the critical diameter of unadulterated AP-PBAN propellant. The results of these calculations are summarized in Table 5. In Figure 40, the calculated critical diameters are compared with the experimentally determined critical diameter ranges for the propellants tested on this program.

4.4.7 Critique of the Refined Theoretical Model

A comparison of the experimental critical diameter data with the calculated values of critical diameter over the entire range of RDX contents employed in this study lends considerable support to the basic assumptions of the theoretical model as to the important physical and chemical processes involved in propagating detonation in RDX-adulterated AP-PBAN propellants.

First, even the simple detonation model, in which the effective AP grain radius (and hence the detonation reaction time and critical diameter) is proportional to $(1/f)^{1/3}$, predicts values of the critical diameter in agreement with the experimental data over a considerable range of RDX contents ($0.10 > f > 0.016$). This suggests that, for this region of f -values, the assumption that AP grain burning is the predominant energy-release process in the detonation reaction zone is a reasonable one.

Second, the fact that an increasing disparity exists between the calculated critical diameter and the experimental data for $f > 0.10$ is in itself supporting evidence for the grain-burning mechanism. In the detonation model the effective AP grain radius (i.e., half the calculated distance between uniformly distributed RDX particles in a continuous AP matrix) can decrease with increasing RDX content until each RDX particle is in contact with its neighbors (i.e., $R_e = 0$), while in the real situation there will be some RDX level at which R_e will equal the average AP grain radius and any further decrease in R_e with increasing RDX content will be prevented by the AP particles. For the propellants tested in this program this apparently occurs

Table 5. Calculated Values of the Critical Diameter of RDX-Adulterated PBAN Propellant of $0 \leq f \leq 0.16$, Using Refined Model.

RDX Weight Fraction, f	$\left(\frac{1}{f + 0.003} \right)^{1/3}$	Critical Diameter d_c (in.)
0.12	2.013	0.4
0.11	2.068	1.3
0.105	2.100	1.8
0.10	2.133	2.3
0.09	2.207	3.4
0.08	2.293	4.7
0.0675	2.420	6.6
0.06	2.512	8.0
0.0475	2.705	11.1
0.04	2.852	13.3
0.034	3.000	15.5
0.024	3.332	20.6
0.02	3.513	23.5
0.01	4.253	34.7
0.0073	4.600	40.0
0.0050	5.000	46.1
0.00375	5.290	50.6
0.0025	5.666	56.5
0.0010	6.300	66.1
0	6.930	75.6

when $f > 0.10$. Grain-burning at higher RDX levels would therefore occur at an essentially constant grain radius, but with an increase in the number of RDX particles surrounding each grain. If the excess RDX particles on the surface of the grains did not affect the grain-burning process, the critical diameter would be expected to remain essentially constant. The fact that the critical diameter actually decreases slowly for $f > 0.10$ (dashed curve of Figure 40) suggests that the energetic decomposition of the high concentration of RDX particles around each AP grain results in a higher-than-normal linear regression rate for the outer portion of the grains. This leads to a somewhat shorter total grain-burning time and hence a somewhat smaller critical diameter than would have resulted had there been no perturbation of the AP grain-burning process by the decomposing RDX particles.

Third, the need to account for the initiation sites that will be present in good-quality propellant, even without RDX adulterant, was anticipated from available evidence on the occurrence of flaws and voids in large AP grains. The fact that the simple model (Equation 15) failed at lower values of f (where the additional initiation sites become an increasingly large fraction of the total number of sites), but could be successfully modified by including a term to account for such additional initiation sites, supports the original assumption that a grain-burning mechanism is largely responsible for propagating detonation in these propellants.

An important implication of the need for an additional parameter in the model to account for such voids and flaws is that the critical diameter of conventionally-manufactured Class II propellants will be a rather sensitive function of the propellant quality, i. e., of the number and size-distribution of flaws introduced into the propellant grain either during manufacture or during handling and storage.

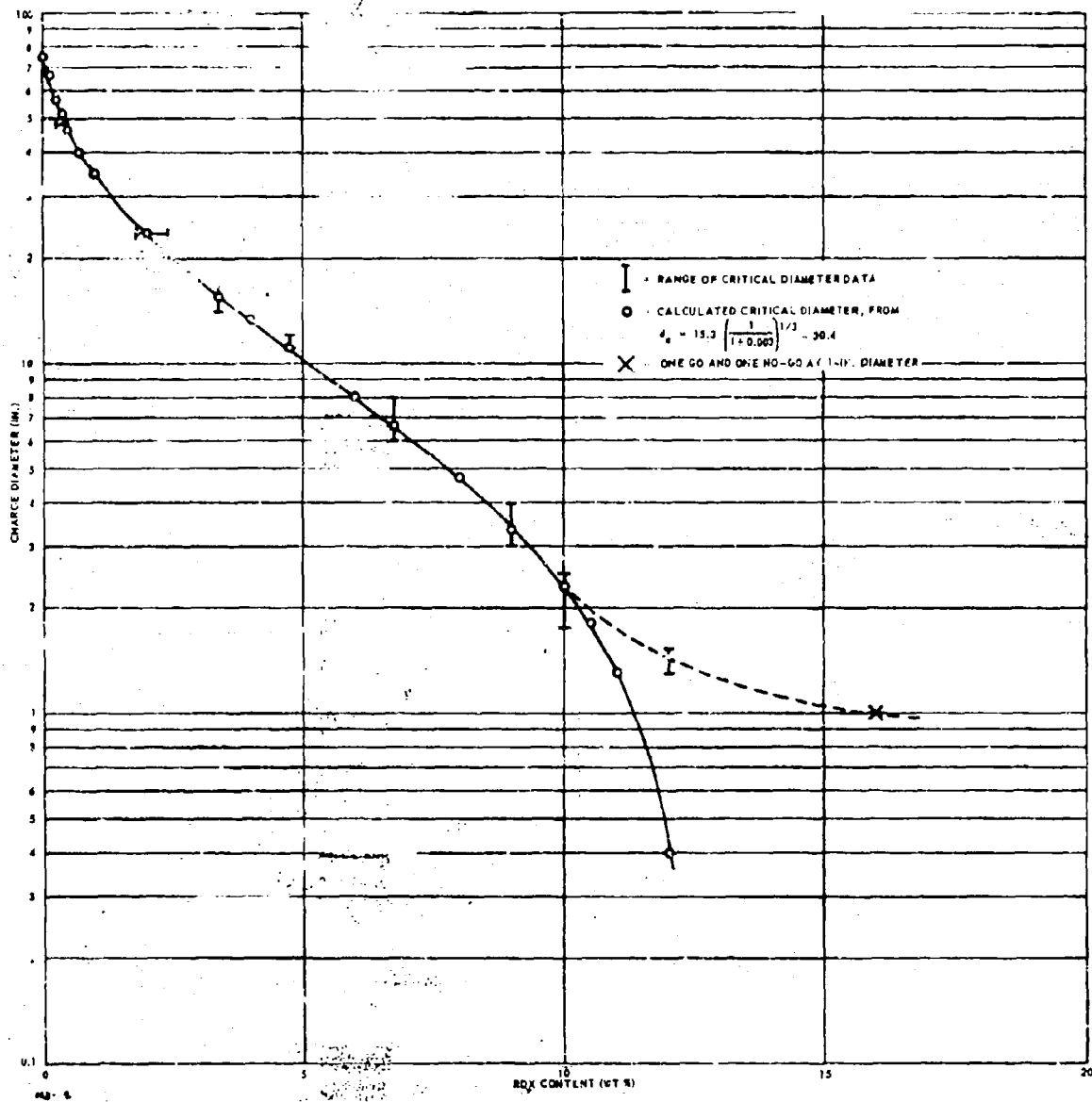


Figure 40. Comparison of Predictions of Theoretical Model with Experimental Critical Diameter Data.

5. CRITICAL GEOMETRY PROGRAM

5.1 OBJECTIVES

The objective of Task B was to develop a reliable theory of critical geometry for predicting the conditions under which detonation could take place in non-right-solid-cylindrical systems. Specifically, this task was divided into two phases:

- a. Determine the critical dimensions for the sustainment of detonation of various (nonperforated and perforated) shapes.
- b. Determine an initiation criterion and demonstrate the applicability of this criterion in predicting the detonation of nonperforated and perforated cylinders using various size cylindrical donors at various locations.

The first objective was studied with a previously developed RDX-wax explosive with a critical diameter of approximately 1-1/2 in. as well as a PBAN-RDX propellant with a critical diameter of approximately 3 in. The second objective was studied with the PBAN-RDX propellant only.

5.2 THEORY

The current theory of critical geometry is presented in detail in Appendix A of this report. However, a brief summary of the main features of theory is useful in understanding the objectives and results of the current program.

The critical geometry theory determines the detonability of a given system formulation by answering the two questions:

- a. Is the given configuration capable of supporting detonation?
- b. If the configuration is capable of supporting detonation, are sufficient (shock) forces available to initiate detonation?

The first question is answered by analyzing the gains and losses of energy in a detonation, and by geometrical reasoning developing a "critical" condition for any configuration, expressed as a simple algebraic equation. This equation relates the critical dimensions of any shape to the critical

diameter of a right-solid cylinder, and determines if it is capable of detonation. Applying this equation to various shapes (nonperforated and perforated) gives the results shown in Figures 41 and 42.

The second question is partly answered by considering the parameter (shock pressure) most important in causing shock-initiated detonation, assuming that the minimum shock pressure required to initiate detonation is independent of shape but varies with size, and then postulating an "initiation criterion" (a property of the given material) expressed in terms of shock pressure. The second question is then fully answered by considering this "initiation criterion" and determining if the shock input from a given stimulus meets the requirement of the criterion. If so, initiation of detonation takes place.

5.3 TECHNICAL DISCUSSION

During this program, an experimental-theoretical program was carried out to evaluate the current theory of critical geometry (Appendix A). In conducting the experimental program seven batches of RDX-wax explosive were cast and 93 critical geometry tests performed whereas three batches of PBAN-RDX propellant were cast and 77 critical geometry tests performed. The remaining 27 tests made were for exploratory purposes and/or calibration purposes only.

In conducting the theoretical program, the fundamental assumptions underlying the current theory of critical geometry were examined in light of the results obtained in the experimental program.

5.3.1 Experimental Studies

An outline of the test plan of the experimental program is shown in Table 6, where the explosive used and the number of tests performed is indicated. For convenience, the program was divided into the subtasks listed.

Because many instrumented tests were required, a specific test site, Aerojet's Chino Hills Laboratory, was selected and secured for this program. This site has facilities for using high-speed framing and/or streak cameras and rasteroscillograph techniques.

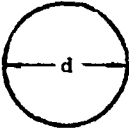
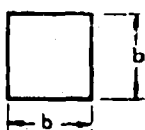
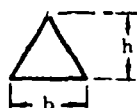
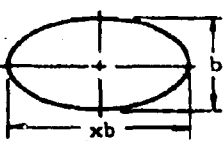
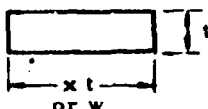
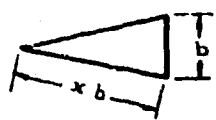
SHAPE AND CHARACTERIZING DIMENSIONS	CRITICAL VALUE OF CHARACTERIZING DIMENSIONS
CIRCLE 	$d_c = d_c$
SQUARE 	$b_c = d_c$
EQUILATERAL TRIANGLE 	$b_c = (\sqrt{3}) d_c$ or $h_c = (\frac{3}{2}) d_c$
ELLIPSE WHERE: $x > 1$ 	$b_c = \left[\frac{\int_0^{\pi/2} \sqrt{1 - \frac{x^2 - 1}{x^2} \sin^2 \phi} d\phi}{\pi} \right]$ $b_{c\infty} = \lim_{x \rightarrow \infty} b_c = \frac{d_c}{\pi}$
RECTANGLE WHERE: $x > 1$ 	$t_c = \left(\frac{x+1}{2x} \right) d_c$ $t_{c\infty} = \lim_{x \rightarrow \infty} t_c = \frac{d_c}{2}$ <p>or if w is fixed</p> $t_c = \frac{wd_c}{2w - d_c}$
ISOSCELES TRIANGLE WHERE: $x > 1$ 	$b_c = \sqrt{\frac{2x+1}{2x-1}} d_c$ $b_{c\infty} = \lim_{x \rightarrow \infty} b_c = d_c$

Figure 41. Critical Dimensions of Various Shapes - Nonperforated Grains.

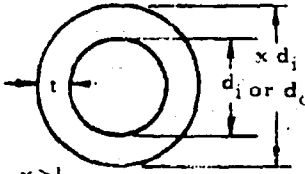
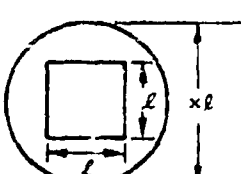
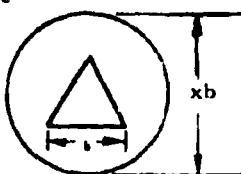
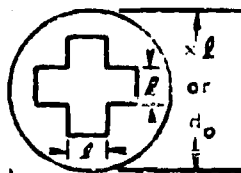
SHAPE AND CHARACTERIZING DIMENSIONS	CRITICAL VALUE OF CHARACTERIZING DIMENSIONS
<p>CIRCULAR CORE</p>  <p>WHERE: $x > 1$</p>	$d_{i_c} = \left(\frac{1}{x - 1} \right) d_c \quad \text{or} \quad t_c = \frac{d_c}{2}$ <p>or if d_i is fixed</p> $d_{o_c} = d_i + d_c$
<p>SQUARE CORE</p>  <p>WHERE: $x > 1$</p>	$l_c = \left(\frac{\pi x + 4}{\pi x^2 - 4} \right) d_c$
<p>EQUILATERAL TRIANGLE CORE</p>  <p>WHERE: $x > 1$</p>	$b_c = \left(\frac{\pi x + 3}{\pi x^2 - \sqrt{3}} \right) d_c$
<p>CROSS CORE</p>  <p>WHERE: $x > 1$</p>	$l_c = \left(\frac{\pi x + 12}{\pi x^2 - 20} \right) d_c$ <p>or if l is fixed</p> $d_{o_c} = \frac{d_c}{2} \left[1 + \sqrt{1 + \frac{16l}{\pi d_c} \left(5 \frac{l}{d_c} + 3 \right)} \right]$

Figure 42. Critical Dimensions of Various Shapes - Perforated Grains.

Table 6. Experimental Program Outline.

Sub-Task and Description	Explosive	Number of Tests
B.1 Preliminary Tests	RDX-Wax, Composition B	22
B.2 Sustainment of Detonation	RDX-Wax	-
B.2.1 Nonperforated Shapes		-
B.2.1.1 Circle		39
B.2.1.2 Square		16
B.2.1.3 Rectangle		8
B.2.1.4 Equilateral Triangle		3
B.2.2 Perforated Shapes		-
B.2.2.1 Circular Core	RDX-Wax	9
B.3 Sustainment of Detonation	PBAN-RDX	-
B.3.1 Nonperforated Shapes		-
B.3.1.1 Circle		19
B.3.1.3 Equilateral Triangle		6
B.3.2 Perforated Shapes	PBAN-RDX	-
B.3.2.1 Circular Core	PBAN-RDX, Composition B	8
B.3.2.2 Cross Core	PBAN-RDX	5
B.4 Initiation of Detonation	PBAN-RDX	-
B.4.1 Sensitivity Measurements		-
B.4.1.1 Initial Shock Pressure		2
B.4.1.2 Shock Attenuation		10
B.4.1.3 Hugoniot Measurements		7
B.4.1.3 Initiation Criterion		32
B.4.2 Attenuation Properties		-
B.4.2.1 Nonperforated Shapes		-
B.4.2.1.1 Axial, End Donor		5
B.4.2.1.3 Side Donor		2
B.4.2.2 Perforated Shapes		-
B.4.2.2.2 Nonaxial, End Donor		2
B.4.2.2.3 Side Donor	PBAN-RDX	2
Total Number of Tests -		197

5.3.1.1 Sustainment of Detonation

During this program, 113 sustainment of detonation tests were performed with RDX-wax and PBAN-RDX explosive. In each test, the determination of a steady detonation ("Go") or a transient detonation ("No-Go") was based on a careful reduction, examination, and evaluation of the reaction velocity-distance data generated by the streak camera and/or rasterscillograph system, as well as the witness plate test result classification illustrated in Figure 43. The range of critical dimensions was determined from the test dimensions below which there were no more "Go's" and the test dimensions above which there were no more "No-Go's."

5.3.1.1.1 RDX-Wax Explosive (Subtask B.2)

Although considerable difficulty was encountered in obtaining samples of adequate quality of RDX-wax explosive, careful examination and reduction of the test records showed that useful results were obtained.


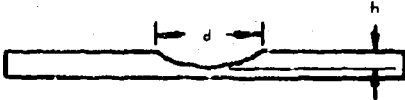
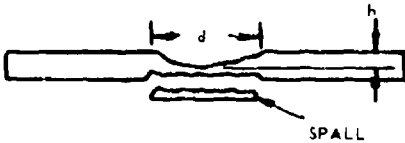
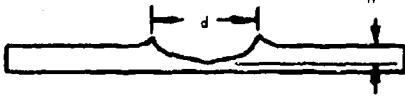
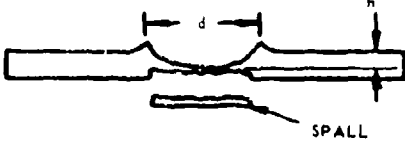

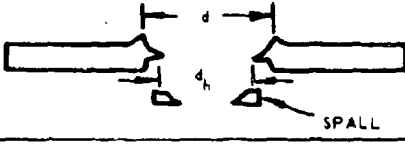
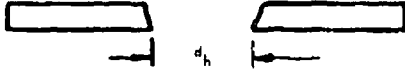
a. Nonperforated Shapes (Subtask B.2.1)

For nonperforated shapes, the shapes considered were the circle, square, rectangle, and equilateral triangle (Subtasks B.2.1.1, B.2.1.2, B.2.1.3, and B.2.1.4 respectively). The objective of each subtask was to determine the critical dimensions of the particular shape. The prediction of the current theory of critical geometry for each shape is shown in Figure 44.

(1) Critical Diameter (Circle) Tests (Subtask B.2.1.1)

The results of 39 critical diameter tests, using samples from five batches of RDX-wax explosive (containing 30.75% RDX) are shown in Table 7. The subtask involved is indicated by the test number.

The test setup is illustrated in Figure 45. A high degree of certainty is placed on most of the determinations in Table 7. However, where evidence for the particular judgement was subject to any doubt, a question mark was placed next to the Go, No-Go determinations.

TYPE	RESULT	WITNESS PLATE SIDE VIEW d = dent diameter, h = dent depth, d_h = hole diameter	CONCLUSION
0	NO DENT		NO GO
1	SMOOTH DENT WITHOUT SPALL		NO GO ?
1S	SMOOTH DENT WITH SPALL		NO GO ??
2	SHARP-EDGE DENT WITHOUT SPALL		GO ??
2S	SHARP-EDGE DENT WITH SPALL		GO ?
3	SHARP-EDGE DENT AND HOLE WITHOUT SPALL		GO
3S	SHARP-EDGE DENT AND HOLE WITH SPALL		GO
4	PUNCH		GO

2544-2-9-1

Figure 43. Witness Plate Test Result Classification.


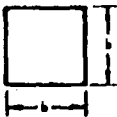
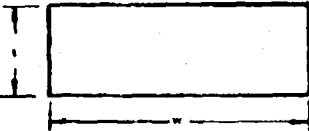
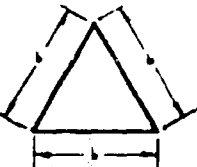
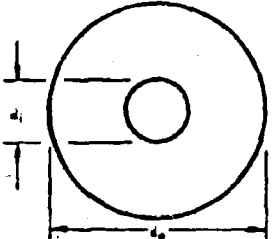
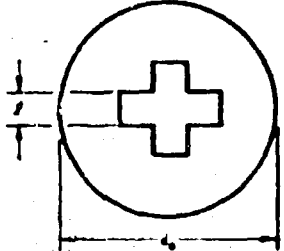
SHAPE AND CHARACTERIZING DIMENSIONS	CRITICAL VALUE OF CHARACTERIZING DIMENSIONS
	$d_c = d_c$
	$b_c = d_c$
 [w fixed]	$t_c = \frac{w d_c}{2w - d_c}$
	$b_c = \sqrt{3} d_c$
 [d_i fixed]	$d_{o_c} = d_i + d_c$
 [b fixed]	$d_{o_c} = \frac{d_c}{2} \left[1 + \sqrt{1 + \frac{16b}{\pi d_c} \left(5 \frac{b}{d_c} + 3 \right)} \right]$

Figure 44. Critical Dimensions of Various Shapes from
Critical Geometry Theory.

Table 7. Critical Diameter Tests - RDX-Wax.

Test Number	Charge Diameter (in.)	Batch Number**	Charge Density (gm/cc)	Result	Instru- mentation***	wp Result****	sc Result
B. 2.1.1.1	0.75	3	1.07	No-Go	wp/sc	0	No data
B. 2.1.1.2	0.75	3	1.07	No-Go	wp/sc	0	No data
B. 2.1.1.3	1.0	3	1.06	No-Go	wp/sc	0	No-Go
B. 2.1.1.4	1.0	3	1.06	No-Go	wp/sc	0	No-Go
B. 2.1.1.5	1.25	3	1.06	No-Go	wp/sc	0	No-Go
B. 2.1.1.6	1.25	3	1.06	No-Go	wp/sc	0	No-Go
B. 2.1.1.7	1.25	3	1.06	No-Go	wp/sc	0	No-Go
B. 2.1.1.8	1.75	3	1.06	No-Go	wp/sc	1	No-Go
B. 2.1.1.9	1.75	3	1.06	Go?	wp/sc	1	Go?
B. 2.1.1.10*	1.5	3	1.06	No-Go	wp/sc	0	No-Go
B. 2.1.1.11	1.50	3	1.06	No-Go	wp/sc	0	No-Go
B. 2.1.1.12	1.97	3	1.05	Go	wp/sc	3S	Go
B. 2.1.1.13	1.961	3	1.05	Go?	wp/sc	3S	Go?
B. 2.1.1.14	1.5	3	1.06	No-Go	wp/sc	0	No-Go
B. 2.1.1.15	1.25	2	1.13	Go?	wp/sc	2S	Go?
B. 2.1.1.16	2.0	4	1.06	Go	wp/sc	3S	Go
B. 2.1.1.17	1.5	4	1.06	No-Go	wp/sc	0	No-Go
B. 2.1.1.18	1.75	4	1.06	Go?	wp/sc	3S	Go?
B. 2.1.1.19	1.63	4	1.06	No-Go	wp/sc	0	No-Go
B. 2.1.1.20	1.63	4	1.06	No-Go	wp/sc	0	No-Go
B. 2.1.1.21	1.75	4	1.06	No-Go	wp/sc	0	No-Go
B. 2.1.1.22	1.63	4	1.05	?	wp/sc	1S	Go?
B. 2.1.1.23	1.88	4	1.05	Go	wp/sc	1	Go?
B. 2.1.1.24*	1.75	4	1.06	Go?	wp/sc	1S	Go?
B. 2.1.1.25	1.50	5	1.10	No-Go	wp/sc	1S	No-Go
B. 2.1.1.26	1.63	5	1.11	Go	wp/sc	3S	Go
B. 2.1.1.27	1.75	5	1.10	-	wp/sc	-	-
B. 2.1.1.28	1.38	5	1.08	No-Go	wp/sc	0	No data
B. 2.1.1.29	1.38	5	1.09	No-Go	wp/sc	0	No data
B. 2.1.1.30	1.25	6	1.09	No-Go	wp/sc	0	No data
B. 2.1.1.31	1.5	6	1.09	?	wp/sc	1	No data
B. 2.1.1.32	1.63	6	1.11	Go?	wp/sc	1	Go?
B. 2.1.1.33	1.50	6	1.08	Go	wp/sc	3S	Go
B. 2.1.1.34	1.38	6	1.06	No-Go	wp/sc	0	No-Go
B. 2.1.1.35	1.25	6	1.08	No-Go	wp/sc	0	No data
B. 2.1.1.36	1.38	6	1.05	No-Go?	wp/sc	0	No-Go?
B. 2.1.1.37	1.63	6	1.11	Go?	wp/sc	1	Go?
B. 2.1.1.38	1.75	6	1.10	Go?	wp/sc	1	Go?
B. 2.1.1.39	1.75	6	1.10	Go?	wp/sc	1	Go?

Argon window used in Test B. 2.1.1.10 through B. 2.1.1.24

**Batches 3-6 contain 30.75% RDX

***wp = witness plate

sc = streak camera (Beckman and Whitley Model 194)

****See Figure 43

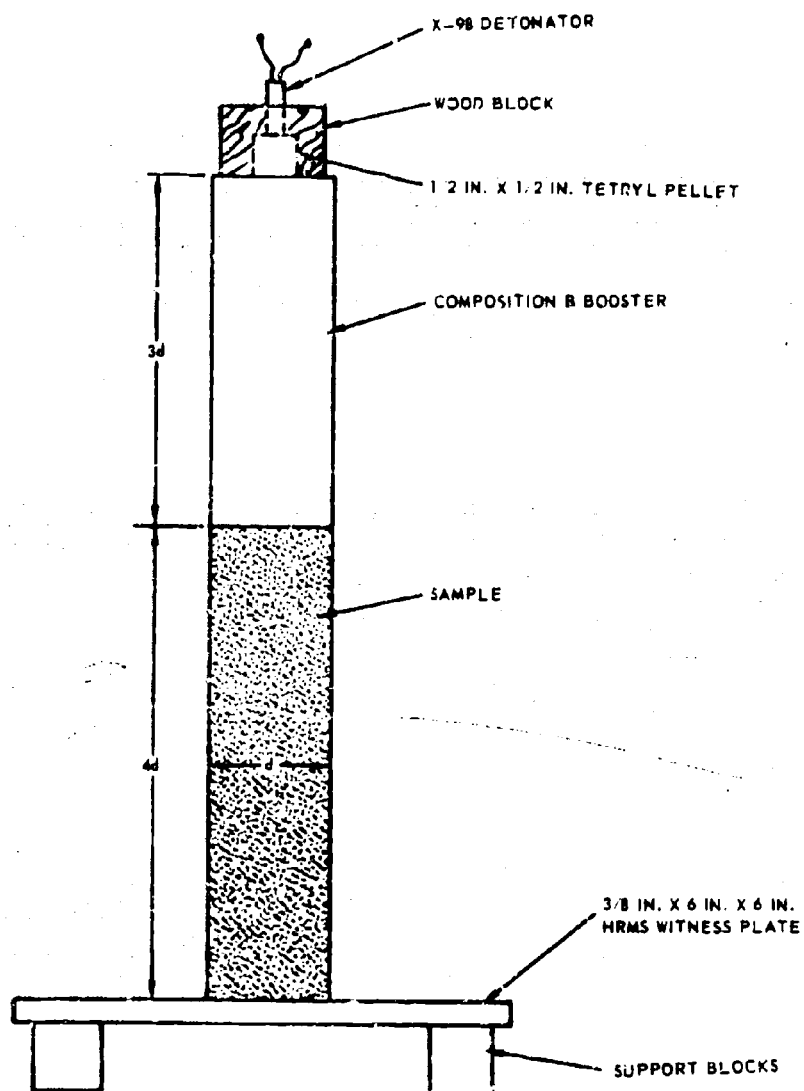


Figure 45. Test Setup - Critical Diameter Tests.

The results for Batches 3, 4, 5, and 6 were analyzed by the scheme shown in Figure 46 which is a plot of the number of Go's and No-Go's vs charge diameter. Batches 1 and 2 contained 31.5% RDX and were used only for the preliminary tests. The Go, No-Go determinations with question marks in Table 7, are identified by open boxes in Figure 46. The results in Figure 46 show that the critical diameter d_c of Batches 3 and 4 RDX-wax explosive is between 1.63 and 1.88 in. while that of Batches 5 and 6 is between 1.38 and 1.63 in. It may be noted that the results for Batches 3 and 4 and for Batches 5 and 6 are consistent with each other and could be respectively combined. The difference in critical diameter between these groups is expected because the latter group was prepared using vacuum melt procedures which resulted in higher densities.

(2) Critical Square Tests (Subtask B.2.1.2)

The results of 16 critical square tests using samples from two batches of RDX-wax explosive are shown in Table 8. The subtask involved is indicated by the test number. The test setup used is shown in Figure 47. An analysis of these results is shown in Figure 48 which is a plot of the number of Go's and No-Go's vs charge diameter for RDX-wax batches 4 and 6. Again, the tests with question marks in Table 8 are indicated by open boxes in Figure 48. The results in Figure 48 indicate that the critical square side b_c of Batch 4 RDX-Wax explosive is between 1.13 and 1.25 in. These figures are below those predicted from the current critical geometry theory, so there is a need of a downward correction.

(3) Critical Rectangle Tests (Subtask B.2.1.3)

The results of eight critical rectangle tests using samples from Batch 6 RDX-wax explosive are shown in Table 9. The test setup is shown in Figure 49. The analysis of these results was carried out in a manner similar to the previous tests and is shown in Figure 50. The results in Figure 50 show that the critical rectangular thickness t_c of Batch 6 RDX-wax explosive is probably less than or equal to 1.0 in. because all charges detonated. This result is consistent with the above result in that it is somewhat below the value predicted by theory.

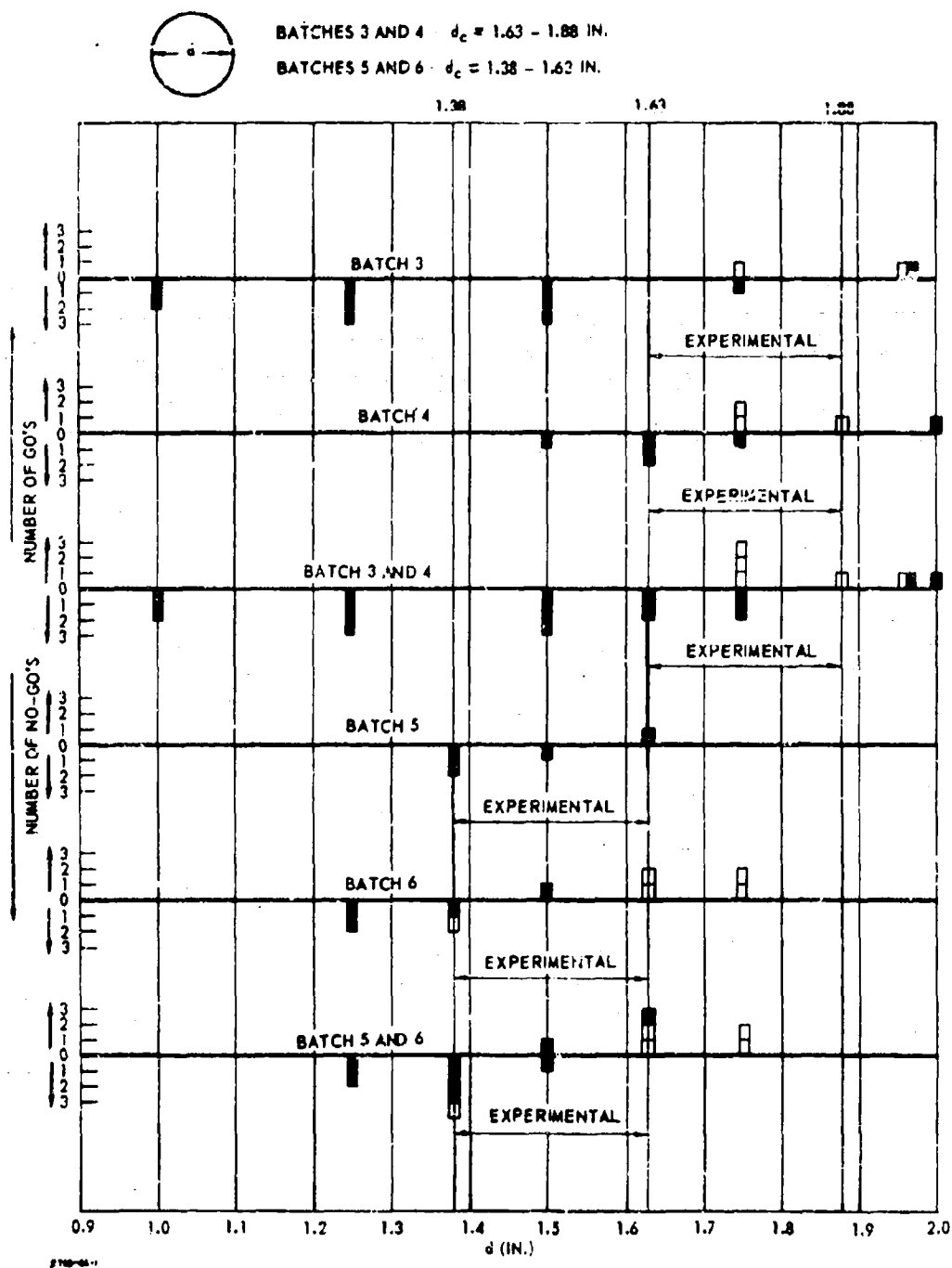


Figure 46. Analysis of Critical Diameter Tests - RDX-Wax.

Table 8. Critical Square Tests - RDX-Wax.

Test Number	Charge Side (in.)	Batch Number	Charge Density (gm/cc)	Result	Instru- mentation*	wp Result**	sc Results
B.2.1.2.1	1.63	4	1.06	Go?	wp/sc	3S	Go?
B.2.1.2.2	1.88	4	1.06	Go	wp/sc	3S	Go
B.2.1.2.3	1.63	4	1.07	Go	wp/sc	3S	Go
B.2.1.2.4	1.5	4	1.07	Go	wp/sc	3S	Go
B.2.1.2.5	1.38	4	1.08	No-Go?	wp/sc	1S	No-Go?
B.2.1.2.6	1.25	4	1.08	No-Go	wp/sc	0	No-Go
B.2.1.2.7	1.25	4	1.08	No-Go	wp/sc	1	No-Go
B.2.1.2.8	1.36	4	1.08	Go?	wp/sc	1S	Go?
B.2.1.2.9	1.5	4	1.07	Go	wp/sc	3S	No data
B.2.1.2.10	1.0	6	1.09	No-Go	wp/sc	0	No data
B.2.1.2.11	1.13	6	1.08	No-Go?	wp/sc	1	No-Go
B.2.1.2.12	1.13	6	1.09	No-Go	wp/sc	1	No-Go
B.2.1.2.13	1.38	6	1.08	Go	wp/sc	2S	Go
B.2.1.2.14	1.5	6	1.10	Go	wp/sc	3S	Go
B.2.1.2.15	1.25	6	1.10	Go	wp/sc	2S	Go
B.2.1.2.16	1.25	6	1.10	Go	wp/sc	2S	Go?

*wp = witness plate

sc = streak camera (Beckman and Whitley Model 194)

**See Figure 43

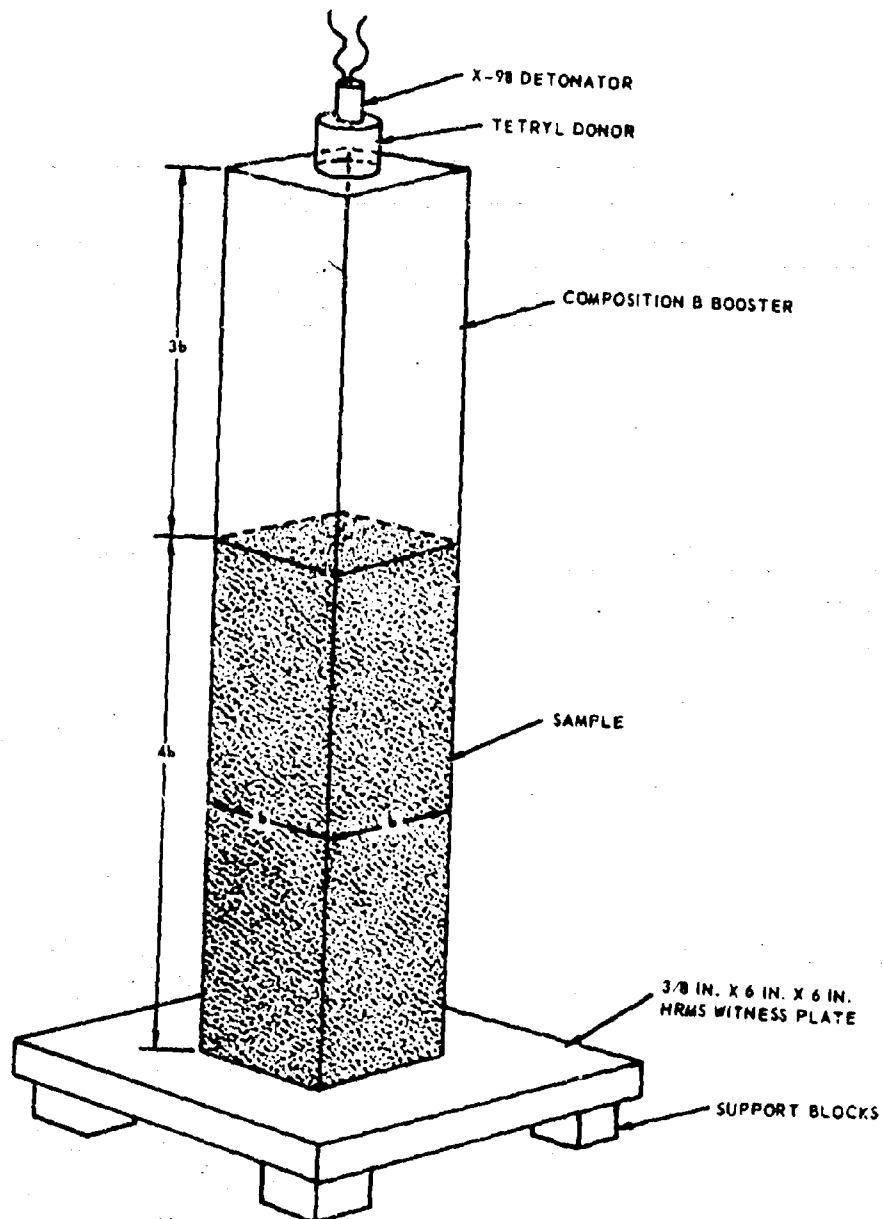


Figure 47. Test Setup - Critical Square Tests.

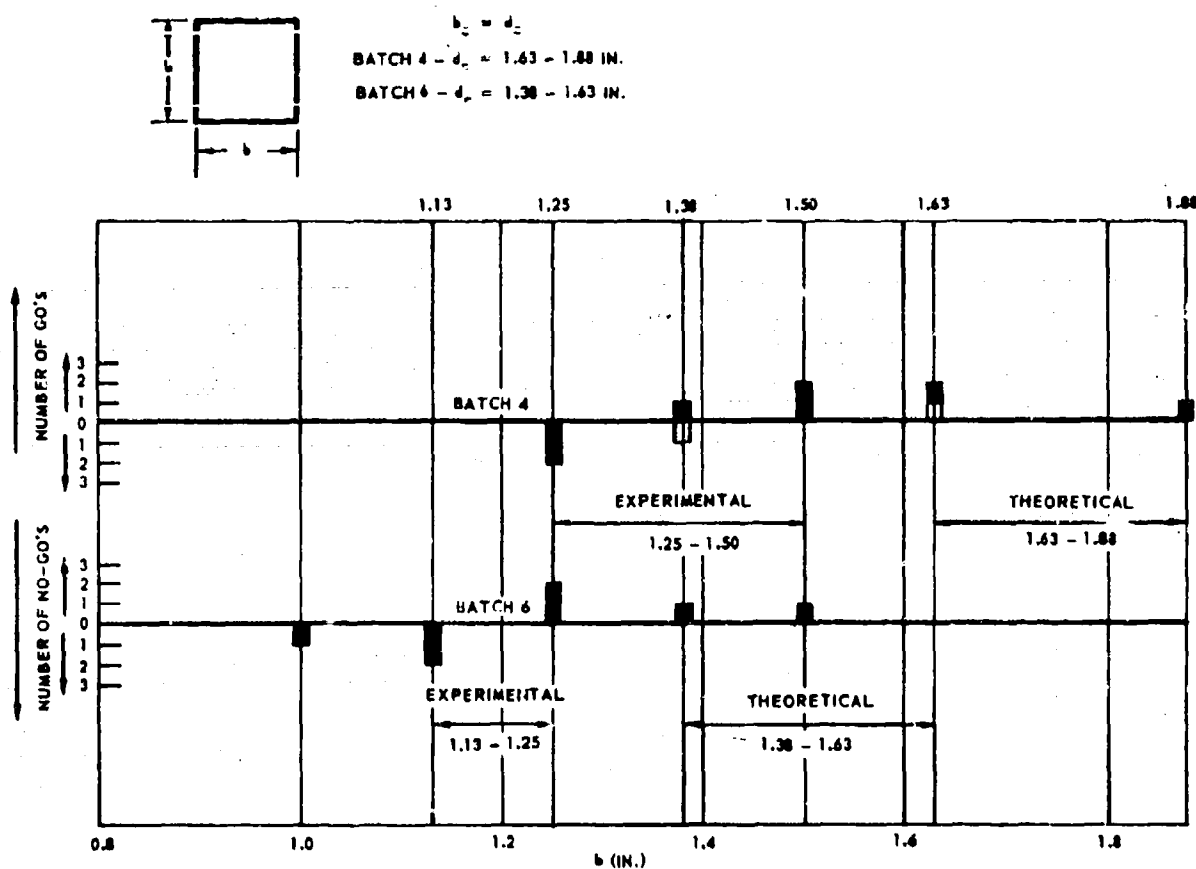


Figure 48. Analysis of Critical Square Tests - RDX-Wax.

Table 9. Critical Rectangle Tests - RDX-Wax.

Test Number	Charge Thickness (in.)*	Batch Number	Charge Density (gm/cc)	Instru-		Result	wp		Result	Comments
				mentation*	mentations*		mentations*	mentations*		
B.2.1.3.1	1.38	6	1.08	wp/sc	3S	Go	No data			
B.2.1.3.2	1.38	6	1.05	wp/sc	2S	Go				Rises!
B.2.1.3.3	1.31	6	1.12	wp/sc	3S	Go				Rises!
B.2.1.3.4	1.31	6	1.10	wp/sc	3S	Go				Rises!
B.2.1.3.5	1.25	6	1.09	wp/sc	3S	Go				Rises!
B.2.1.3.6	1.19	6	1.11	wp/sc	3S	Go				Rises!
B.2.1.3.7	1.13	6	1.08	wp/sc	2S	Go				Rises!
B.2.1.3.8	1.0	6	1.09	wp/sc	1S	Go				Rises!

*Charge width = 2.75 in.

**wp = witness plate

sc = streak camera (Beckman and Whitley Model 194)

***See Figure 43

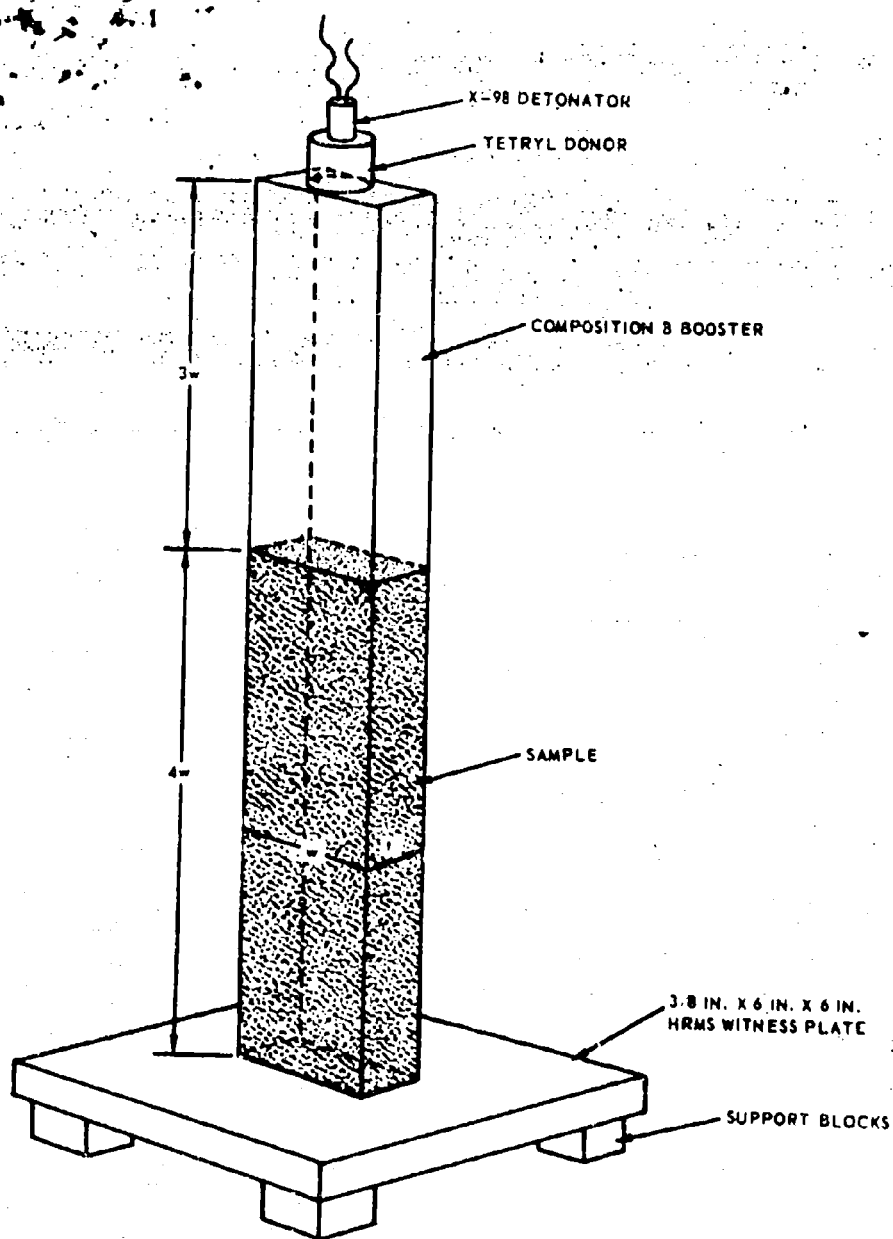


Figure 49. Test Setup - Critical Rectangle Tests.

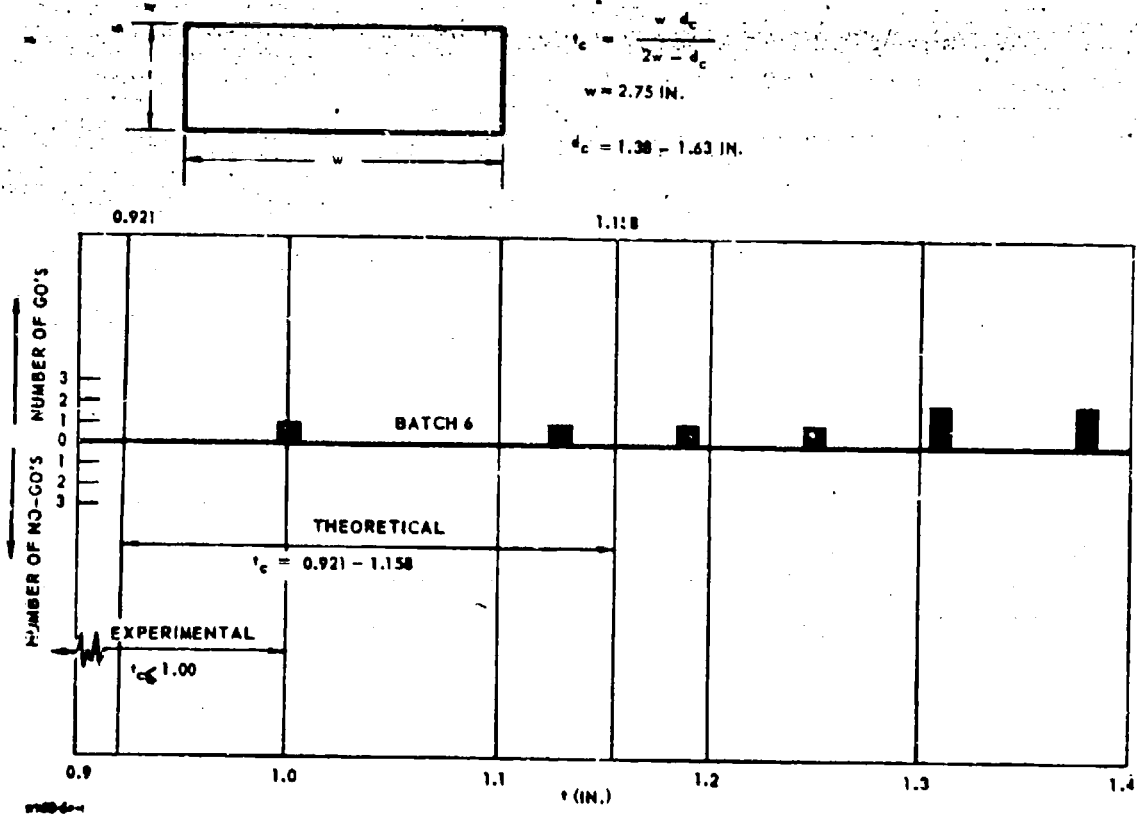


Figure 50. Analysis of Critical Rectangle Tests - RDX-Wax.

(4) Critical Equilateral Triangle Tests (Subtask B.2.1.4)

The results of three critical equilateral triangle tests using samples from Batch 6 RDX-wax explosive are shown in Table 10. The test setup used is shown in Figure 51 and the analysis of the results is shown in Figure 52. Because of limited data, no specific conclusions were drawn but it is probable that the critical equilateral triangular base b_c of Batch 6 RDX-wax explosive is less than or equal to 2.5 in. because the three charges apparently detonated.

b. Perforated Shapes (Subtask B.2.2)

The perforated shape considered was the circular-core cylinder (Subtask B.2.2.1). The objective of this subtask was to determine the critical outside diameter for a fixed inside diameter. The prediction of the current theory for circular core cylinders is shown in Figure 44.

Critical Circular-Core Cylinder Tests (Subtask B.2.2.1)

The results of nine critical circular-core cylinder tests using samples from Batch 6 RDX-wax explosive are shown in Table 11. The test setup is shown in Figure 53.

When the central cavity was left empty, a jet was produced that punched the witness plate. Since such a jet would obscure the witness plate result whether the charge detonated or not, a filler material was sought that would attenuate the jet and still provide little confinement. These included a dry soil, Cab-O-Sil, and dry casting plaster. It was found that only the soil and plaster were effective in eliminating witness plate damage. But, because it was also noted that none of the witness plates were damaged in any of these tests, it might be concluded that all the samples did not sustain detonation. However, from a study of central cavity jetting by Sultanoff (Reference 7) and a careful examination of the streak camera records, it was possible to explain why no dents occurred and to make a determination of which charges did or did not detonate. On this basis the results were established as shown in Table 11. The analysis of these results is shown in Figure 54, where it is indicated that the critical circular-core outside diameter d_{oc} of RDX-wax explosive is between 2.38 and 2.50 in.

Table 10. Critical Equilateral Triangle Tests - RDX-Wax.

Test Number	Charge Base (in.)	Batch Number	Charge Density (gm/cc)	Instrumentation*		wp Result**	sc Result	Comments
				Result	mentation*			
B.2.1.4.1	2.5	6	1.09	Go?	wp/sc	15	Go?	
B.2.1.4.2	2.75	6	1.09	Go	wp/sc	35	Go	
B.2.1.4.3	3.0	6	1.08	Go?	wp/sc	0	Go?	Very short streak; wobbles; contra- dictory wp result

*wp = witness plate

sc = streak camera (Beckman and Whitley Model 194)

**See Figure 43

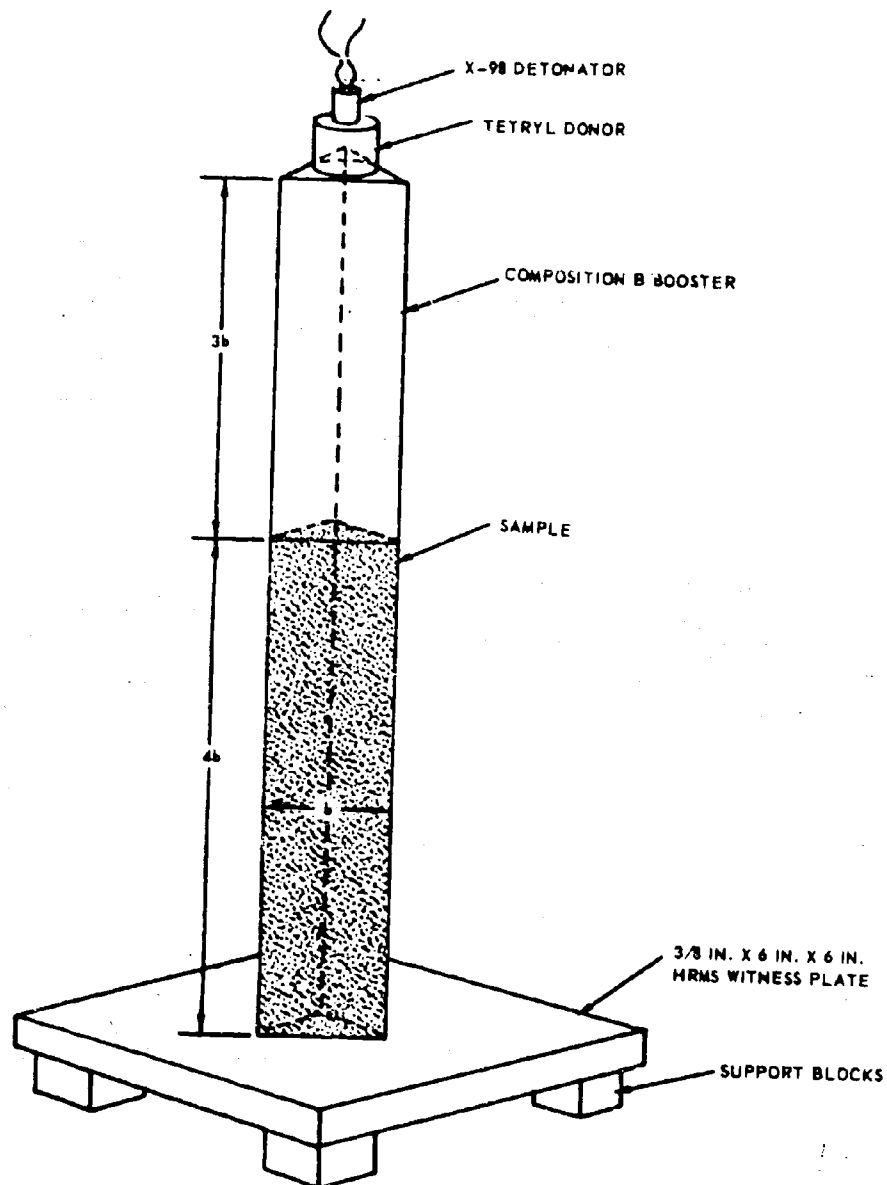


Figure 51. Test Setup - Critical Equilateral Triangle Tests.

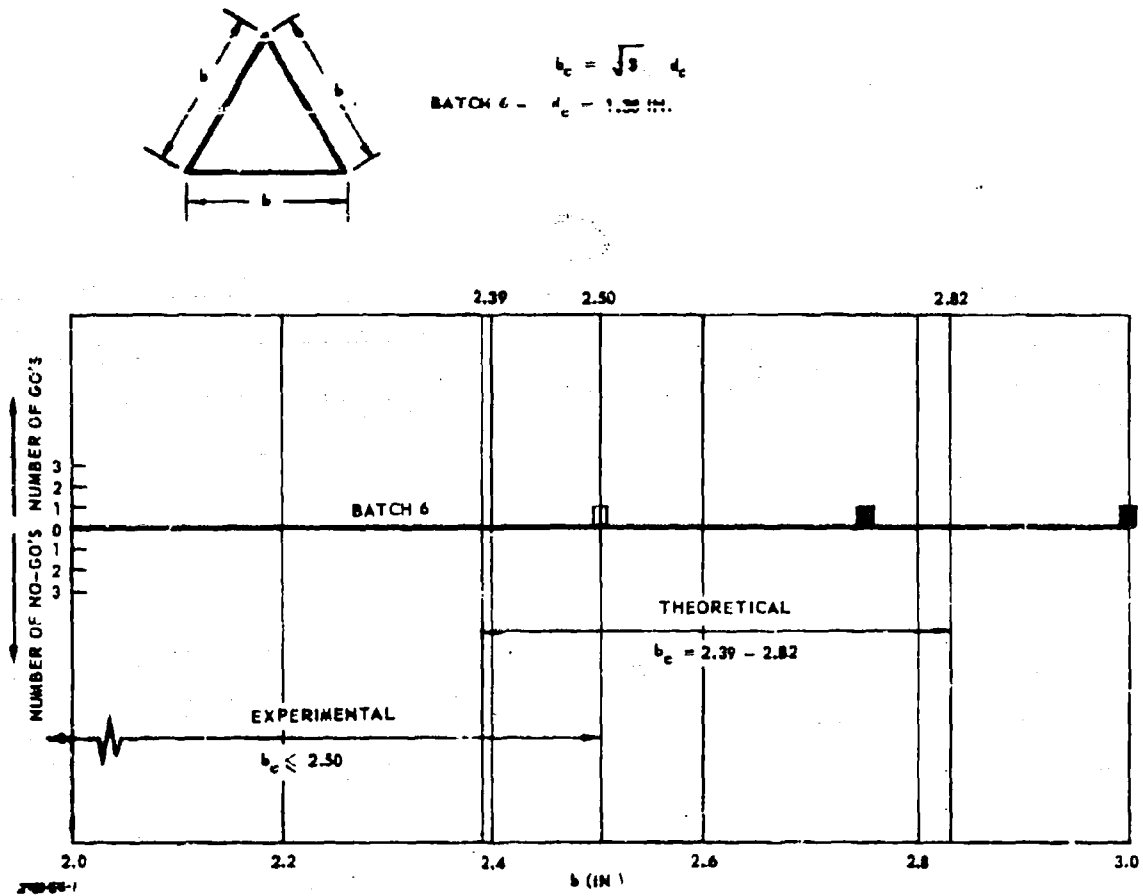


Figure 52. Analysis of Critical Equilateral Triangular Tests - RDX-Wax.

Table 11. Critical Circular Core Cylinder Tests - RDX-Wax.

Test Number	Charge Outside Diameter* (in.)	Batch Number	Charge Density (gm/cc)	Result		Instrumentation	wp		sc	Comments
B.2.2.1.1	2.63	6	1.09	Go?	Go?	wp/sc	-	-	Go?	Steady, then fades
B.2.2.1.2	2.63	6	1.07	Go?	Go?	wp/sc	0	0	Go?	Rises, then fades; no fill
B.2.2.1.3	2.5	6	1.09	Go?	Go?	wp/sc	0	0	Go?	Steady, then fades; dirt fill
B.2.2.1.4	2.38	6	1.05	No-Go?	No-Go?	wp/sc	0	0	No-Go?	Slow fade, then rapid fade; dirt fill
B.2.2.1.5	2.38	6	1.09	No-Go	No-Go	wp/sc	0	0	No-Go	Rapid fade; dirt fill
B.2.2.1.6	2.13	6	1.10	?	?	wp/sc	-	-	No data	Cab-O-Sil fill
B.2.2.1.7	2.13	6	1.09	No-Go	No-Go	wp/sc	0	0	No-Go	Rapid fade; dirt fill
B.2.2.1.8	2.0	6	1.03	?	?	wp/sc	0	0	No data	Dry casting plaster fill
B.2.2.1.9	2.0	6	1.09	No-Go	No-Go	wp/sc	0	0	No-Go	Very rapid fade; dry casting plaster fill

*Charge inside diameter = 0.81 in.

**wp = witness plate

sc = streak camera (Beckman and Whitley Model 194)

***See Figure 43

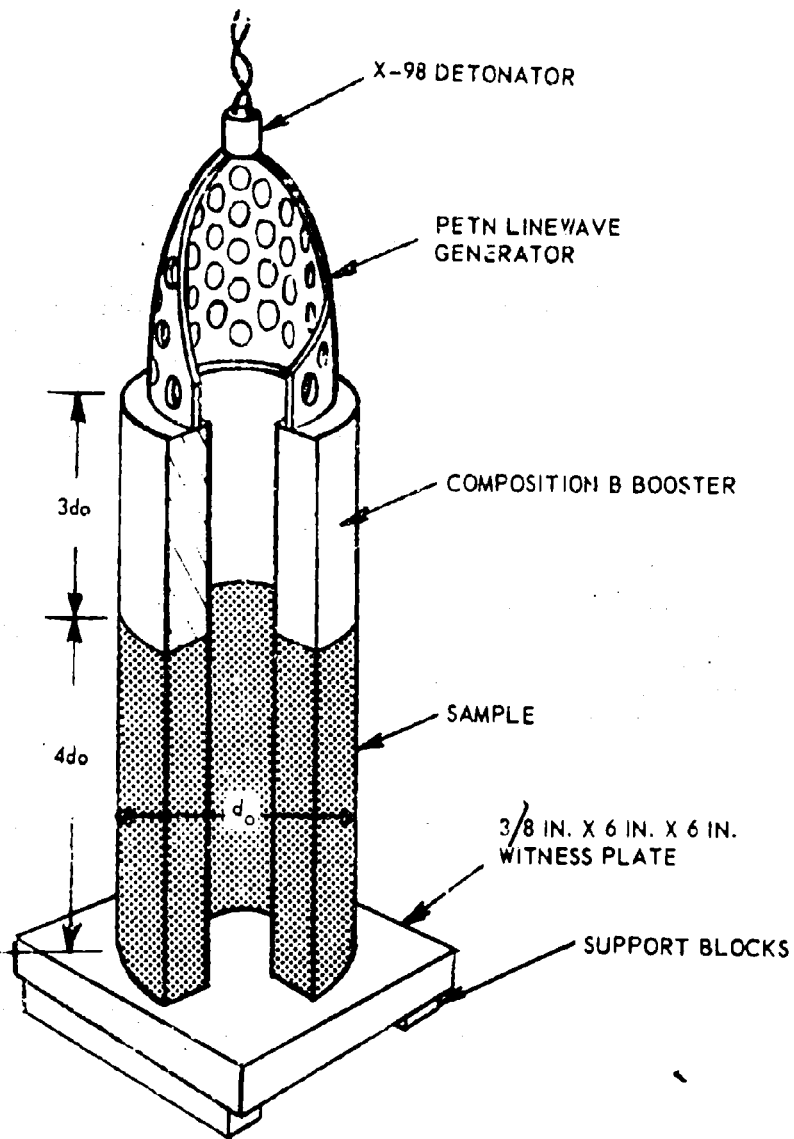


Figure 53. Test Setup - Critical Circular Core Cylinder Tests.



$$d_{ec} = d_1 + d_2$$

$$d_1 = 0.81 \text{ IN.}$$

BATCH 6 $d_2 = 1.38 - 1.63 \text{ IN.}$

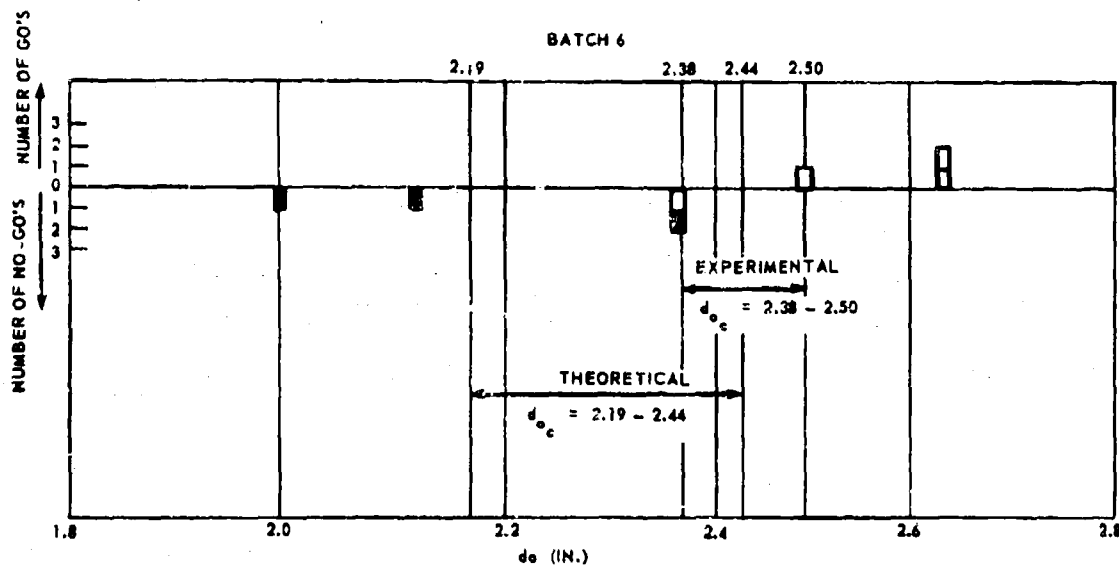


Figure 54. Analysis of Critical Circular Core
Cylinder Tests - RDX-Wax.

5.3.1.1.2 PBAN-RDX Explosive (Subtask B.3)

Because of the uniformity and reproducibility of the PBAN-RDX explosive samples received, excellent results were obtained in this part of the program.

a. Nonperforated Shapes (Subtask B.3.1)

The shapes considered among nonperforated shapes were the circle (Subtask B.3.1.1) and the equilateral triangle (Subtask B.3.1.3). The objective of each subtask was to determine the critical dimensions of the particular shape. The prediction of the current theory of critical geometry for these shapes is shown in Figure 44.

(1) Critical Diameter (Circle) Tests (Subtask B.3.1.1)

The results of 19 critical diameter tests using samples from three batches of PBAN-RDX explosive (containing 9.20% RDX) are shown in Table 12. The test setup in each case is the same as shown in Figure 45 except that a wooden block was not used and the donor charge was a 1/2-in. by 1/2-in. C-4 high explosive pellet. As in the RDX-wax tests, question marks were placed next to those determinations where the evidence was in any doubt. The other determinations are considered highly reliable.

The results shown in Table 13 were analyzed by the scheme in Figure 55. Those results with question marks in Table 12 are indicated by the open boxes in Figure 55. From Figure 55, it was tentatively concluded that the critical diameter d_c of Batch 1 of this material is between 2.66 and 2.80 in. It may be noted that the individual results for Batches 2 and 3 are consistent with each other and with those for Batch 1. For this reason the critical diameter of these batches was assumed to be the same as for Batch 1.

(2) Critical Equilateral Triangle Tests (Subtask B.3.1.3)

The results of six critical equilateral triangle tests using samples from Batch 2 PBAN-RDX explosive are shown in Table 13. The test setup is the same as that shown in Figure 51 except that a C-4 donor was used. The analysis of the results is shown in Figure 56. The result is somewhat below the value predicted by current theory.

Table 12. Critical Diameter Tests - PBAN-RDX.

Num ^{er}	Charge Diameter (in.)	Batch Number	Charge Density (gm/cc)	Instru- mentation*		wp	sc	ro	Comments
				Result	wp/sc	Result**	Result	Result	
B.3.1.1.1	2.88	1	--	Go	wp/sc	3S	No data	-	
B.3.1.1.2	2.44	1	1.720	No-Go	wp	0	-	-	
B.3.1.1.3	2.80	1	1.720	Go	wp/sc	3S	No data	-	
B.3.1.1.4	2.67	1	1.720	Go??	wp/sc	2?	No data	-	
B.3.1.1.5	2.50	1	1.718	No-Go?	wp/sc	1	No data	-	
B.3.1.1.6	2.75	1	1.716	Go	wp/sc/ro	2S	Go	Go	
B.3.1.1.7	2.66	1	1.718	No-Go	wp/sc/ro	1	No-Go	No-Go	Very slow fade
B.3.1.1.8	2.65	1	1.720	No-Go	wp/sc/ro	0	No-Go?	No-Go	Wobbles
B.3.1.1.9	2.74	1	1.723	No-Go	wp/sc/ro	0	No data	No-Go	
B.3.1.1.10	2.75	1	1.723	No-Go?	wp/sc/ro	0	Go?	No data	Rises!
B.3.1.1.11	2.85	1	1.721	Go	wp/sc/ro	2S	Go	No data	Rises!
B.3.1.1.12	2.88	1	1.724	Go	wp/sc/ro	2-3S	No data	Go	
B.3.1.1.13	2.62	1	1.719	No-Go?	wp/sc/ro	0	No-Go?	No-Go?	Wobbles
B.3.1.1.14	2.60	1	1.723	No-Go?	wp/sc/ro	0	No data	No-Go?	Slow fade
B.3.1.1.18	2.74	1	1.724	Go	wp/sc/ro	2S	Go	Go	
B.3.1.1.15	2.75	2	1.728	Go	wp/sc/ro	2S	No data	Go	
B.3.1.1.19	2.62	2	1.732	No-Go	wp/sc/ro	1	No-Go	No-Go	Very slow fade
B.3.1.1.16	2.70	3	1.731	Go?	wp/ro	0	-	Go	Contradictory wp results
B.3.1.1.17	2.82	3	1.728	Go	wp/sc/ro	2S	Go	Go	
B.3.1.1.20	2.62	3	1.726	No-Go	wp/ro	1	-	No-Go	

*wp = witness plate

sc = streak camera (Beckman and Whitley Model 194)

ro = rasterscillograph (Moran and Polaroid)

**See Figure 43

Table 13. Critical Equilateral Triangle Tests - PBAN-RDX.

Test Number	Charge Base (in.)	Batch Number	Charge Density (gm/cc)	Instrumentation*		wp		sc		ro		Comments
				Result	mentation*	Result**	Result	Result	Result	Result	Result	
B. 3.1.3.1	4.93	2	1.726	Go	wp/sc/ro	3S	Go?	Go?	Go	Go		
B. 3.1.3.2	4.13	2	1.727	No-Go	wp/sc/ro	0	No-Go	No-Go	No-Go	No-Go		
B. 3.1.3.3	4.45	2	1.726	Go	wp/sc/ro	3S	No data	No data	Go	Go		Small dip
B. 3.1.3.4	4.25	2	1.729	No-Go	wf/sc/ro	0	No data	No data	No data	No data		
B. 3.1.3.5	4.25	2	1.728	No-Go	wp/sc/ro	0	?	?	No-Go	No-Go		Wobbles
B. 3.1.3.6	4.5	2	1.731	Go	wp/sc/ro	3S?	No data	No data	Go	Go		Wobbles

*wp = witness plate

sc = streak camera (Beckman and Whitley Model 194)

ro = rasterscillograph (Motan and Polaroid)

**See Figure 43

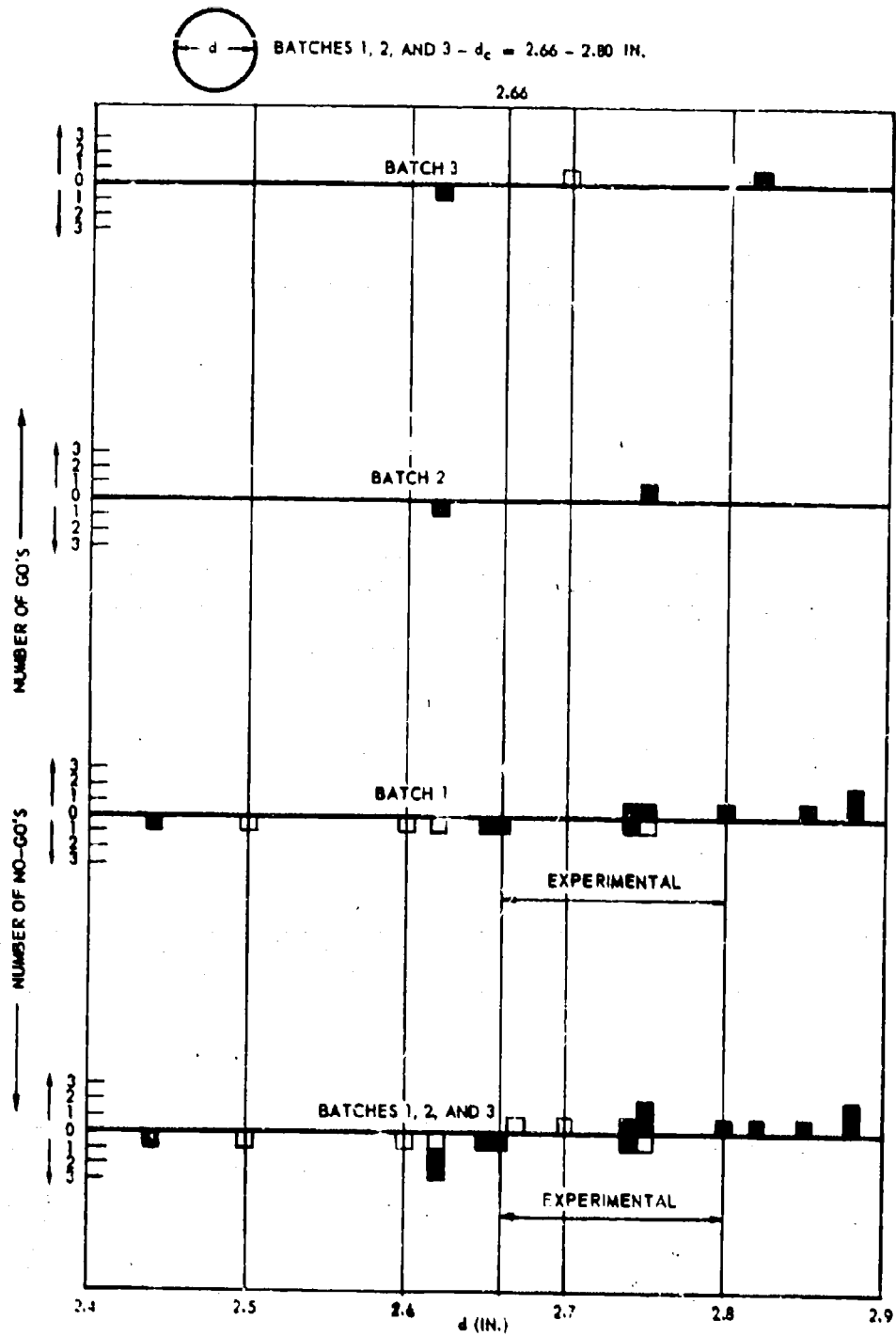


Figure 55. Analysis of Critical Diameter Tests - PBAN-RDX.

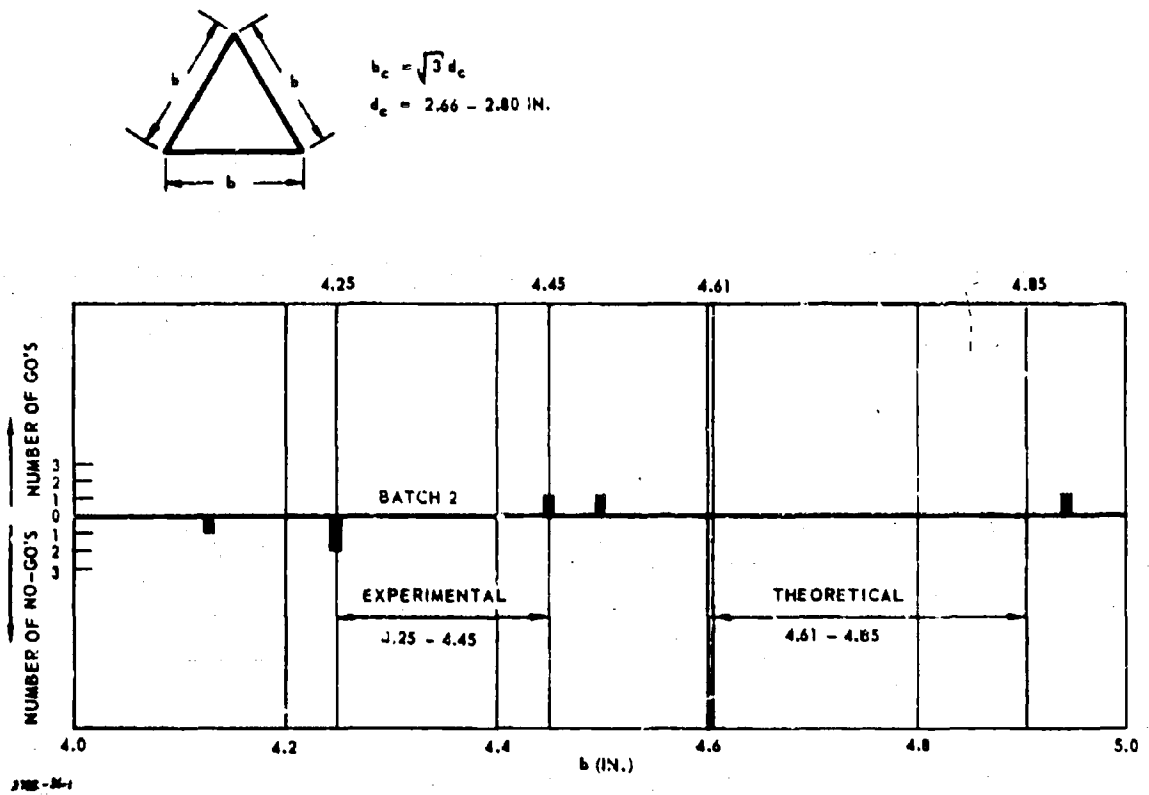


Figure 56. Analysis of Critical Equilateral Triangle Tests - PBAN-RDX.

b. Perforated Shapes (Subtask B. 3. 2)

The perforated shapes considered were the circular-core cylinder (Subtask B. 3. 2. 1) and the cross-core cylinder (Subtask B. 3. 2. 2). The objective of each subtask was to find the critical outside diameter of the shape for a fixed inside dimension. The prediction of the current theory for circular- and cross-core cylinders is shown in Figure 44. As discussed earlier, the jet formed in the central cavity of hollow core charges made it difficult to distinguish between a Go and No-Go in a particular test. However, improvements in the test setup and careful examination of the streak camera and rasteroscillograph records made this determination possible.

(1) Critical Circular-Core Cylinder Tests (Subtask B. 3. 2. 1)

The results of four critical circular-core cylinder tests using samples from Batch 3 PBAN-RDX explosive are shown in Table 14. The test setup for the first two tests (B. 3. 2. 1. 1 and B. 3. 2. 1. 2) is shown in Figure 53 whereas the test setup for the remaining two tests is shown in Figure 57. The analysis of the results in Table 14 is shown in Figure 58. Because of limited data no specific conclusions were made but the indication was that the critical circular-core outside diameter d_{oc} of PBAN-RDX explosive was between 3.54 and 4.02 in.

(2) Critical Cross-Core Cylinder Tests (Subtask B. 3. 2. 2)

The results of five critical cross-core cylinder tests using samples from Batch 3 are shown in Table 15. The test setup is similar to that shown in Figure 57. The analysis of these results is presented in Figure 59, where it is shown that the critical cross-core outside diameter d_{oc} is between 3.87 and 4.00 in.

The interpretation of the results for the cross- and circular-core cylinder tests and the conclusions made, depend heavily on the assumption that the proposed mechanism for central cavity jetting is correct.

5.3.1.1.3 Summary of Sustainment of Detonation Tests

It was originally intended to check the validity of the current theory of critical geometry with RDX-wax and PBAN-RDX explosives but difficulties were encountered with some RDX-wax samples. Therefore, the results obtained with RDX-wax explosive were only estimates of whether the theory was high or low in its predictions, and were not considered on an equal basis with the more uniform PBAN-RDX results.

Table 14. Circular Core Cylinder Tests - PBAN-RDX.

Test Number	Charge Outside Diameter (in.)#	Batch Number	Charge Density (gm/cc)	Results	Instrumentation*	wp		sc		ro		Comments
						Result**		Result		Result		
B. 3. 2. 1. 1	4. 23	3	1. 724	-	wp/sc/ro	-		-		-		Charge fell over
B. 3. 2. 1. 2	4. 33	3	1. 720	Go?	wp/sc/ro	Lost		Go?		Go?		Hollow core booster
B. 3. 2. 1. 3	4. 02	3	1. 728	Go??	wp/sc/ro	-		No-Go?		Go?		With 1 in. Plexiglas attenuation
B. 3. 2. 1. 4	3. 54	3	1. 727	No-Go	vp/sc/ro	-		No-Go?		No-Go?		With 1 in. Plexiglas attenuation

*Charge inside diameter = 1. 50 in.

**wp = witness plate

sc = streak camera (Beckman and Whitley Model 194)

ro = rasterscilloscope (Moran and Polaroid)

***See Figure 43

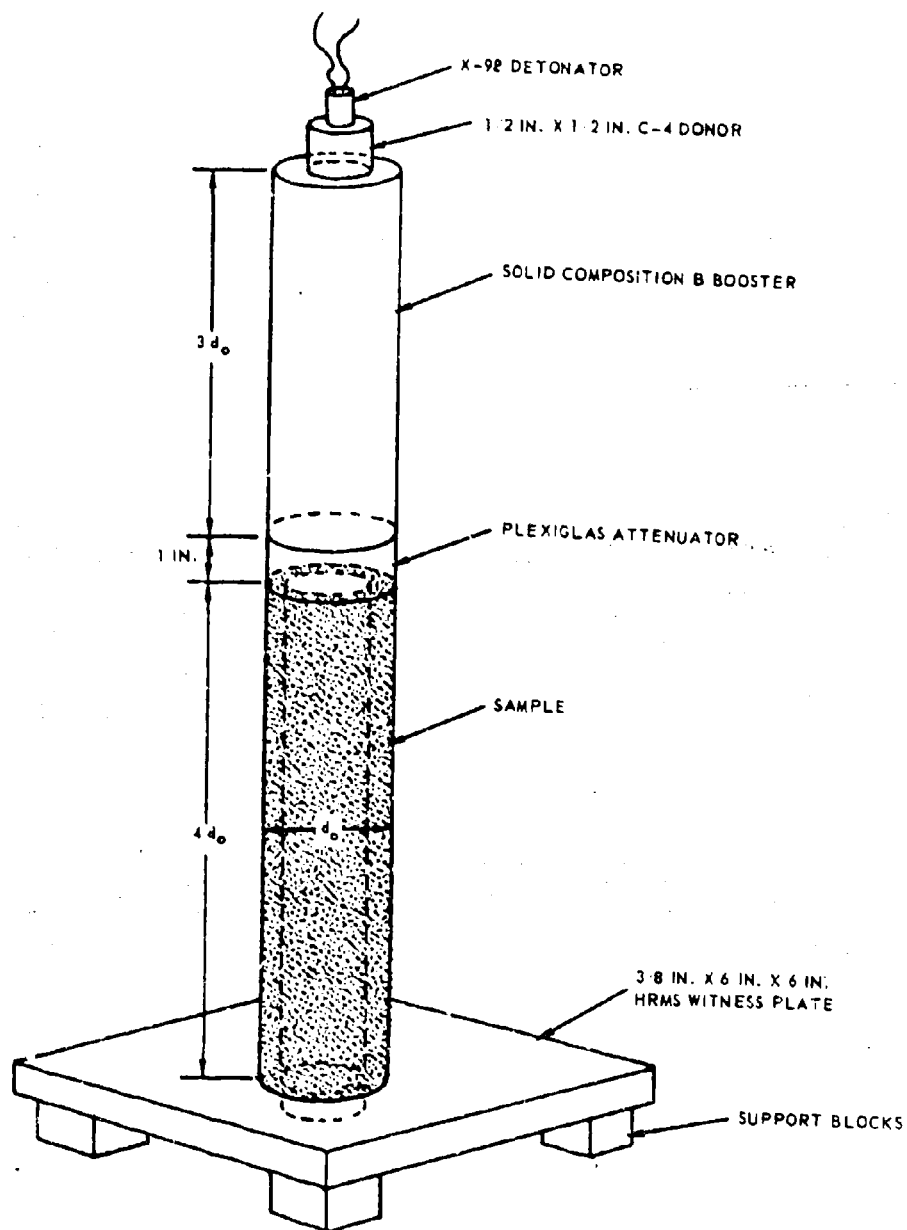


Figure 57. Test Setup - Critical Circular Core Cylinder Tests (PBAN-RDX).

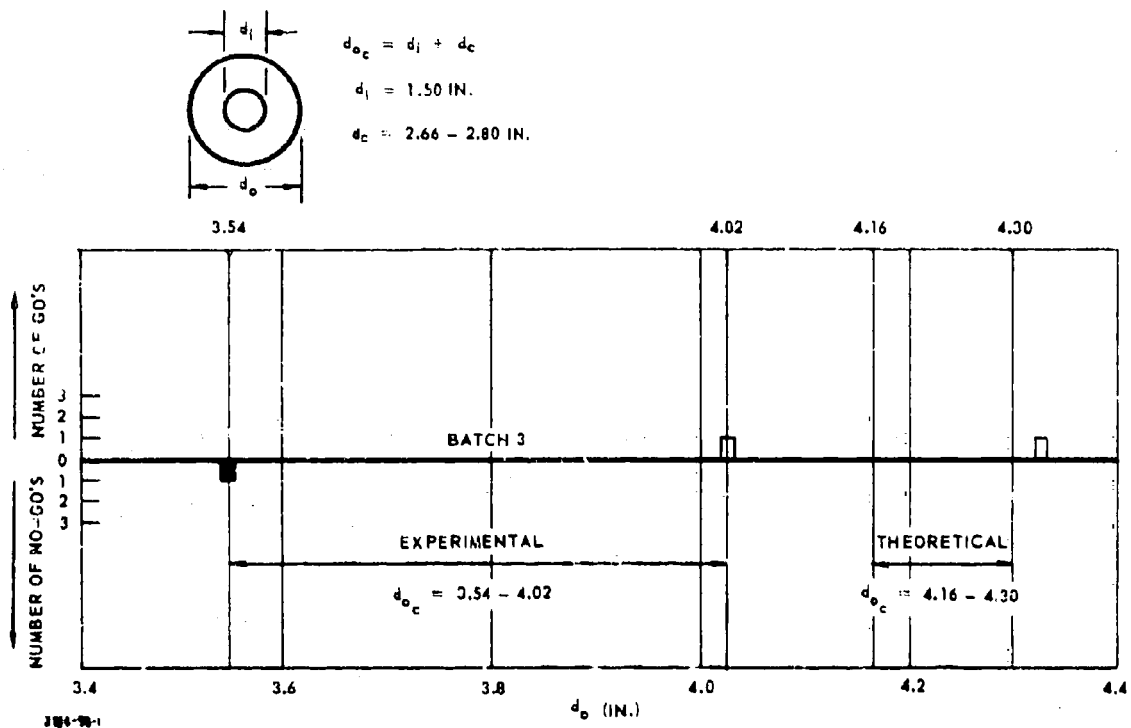


Figure 58. Analysis of Critical Circular-Core
Cylinder Tests - PBAN-RDX.

Table 15. Cross Core Cylinder Tests - PBAN-RDX.

Number	Charge Outside Diameter (in.)*	Batch Number	Charge Density (gm/cc)	Instru- mentation**		wp		sc		ro		Comments
				Result	mentation**	Result	**	Result	**	Result	**	
B. 3. 2. 2. 1	4. 09	3	1. 728	Go	wp/sc/ro	-	-	Go	Go?	1 in. Plexiglas attenuation		
B. 3. 2. 2. 2	3. 52	3	1. 731	No-Go	wp/sc/ro	-	-	No-Go	No-Go	1 in. Plexiglas attenuation		
B. 3. 2. 2. 3	3. 77	3	1. 729	No-Go	wp/sc/ro	-	-	?	No-Go	1 in. Plexiglas attenuation		
B. 3. 2. 2. 4	4. 49	3	1. 722	Go	wp/sc/ro	4	4	Go?	Go	1 in. Plexiglas attenuation; wobbles		
B. 3. 2. 2. 5	3. 87	3	1. 728	No-Go	wp/sc/ro	-	-	No-Go	No-Go	1 in. Plexiglas attenuation		

*Edge of cross = 0. 475 in.

**wp = witness plate

sc = streak camera (Beckman and Whitley Model 194)

ro = rasterscillograph (Moran and Polaroid)

**See Figure 43

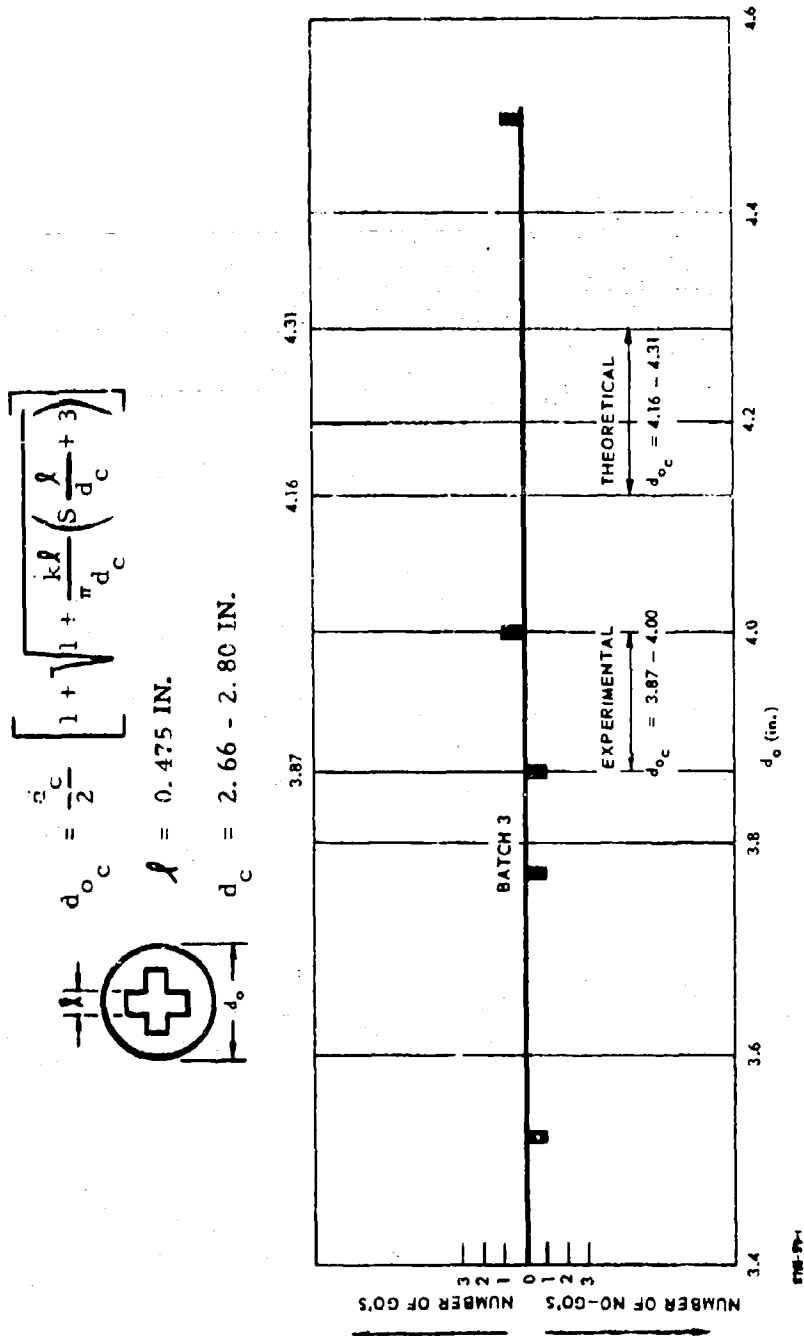



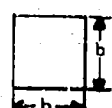


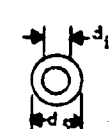
Figure 59. Analysis of Critical Cross-Core
Cylinder Tests - PBAN-RDX.

A summary of RDX-wax explosive results for perforated and nonperforated shapes is shown in Table 16. Although some difficulty was encountered in sample preparation, there were no inconsistencies in the data (see Figures 44, 47, 50, 52, and 54). The theory was high in predicting the critical dimensions in every case for solid shapes. The magnitude of the adjustment in the theory was determined quantitatively only for the critical square tests and was estimated to be about 10 to 50% for the Batch 4 and Batch 6 material. For the perforated shape (the circular core cylinder), the opposite effect is indicated because most of the range of values of d_c predicted by current theory is lower than the experimental data (up to 12% lower). However, since the ranges overlap it is still possible that these results are really consistent with those above; i. e., predictions of theory are high. In an attempt to correlate these results on an equal basis, an equivalent diameter, d_c' , was computed by using the equations in Figure 44 and solving for the diameter associated with the critical dimension found. The ranges of these values are shown in Table 16, wherein the results for the rectangle and triangle are found to be generally consistent with the square for Batch 6 material although quantitative comparison is not possible. The equivalent diameter range for the circular core cylinder is high because the critical dimension was opposite in trend from the nonperforated shapes.

From the results with RDX-wax explosive, there is some indication that the critical geometry theory is too high in its predictions for nonperforated shapes, and that it may be too low in its predictions for perforated shapes. Because of the limitations on sample quality, definitive conclusions should not be drawn from this data.



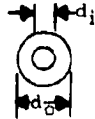

A summary of the PBAN-RDX explosive results for perforated and nonperforated shapes is presented in Table 17. As opposed to the case with RDX-wax explosive, the results in Table 17 show that the critical geometry theory is high in predicting the critical dimensions for both solid and perforated shapes. Also in this case, the magnitude of the adjustment in the theory amounted to a range of only 3 to 20%. In an attempt to correlate these data on an equal basis the equivalent diameter d_c' (using the equations in Figure 44) was computed for each of these results. The range of these values is shown in Table 17. Because the ranges are very similar, these values might be close enough to constitute a basis for correlating data for other shapes. That is, if the equations in Figure 44 are used to compute the critical dimensions of any shape (perforated or nonperforated), use of d_c' (≈ 2.4 in.) instead of d_c (≈ 2.7 in.) should give the true value within about 5%. Furthermore, since the total range for each shape is equal to or greater than the corresponding range for the critical

Table 16. Summary of Critical Geometry Tests - RDX-Wax.

Shape	Batch Number	Symbol	Range of Critical Dimension		Equivalent Diameter d_c' (in.)	% Difference in Theoretical and Experimental*
			Theoretical (in.)	Experimental (in.)		
	3 and 4	d_c	--	1.63 to 1.88	--	--
	5 and 6	d_c	--	1.38 to 1.63	--	--
	4	b_c	1.63 to 1.88	1.25 to 1.50	1.25 to 1.50	-8.7 to -50.4
	6	b_c	1.38 to 1.63	1.13 to 1.25	1.13 to 1.25	-10.4 to -44.2
 $w = 2.75$ in.	6	t_c	0.921 to 1.158	≤ 1.00	≤ 1.47	--
	6	b_c	2.39 to 2.82	≤ 2.50	≤ 1.44	--
 $d_1 = 0.81$	6	d_{cc}	2.19 to 2.44	2.38 to 2.50	1.57 to 1.69	-2.5 to +12.4

$$*\% \text{ difference} = \frac{\text{Experimental} - \text{Theoretical}}{\text{Experimental}} \times 100$$

Table 17. Summary of Critical Geometry Tests - PBAN-RDX.

Shape	Batch Number	Symbol	Range of Critical Dimension		Equivalent Diameter d' (in.)	Difference in Theoretical and Experimental* %
			Theoretical (in.)	Experimental (in.)		
	1, 2, 3	d_c	--	2.66 to 2.80	-	--
	2	b_c	4.61 to 4.	4.25 to 4.45	2.45 to 2.57	-3.6 to -14.1
 $d_i = 1.50$ in.	3	d_{oc}	4.16 to 4.30	3.54 to 4.02	2.04 to 2.52	-3.5 to -21.5
 $l = 0.475$ in.	3	d_{oc}	4.16 to 4.31	3.87 to 4.00	2.38 to 2.51	-4.0 to -11.4

$$*\% \text{ difference} = \frac{\text{Experimental} - \text{Theoretical}}{\text{Experimental}} \times 100$$

diameter, a relatively high degree of confidence may be placed on the supposition that the true critical dimension is in the given range, even though only limited numbers of tests were conducted.

Because of the relatively high quality of the PBAN-RDX samples, and of the definitiveness of the data obtained with these samples, it may be tentatively concluded that for PBAN-RDX the current critical geometry theory gives an excellent first estimate of the critical geometry of any shape and this estimate may be improved by using a simple adjustment factor, the equivalent diameter.

The critical web thickness of a circular core cylinder appears to be considerably less than the critical diameter of the material for RDX-wax and PBAN-RDX explosive. The range of critical web thickness is from 0.79 to 0.85 in. while the critical diameter range is from 1.38 to 1.63 in. for RDX-wax. These ranges are 1.19 to 1.25 in. and 2.66 to 2.80 in. respectively, for PBAN-RDX. These figures show that the critical web thickness is only from 48 to 61% of the critical diameter for the RDX-wax explosive and from 42 to 47% for the PBAN-RDX explosives, thus implying that the critical web thickness of hollow-core propellant grains is probably closer to one-half the critical diameter of the material than to the critical diameter itself.

5.3.1.2 Initiation of Detonation (Subtask B.4)

During this effort, 43 initiation of detonation and 19 associated tests were performed. Again, determination of a steady or transient detonation was made by the streak camera and/or rasterscillograph reaction velocity-distance data as well as by the witness plate test result classification shown in Figure 43.

5.3.1.2.1 Sensitivity Measurements (Subtask B.4.1)

The objective of the tests in Subtask B.4.1 was to determine an initiation criterion for PBAN-RDX propellant containing 9.20 wt % RDX. This was done using standard card-gap sensitivity tests which were calibrated in terms of shock pressure knowing the impedance mismatch at the attenuator-sample interface. This was accomplished by (a) determining the initial

shock pressure in the attenuator (Plexiglas) for the Composition B booster, (b) measuring the shock pressure attenuation in Plexiglas for various diameter columns, (c) determining the Hugoniot of the propellant, and (d) computing the criterion.

a. Initial Shock Pressure

To determine the initial shock pressure (P_0) in the Plexiglas attenuator from a Composition B booster, two tests were conducted with the test setup shown in Figure 60. The resultant streak camera velocity-distance data are shown in Table 18 and plotted in Figure 61. Based on knowledge of the detonation velocity of the booster and the general shape of attenuation curves in Plexiglas, the best eye-fit curve was drawn through the combined data and extrapolated to the booster-Plexiglas interface (at $x = 0$). The value of U_0 (the initial shock velocity in the Plexiglas) was found to be 7.25 mm/ μ sec. From the previously reported Hugoniot of Plexiglas (Reference 8),

$$P_0 = 5.51 U_0^2 - 14.03 U_0, \text{ Kbar}$$

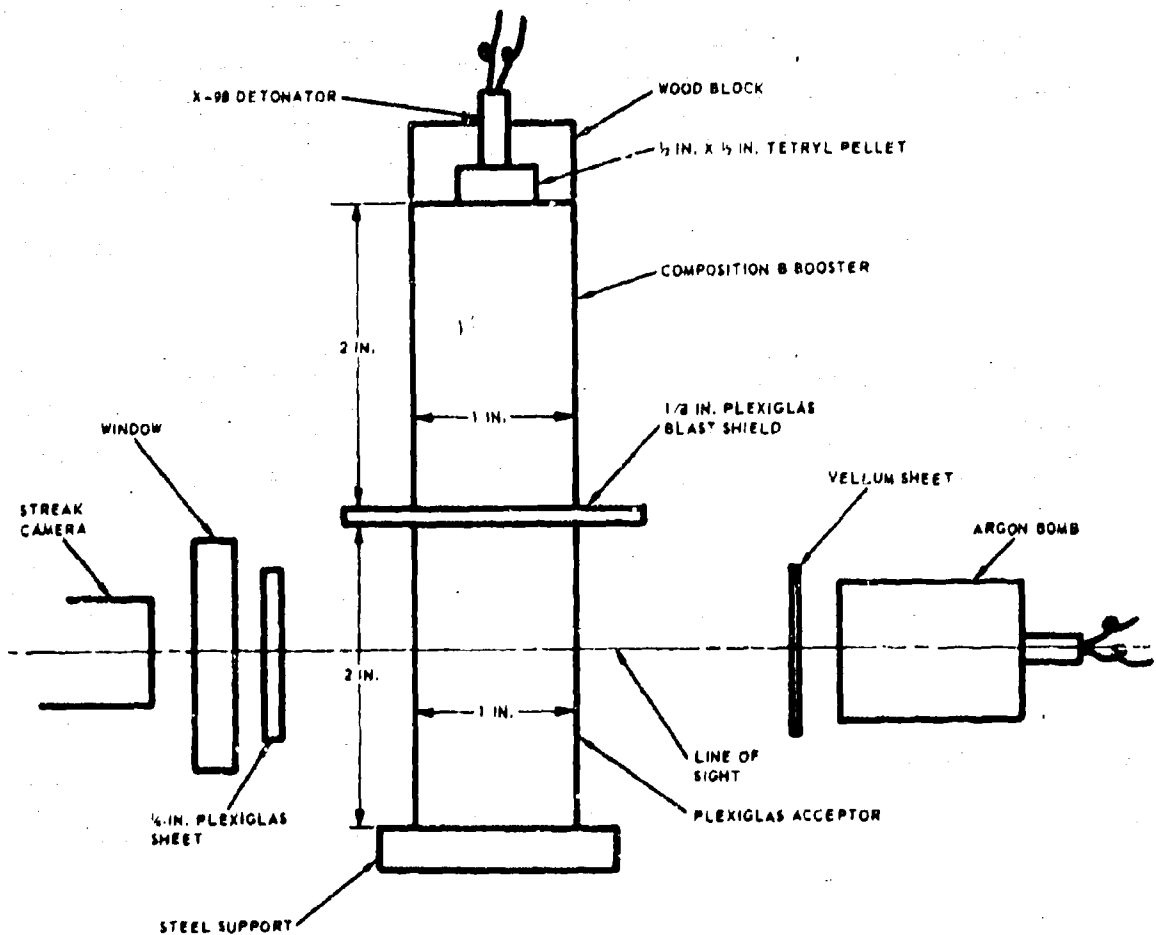
Therefore, from the value of U_0 , P_0 is found to be 188 Kbar. This value is used in subsequent determinations.

b. Shock Attenuation

To determine the shock attenuation in Plexiglas, 10 tests were conducted with the test setup shown in Figure 62. In each case, the Plexiglas acceptor is a right solid cylinder (length equal to diameter) with parallel flat surfaces machined along the entire length to provide an undistorted view through the sample. Table 19 gives the dimensions of each test and includes the densities of the Plexiglas columns and explosive boosters. It may be noted that the Plexiglas density is uniform within about 0.1%, whereas for Composition B this figure is approximately 0.45%.

The resultant streak camera velocity(U)-distance (x) data are shown in Figures 63 through 67 where a best eye-fit curve was drawn through the combined data for each column diameter, since no specific analytical expressions for these curves are known. These curves are redrawn in Figure 68 and show the effect of diameter on shock-velocity attenuation in Plexiglas. Using the previously reported Hugoniot of Plexiglas (Reference 8)

$$P = 5.51 U^2 - 14.03U, \text{ bar}$$



3300-11

Figure 60. Test Setup Used to Determine Initial Pressure in Plexiglas.

Table 18. Shock Velocity in Plexiglas.

Test	Distance From Booster-Plexiglas Interface (in.)	Shock Velocity (mm/ μ sec)
1	0.183	6.61
	0.240	6.15
	0.339	5.64
	0.436	5.40
	0.527	5.21
	0.618	4.95
	0.700	4.61
2	0.778	4.37
	0.229	5.99
	0.334	5.39
	0.500	5.22
	0.697	5.00
	0.849	4.21
	0.991	3.84

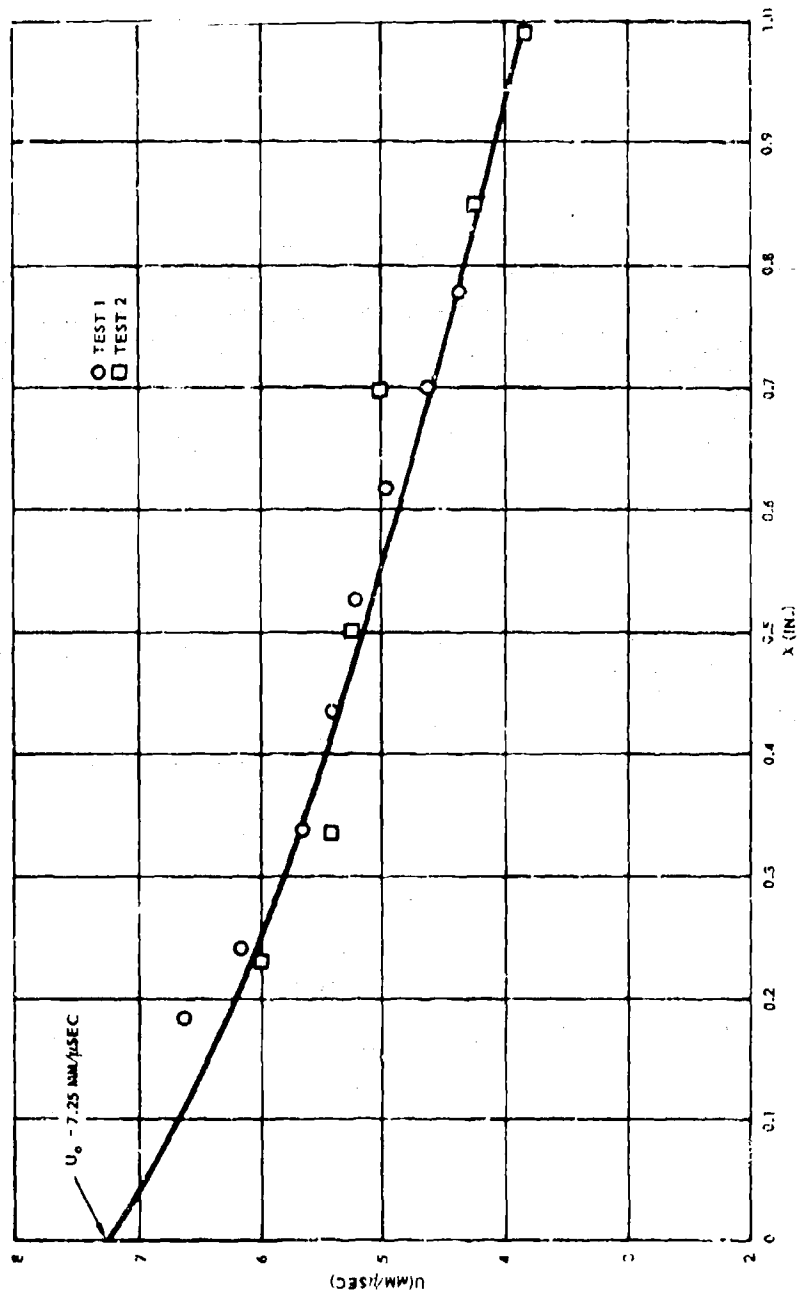


Figure 61. Determination of Initial Shock Velocity in Plexiglas.

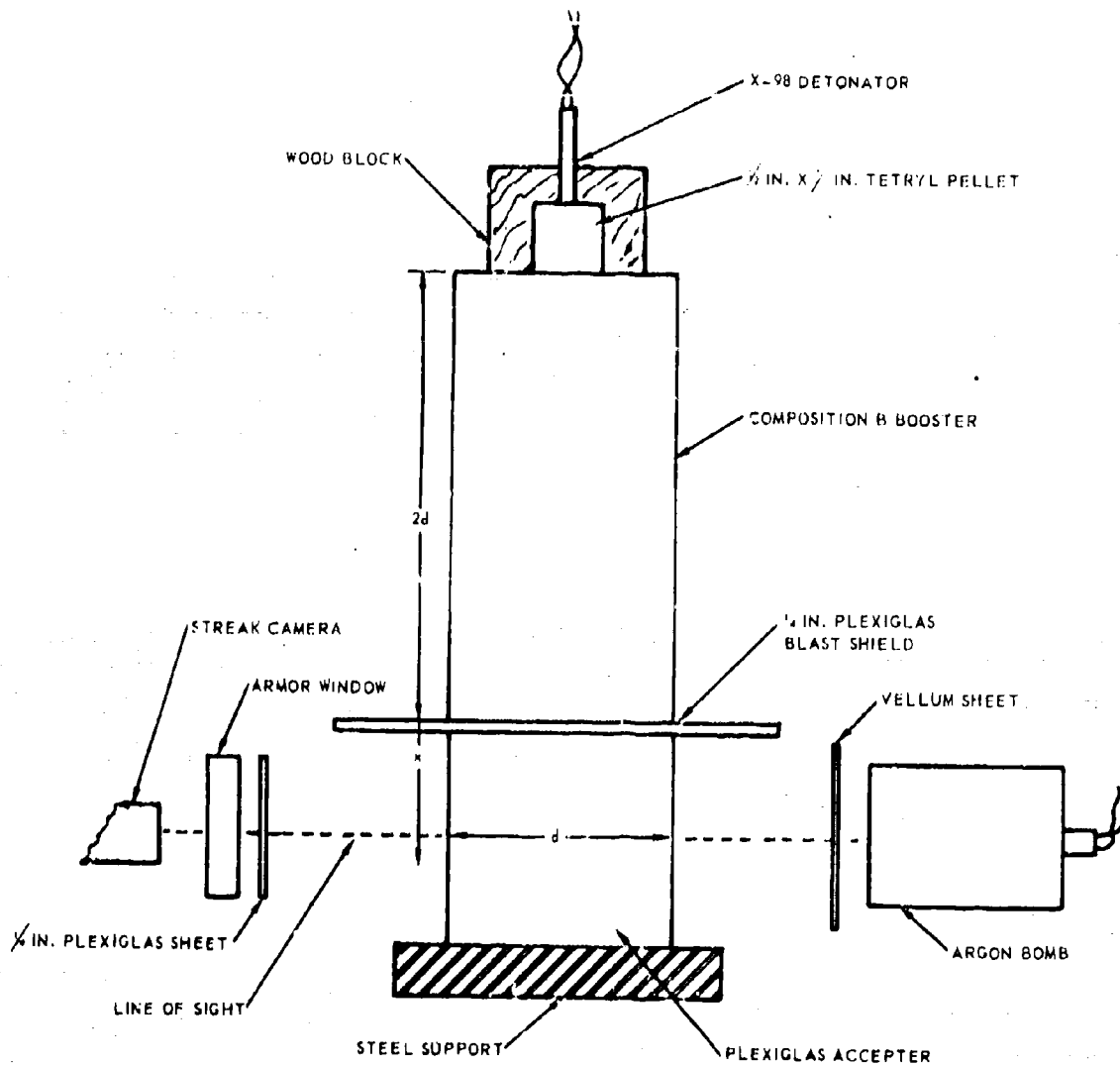


Figure 62. Test Setup Used to Determine Shock Attenuation in Plexiglas.

Table 19. Densities of Plexiglas Columns and Composition B Boosters Prepared for Attenuation Tests.

Test No.	Sample Dimension Length x Diameter (in.)	Density (gm/cc)	
		Plexiglas	Composition B
1	3.00 x 3.00	1.189	1.695
2	3.01 x 3.00	1.189	1.693
3	3.58 x 3.38	1.189	1.696
4	3.58 x 3.50	1.190	1.692
5	4.04 x 3.96	1.190	1.670
6	4.04 x 3.95	1.189	1.693
7	5.02 x 5.00	1.188	1.687
8	5.02 x 4.99	1.188	1.682
9	6.03 x 6.01	1.187	1.692
10	6.03 x 6.00	1.187	1.691

Average density of Plexiglas 1.1886 gm/cc

Standard deviation ± 0.0010 gm/cc

Average density of Composition B 1.6891 gm/cc

Standard deviation ± 0.0074 gm/cc

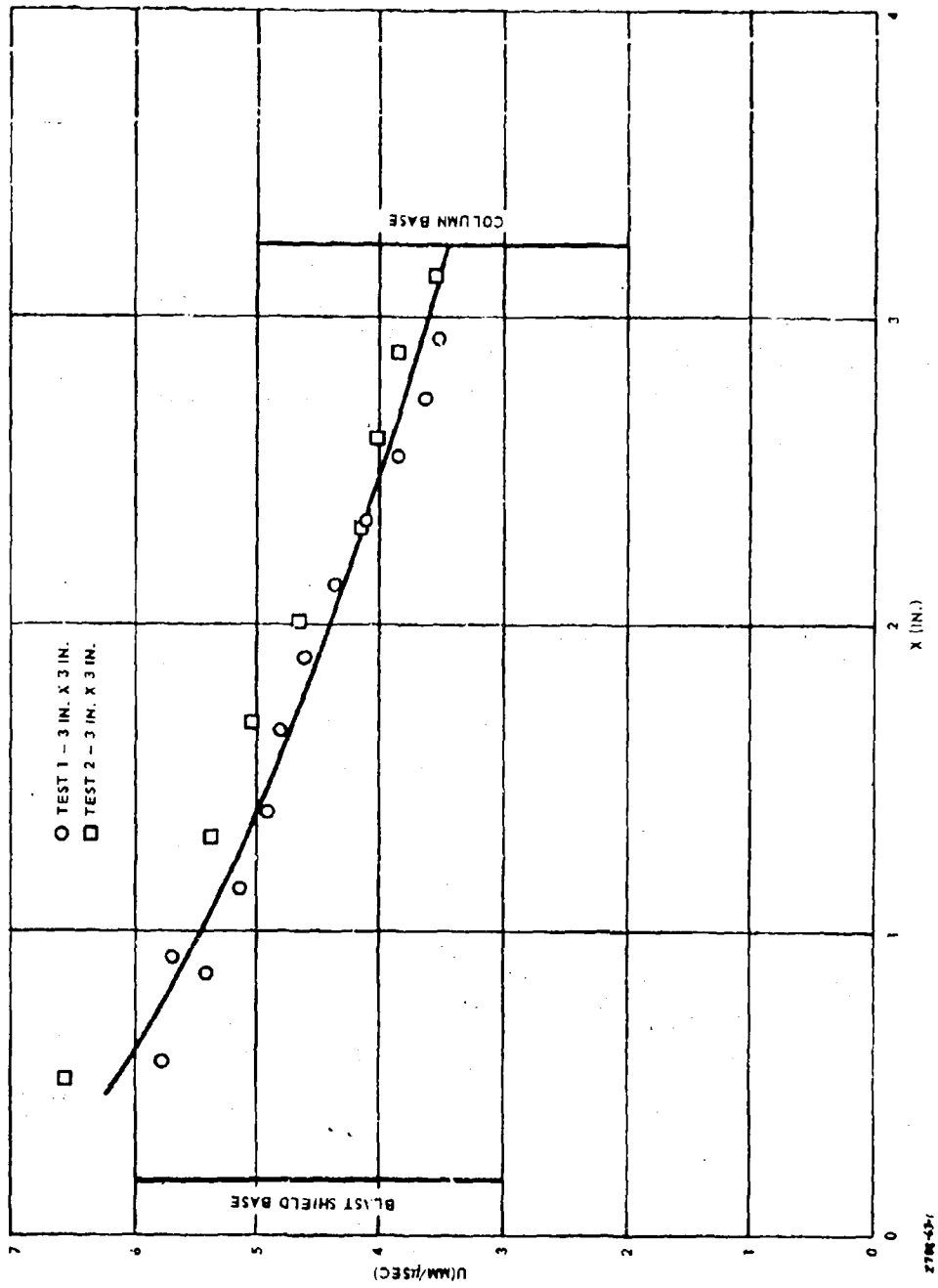


Figure 63. Shock Attenuation in Plexiglas, 3-in.-Diameter Column.

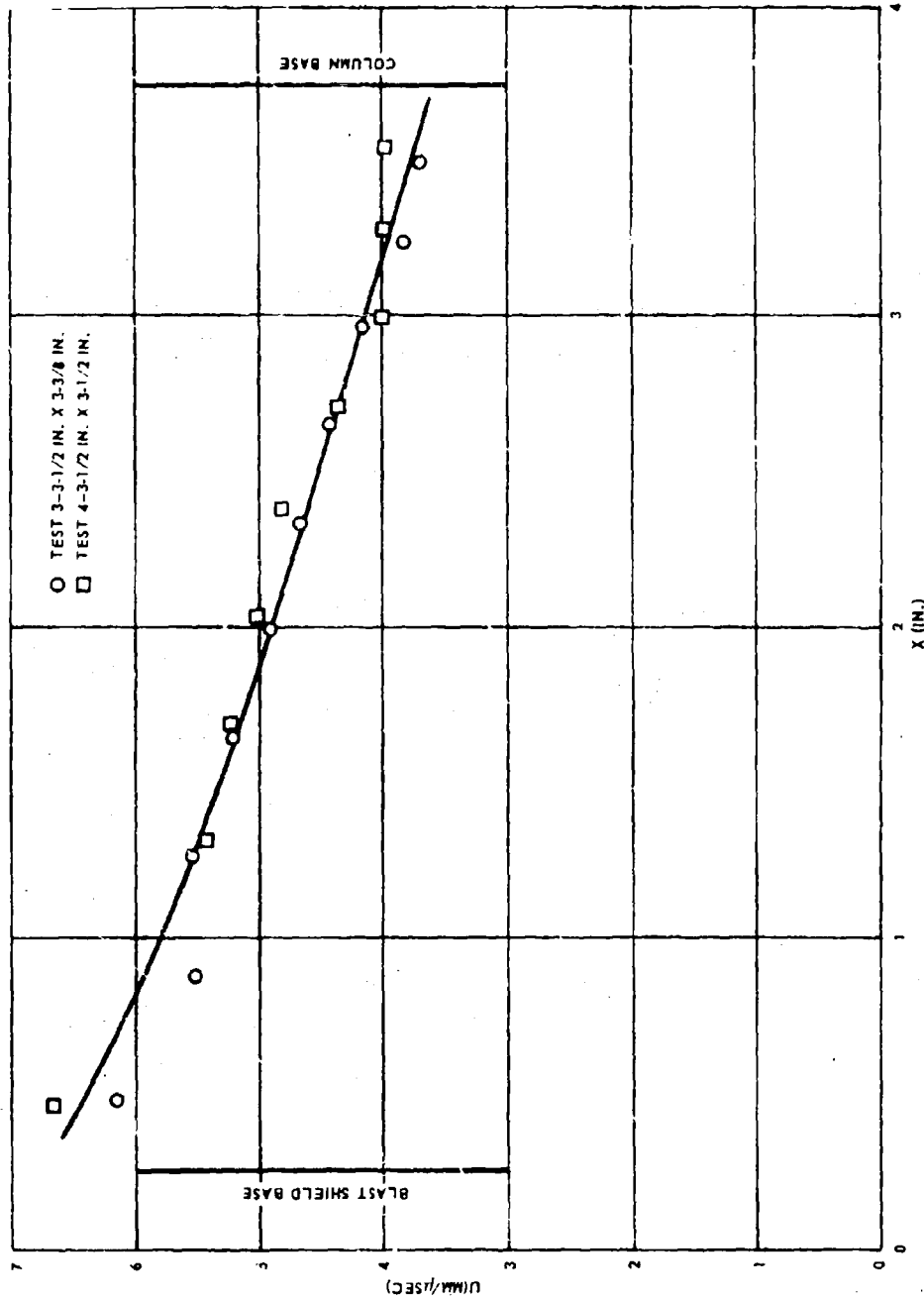


Figure 64. Shock Attenuation in Plexiglas, 3-1/2 in. Diameter Column.

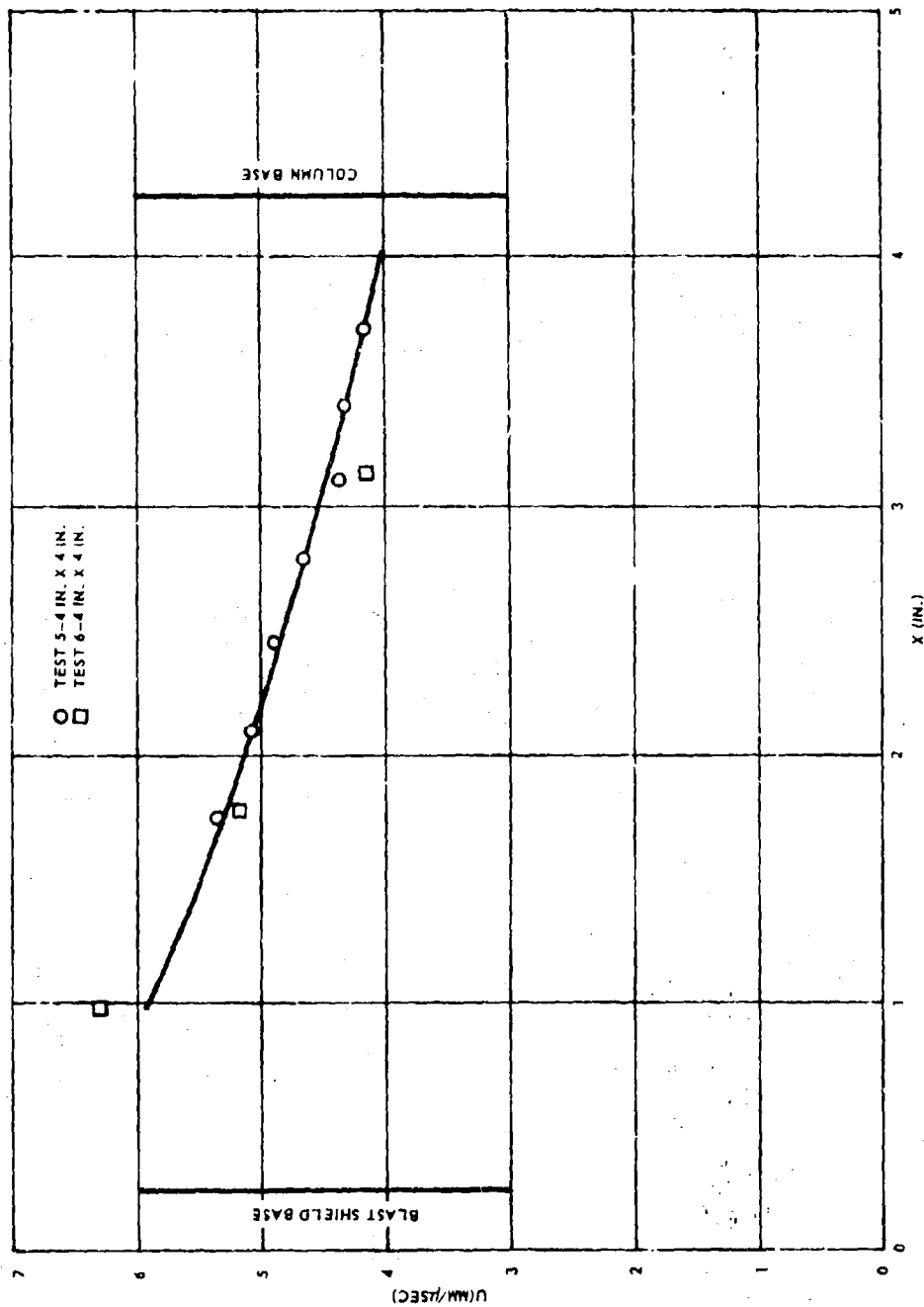


Figure 65. Shock Attenuation in Plexiglas, 4-in. -Diameter Column.

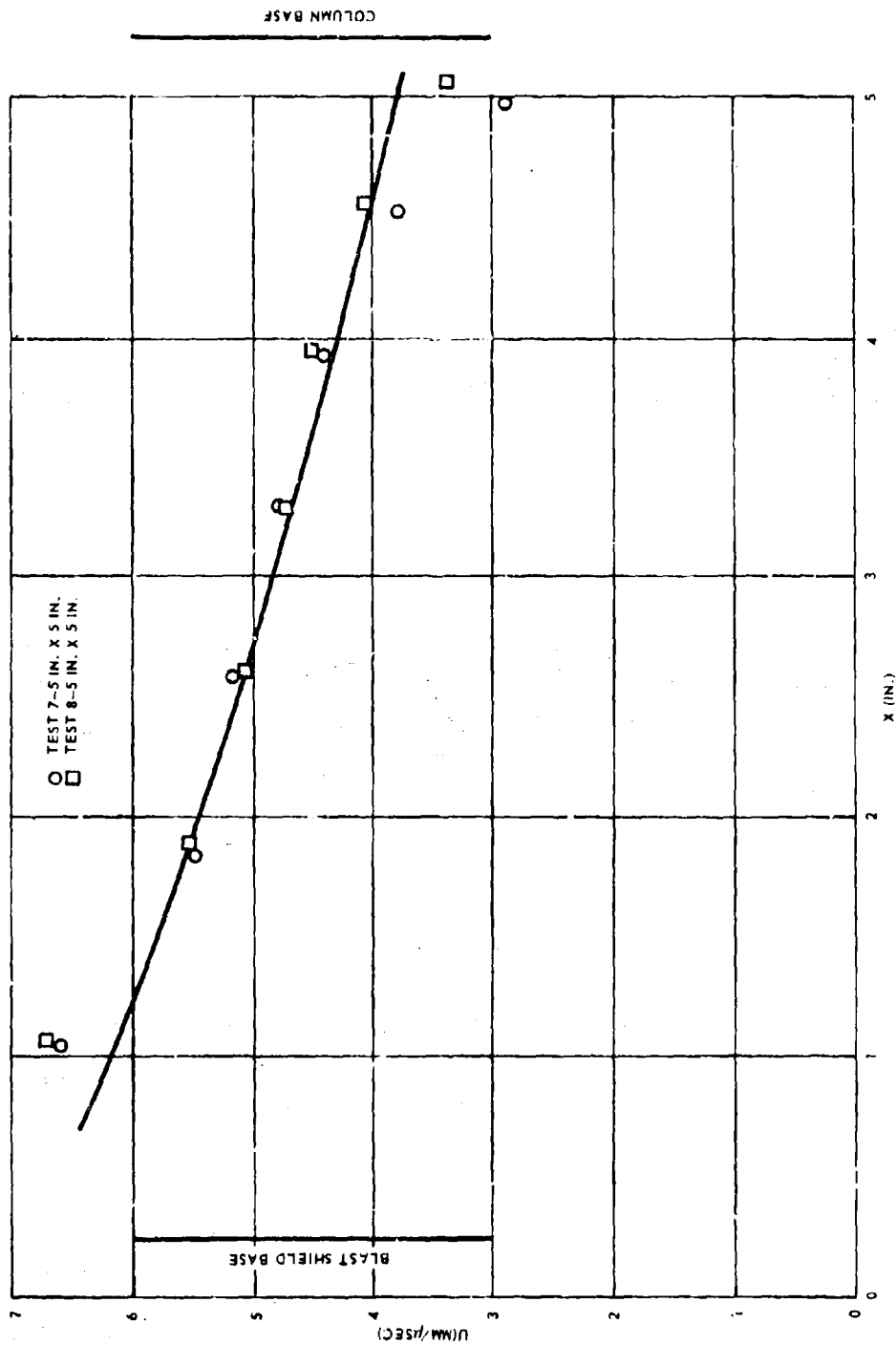


Figure 66. Shock Attenuation in Plexiglas, 5-in. Diameter Column.

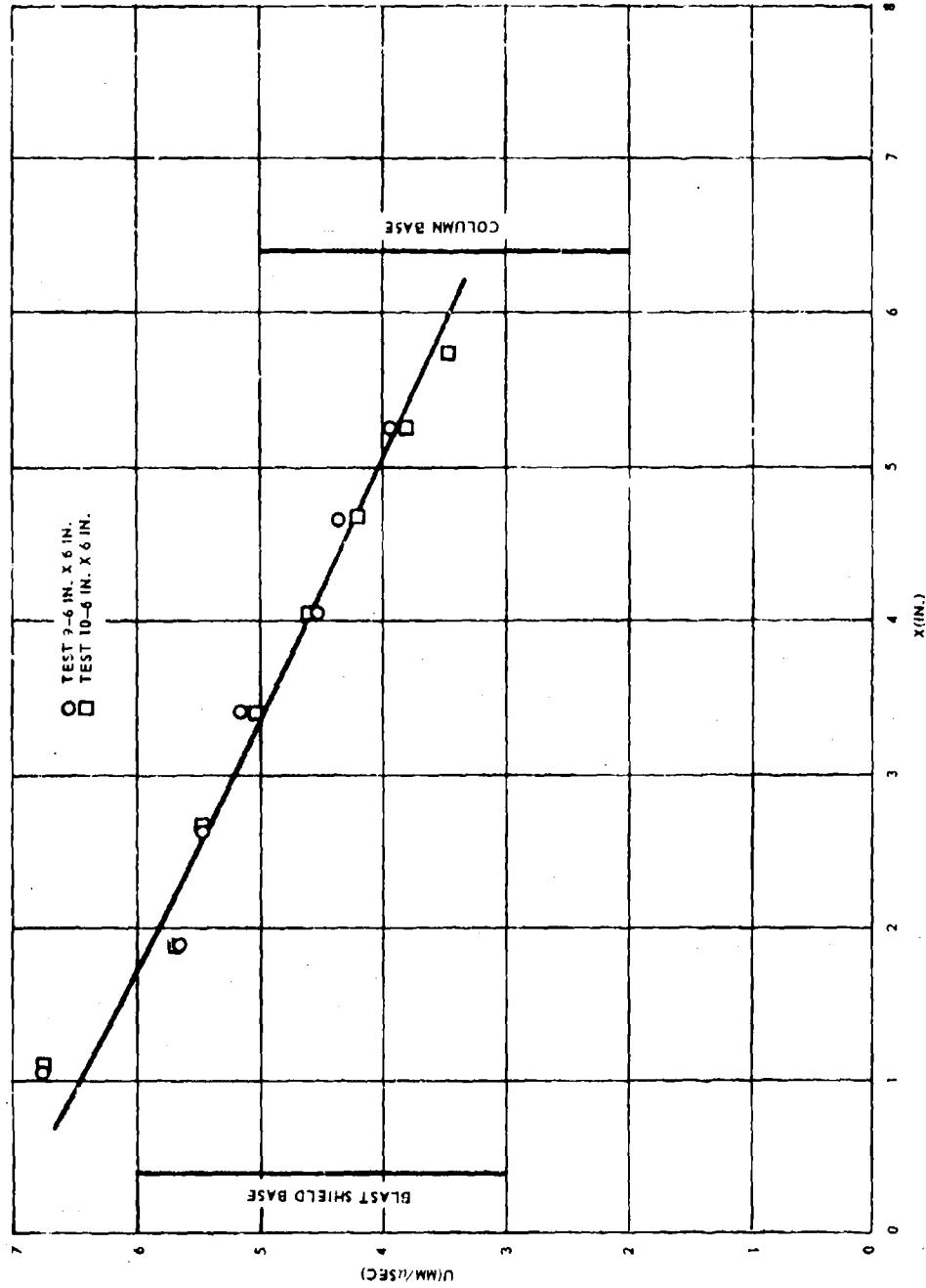


Figure 67. Shock Attenuation in Plexiglas, 6-in. Diameter Column.

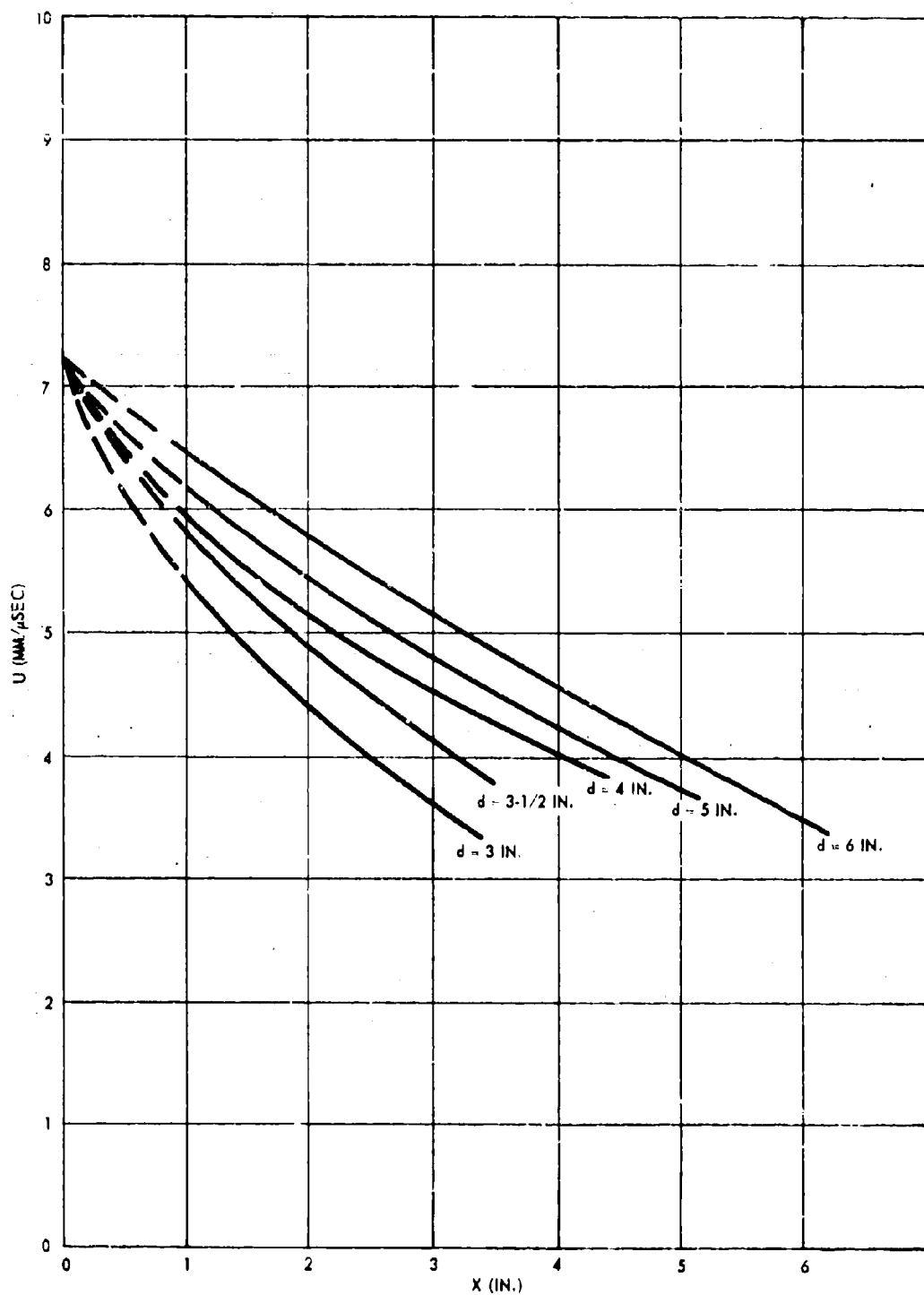


Figure 68. Shock Attenuation in Plexiglas, U vs X , Column Diameters of 3, 3-1/2, 4, 5, and 6 in.

the curves in Figure 68 were converted to shock pressure attenuation curves and are plotted in Figure 69. By using the value of P_0 these data were normalized by plotting P/P_0 vs x/d , where d is the column diameter. The result, shown in Figure 70, may be considered a universal attenuation curve for Plexiglas cylinders 3, 3.5, 4, 5, and 6 in. in diameter.

c. Hugoniot Measurements

To determine the Hugoniot of PBAN-RDX propellant, seven tests were conducted with the test setup shown in Figure 71. In two of these tests, multiple alternate layers of Plexiglas and propellant were used. This setup represents a variation of a well-known technique for measuring the Hugoniot of opaque materials and depends on measuring the shock velocity in the Plexiglas immediately before the shock wave enters the opaque propellant and the shock velocity in the propellant. Additional data might be obtained by measuring the shock velocity entering the Plexiglas from the propellant.

The results of the seven tests are shown in Table 20 and in Figures 72 through 75. Also shown are the still and streak camera records for the four data producing tests. The $P-\mu$ (Hugoniot) data in Table 20 were determined as follows. From the distance data (Figures 72 through 75) the shock velocity attenuation in Plexiglas above each propellant sample was determined by the aforementioned numerical differentiation technique. The velocity at the Plexiglas-sample interface U_p , was then found by extrapolation of this result to that interface. The average shock velocity in the PBAN-RDX sample \bar{U}_R was determined from the measured propellant thickness and the time taken to traverse that thickness (Figures 72 through 75). From U_p , P_p (shock pressure in the Plexiglas at the Plexiglas-sample interface) may be computed from the known Hugoniot of Plexiglas (Reference 2). Knowing this, \bar{U}_R , and the density of the PBAN-RDX sample ρ_{OR} , $P-\mu$ (particle velocity) data for the sample may be generated in the following manner. The Hugoniot of Plexiglas is plotted on the $P-\mu$ plane and the curve is reflected about a vertical line passing through P_p . The intersection of the "reflected" Hugoniot with a line passing through the origin, having a slope of $10 \rho_{OR} \bar{U}_R$, can be shown to be (Reference 9) a point on the Hugoniot of the sample. This procedure is illustrated in Figures 76 through 79 for the data in Table 20 where the resultant $P-\mu$ data are listed. These results are plotted in Figure 80 where the best-fit quadratic expression (as determined by the method of least-squares) passing through the data is shown. This expression

$$P = 33.27 \mu + 44.45 \mu^2, \text{ Kbar } (\mu \text{ in mm}/\mu\text{sec})$$

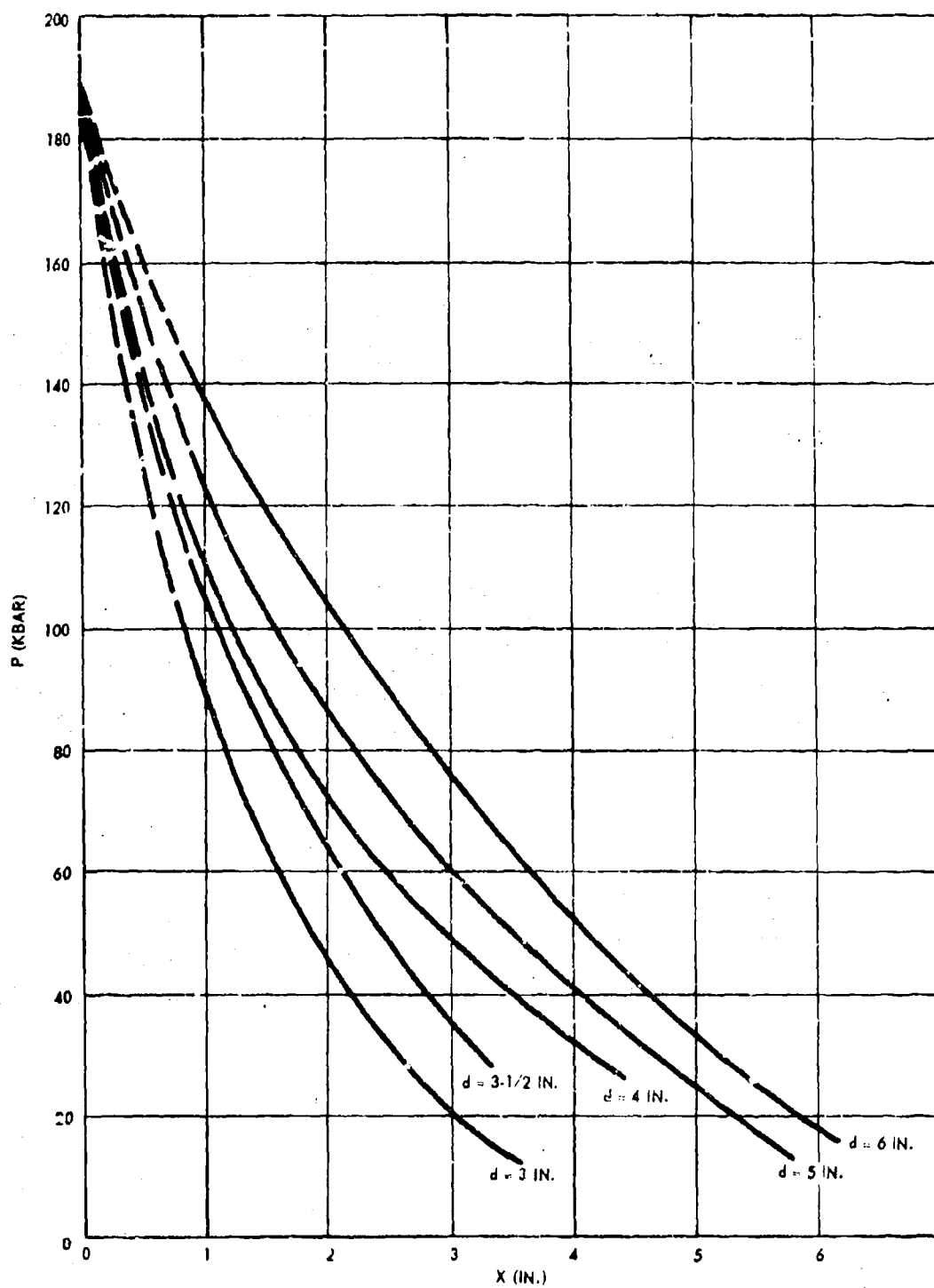


Figure 69. Shock Attenuation in Plexiglas, P vs X , Column Diameters of 3, 3-1/2, 4, 5, and 6 in.

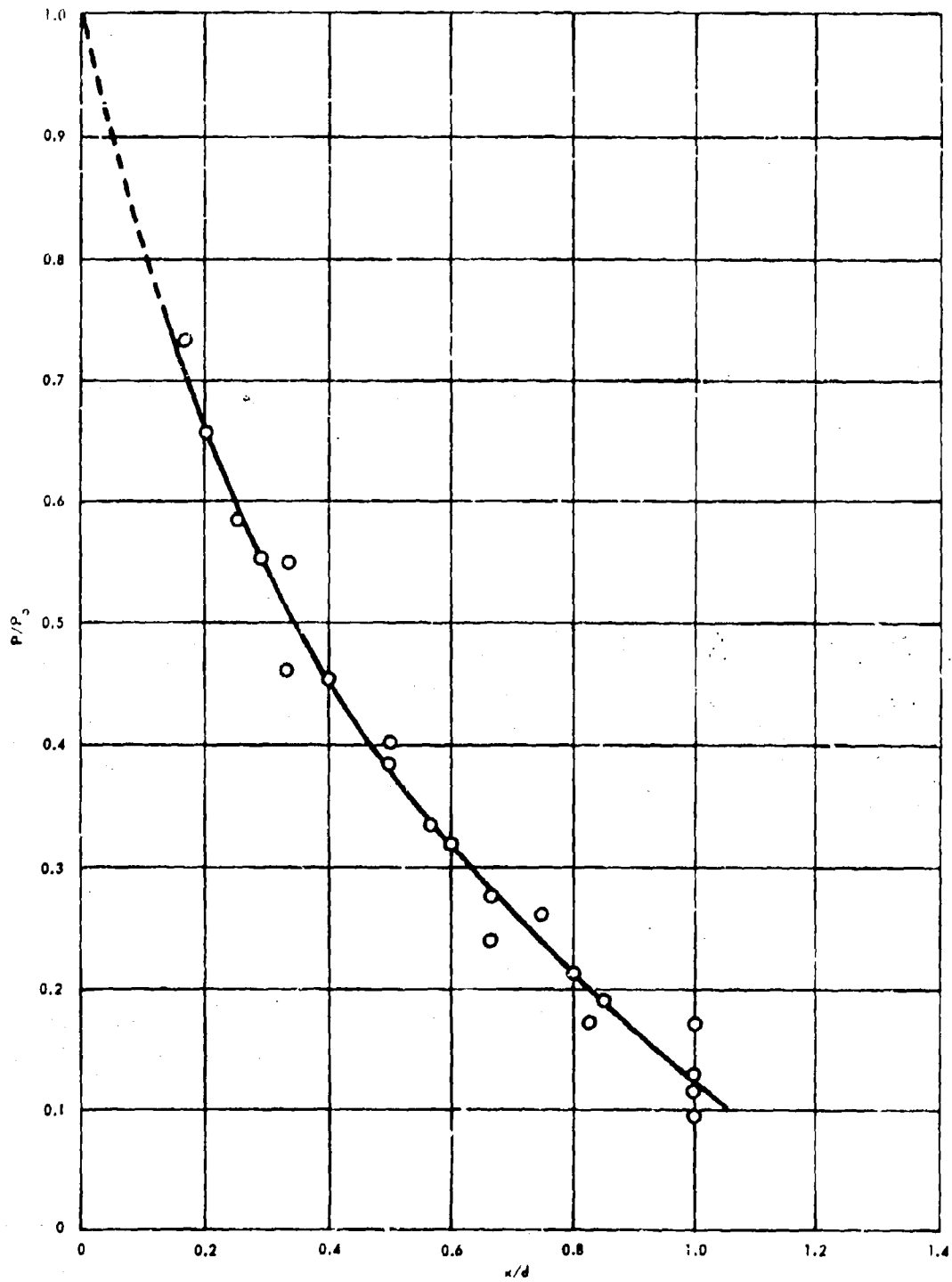


Figure 70. Shock Attenuation in Plexiglas, P/P_0 vs x/d .

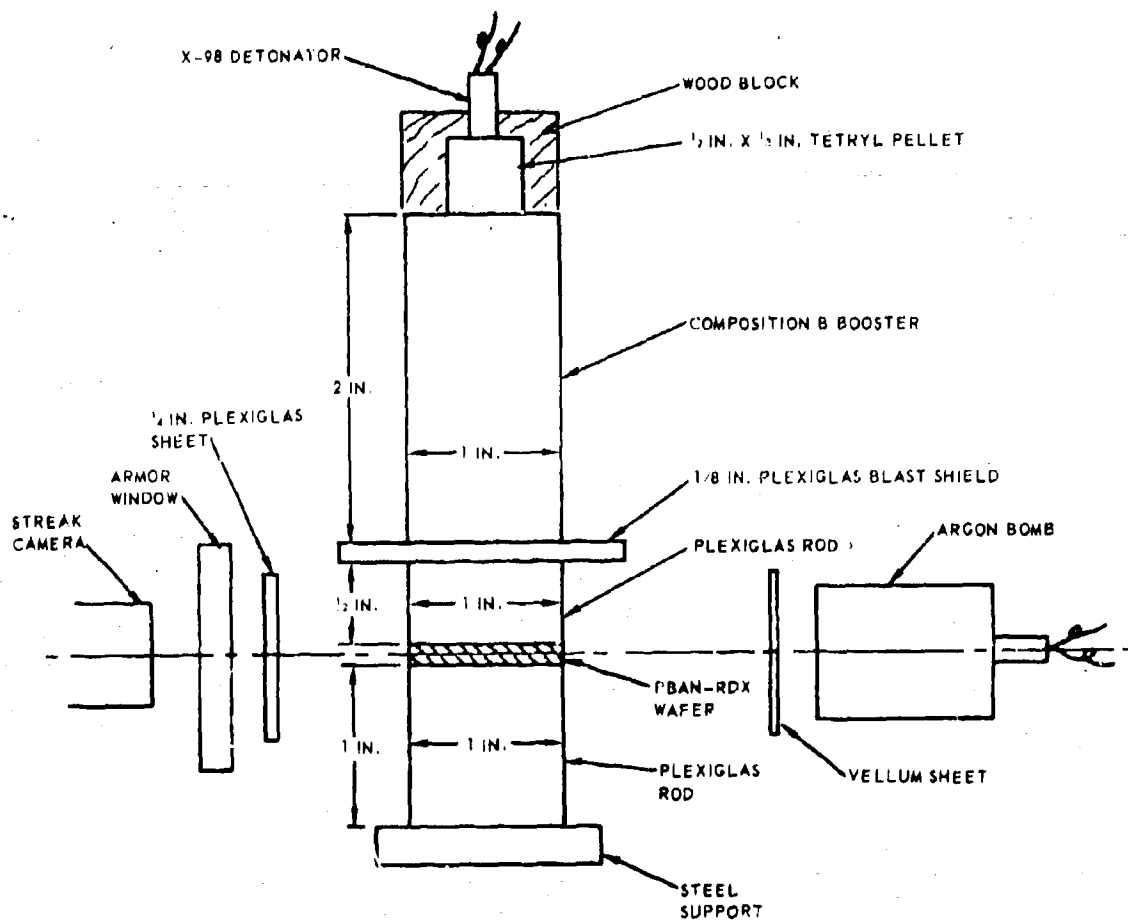


Figure 71. Test Setup - Hugoniot of PBAN-RDX Propellant.

Table 20. Hugoniot of PBAN-RDX Explosive.

Test Number	U_p (mm/μsec)	U_R (mm/μsec)	P_p^* (Kbar)	$10\rho_0 U_R^2$ (kbar-μsec/mm)	P (Kbar)	μ (mm/μsec)	Comments
1	—	—	—	—	—	—	Failure of Argon Bomb
2	4.93	3.85	64.75	66.41	69.9	1.050	Looks poor
3	4.53	4.37	49.51	75.38	59.8	0.795	
4	—	—	—	—	—	—	Failure of Argon Bomb
5	—	—	—	—	—	—	Failure of Argon Bomb
6-1	5.74	5.53	101.01	95.39	123.3	1.299	
6-2	4.34	4.34	42.89	74.87	52.5	0.705	
6-3	3.39	3.27	15.76	56.41	18.8	0.330	
6-4	3.03	2.25	8.08	38.81	8.5	0.220	
7-1	5.09	4.67	71.34	80.56	84.3	1.050	
7-2	4.02	3.64	32.64	62.79	37.9	0.605	
7-3	3.56	2.61	19.88	45.02	20.4	0.450	
7-4	3.13	2.32	10.07	40.02	10.4	0.260	
7-5	3.05	1.66	8.47	28.64	7.3	0.255	

$$* P_p = 5.51 U_p^2 - 14.03 U_p$$

$$** \rho_{0R} = 1.725 \text{ gm/cc}$$

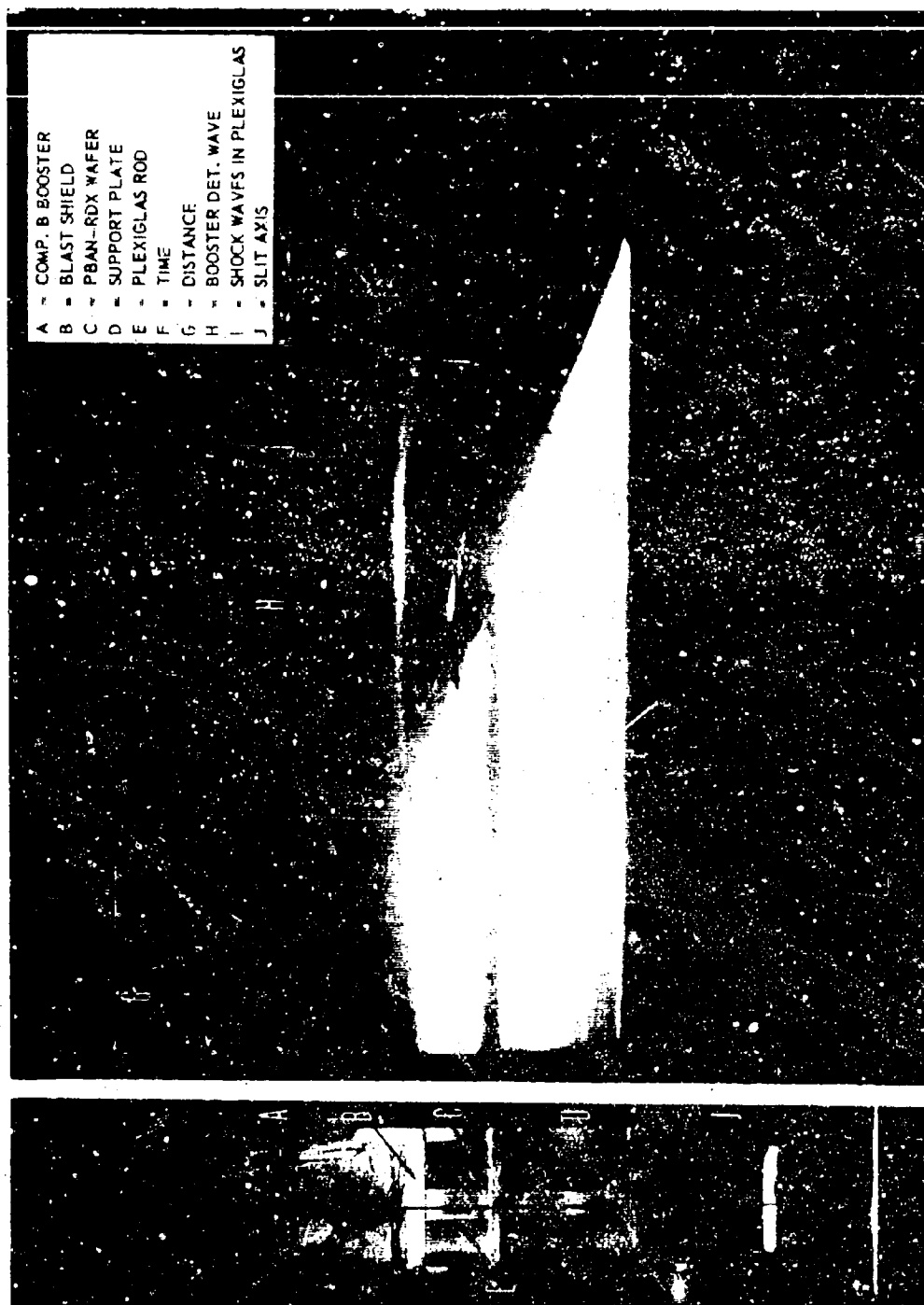


Figure 72. Streak Record-Hugoniot of PBAN-RDX Explosive - Test No. 2.



Figure 73. Streak Record-Hugoniot of PBAN-RDX Explosive - Test No. 3.

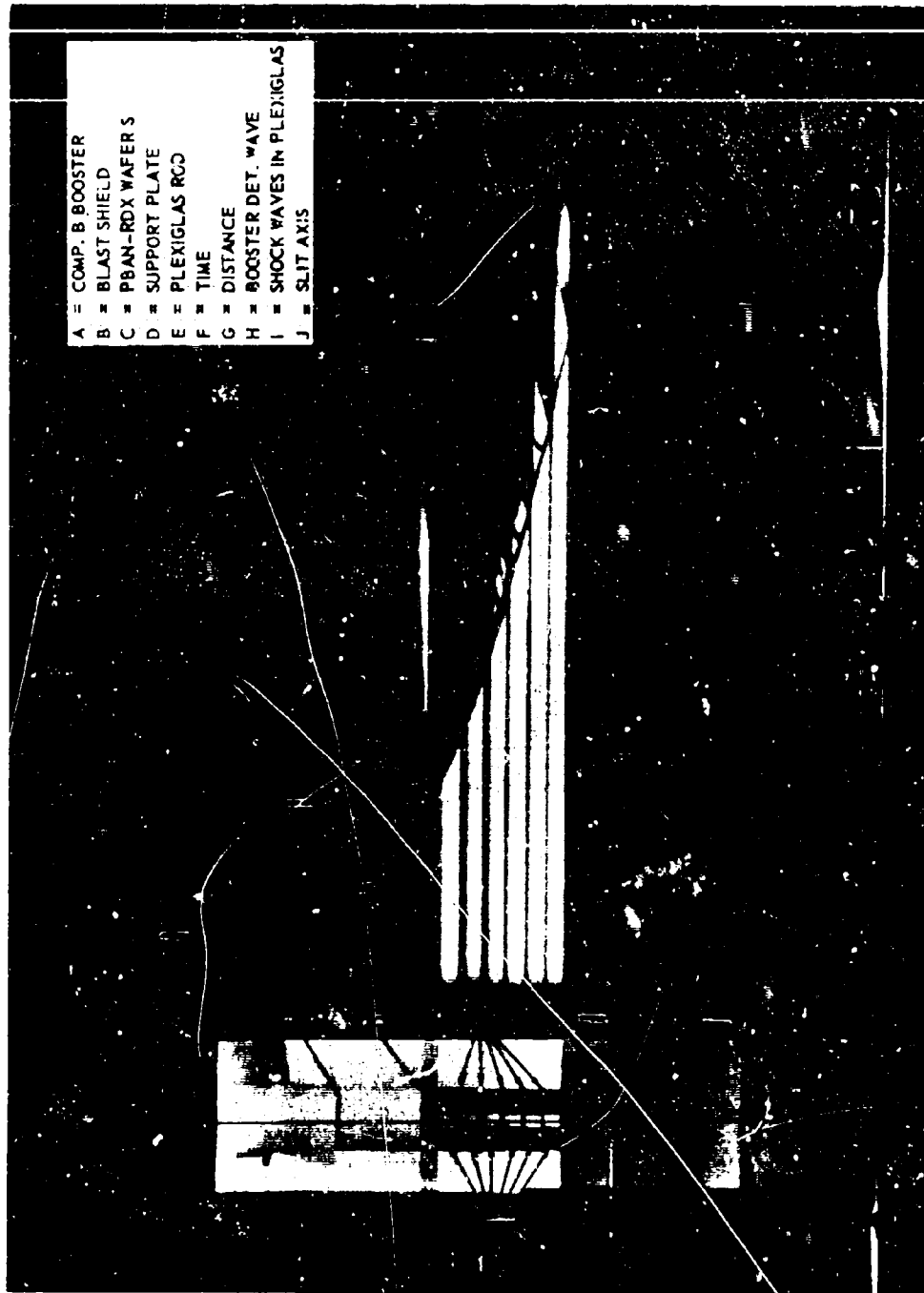


Figure 74. Streak Record-Hugoniot of PBAN-RDX Explosive - Test No. 6.

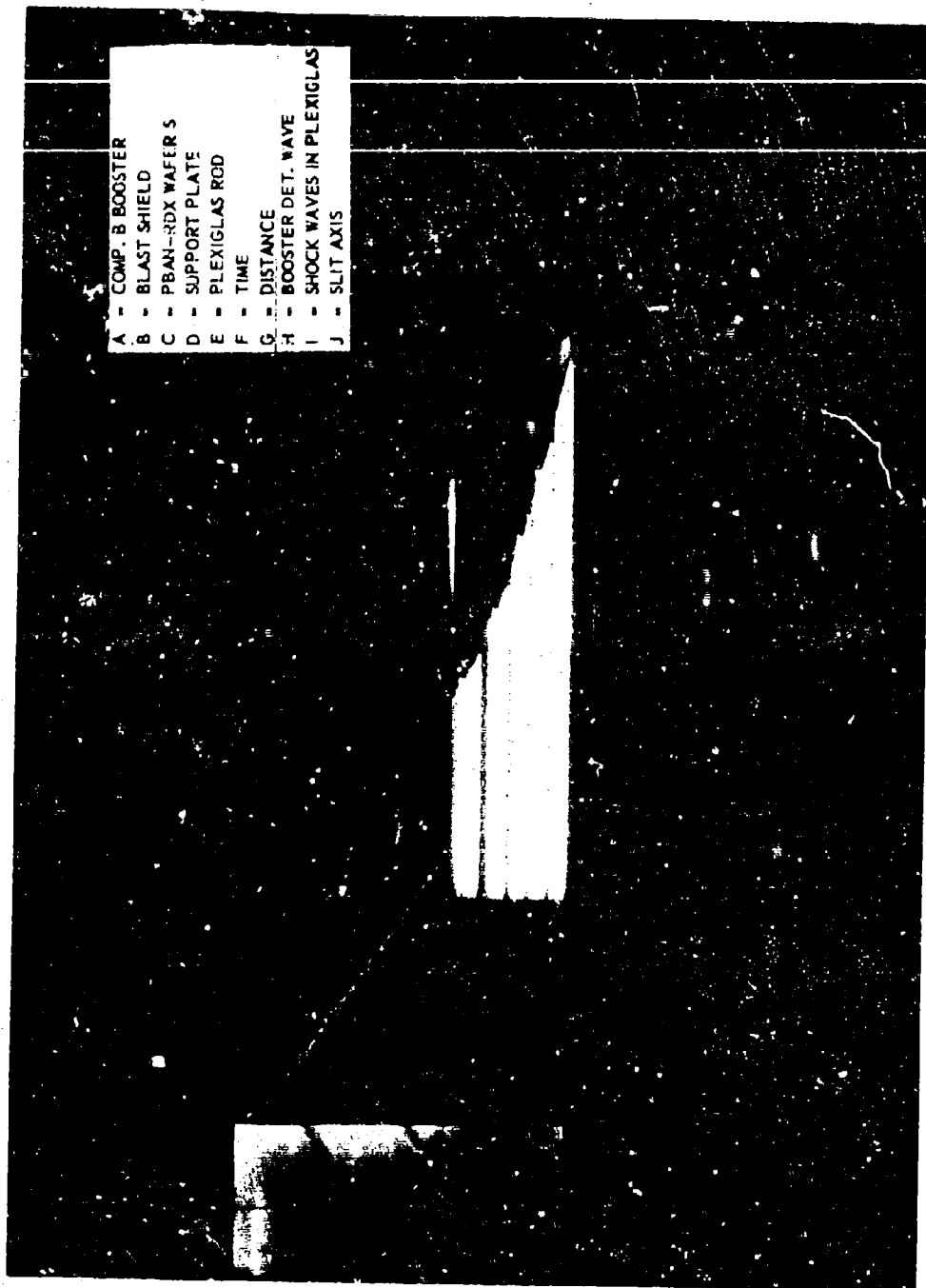


Figure 75. Streak Record - Hugoniot of PBAN-RDX Explosive - Test No. 7.

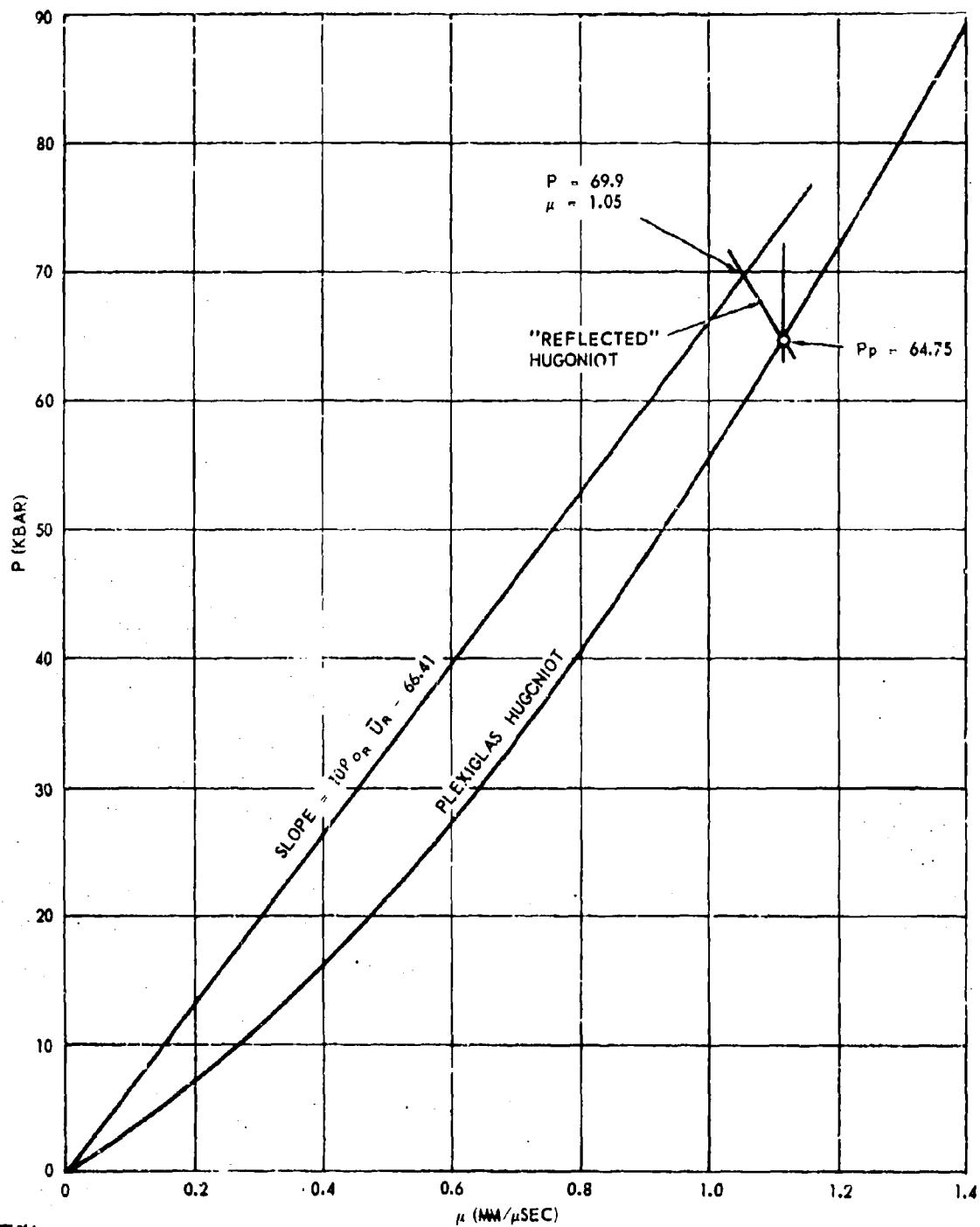


Figure 76. Determination of PBAN-RDX Hugoniot - Test No. 2.

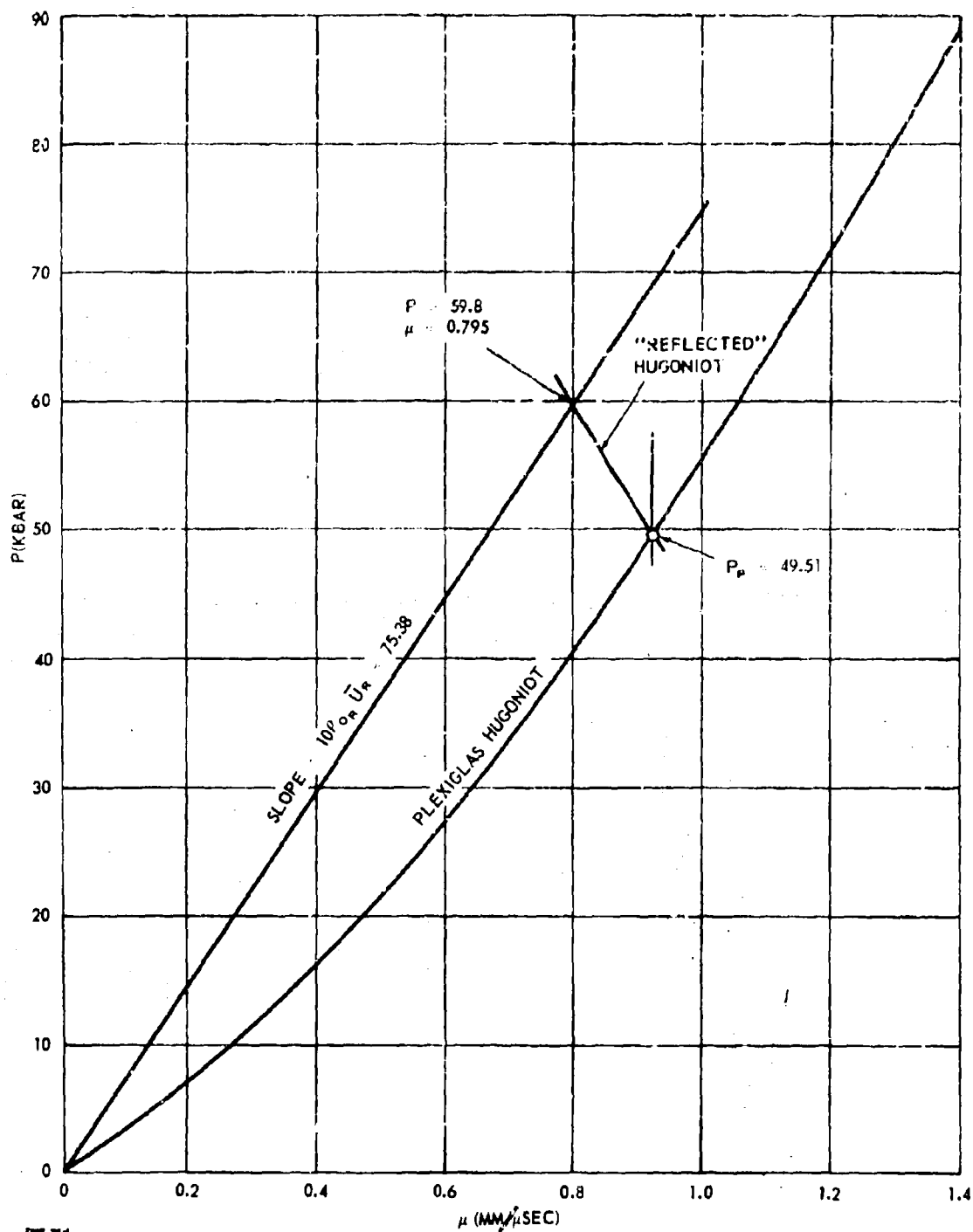


Figure 77. Determination of PBAN-RDX Hugoniot - Test No. 3.

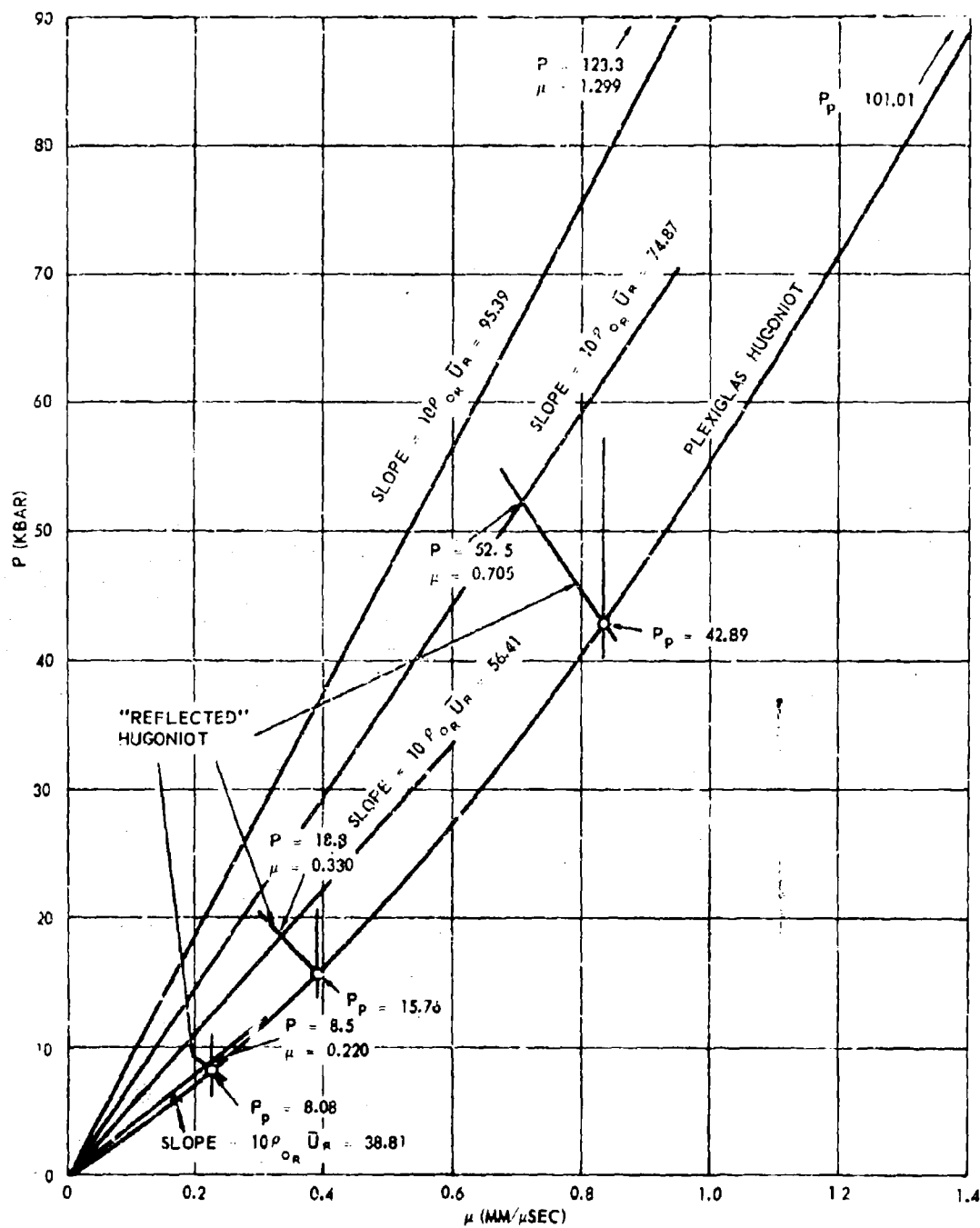


Figure 78. Determination of PBAN-RDX Hugoniot - Test No. 6.

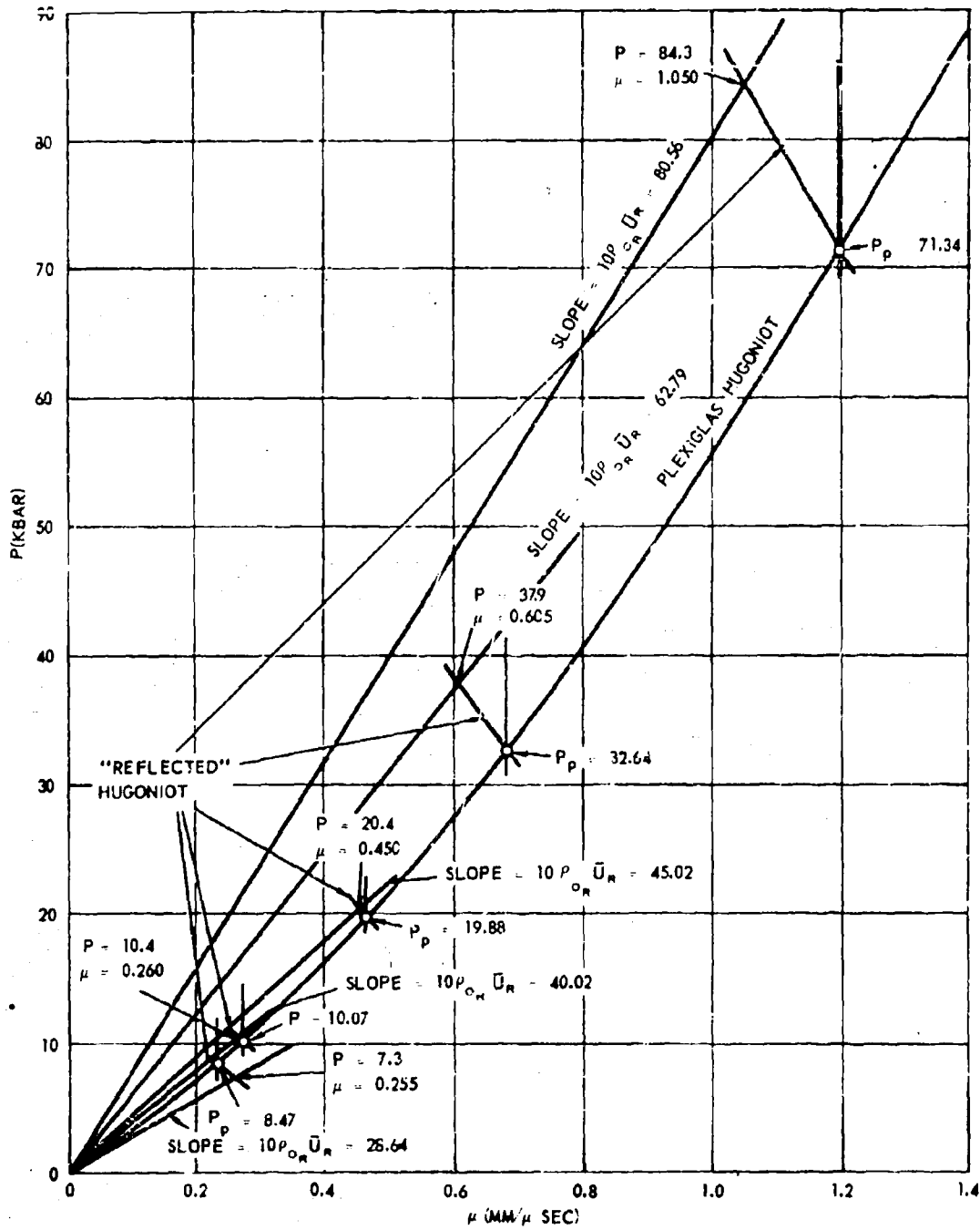


Figure 79. Determination of PBAN-RDX Hugoniot - Test No. 7.

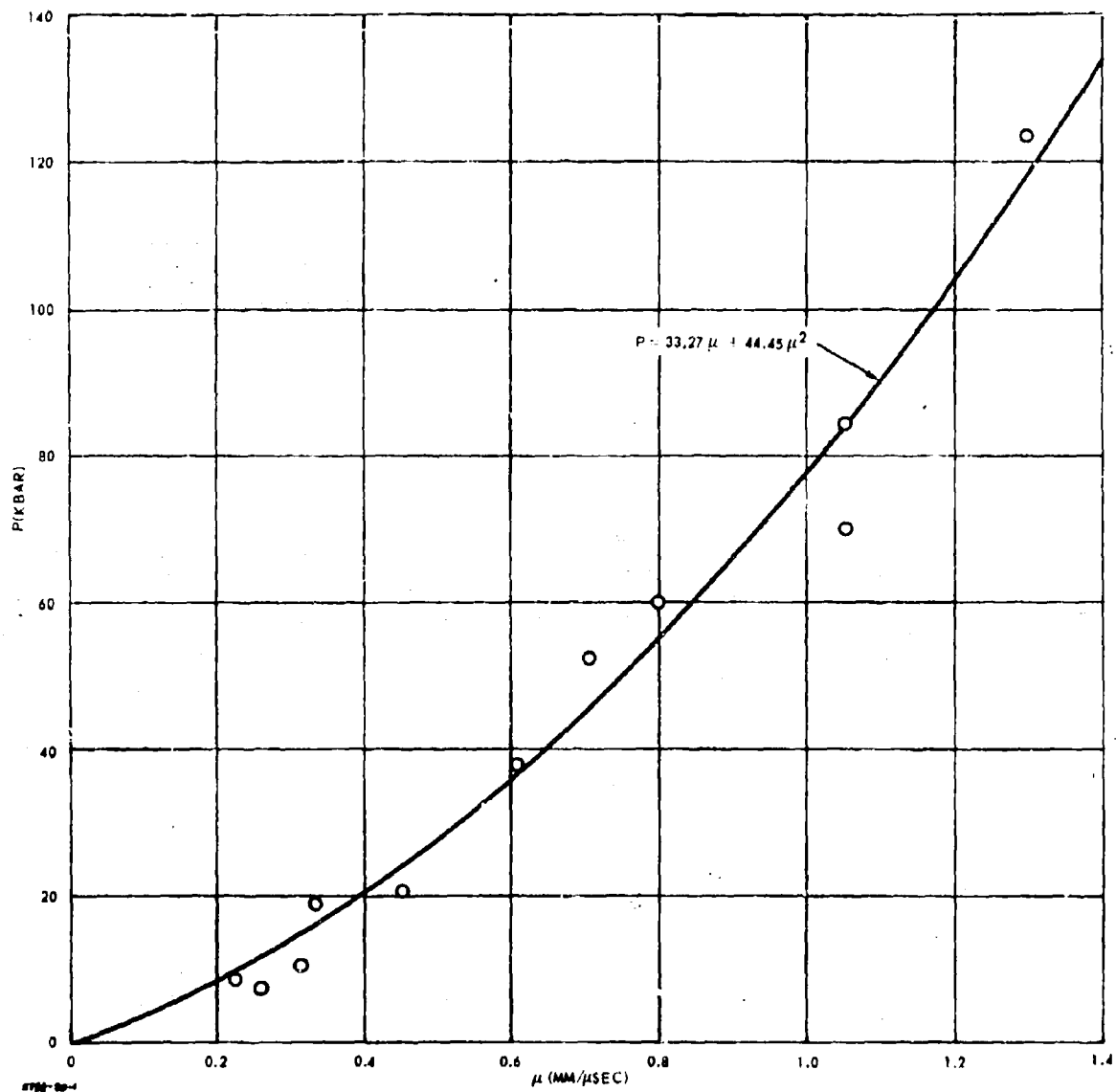


Figure 80. Hugoniot of PBAN-RDX Explosive.

may be converted to a more desirable form by use of the well known hydrodynamic relation

$$P = 10 \rho_0 U \mu, \text{ Kbar } (\rho_0 \text{ in gm/cc; } U \text{ and } \mu \text{ in mm}/\mu\text{sec})$$

This gives

$$P = 6.694 U^2 - 12.913 U, \text{ Kbar}$$

which is the expression desired for subsequent determinations.

It may be noted that only the shock velocity in the Plexiglas above the sample was used in these procedures and that the use of the shock velocity in the Plexiglas below the sample to obtain additional data was ignored. This was done because it was found that these velocities were very close to the upper velocities and made the graphical distinction between the two (Figures 76 through 79) very difficult.

d. Initiation Criterion

In order to determine the initiation criterion, 32 card-gap sensitivity tests at five diameters were conducted with the test setup shown in Figure 81 using samples from Batches 1, 2, and 3. The results are shown in Table 21. Using the value of P_0 (188 Kbar), values of the shock pressure at the end of the column P_p for each test were computed using the data in Table 21 and Figure 70. Knowing the Hugoniot of PBAN-RDX explosive (Figure 80), values of P_R (the shock pressure entering the sample) were computed using the Hugoniot reflection method (Reference 10) as shown in Figure 82. A plot of the shock pressure entering the sample P_R vs charge diameter d is shown in Figure 83 where it is noted that only one inconsistency of all the tests made was found. The vertical span drawn between the Go and No-Go results at any diameter represents the region where the shock pressure required to cause detonation P^+ may be found. Accordingly the best eye-fit curve was drawn through these data. This curve was then plotted vs diameter in Figure 84. Knowing that detonation cannot be sustained below the critical diameter d_c of the material, a left-hand bound on the curve was drawn at 2.73 in. (the midpoint of the critical diameter range determined in Section 5.3.1.1.2a(1)). This curve is the desired initiation criterion for PBAN-RDX explosive since it divides the pressure-diameter plane into Go and No-Go regions.

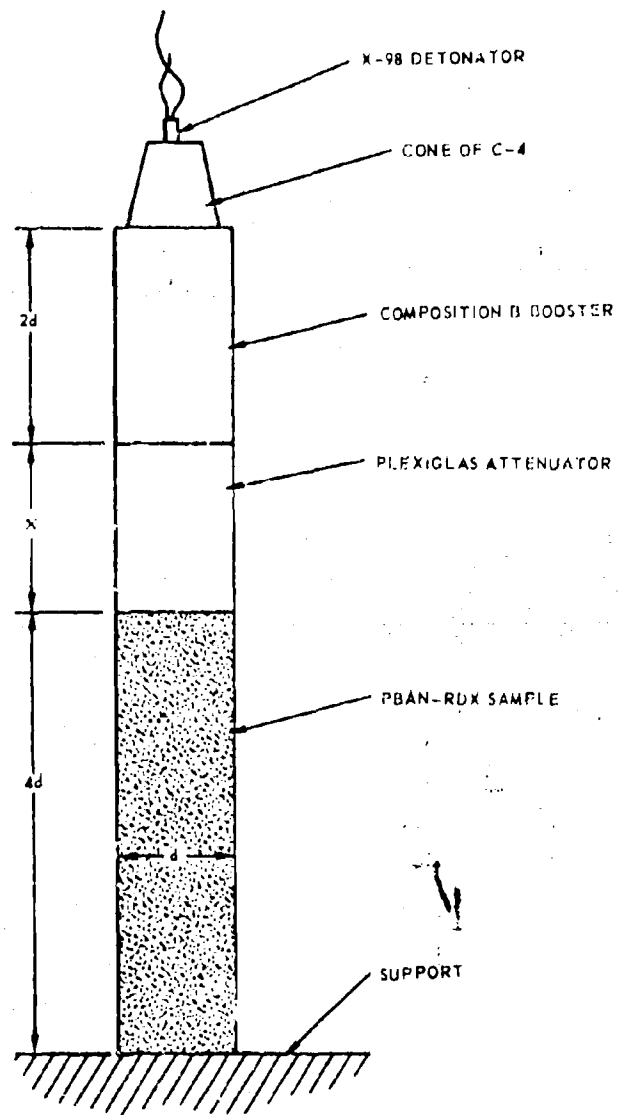


Figure 81. Test Setup - Initiation Criterion Tests.

Table 21. Initiation Criterion Tests.

Charge Diameter (in.)	Charge Density (gm/cc)	Booster Density (gm/cc)	Attenuator Length, x (in.)	Pp (Kbar)	PR (Kbar)	Result	Test Number
3.0	1.723	1.692	2.03	51.3	59.7	Go	B.4.1.1
3.0	1.720	1.688	2.19	46.1	53.0	No-Go?	B.4.1.1
3.0	1.729	1.677	2.19	46.1	53.0	Go	B.4.1.1
3.0	1.722	1.694	2.30	42.9	49.3	No-Go	B.4.1.2
3.0	1.722	1.690	2.24	44.6	51.4	No-Go	B.4.1.2
3.0	1.717	1.670	2.13	47.9	55.1	No-Go	B.4.1.2
3.5	1.721	1.683	2.59	45.1	52.0	Go	B.4.1.8
3.5	1.728	1.672	2.70	42.3	48.7	Go	B.4.1.12
3.5	1.730	1.684	2.99	35.2	40.1	No-Go	B.4.1.12
3.5	1.730	1.684	2.88	37.6	42.9	No-Go	B.4.1.2
3.5	1.729	1.675	2.78	40.0	45.9	Go	B.4.1.2
3.5	—	—	1.0	103.6	—	Go	Prelim 1
3.5	—	—	2.0	63.0	73.7	Go	Prelim 2
3.99	1.727	1.692	4.01	23.5	26.3	No-Go	B.4.1.1
3.97	1.728	1.689	2.99	44.2	50.9	Go	B.4.1.2
3.99	1.727	1.691	3.50	33.3	37.9	No-Go	B.4.1.3
3.98	1.726	1.667	3.25	38.4	44.0	Go	B.4.1.4
3.98	1.727	1.690	3.38	35.5	40.6	No-Go	B.4.1.5
3.97	1.726	1.682	3.25	38.0	43.4	Go	B.4.1.6
4.0	1.728	1.684	3.38	35.9	41.2	No-Go	B.4.1.7
5.0	1.726	1.681	3.88	41.7	47.6	Go	B.4.1.10
5.0	1.721	1.690	4.19	36.5	42.0	Go	B.4.1.13
5.0	1.726	1.690	5.00	23.5	26.3	No-Go	B.4.1.16
5.0	1.725	1.690	4.58	30.1	34.2	No-Go	B.4.1.20
5.0	1.729	1.682	4.42	32.1	36.8	Go	B.4.1.24
5.0	1.724	1.682	4.57	30.1	34.2	No-Go	B.4.1.28
5.0	1.727	1.692	4.38	33.3	37.9	Go	B.4.1.30
6.0	1.724	1.687	4.49	44.7	51.5	Go	B.4.1.11
6.0	1.727	1.686	4.81	39.5	45.4	Go	B.4.1.12
6.0	1.726	1.686	5.50	30.1	34.2	Go	B.4.1.18
6.0	1.728	1.687	6.00	23.5	26.3	No-Go	B.4.1.23
6.0	1.726	1.695	5.75	26.7	30.1	No-Go	B.4.1.25

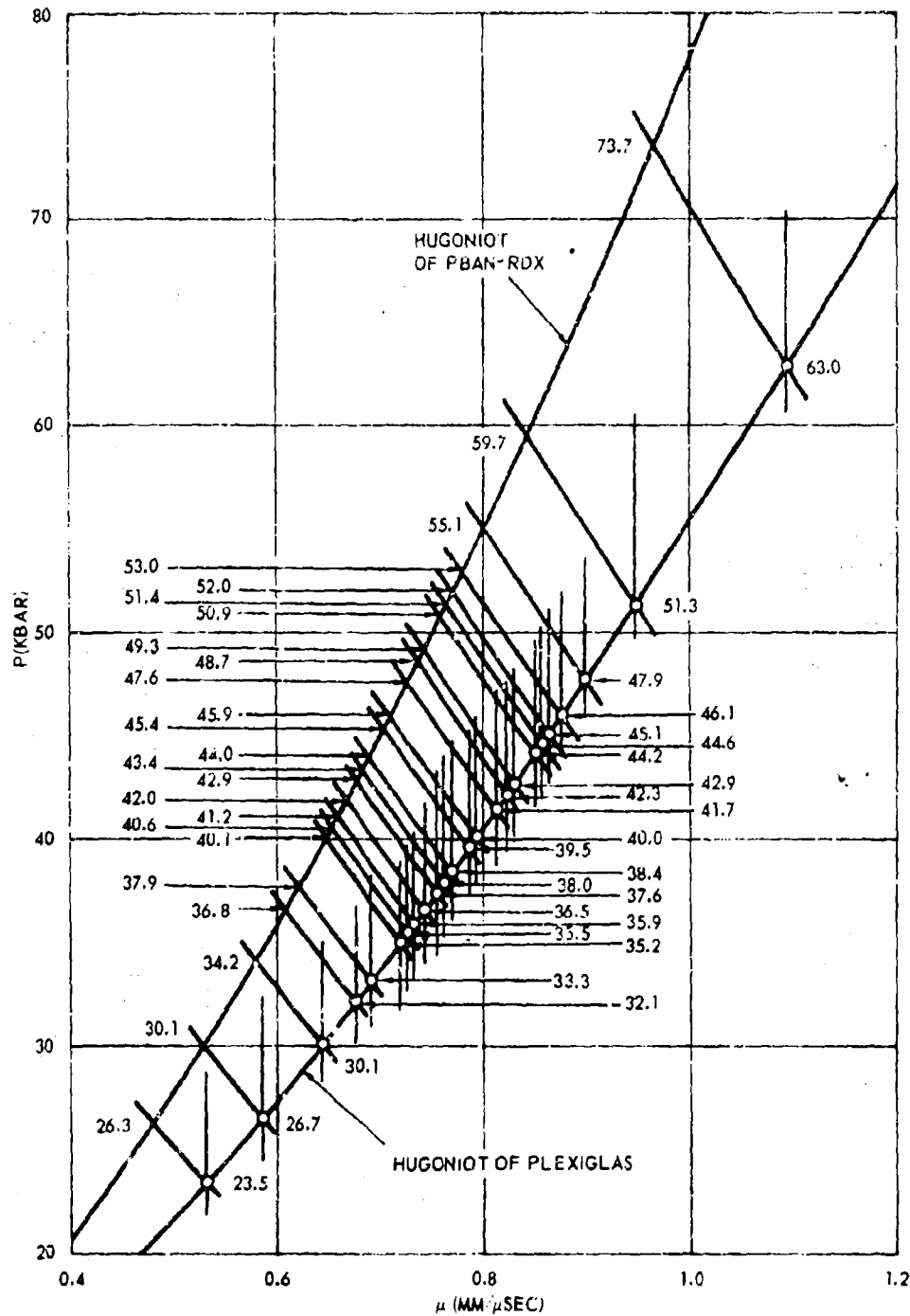


Figure 82. Pressure Entering PBAN-RDX Explosive - Hugoniot Reflection Method.

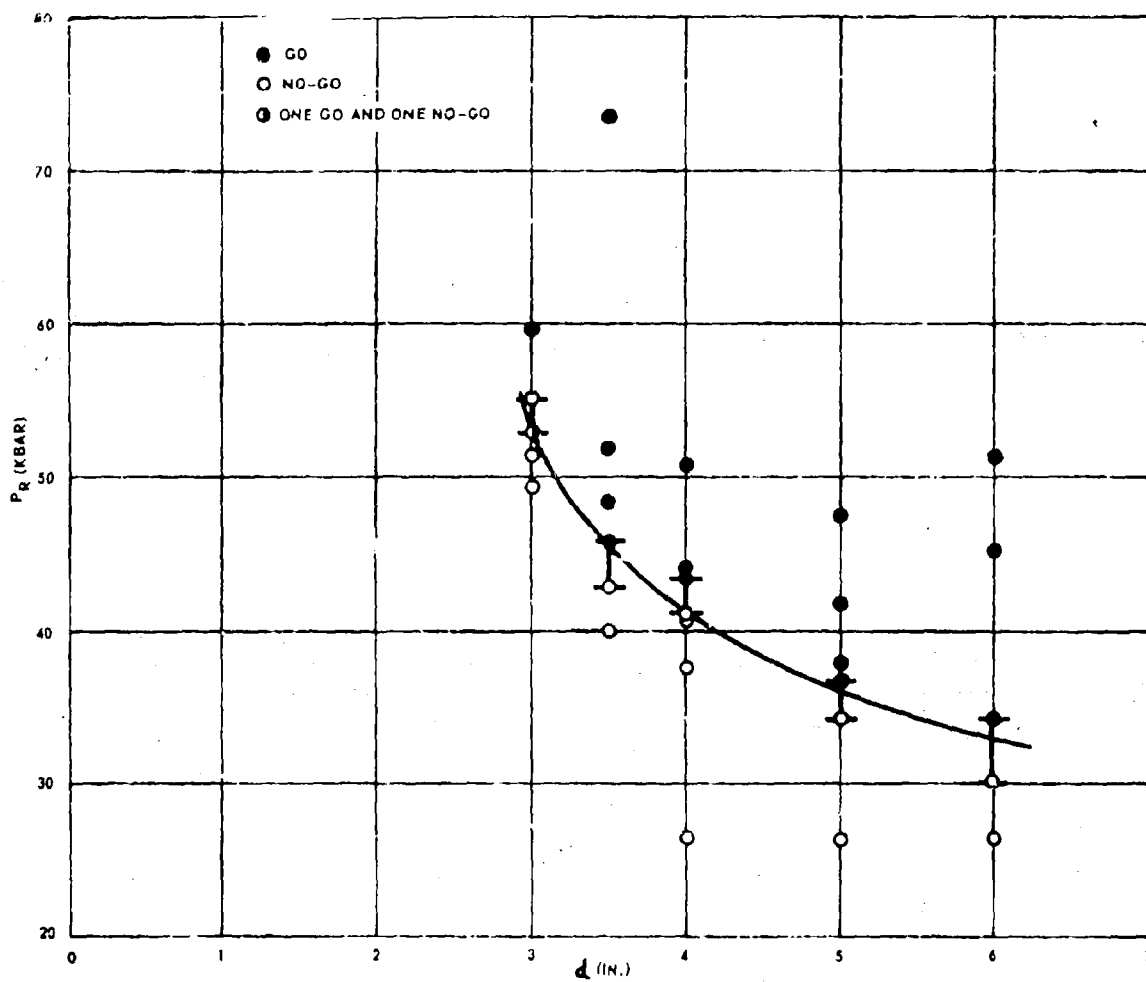


Figure 83. P_R vs d for PBAN-RDX Explosive.

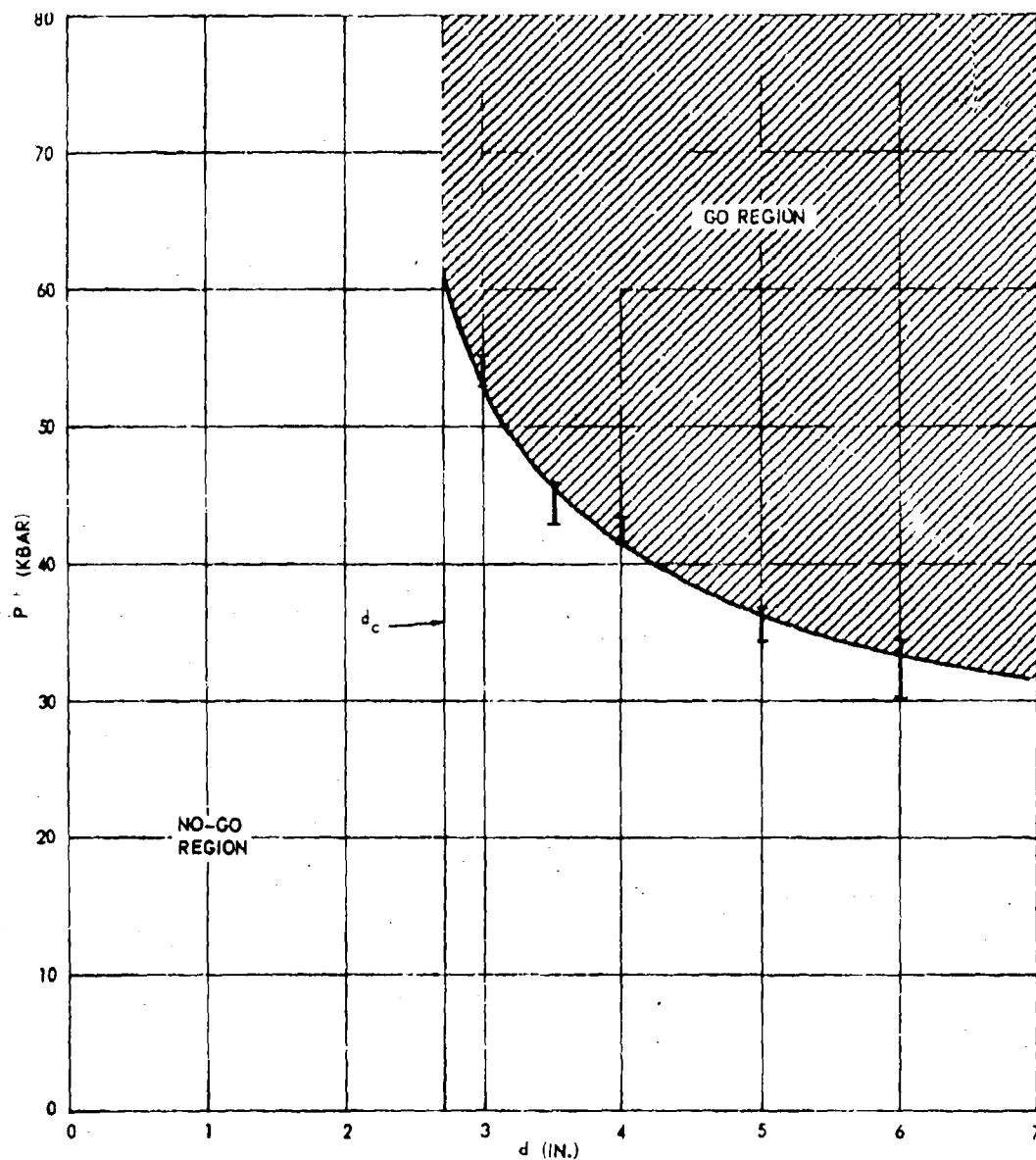


Figure 84. Initiation Criterion of PBAN-RDX Explosive - P^+ vs d .

Because it is also possible to define the initiation criterion using area of the wave instead of diameter of the test, a criterion alternative to that in Figure 84 was found as follows. Assuming spherical expansion of the detonation wave from the point of initiation in each test, it was possible from the test dimensions and geometry to determine the area of the wave entering the propellant in each case. It was found that this area varied only slightly from test to test at the same diameter and thus an average area A for each diameter was established. The area A_c , associated with critical diameter d_c , was computed by extrapolation of this data. From these computations the initiation criterion in terms of A was drawn and is shown in Figure 85.

5.3.1.2.2 Attenuation Properties (Subtask B.4.2)

The general objective of the tests in Subtask B.4.2 was to determine how input shock waves from various size cylindrical donors attenuate, when placed at various locations on nonperforated (Subtask B.4.2.1) and perforated (Subtask B.4.2.2) supercritical acceptor charges.

a. Nonperforated Shapes (Subtask B.4.2.1)

The primary objectives of the tests in Subtask B.4.2.1 were to (1) determine in detail how the input shock waves attenuated when axial, end donors of various sizes were placed on nonperforated, supercritical, cylindrical acceptor charges (Subtask B.4.2.1.1) and to (2) demonstrate how detonation took place when side donors of two sizes were placed on the same type of acceptor charge (Subtask B.4.2.1.2). A secondary objective in both cases was to estimate the critical size of the donor required to cause detonation.

(1) Axial, End Donor (Subtask B.4.2.1.1)

The results of five axial, end donor tests using samples from Batches 1 and 3 are shown in Table 22, where the subtask is indicated by the test number. The test setup is shown in Figure 86 and a framing camera record of Test B.4.2.1.1.1 is shown in Figure 87. In order to follow the progress of the entering shockwave for each test in detail, sets of probes were inserted at depths of 0.5, 1.0, 1.5, and 2.0 in. into the charge. The vertical distance between probes was 1 in. The resultant distance-time data (shown in Figures 88 through 91) were interpolated to establish the position and size of the wave at any time as well as the vertical velocity of propagation at the different insertion depths at any time.

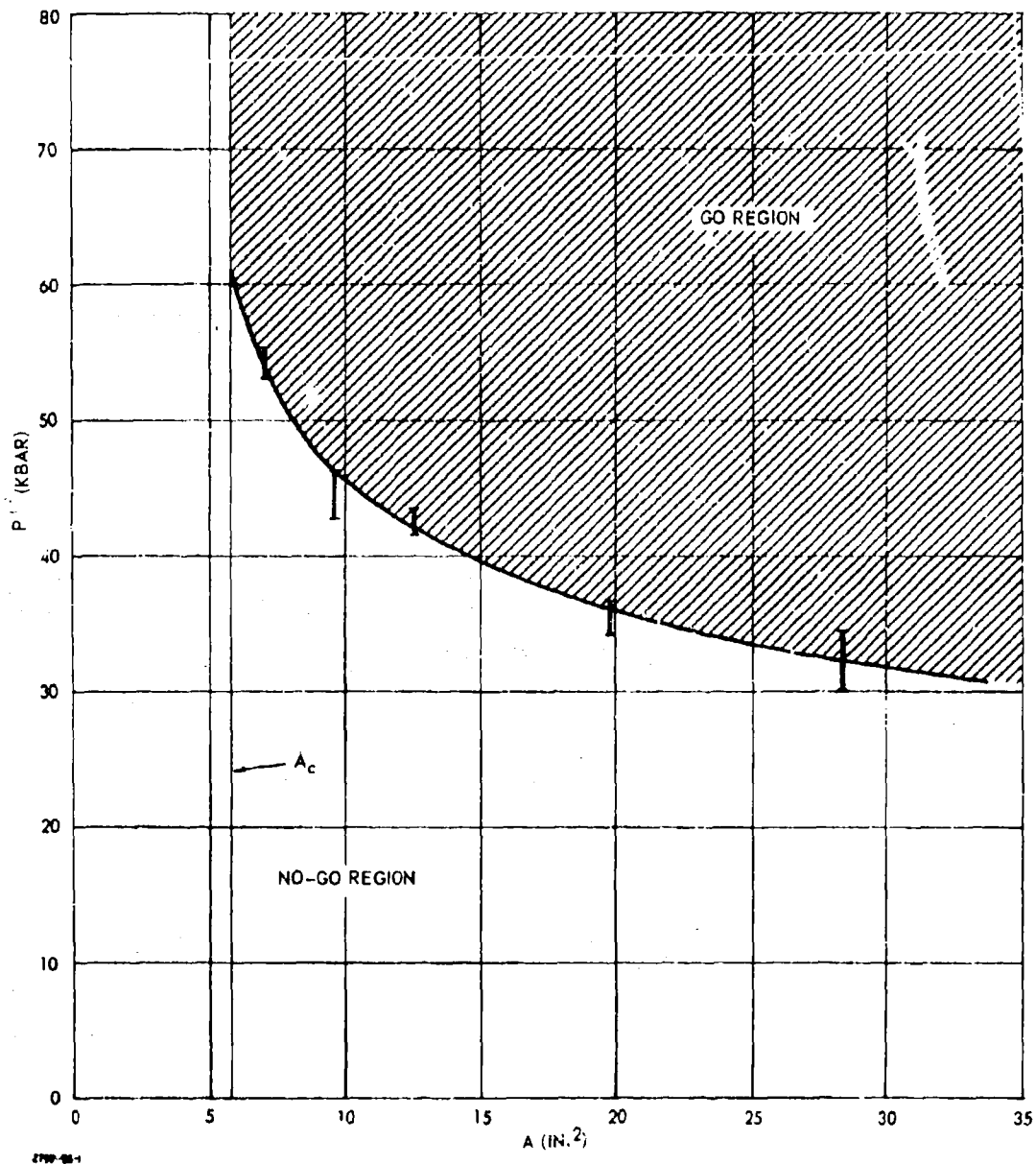


Figure 85. Initiation Criterion of PBAN-RDX Explosive - P^+ vs A .

Table 22. Axial, End Donor Tests.

Test Number	Charge Diameter (in.)	Charge Density (gm/cc)	Booster Diameter (in.)	Result	Instru- mentation*	sc		ro	
						Results	No-Go?	Results	Comments
B. 4. 2. 1. 1. 1	4. 03	1. 730	1. 0	No-Go	sc/ro	No-Go?	No-Go	No-Go	
B. 4. 2. 1. 1. 2	3. 99	1. 722	2. 0	Go	sc/ro	No data	No data	Go	
B. 4. 2. 1. 1. 3	3. 98	1. 723	1. 5	No-Go	sc/ro	No data	No data	No-Go	
B. 4. 2. 1. 1. 4	3. 99	1. 725	1. 75	-	sc/ro	-	-	-	Misfire
B. 4. 2. 1. 1. 5	3. 99	1. 723	1. 75	Go	sc/ro	No data	No data	Go?	

*sc = streak camera (Beckman and Whitley Model 194)
ro = raster oscillograph (Moran and Polaroid)

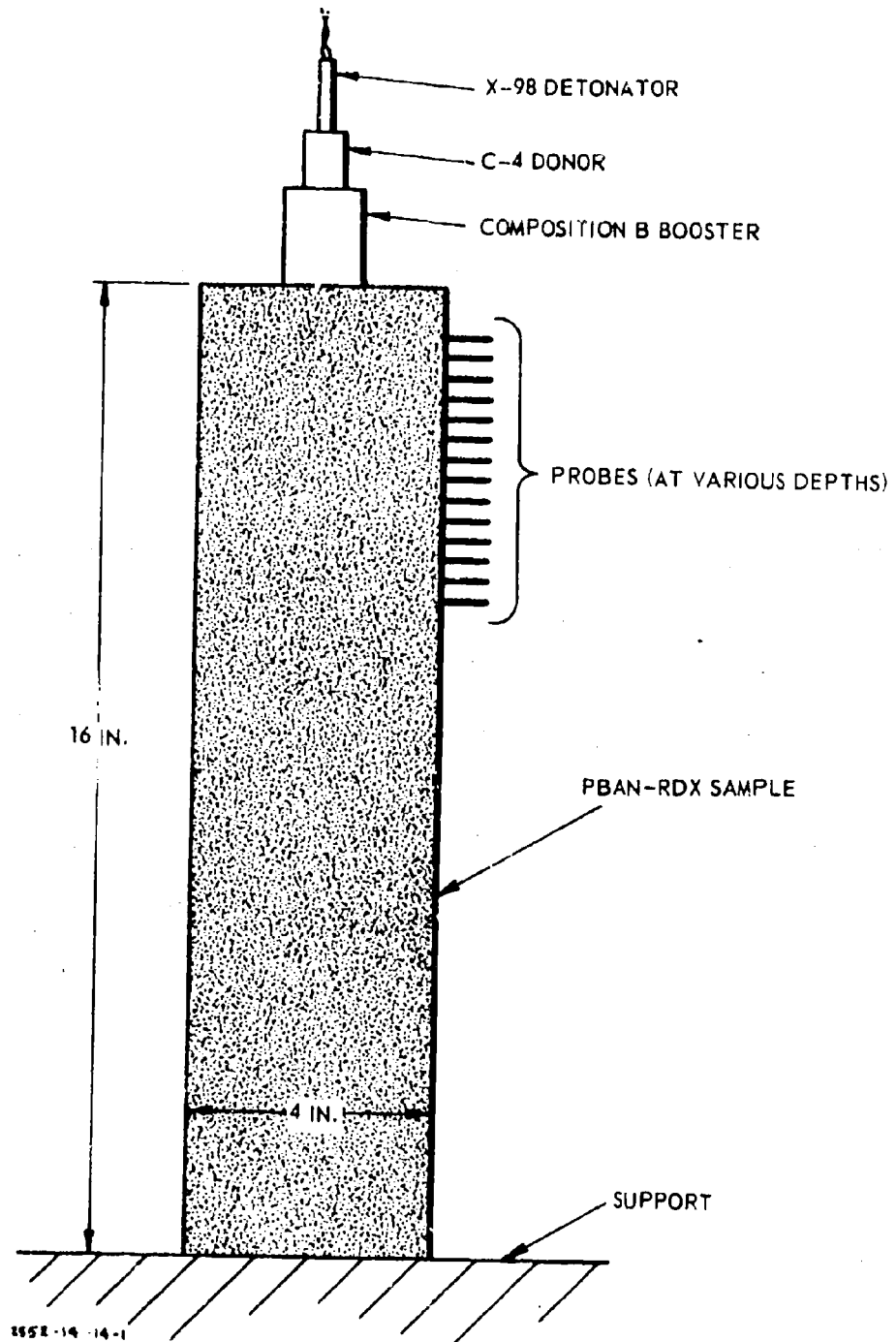


Figure 86. Axial End Donor Test Setup for Nonperforated Acceptor.

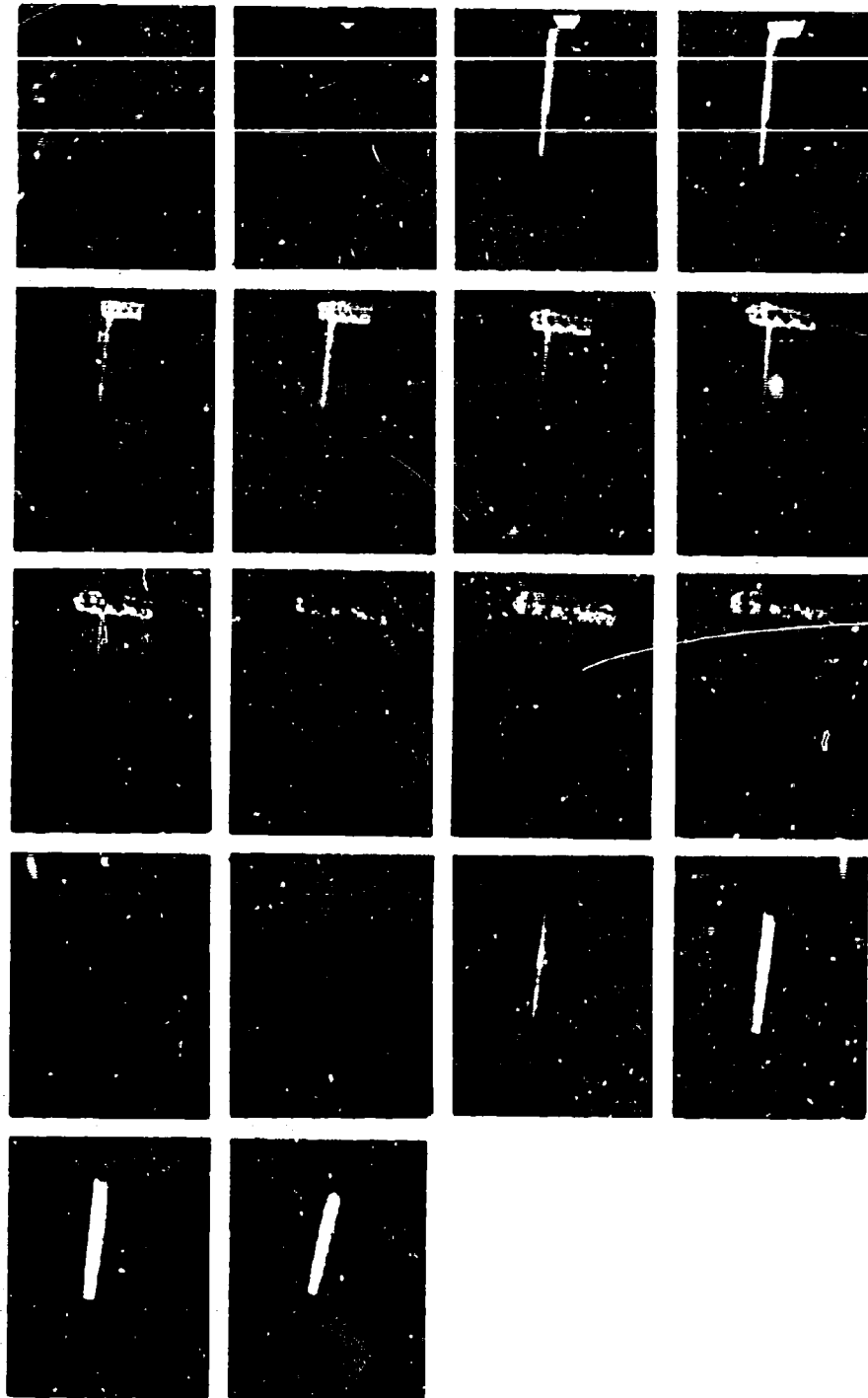


Figure 87. Axial, End Donor Test - Test No. B.4.2.1.1.1
(Time Increment = 2.76 μ sec/frame).

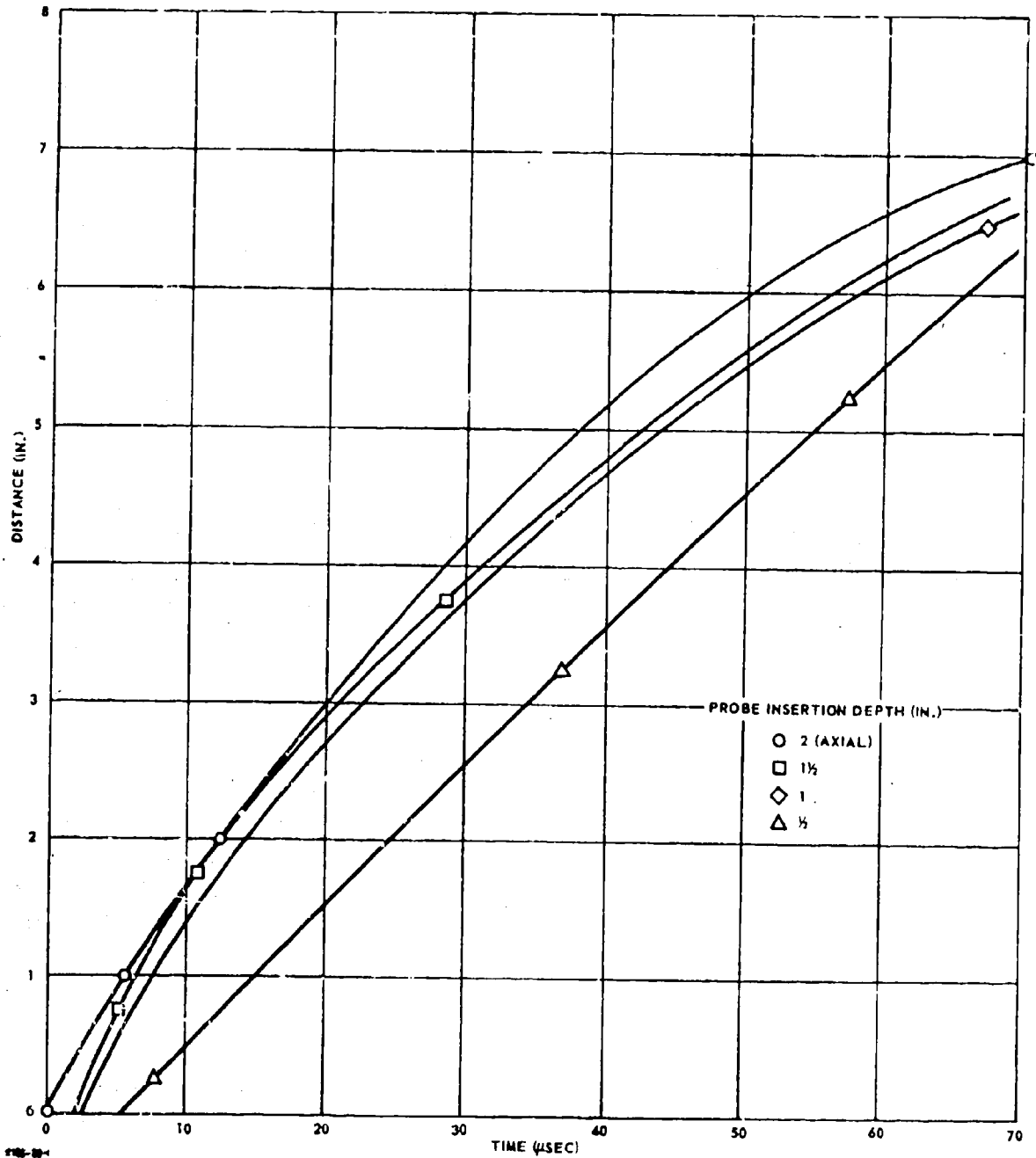


Figure 88. Axial, End Donor Test B.4.2.1.1.1, Distance vs Time Data, 1.0-in.-Diameter Booster.

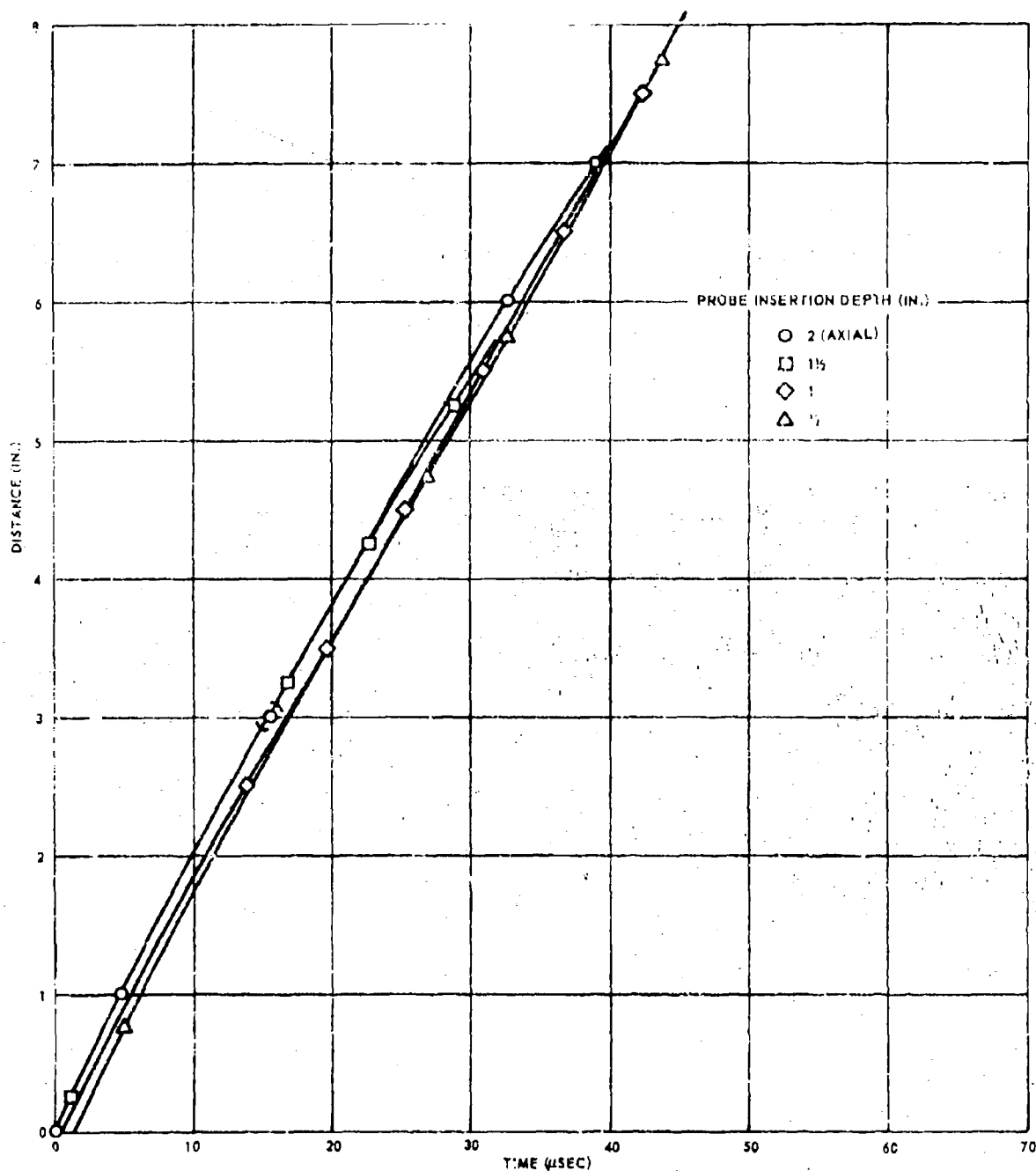


Figure 89. Axial, End Donor Test B.4.2.1.1.2, Distance vs Time Data
2.0-in.-Diameter Booster.

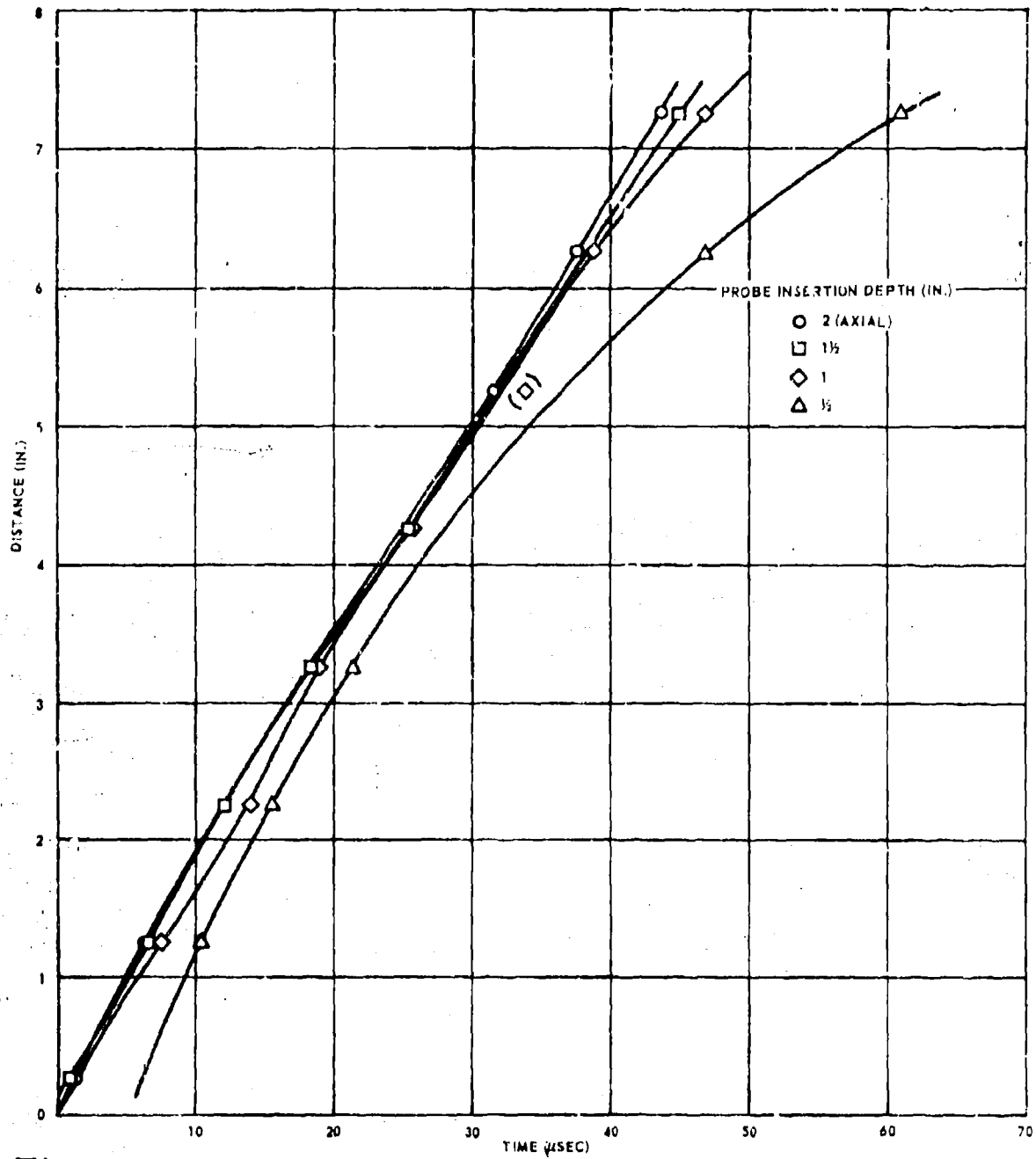


Figure 90. Axial, End Donor Test B.4.2.1.1.3, Distance vs Time Data.
1. 50-in.-Diameter Booster.

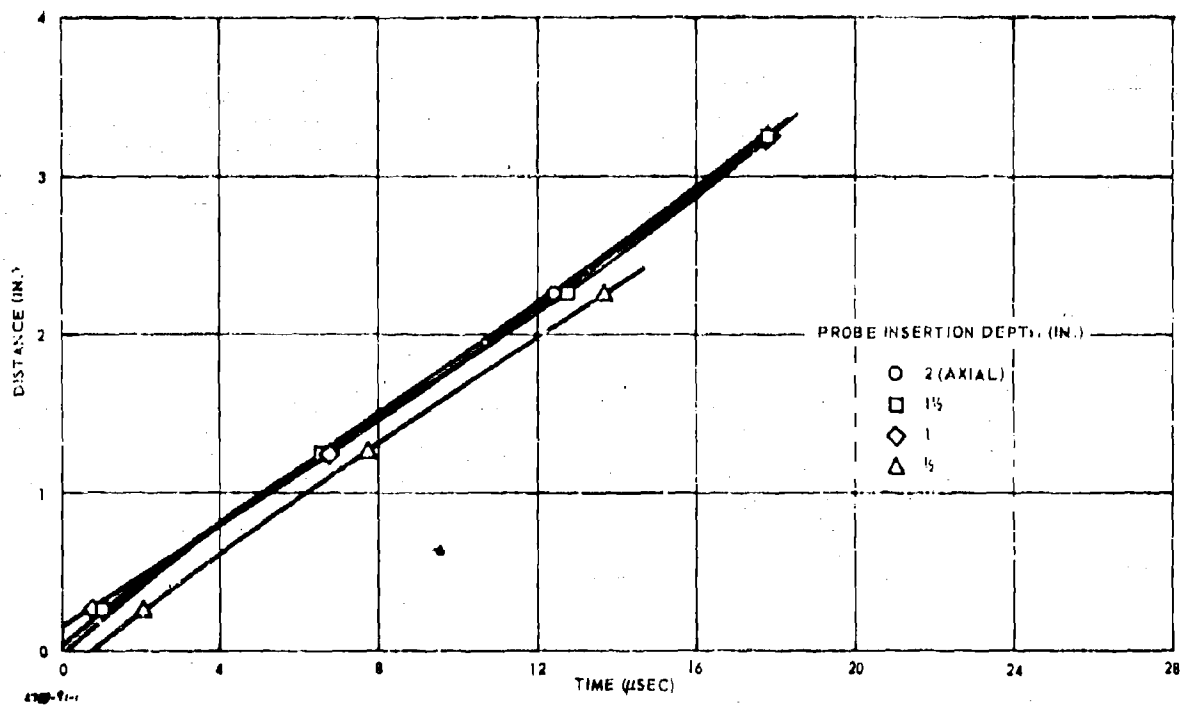


Figure 91. Axial, End Donor Test B. 4. 2. 1. 1. 5 - Distance-Time Data
1.75-in.-Diameter Booster.

From this information it was desired to determine the wave diameter and area as well as shock pressure, as it attenuated.

Wave Diameter and Area

By assuming the waves propagate spherically and symmetrically it was possible to use the position-time data to generate the least-squares best fit (circular) wave profiles as a function of time. This data and the resulting profiles are shown in Figures 92 through 95. In Test B.4.2.1.1.1, the curvature became so great for time greater than 5 μsec that straight lines had to be drawn to fill out the wave profile. These lines were drawn from the point of intersection of a vertical line (drawn at the arbitrary depth shown in Figure 92) with the best-fit circles and the data obtained at a depth of 0.5 in. They are probably good approximations to the actual wave profile. Since the least-squares best fit equations required at least three points to give a solution, data were added in Tests B.4.2.1.1.1, B.4.2.1.1.3, and B.4.2.1.1.5 to fulfill this requirement. These data were chosen carefully so as to be representative of the type of wave profile occurring in that particular test and to be consistent with other data. The best-fit circle for each profile is defined in terms of the radius of the circle r and the position h of its center on the axis with respect to the booster-sample interface. These data are shown in Table 23 for each of the profiles in Figures 92 through 95. From the calculus, it can be shown that the surface area of revolution of a body about the x -axis (i. e., the axis of the cylinder) for x ranging from x_0 to x_1 is given by

$$A = 2\pi \int_{x_0}^{x_1} y \sqrt{1 + \left(\frac{dy}{dx}\right)^2} dx$$

The equation for the circles of the type being considered is

$$(x + h)^2 + y^2 = r^2$$

and it is easy to show that, from the above,

$$A = 2\pi r (r - h), \text{ in.}^2; d = 2 \sqrt{r^2 - h^2}, \text{ in.}$$

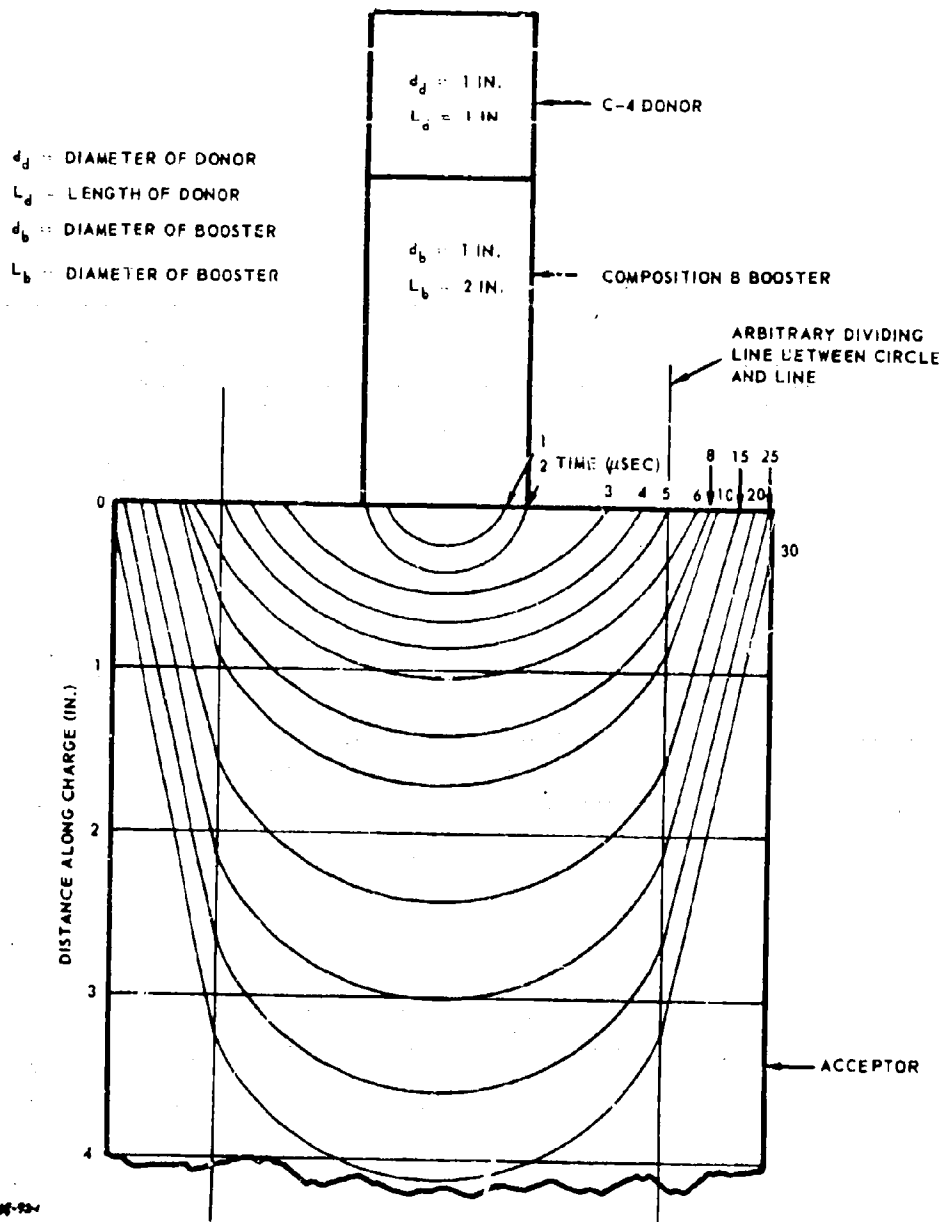


Figure 92. Wave Profiles - Test No. B.4.2.1.1.1.

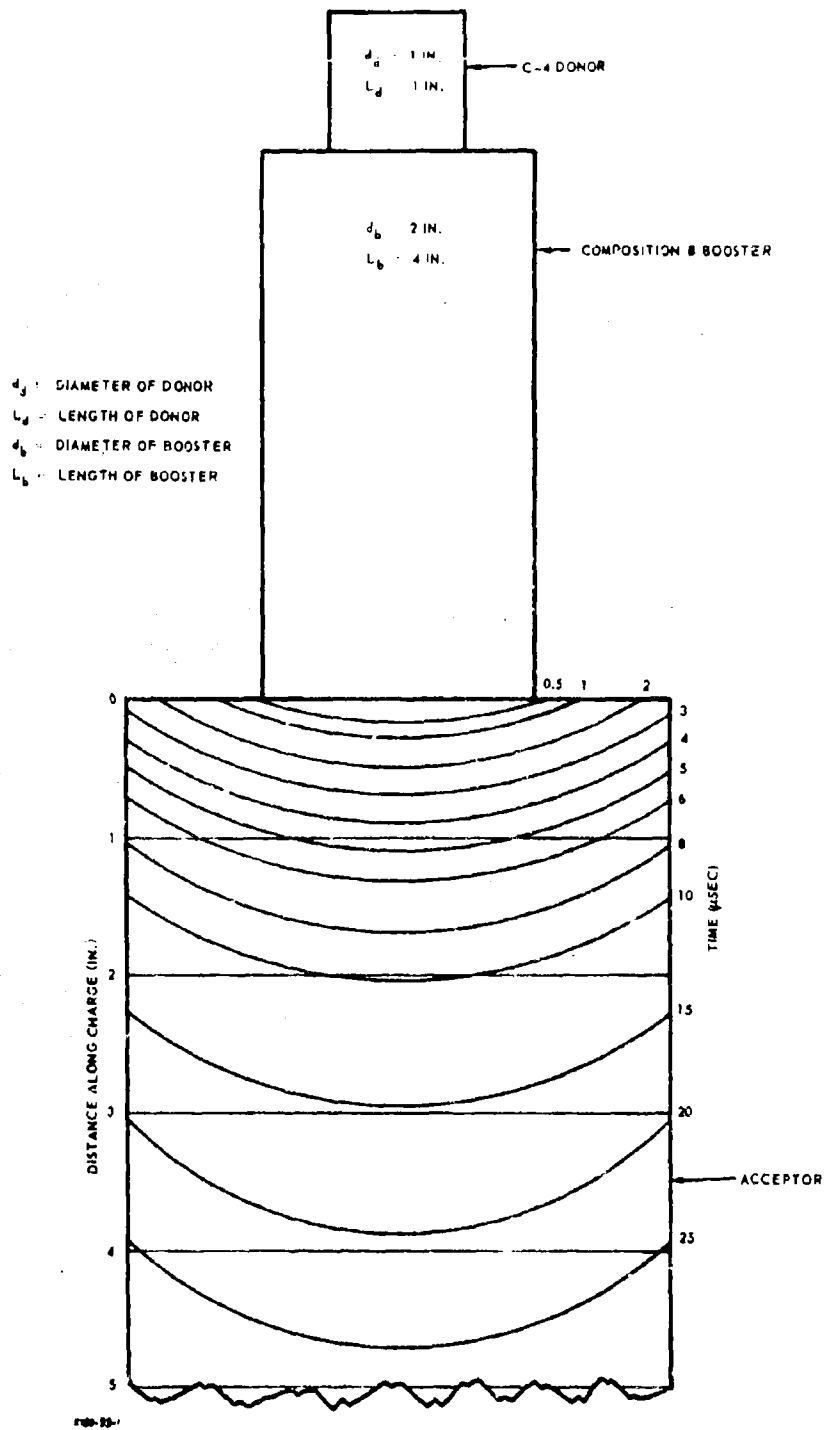


Figure 93. Wave Profiles - Test No. B 4.2.1.1.2.

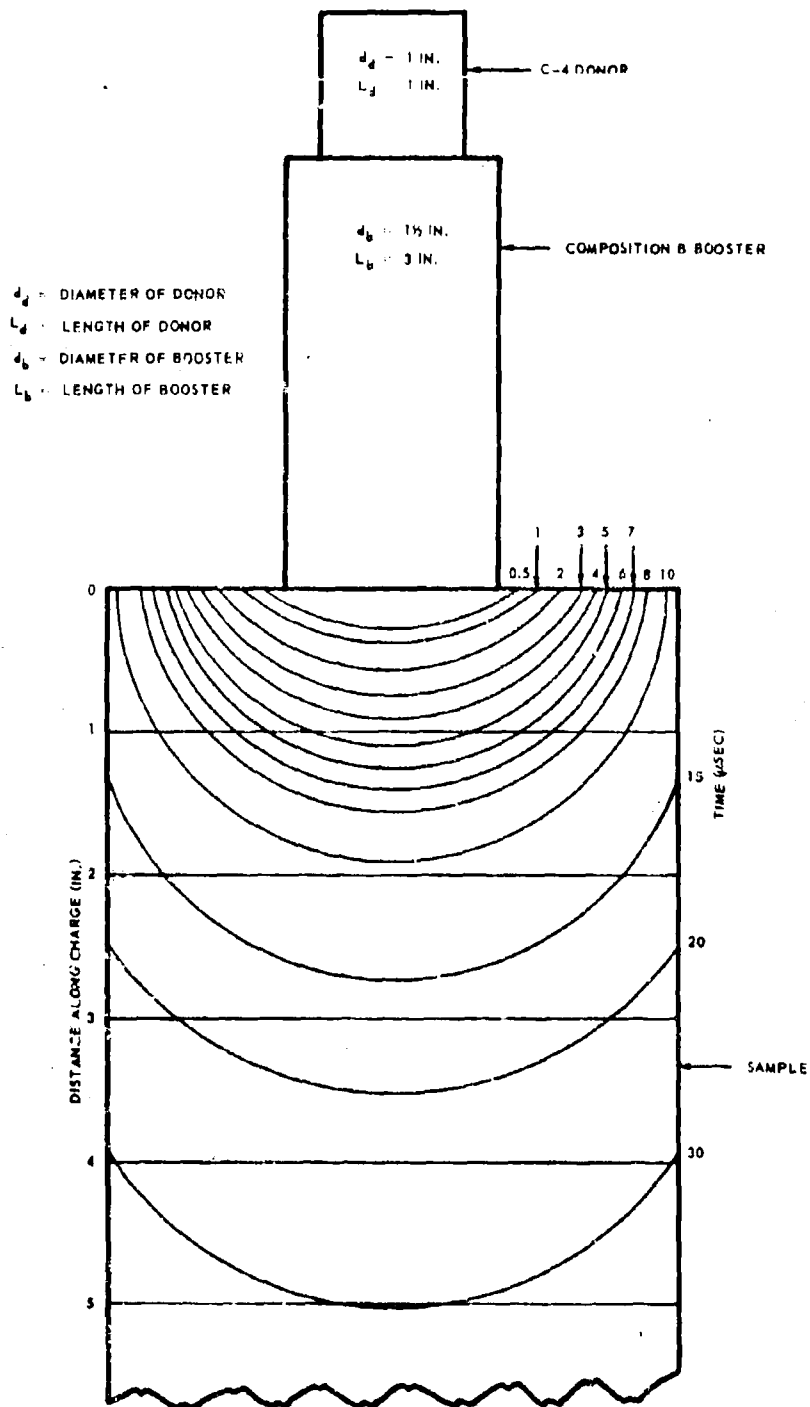
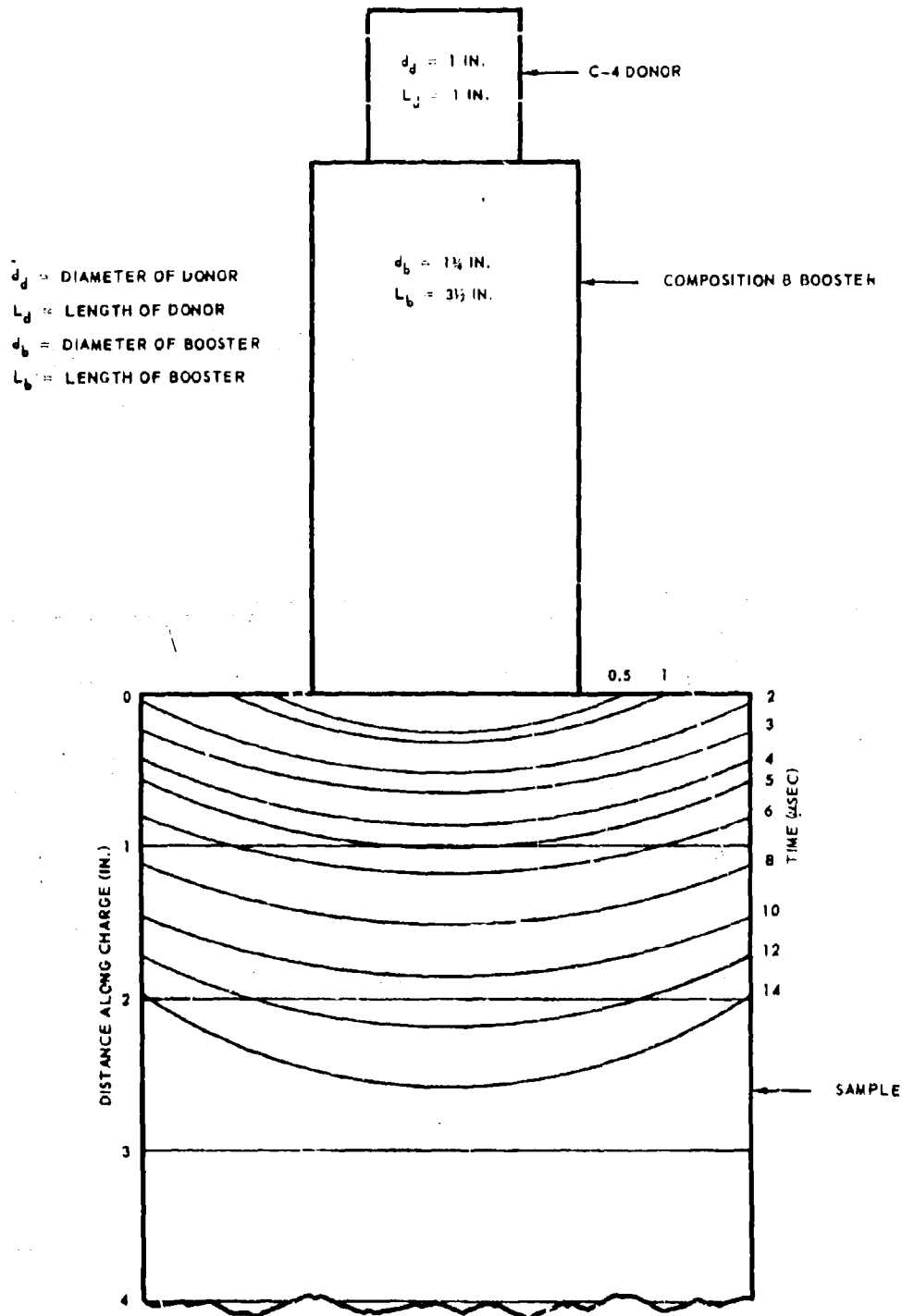


Figure 94. Wave Profiles - Test No. B.4.2.1.1.3.



878-76-

Figure 95. Wave Profiles - Test No. B.4.2.1.1.5.

if

$$r \leq 2 \text{ or if } r > 2 \text{ and } h > \sqrt{r^2 - 4} \text{ and}$$

$$A = 2 \pi r \left[r - \sqrt{r^2 - 4} \right] \text{ in. ; } d = 4 \text{ in.}$$

if

$$r > 2 \text{ and } h < \sqrt{r^2 - 4}$$

Using these equations, the desired diameters and areas were computed and are also shown in Table 23. It may be noted that the profiles in Test B. 4. 2. 1. 1. 1 are not all spherical since the straight lines shown give a conical surface when revolved about the x-axis. By adding an appropriate term to the above equations, the correct surface area was computed and appears in Table 23.

Wave Shock Pressure

Because of the fact that the wave profiles are curved (see Figures 92 through 95) and the probe measurements are made only in a vertical direction, the raw velocity-time data for each insertion depth is not the true wave propagational velocity (i. e., the velocity normal to the wave front). Based on the equations of the best-fit wave profiles and geometry, appropriate adjustment factors were computed and the true velocity-time data found for each profile. From the Hugoniot of PBAN-RDX explosive found earlier, these velocity data were converted to shock pressure using the equation

$$P = 6.694 U^2 - 12.913 U, \text{ Kbar}$$

In order to associate a unique shock pressure with any wave at any time, an average shock pressure \bar{P} was defined by the equation:

$$\bar{P} = \frac{\int_0^A P dA}{\int_0^A dA} = \frac{1}{A} \int_0^A P dA$$

Table 23. Wave Diameter, Area and Shock Pressure.

<u>Test Number</u>	<u>Time (μsec)</u>	<u>b (in.)</u>	<u>r (in.)</u>	<u>d (in.)</u>	<u>A (in.²)</u>	<u>\bar{P} (Kbar)</u>
B. 4. 2. 1. 1. 1	1	0.185	0.405	0.72	0.560	118.9
	2	0.102	0.506	1.00	1.284	105.5
	3	0.668	1.195	2.00	3.957	90.2
	4	0.616	1.328	2.38	5.941	70.5
	5	0.633	1.513	2.74	8.366	51.2
	6	0.573	1.636	3.06	10.885	39.6
	8	0.178	1.581	3.20	13.862	32.5
	10	-0.168	1.542	3.32	16.723	26.9
	15	-0.903	1.513	3.56	23.857	15.1
	20	-1.509	1.508	3.76	30.480	5.7
	25	-2.076	1.503	-	36.741	-
	30	-2.620	1.488	-	41.144	-
	0.5	4.572	4.730	2.30	4.696	121.5
B. 4. 2. 1. 1. 2	1	3.091	3.364	2.68	5.770	116.1
	2	2.818	3.318	3.46	10.424	107.3
	3	2.956	3.657	4.00	13.908	84.0
	4	2.639	3.545	4.00	13.767	92.8
	5	2.491	3.602	4.00	13.722	93.3
	6	2.340	3.639	4.00	13.693	86.0
	8	1.830	3.524	4.00	14.003	71.0
	10	1.621	3.681	4.00	13.660	66.6
	15	0.365	3.324	4.00	14.181	57.7
	20	-1.152	2.733	4.00	14.948	47.1
	25	-1.764	2.955	4.00	14.478	59.2
	0.5	1.221	1.509	1.84	2.731	70.2
	1	1.140	1.528	2.06	3.725	64.3
B. 4. 2. 1. 1. 3	2	0.994	1.545	2.38	5.349	55.4
	3	0.805	1.558	2.68	7.371	48.6
	4	0.660	1.578	2.82	9.102	41.0
	5	0.505	1.598	3.02	10.974	38.2
	6	0.377	1.630	3.20	12.933	38.1
	7	0.297	1.714	3.36	15.260	36.2
	8	0.231	1.801	3.56	17.766	32.6
	10	0.018	1.924	3.84	23.041	30.4
	15	-0.666	2.104	4.00	19.178	28.7
	20	-1.101	2.471	4.00	15.833	29.7
	30	-2.684	2.391	4.00	16.235	18.3
	0.5	2.487	2.731	2.30	4.187	99.0
	1	3.036	3.373	2.90	7.142	98.7
B. 4. 2. 1. 1. 5	2	4.032	4.515	4.00	13.235	83.0
	3	4.783	5.434	4.00	13.018	77.6
	4	4.052	4.891	4.00	13.147	64.2
	5	3.556	4.576	4.00	13.231	74.1
	6	4.686	5.866	4.00	12.988	70.2
	8	5.574	5.106	4.00	13.094	62.7
	10	3.295	5.169	4.00	13.071	60.3
	12	2.317	4.538	4.00	13.256	52.8
	14	1.060	3.568	4.00	13.673	45.5

where the integration is made over the entire wave surface. Knowing that the equation of the circles being considered is

$$(x + h)^2 + y^2 = r^2$$

it is easy to show that

$$dA = 2 \pi r \, dx \text{ and}$$

$$\int_0^A dA = \int_{x_0}^{x_1} 2 \pi r \, dx$$

or

$$A = 2 \pi r (x_1 - x_0)$$

Substituting above gives

$$\bar{P} = 1/(x_1 - x_0) \int_{x_0}^{x_1} P \, dx$$

When $r \leq 2$ or if $r > 2$ and $h > \sqrt{r^2 - 4}$ this becomes

$$\bar{P} = 1/(r-h) \int_0^x P \, dx$$

and when $r > 2$ and $h < \sqrt{r^2 - 4}$ this becomes

$$\bar{P} = \frac{1}{r - \sqrt{r^2 - 4}} \int_{x_0}^{x_1} P \, dx$$

The value of the integral, $\int P \, dx$ (which is contained in both expressions) was found by numerically integrating the shock-pressure (vs x) data mentioned above for each wave profile and the average pressure found from the values of r , h , x_0 , and x_1 for that profile. These results are also listed in Table 23.

The data in Table 23 represent the desired information on the detailed attenuation process of input shock waves from an axial, end donor. It may also be noted from Table 22 that the critical size of an axial, end donor required to cause detonation in this case is probably between 1.50 and 1.75 in.

(2) Side Donor (Subtask B. 4. 2. 1. 3)

The results of two side donor tests using samples from Batches 1 and 3 are shown in Table 24. The test setup used is shown in Figure 96. The booster was placed one-quarter of the way down the acceptor charge so that enough material would be available to allow the detonation to reach steady state if initiation took place.

In order to have complete interfacial contact between the booster and propellant for this particular geometric arrangement, it was necessary to cut a small flat section on the sample at the booster site. The character of the detonation taking place in these tests is illustrated in Figures 97 and 98 which are framing camera studies of the events. It may be noted that in the first test (where initiation in the axial direction apparently did not take place), the wave front near the bottom of the charge never became flat as was the case in the second test (when axial detonation was apparently initiated). These results indicate that the critical donor size for this donor geometry and location is between 2.0 and 3.0 in. Comparison of Test B. 4. 2. 1. 3. 1 with that of Test B. 4. 2. 1. 1. 2 indicates that donor location is an important parameter in determining if axial initiation takes place in a given instance.

b. Perforated Shapes (Subtask B. 4. 2. 2)

The primary objective of the tests in Subtask B. 4. 2. 2 was to demonstrate how detonation took place when nonaxial, end donors (Subtask B. 4. 2. 2. 2) and side donors (Subtask B. 4. 2. 2. 3) were placed on supercritical, circular-core cylindrical acceptors. A secondary objective in both cases was, as before, to estimate the critical size of the donor required to cause detonation.

Table 24. Demonstration Tests.

Test Number	Acceptor		Booster Diameter (in.)	Result		Instru- mentation*	wp**		sc		fc	
	Outside Diameter (in.)	Inside Diameter (in.)		Result	No-Go		wp/sc	fc	Result	No data	Result	No-Go
B.4.2.1.3.1	4.0	--	2.0	No-Go	No-Go	wp/sc	0	No data	No data	No-Go	No-Go	No-Go
B.4.2.1.3.2	4.0	--	3.0	Go	Go	wp/fc	2S	-	-	-	Go	Go
B.4.2.2.2.1	8.0	3.25	1.75	Go?	Go?	wp/fc	-	-	-	-	Go?	Go?
B.4.2.2.2.2	8.0	3.25	0.75	No-Go	No-Go	wp/fc	0	-	-	-	No-Go	No-Go
B.4.2.2.3.1	8.0	3.25	2.0	No-Go?	No-Go?	wp/fc	0	-	-	-	No data	No data
B.4.2.2.3.2	8.0	3.25	2.0	No-Go	No-Go	wp/fc	0	-	-	-	No-Go	No-Go

*wp = witness plate

sc = streak camera (Beckman and Whitley Model 194)

fc = framing camera (Beckman and Whitley Model 189)

**See Figure 43

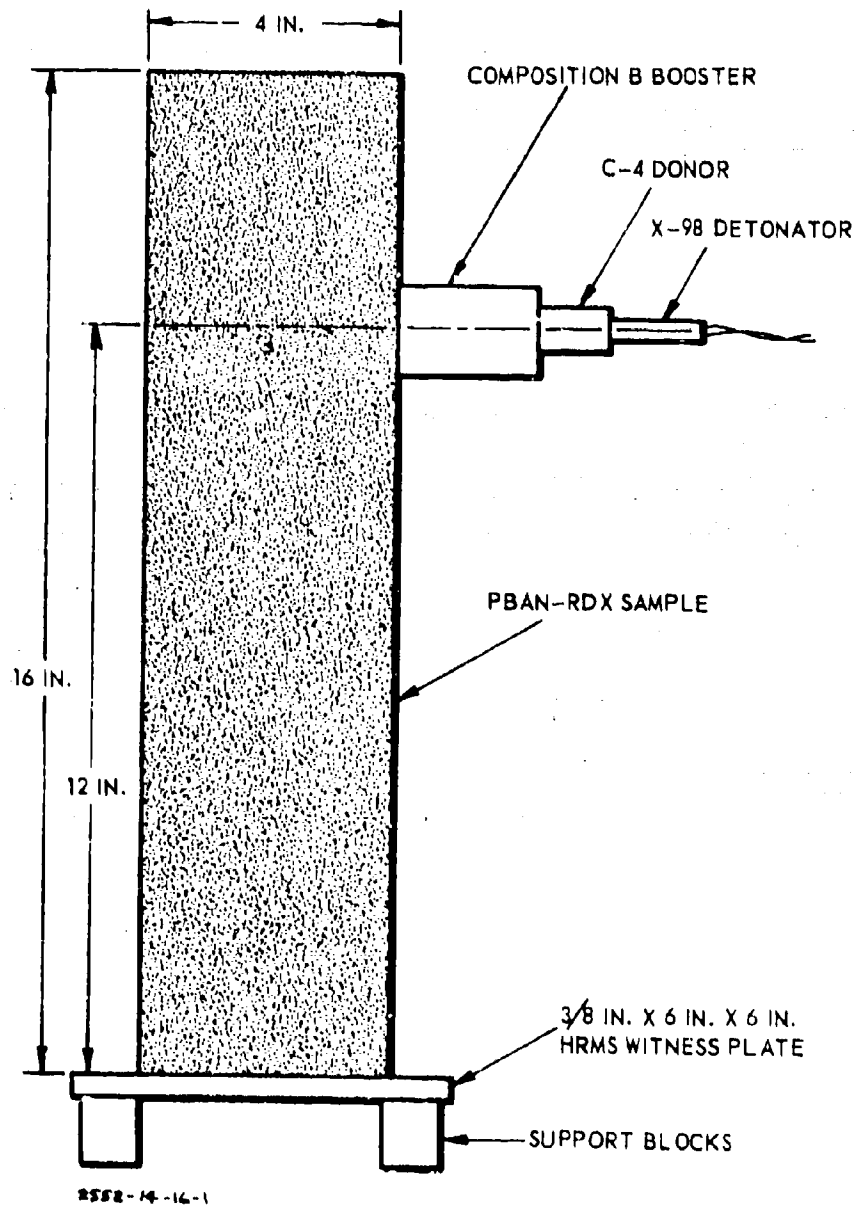


Figure 96. Side Donor Attenuation Test Setup for Nonperforated Acceptor.

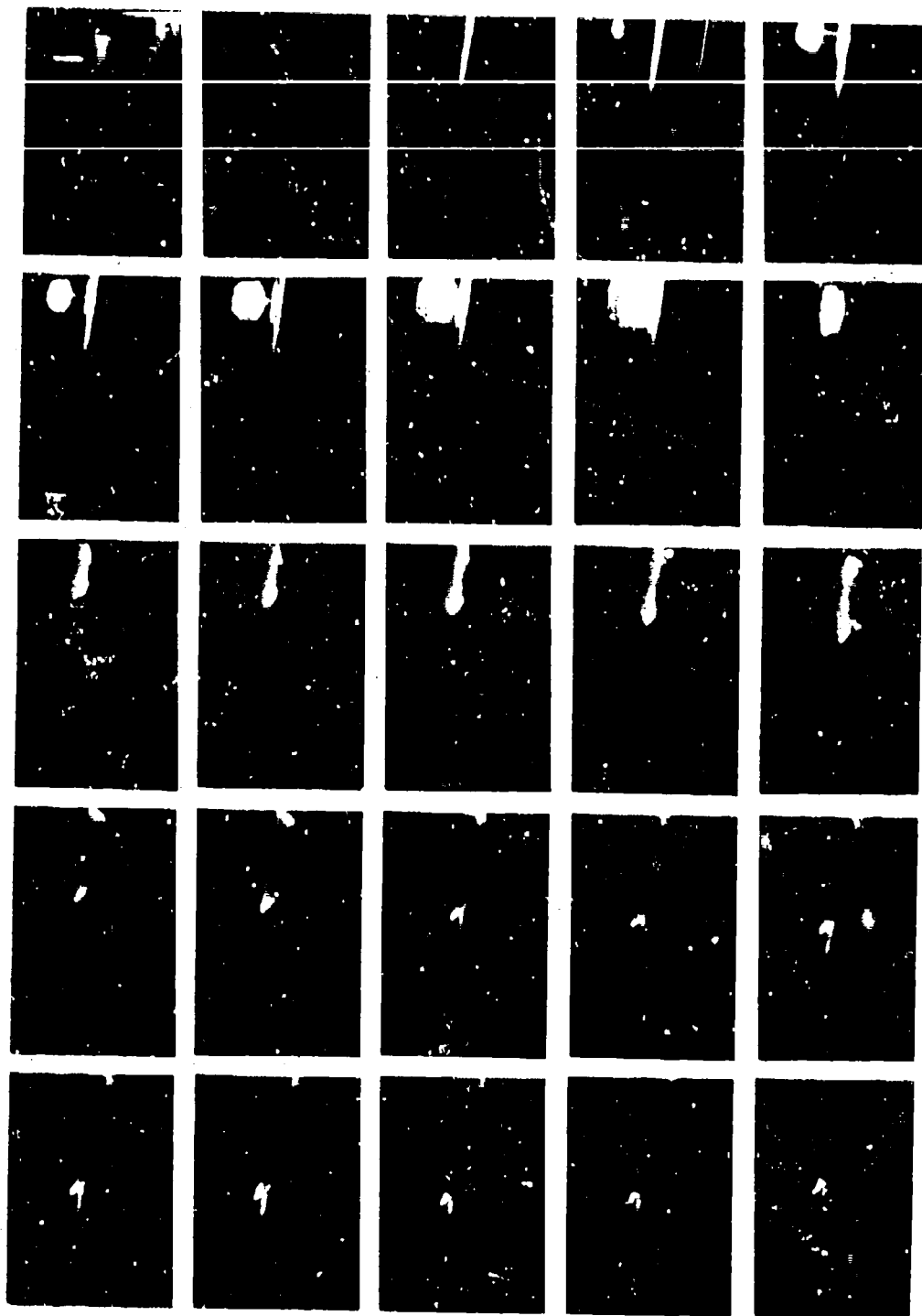


Figure 97. Side Donor Test - Test No. B. 4. 2. 1. 3. 1
(Time Increment = 2.76 μ sec/frame).

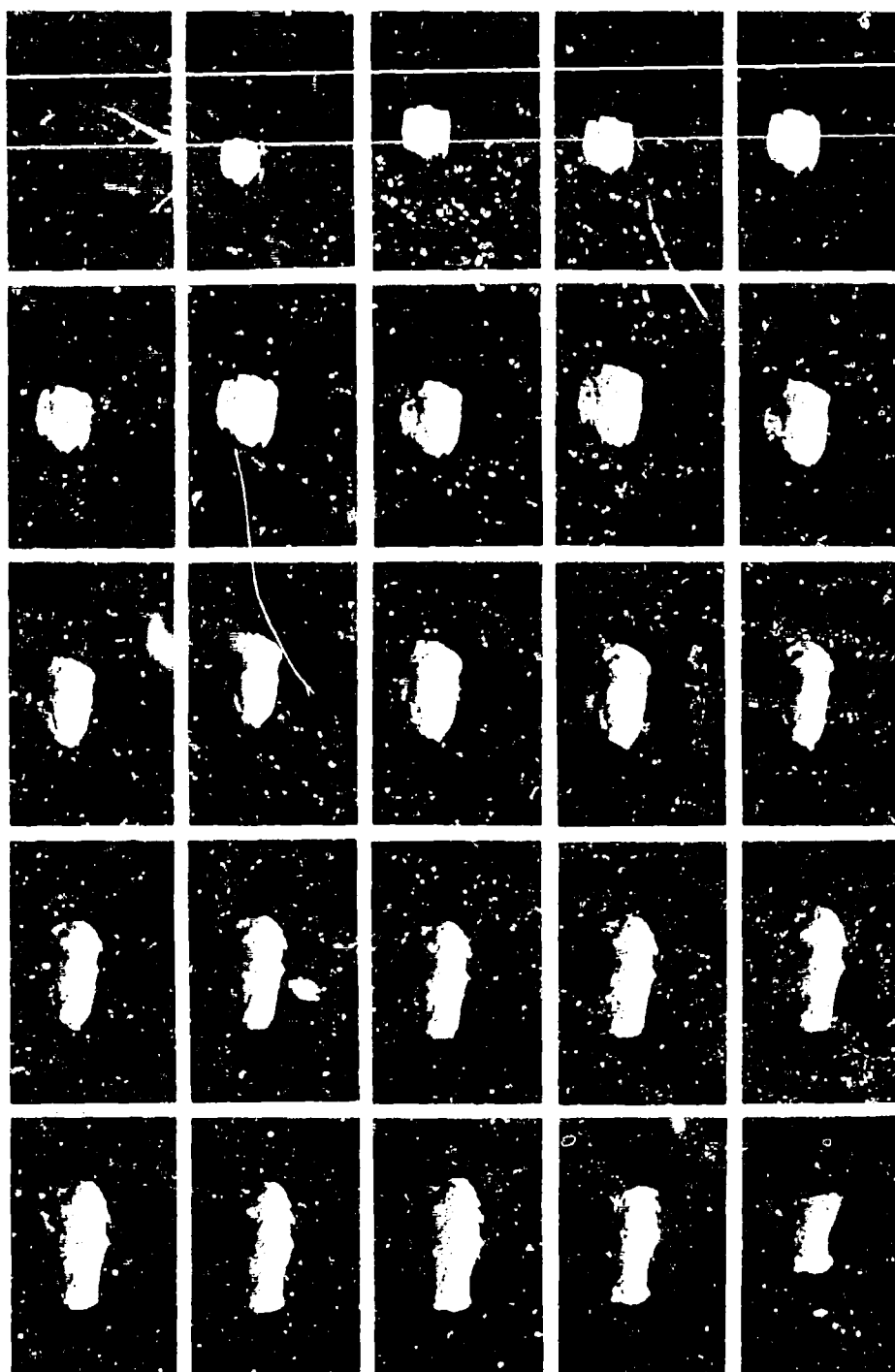


Figure 98. Side Donor Test - Test No. P. 4. 2. 1. 3. 2
(Time Increment = 2.76 μ sec/frame).

(1) Nonaxial, End Donor (Subtask B. 4. 2. 2. 2)

The results of two nonaxial, end donor tests using samples from Batch 2 are shown in Table 24. The test setup is shown in Figure 99. For symmetry, the booster was placed in the center of the web. The character of the detonation taking place is illustrated in Figures 100 and 101 which are framing camera studies of the events. In the first test (Figure 100) when initiation apparently took place, a general consumption of the grain takes place although this occurs in a very nonsymmetrical manner. In Figure 101, it is seen that consumption of the grain does not take place. In both cases, the jet phenomena mentioned earlier is seen to occur. The dark gas cloud in Figure 101 is the expansion of the gases from the Primacord charge used for timing purposes and is not associated with the event. The results in Table 24 indicate that the critical donor size for this donor geometry and location is between 0.75 and 1.75 in. This result compares favorably with that shown in the Subtask B. 4. 2. 1. 1 and is less than that shown in Subtask B. 4. 2. 1. 3.

(2) Side Donor (Subtask B. 4. 2. 2. 3)

The results of two side donor tests using samples from Batch 2 are also shown in Table 24. The test setup is the same as in Figure 96 except that the sample is the larger circular cylinder. Because no framing camera data were obtained in Test B. 4. 2. 2. 3. 1, the test result was considered uncertain and the same test conditions were repeated in Test B. 4. 2. 2. 3. 2. The character of the reaction taking place in this case is illustrated in Figure 102 which is a framing camera record of the event. Careful examination of this record shows that general consumption of the grain does not take place, and axial initiation was assumed not to have taken place. This result suggests that the critical donor size for this donor geometry and location is greater than 2.0 in. This compares favorably with the result in Subtask B. 4. 2. 1. 3 and is, as expected, greater than that in Subtask B. 4. 2. 2. 2.

It can be seen from these tests and those discussed in Section 5. 3. 1. 2. 2(a)(2) that it is more difficult to initiate a charge from the side than from the end and that the magnitudes involved do not depend on whether or not the acceptor charge is perforated.

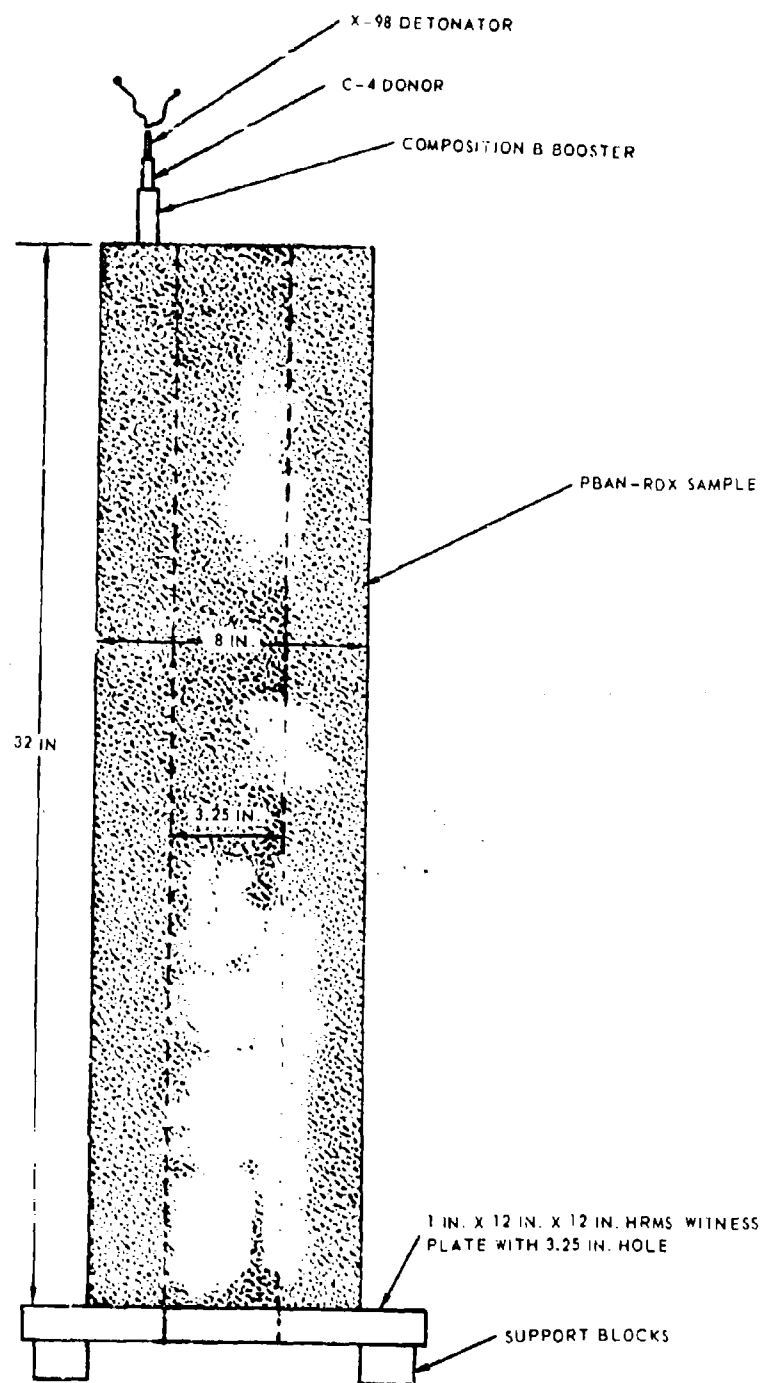


Figure 99. Nonaxial End Donor Attenuation Test Setup
for Perforated Acceptor.

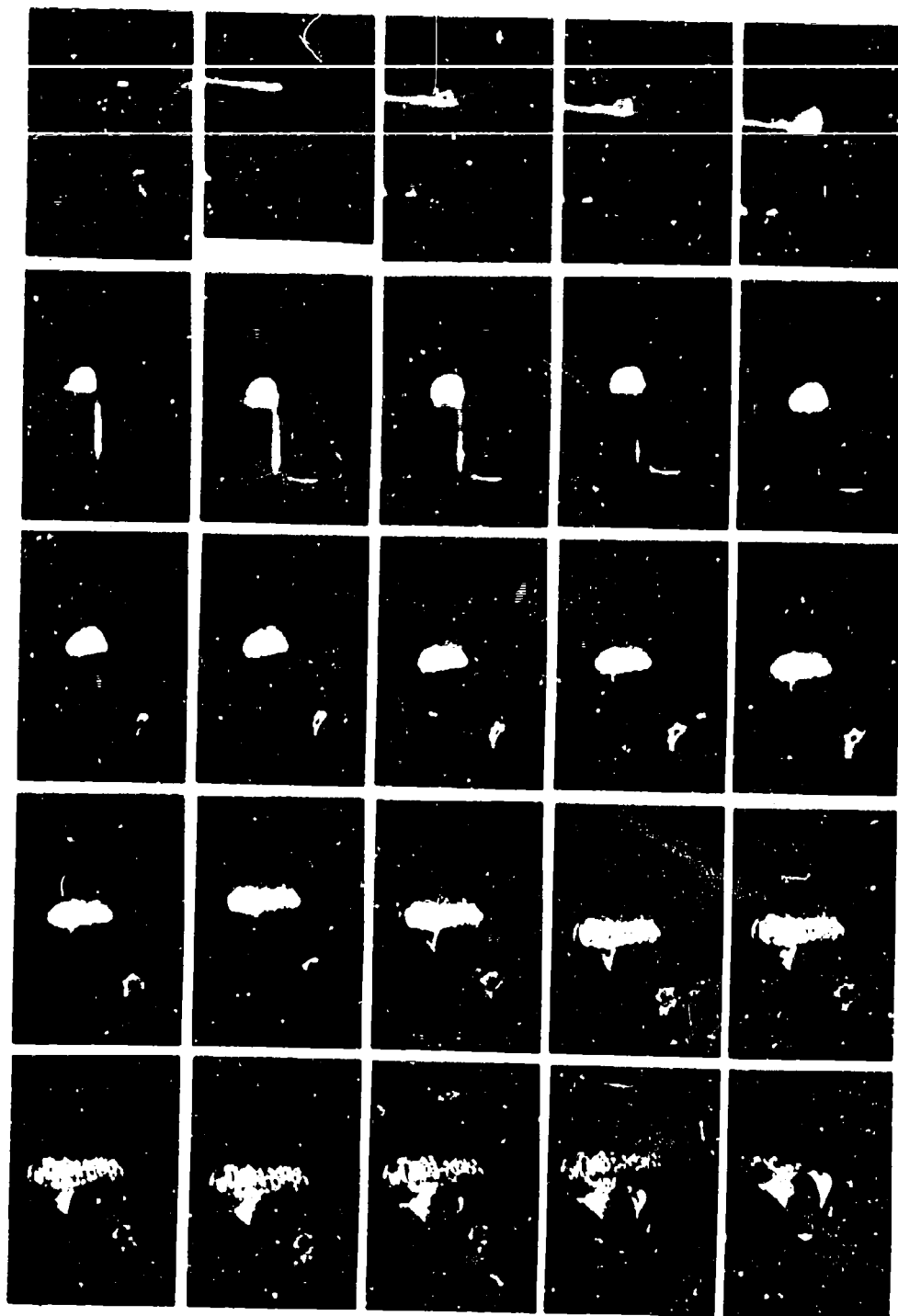


Figure 100. Nonaxial, End Donor Test - Hollow Core Acceptor -
Test No. B.4. 2. 2. 2. 1 (Time Increment = 8.4 μ sec/frame).

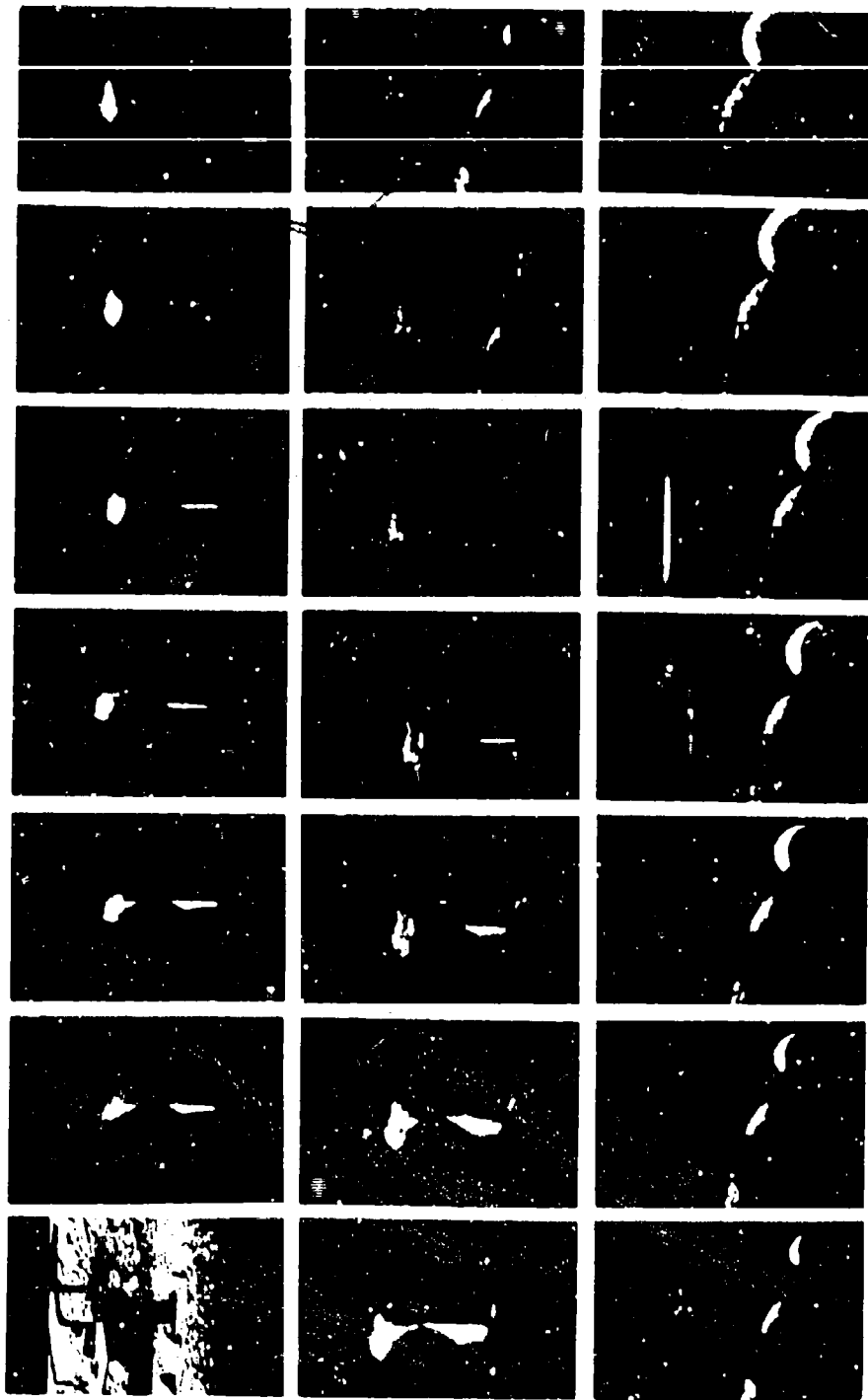


Figure 101. Nonaxial, End Donor Test - Hollow Core Acceptor -
Test No. B.4.2.2.2 (Time increment 8.4 μ sec/frame).

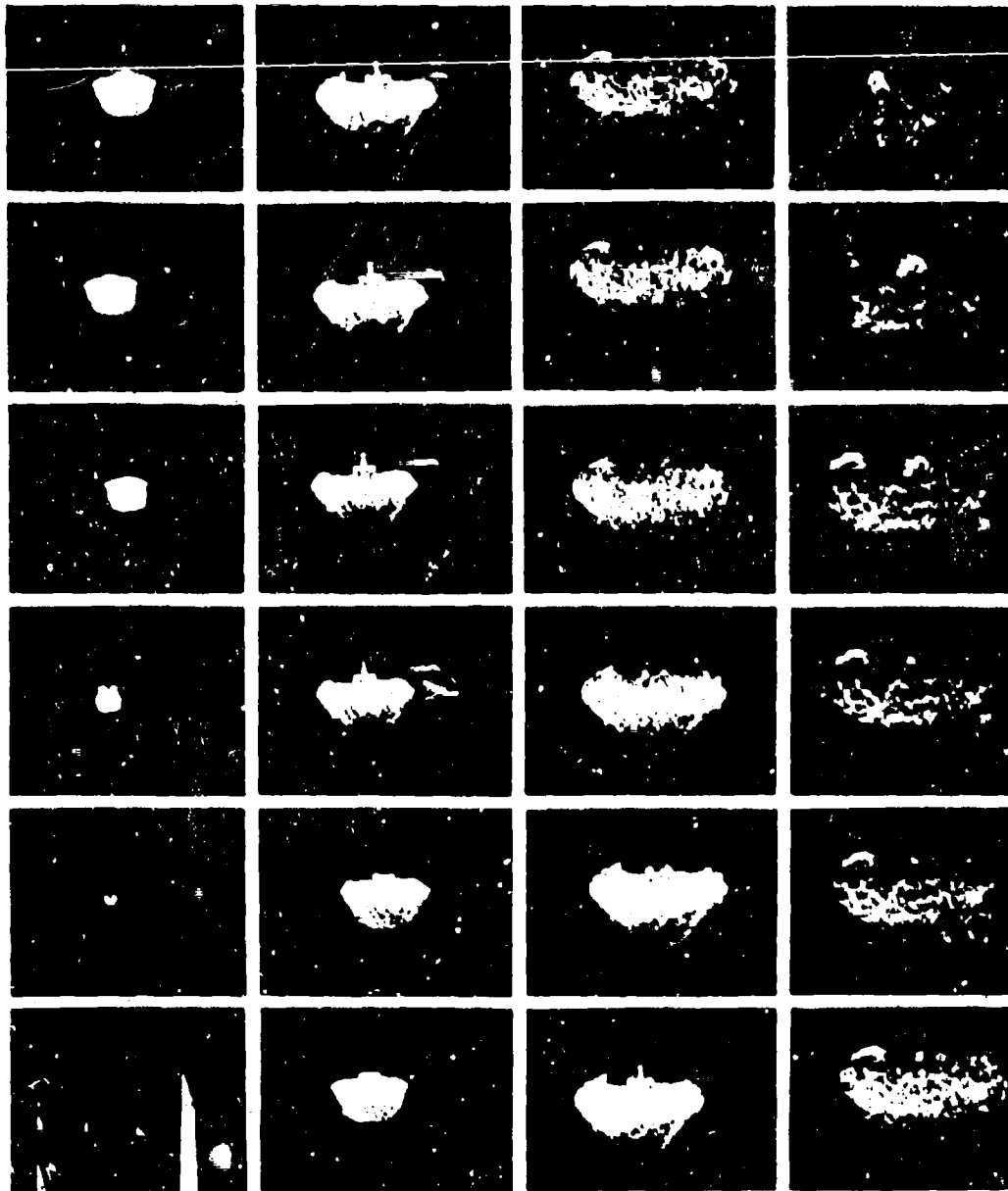


Figure 102. Side Donor Test - Hollow Core Acceptor -
Test No. B.4.2.2.3.2 (Time Increment = 8.4 μ sec/frame).

5.3.1.2.3 Summary of the Initiation of Detonation Tests

The major objective of the initiation of detonation studies (Subtask B.4) is to determine if the measured initiation criterion (Subtask B.4.1.d) can be used to predict whether or not shock initiation will take place for a given booster, based on how the input shock wave attenuates (Subtask B.4.2). As the initiation criterion and attenuation properties have been determined in Sections 5.3.1.2.1.d and 5.3.1.2.2.a, the applicability of the criterion can be tested at least for axial, end donor charges on nonperforated cylindrical acceptors. That is, it may be determined whether for this situation when detonation occurs, the initiation criterion is met or not. This was done by plotting the \bar{P} vs d data in Table 23, on the P^+ vs d initiation criterion shown in Figure 84. Since the criterion might also be defined in terms of wave area the analysis was also done by plotting the \bar{P} vs A data, in Table 23, on the P^+ vs A initiation criterion shown in Figure 85. These analyses are shown in Figures 103 and 104. Figure 103 and Table 22 show that in those tests where initiation took place (B.4.2.1.1.2 and B.4.2.1.1.5) the initiation criterion was met (i.e., the Go-region was entered) whereas for those tests where initiation did not take place (B.4.2.1.1.1 and B.4.2.1.1.3) the input shock pressure attenuation curve was such that the criterion was not met. This indicates that, at least for the situations considered, the criterion as measured (P^+ vs d) can be used to predict whether initiation will take place or not for axial, end donors on nonperforated supercritical acceptors. Also in Table 22, the average radius of curvature of the input waves is larger when initiation took place than when it didn't (3 to 5 in. compared to 0.5 to 2.5 in.). Consideration of Figure 104 shows that the criterion in terms of area did not predict the result correctly for Test B.4.2.1.1.1. The attenuation curve does intersect the initiation criterion (at about 70.5 Kbar) although no detonation took place in this test. However, it is noteworthy that the attenuation continues through the criterion, emerges below it at $A = 9.5 \text{ in.}^2$, and stays below it for the remainder of its path. Since it is not expected that in this situation such a path is possible (i.e., entering and then leaving the Go-region) it implies that the criterion should be shifted to the right or the attenuation curves to the left (as is shown in Figure 103). The results of the other three tests do conform to the criterion in Figure 104. From these tests, it was tentatively concluded that the criterion in terms of wave diameter is more accurate in predicting initiation of detonation than the criterion in terms of wave area.

It may also be noted that the results with axial, end donors show that for this geometry the donor diameter need not be equal to or greater than the critical diameter of the acceptor in order for initiation to take place. In fact, in this case, the required diameter, 1.50 to 1.75 in. is only from 54 to 66% of the critical diameter, 2.66 to 2.80 in.

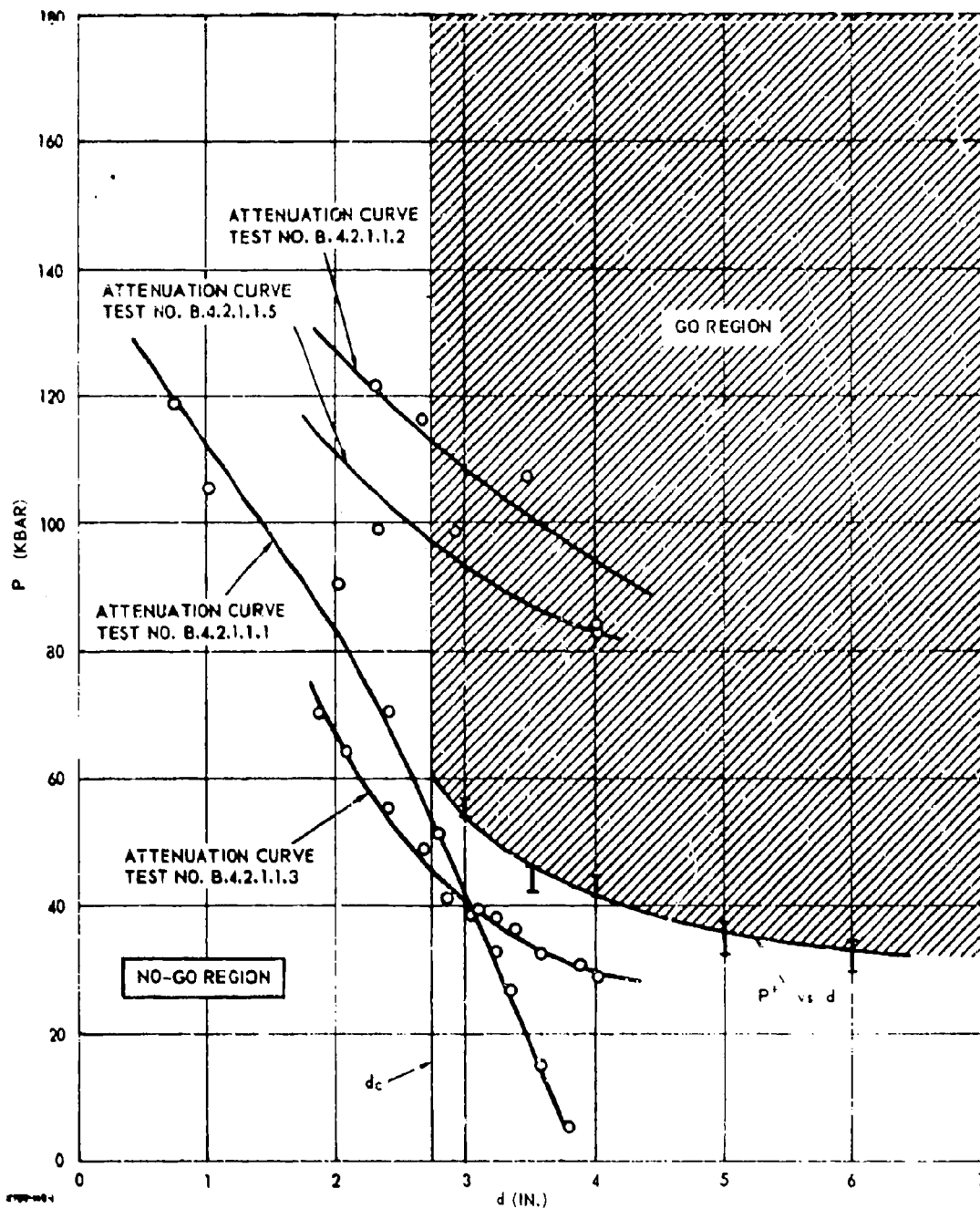


Figure 103. Test of Initiation Criterion.

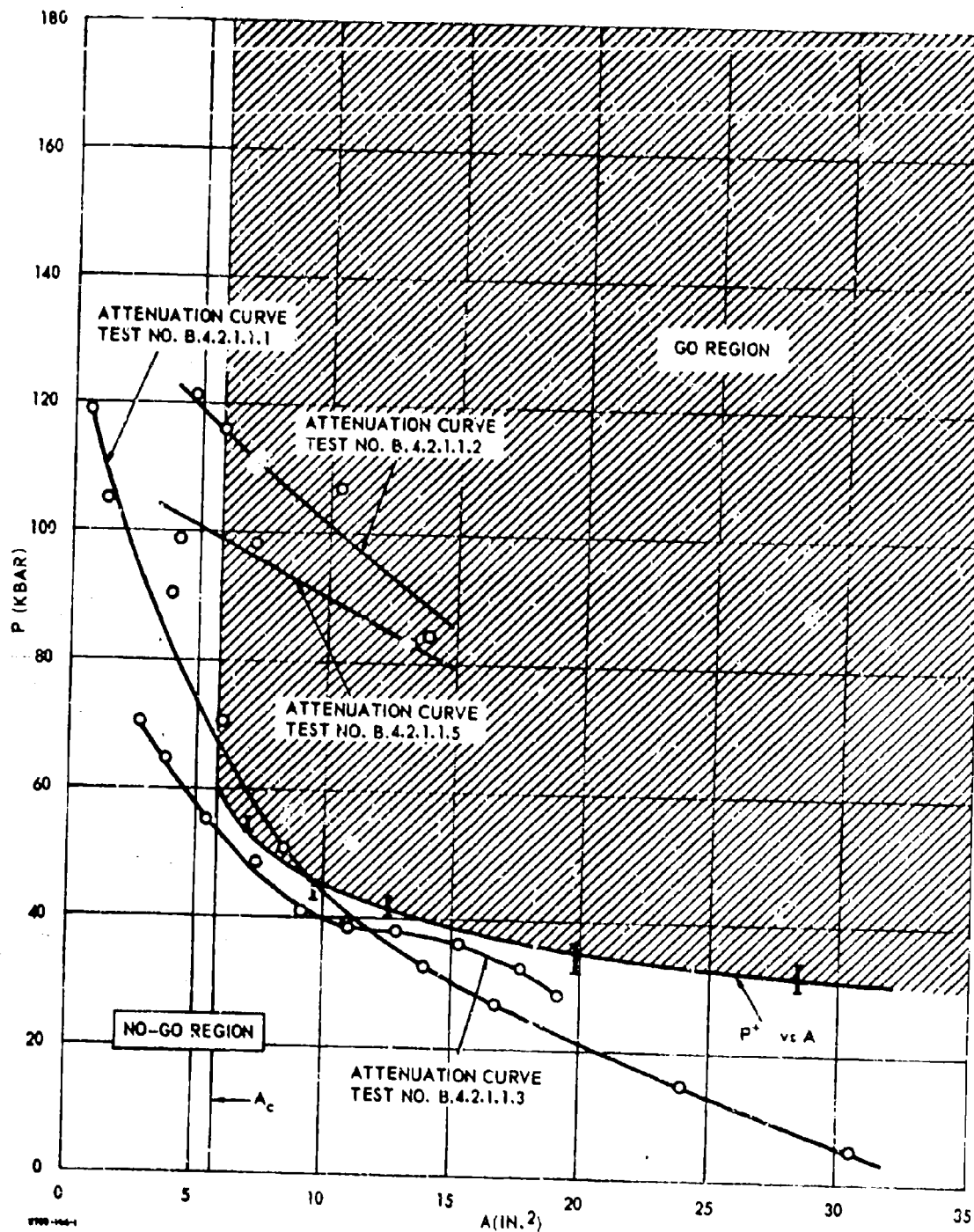


Figure 104. Test of Initiation Criterion.

5.3.2 Theoretical Studies

An outline of the test plan of the theoretical program is shown in Table 2. The major objectives of this program were to evaluate the validity of the underlying assumption of the current theory of critical geometry and to consider the importance of additional system parameters.

5.3.2.1 Sustainment of Detonation (Subtask B.5)

In the sustainment theory of critical geometry, the critical dimensions of any shape depend on geometry and the critical diameter for the given material. From results obtained in the present study, the validity of the assumptions underlying this theory were investigated.

5.3.2.1.1 Assumption of Equal Critical Detonation Velocities (Subtask B.5.1)

One of the major assumptions underlying the current theory of critical geometry is that all shapes (for a particular formulation) should have the same detonation velocity at the critical dimensions of that shape (Appendix A). This was investigated by plotting the observed detonation velocity for all Go tests (for both RDX-wax and PBAN-RDX explosive) vs charge dimension and extrapolating to the critical dimension. The data are shown in Tables 26 and 27, and the extrapolated results in Table 28. Although the data for RDX-wax explosive were widely scattered, the results for Batch 6 material showed only a 3% variation in the estimated critical velocities. The variation was higher (~14%) for Batch 4 material but still within experimental (and extrapolation) error. Within the limits of the extrapolations, it was concluded that the assumption was not contradicted by the RDX-wax results. The more accurate detonation velocity data from the PBAN-RDX tests agreed within about 12% for all the charges. Because this is within the experimental (and extrapolation) error for these data it was concluded that there was no evidence that the critical detonation velocity varied from shape to shape.

5.3.2.1.2 Assumption of a General Criterion (Subtask B.5.2)

Another major assumption of the theory is that if there is a criterion for sustainment of detonation for any given shape it might be assumed that there is a general criterion for all shapes (Appendix A). This was investigated when an attempt was made to correlate the summarized critical

Table.25. Theoretical Program Outline.

B. 5 Sustainment of Detonation

B. 5. 1 Assumption of Equal Critical Detonation Velocities

B. 5. 2 Assumption of a General Criterion

B. 5. 3 Interactions

B. 5. 4 Explosive Properties

B. 5. 4. 1 Composition

B. 5. 4. 2 Particle Size

B. 5. 4. 3 Density

B. 5. 4. 4 Temperature

B. 5. 5 Confinement

B. 6 Initiation of Detonation

B. 6. 1 Initiation Criterion

B. 6. 1. 1 Pulse Duration

B. 6. 1. 2 Pulse Shape


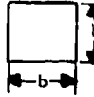
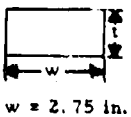

B. 6. 1. 3 Distribution of Parameters

B. 6. 2 Attenuation Properties

B. 6. 2. 1 Local Reaction

B. 6. 2. 2 Detonation Cut-off.

Table 26. Detonation Velocity vs Dimension RDX-Wax.

Charge Shape	Charge Dimension (in.)	Batch Number	Charge Density (gm/cc)	Velocity Range	Average Detonation Velocity (mm/ μ sec)	Standard Deviation (\pm mm/ μ sec)	Test Number
	1.75	3	1.06	1.5 - 2.5	4.57	0.14	B.2.1.1.7
	1.97	3	1.05	1.5 - 3.75	4.69	0.06	B.2.1.1.12
	1.961	3	1.05	1.5 - 3.5	4.29	0.25	B.2.1.1.13
	1.25	2	1.13	2.0 - 3.75	6.65	0.24	B.2.1.1.15
	1.998	4	1.06	2.0 - 4.25	4.65	0.30	B.2.1.1.16
	1.758	4	1.06	1.25 - 3.25	4.28	0.29	B.2.1.1.18
	1.88	4	1.05	—	—	—	B.2.1.1.23
	1.75	4	1.06	—	—	—	B.2.1.1.24
	1.63	5	1.11	0.75 - 4.0	6.11	0.54	B.2.1.1.26
	1.63	6	1.11	0.5 - 2.5	6.52	0.07	B.2.1.1.32
	1.50	6	1.08	0.5 - 4.25	6.13	0.41	B.2.1.1.33
	1.63	6	1.11	0.5 - 2.75	6.64	0.14	B.2.1.1.37
	1.75	6	1.10	0.5 - 2.25	6.57	0.05	B.2.1.1.38
	1.75	6	1.10	0.5 - 2.75	6.50	0.09	B.2.1.1.39
	1.63	4	1.06	1.25 - 3.0	5.07	0.29	B.2.1.2.1
	1.88	4	1.06	—	—	—	B.2.1.2.2
	1.63	4	1.07	1.75 - 4.0	5.51	0.12	B.2.1.2.3
	1.5	4	1.07	1.5 - 3.5	5.07	0.07	B.2.1.2.4
	1.38	4	1.08	1.5 - 3.5	5.07	0.14	B.2.1.2.8
	1.5	4	1.07	—	—	—	B.2.1.2.9
	1.38	6	1.08	0.75 - 3.75	6.25	0.50	B.2.1.2.13
	1.5	6	1.10	0.75 - 3.25	6.16	0.21	B.2.1.2.14
	1.25	6	1.10	0.25 - 3.0	6.33	0.07	B.2.1.2.15
	1.25	6	1.10	0.75 - 1.75	5.69	0.11	B.2.1.2.16
	1.38	6	1.08	—	—	—	B.2.1.3.1
	1.38	6	1.05	1.0 - 3.5	6.88	0.07	B.2.1.3.2
	1.31	6	1.12	1.75 - 3.75	6.84	0.13	B.2.1.3.3
	1.31	6	1.10	1.5 - 3.5	6.58	0.08	B.2.1.3.4
	1.25	6	1.09	1.5 - 3.75	6.67	0.11	B.2.1.3.5
	1.19	6	1.11	1.5 - 4.0	6.62	0.13	B.2.1.3.6
	1.13	6	1.08	1.75 - 3.5	6.44	0.09	B.2.1.3.7
	1.0	6	1.09	2.0 - 3.75	6.75	0.16	B.2.1.3.8
	2.5	6	1.09	0.75 - 1.75	6.14	0.18	B.2.1.4.1
	2.75	6	1.09	0.5 - 2.75	5.97	0.49	B.2.1.4.2
	3.0	6	1.08	0.75 - 1.5	4.82	0.52	B.2.1.4.3
	2.63	6	1.03	1.5 - 2.25	7.59	0.07	B.2.2.1.1
	2.63	6	1.07	1.0 - 1.5	6.63	0.02	B.2.2.1.2
	2.5	6	1.09	0.25 - 2.0	6.32	0.04	B.2.2.1.3

 $d_1 = 0.81$ in.

Table 27. Detonation Velocity vs Dimension - PBAN-RDX.


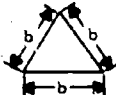


Charge Shape	Charge Dimension (in.)	Batch Number	Charge Density (gm/cc)	sc Velocity Range	ro Velocity Range	Velocity Based On	Average Detonation Velocity (mm/μsec)	Standard Deviation (mm/μsec)	Test Number
	2.88	1	-	-	-	-	-	-	B.3.1.1.1
	2.80	1	1.720	-	-	-	-	-	B.3.1.1.3
	2.67	1	1.720	-	-	-	-	-	B.3.1.1.4
	2.75	1	1.716	2.0-4.0	2.0-4.0	sc/ro	4.19	0.06	B.3.1.1.6
	2.85	1	1.721	1.75-3.25	1.75-3.25	sc	4.39	0.13	B.3.1.1.11
	2.88	1	1.724	2.0-3.75	2.0-3.75	ro	4.25	0.02	B.3.1.1.12
	2.74	1	1.721	2.25-3.75	2.25-3.75	sc/ro	4.08	0.11	B.3.1.1.18
	2.75	2	1.728	2.0-4.0	2.0-4.0	ro	4.32	0.08	B.3.1.1.15
	2.70	3	1.731	2.5-3.75	2.0-4.0	ro	3.97	0.04	D.3.1.1.16
	2.82	3	1.728	2.5-3.50	2.5-3.50	sc/ro	4.14	0.17	B.3.1.1.17
	3.0	1	1.723	-	1.0-3.5	ro	4.29	0.12	B.4.1.9
	3.0	1	1.729	-	1.0-3.5	ro	4.24	0.08	B.4.1.18
	3.5	3	1.721	-	0.25-3.5	ro	4.43	0.08	B.4.1.8
	3.5	3	1.728	-	0.6-3.75	ro	4.42	0.11	B.4.1.14
	3.5	3	1.725	-	0.5-3.5	ro	4.39	0.09	B.4.1.25
	4.0	1	1.728	1.0-2.0	0.5-3.5	sc/ro	4.47	0.12	B.4.1.2
	4.0	1	1.726	1.0-3.0	0.5-3.75	sc/ro	4.49	0.21	B.4.1.4
	4.0	1	1.726	0.75-2.5	1.25-3.75	sc/ro	4.54	0.16	B.4.1.6
	5.0	1	1.726	-	1.25-3.0	ro	4.51	0.04	B.4.1.10
	5.0	1	1.727	-	1.25-3.25	ro	4.54	0.04	B.4.1.30
5.0	3	1.721	-	0.5-3.75	ro	4.57	0.09	B.4.1.13	
5.0	3	1.729	-	1.0-3.25	ro	4.61	0.07	B.4.1.24	
6.0	1	1.724	-	0.75-3.5	ro	4.58	0.07	B.4.1.11	
6.0	3	1.727	-	1.0-4.0	ro	4.65	0.06	B.4.1.12	
6.0	3	1.729	-	1.5-3.25	ro	4.80	0.15	B.4.1.19	
	4.95	2	1.726	1.0-3.0	1.0-3.0	ro	4.40	0.18	B.3.1.3.1
	4.45	2	1.726	1.5-3.75	1.5-3.75	ro	4.37	0.14	B.3.1.3.3
	4.5	2	1.731	1.5-3.75	1.5-3.75	ro	4.39	0.10	B.3.1.3.6
	4.33	3	1.720	0.75-1.4	0.75-1.4	sc	4.42	0.05	B.3.2.1.2
	4.02	3	1.728	1.0-1.25	1.0-1.25	ro	4.12	0.00	B.3.2.1.3
$d_i = 1.50$ in.									
	4.00	3	1.728	1.0-2.0	1.0-2.0	sc	4.09	0.01	B.3.2.2.1
	4.49	3	1.722	1.25-3.75	1.25-3.75	ro	4.53	0.14	B.3.2.2.4
$l = 0.475$ in.									

Table 28. Critical Detonation Velocities.

Explosive	Shape	Batch	Estimated Critical Detonation Velocity (mm/ μ sec)
RDX-Wax	Cylinder	3 and 4	4.2
		5 and 6	6.1
	Square	4	5.0
		6	5.9
	Rectangle	6	< 6.3
	Equilateral Triangle	6	< 6.0
PBAN-RDX	Circular-Core Cylinder	6	6.0
	Cylinder	1, 2, and 3	4.0
	Equilateral Triangle	2	4.1
	Circular-Core Cylinder	3	3.8
	Cross-Core Cylinder	3	3.9

geometry results in Table 9 for RDX-wax and in Table 16 for PBAN-RDX. Comparison of equivalent diameters for Batch 4 and 8 material for RDX-wax showed that the correlation was weak and therefore a general criterion had not been found.

As these data were not considered very accurate, the PBAN-RDX results were used in an attempt to more accurately assess the evidence of correlation. In this case, the equivalent diameter for all the shapes was in agreement to within 5% thereby suggesting that this correlation was valid. It may be tentatively concluded that, within the limitations of the shapes considered, a general criterion in the form of the original theory may be considered to exist, if the critical diameter is replaced by the "equivalent diameter."

5.3.2.1.3 Interactions

The effects of interactions in the core of perforated shapes was ignored in the original theory of critical geometry. The validity of this may be investigated by studying the results of the critical geometry tests summarized in Tables 16 and 17. In Table 16 the result for RDX-wax circular core cylinders is unclear; the result is opposite to that expected (i. e., only if interactions increased the rate at which rarefaction waves move in, would an increase in the critical dimension over theory be expected). Again because of the lack of precision in the RDX-wax results, consideration of the PBAN-RDX results (Table 17) seemed advisable. In this case, the low value of the equivalent diameter for circular-core cylinders implied interaction effects but the higher value for the cross-core cylinders conflicted with this since more interaction was expected in the latter case than in the former. It was therefore tentatively concluded that for the core sizes considered in these tests, the effects of interactions on the critical dimensions was small.

5.3.2.1.4 Explosive Properties (Subtask B. 5. 4)

The effects of variations in composition (Subtask B. 5. 4. 1), particle size (Subtask B. 5. 4. 2), density (Subtask B. 5. 4. 3) and initial temperature (Subtask B. 5. 4. 3) on the current theory of critical geometry were not specifically studied in this program but it is expected that they would mainly effect only critical (and/or "equivalent") diameter. These effects, not including initial temperature, were considered (theoretically) in the critical diameter portion of the program (Section 4. 4). The effects of confinement on the critical geometry theory also have not been studied in the current program. Because this consideration is complex, no definitive or expected effects can be anticipated without experimental data.

5.3.2.2 Initiation of Detonation (Subtask B. 6)

In the initiation of detonation theory of critical geometry, the phenomenon of initiation depends only on an initiation criterion for the given material and the way in which the input wave attenuates. The effects of parameters other than those considered in the present study are discussed below.

5.3.2.2.1 Initiation Criterion (Subtask B. 6. 1)

In the development of the initiation criterion the effects of pulse duration (Subtask B. 6. 1. 1), pulse shape (Subtask B. 6. 1. 2) and the possible use of distributed parameters (Subtask B. 6. 1. 2) might be considered. However, in developing the initiation criterion in this study (Figures 84 and 95) only peak pressure was used. Although no direct evidence of the necessity to consider these additional effects exists in the successful results obtained (Figure 103), it is possible that a more clear-cut result (Figure 64) would have been obtained if a pressure averaged over the pulse duration were considered. Because no data were obtained the effects of variations in pulse width and shape could not be determined at this time and the need for distributed parameters is not evident.

5.3.2.2.2 Attenuation Properties (Subtask B. 6. 2)

In consideration of the attenuation properties the effects of local reaction (Subtask B. 6. 2. 1) and possible detonation cut-off (Subtask B. 6. 2. 2) might be considered. In the attenuation curves of Figures 103 and 104 the effects of local reaction can be seen because in the two "Go" tests the slopes of the curves are much lower even in the "No-Go" region (i. e. , local reaction is supporting the waves). It is clear that this must occur because the diameter (or area) for the same shock pressure is larger in these cases, thereby causing more total reaction to take place. It is concluded that the amount of local reaction and its effect on the attenuation of the input shockwaves depended strongly on the initial diameter (or area) of the input wave. Since no specific results of the studies of Shock Hydrodynamics, Inc. applicable to these materials had been obtained a more detailed examination of local reaction could not be made. Because detonation cut-off was expected with nonsymmetric initiation geometries (such as in Figures 97, 98, 101, and 102) and no specific attenuation data were obtained in these cases, the possible effects could not be determined. Note, however, that this phenomenon might have caused the No-Go results in Tests B. 4. 2. 1. 3. 1 and B. 4. 2. 2. 3. 2. It should also be noted that no significance to the results in Figure 104 should be attached to the concept of detonation cut-off since no evidence of an approach to steady detonation was evident in the attenuation curve.

5.3.3 Test Development

In order to help obtain data having maximum possible accuracy, the following tests, improvements, and suggestions were made.

5.3.3.1 Preliminary Tests - RDX-Wax Explosive (Subtask B.1)

The objectives of the preliminary tests are:

- a. To observe detonation in Composition B and RDX-wax charges using a framing camera and to determine a general comparison between the two (Subtask B.1.a).
- b. To check detonation velocity techniques on Composition B charges for correctness, agreement, and technique (Subtask B.1.b).
- c. To determine if a streak camera (and/or pinswitches) can be used to measure detonation velocity in RDX-wax charges with and without external lighting (Subtask B.1.c).
- d. To determine if the witness plate criterion for detonation is accurate by comparing detonation velocity vs dent reproducibility within a batch and from batch to batch (Subtask B.1.d).

The results of 22 tests using samples from two batches of RDX-wax explosive, are shown in Table 29. The dent type is determined from the test result classification scheme shown in Figure 43.

5.3.3.1.1 Subtask B.1.a

Using the test setup shown in Figure 44, the detonations of Composition B and RDX-wax charges were observed with a framing camera in Tests B.1.a.1 through B.1.a.13. The results are shown in Table 29 and in Figures 105 through 109 which are the framing camera records for some of the tests. It was found that, for the explosive samples, lighting was necessary if the detonation was to be clearly recorded by the high speed camera (compare Figures 105 and 106 with Figures 107 and 108). Further, comparison of the explosive charges (Figure 105 with Figures 106, 107, and 108) showed general similarities except that the detonation products of the RDX-wax charges were of relatively low luminosity.

Table 29. Preliminary Tests - RDX-Wax.

Test Number	Charge Diameter (in.)	Batch Number*	Charge Density (gm/cc)	Result	Instru-mentation**	wp Result***	sc Result	ro Result	fc Result	Comments
B.1.a.1	1.25	-	1.66	Go	wp/ic	4	-	-	7.53	Composition B
B.1.a.2	1.25	-	1.68	Go	wp/ic	4	-	-	7.64	Composition B
B.1.a.3	1.25	1	1.11	Go	wp/ic	1	-	-	6.54	
B.1.a.4	1.5	1	1.12	Go	wp/ic	1	-	-	6.34	
B.1.a.5	1.75	1	1.14	Go	wp/ic	3	-	-	6.73	
B.1.a.6	1.75	1	1.13	Go	wp/ic	3	-	-	6.63	
B.1.a.7	1.5	1	1.12	Go	wp/ic	2S	-	-	6.19	
B.1.a.8	1.25	1	1.11	Go	wp/ic	2	-	-	6.67	
B.1.a.9	1.0	2	1.12	Go	wp/ic	2S	-	-	6.35	
B.1.a.10	1.25	2	1.13	Go	wp/ic	2S	-	-	6.53	
B.1.a.11	1.5	-	1.0	No-Go	wp/ic	0	-	-	-	Paraffin
B.1.a.12	0.75	-	<1.0	No-Go	wp/ic	0	-	-	-	Paraffin
B.1.a.13	0.75	2	1.11	Go	wp/ic	2S	-	-	5.53	
B.1.b.1	1.5	-	1.69	Go	wp/sc/ro	4	7.86	8.30	-	Composition B
B.1.b.2	1.5	-	1.70	Go	wp/sc/ro	4	7.92	8.20	-	Composition B
B.1.c.1	1.75	1	1.13	Go	wp/sc/ro	1S	-	6.41	-	
B.1.c.2	1.75	1	1.14	Go	wp/sc/ro	2S-3	7.13	6.43	-	
B.1.c.3	1.75	1	1.13	Go	wp/sc/ro	1S	7.19	6.29	-	
B.1.c.4	0.742	2	1.05	No-Go	wp/sc/ro	0	-	-	-	
B.1.c.5	1.011	2	1.11	Go	wp/sc/ro	2S	6.42	6.54	-	
B.1.d.1	1.75	2	1.11	Go?	wp	3	-	-	-	
B.1.d.2	1.5	2	<1.00	No-Go?	wp	0	-	-	-	

* Batches 1 and 2 contain 31.5% RDX.

** wp = witness plate

fc = framing camera (Beckman and Whitley Model 189)

sc = streak camera (Beckman and Whitley Model 194)

ro = rasterscillograph (Moran and Polaroid)

*** see Figure 43.

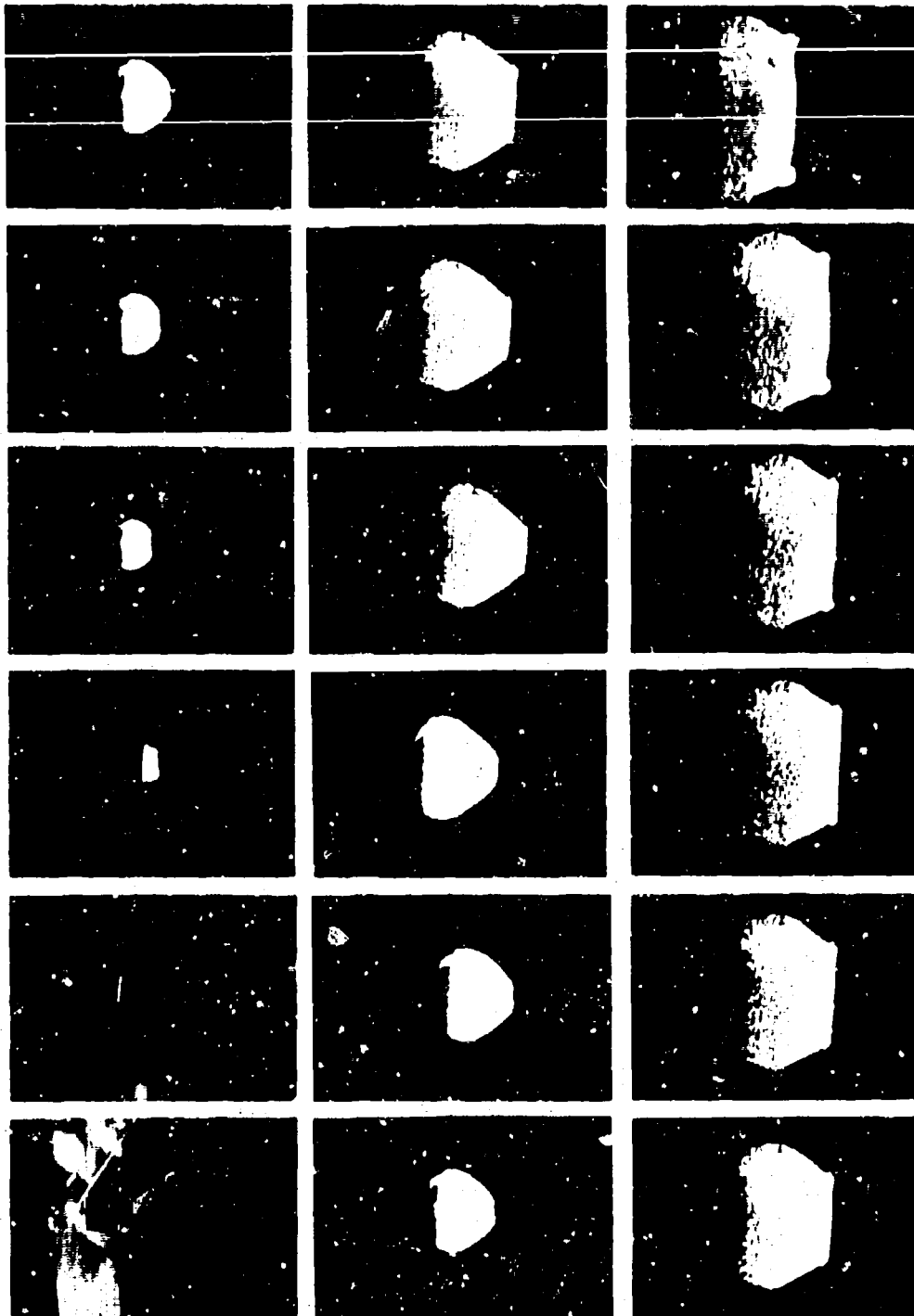


Figure 105. Detonation of Composition B Charge - Test No. B.1.a.2
(Time Increment = 1.4 μ sec/frame).

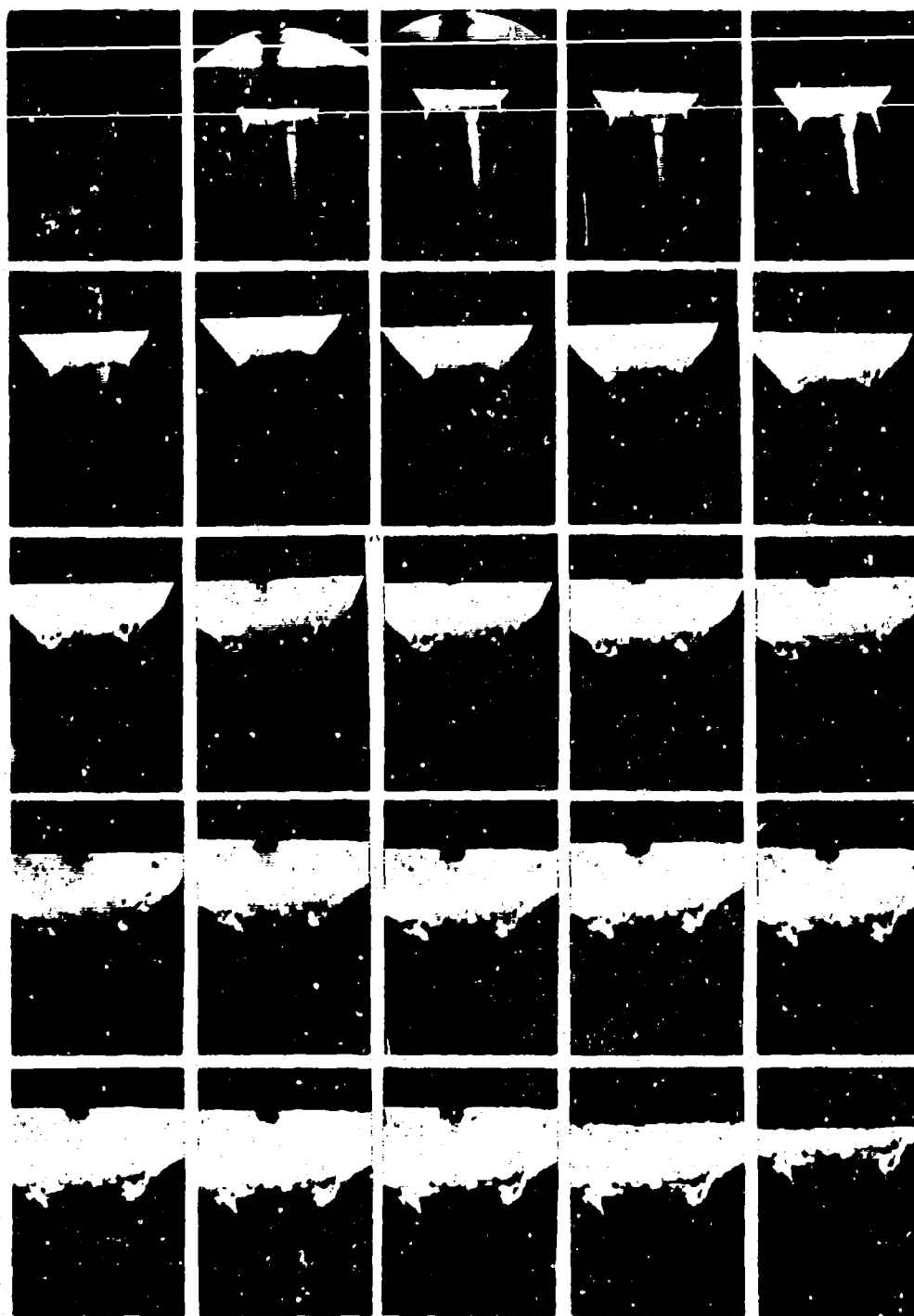


Figure 106. Detonation of RDX-Wax Charge - Test No. B. 1. a. 5
(Time Increment = 1.4 μ sec/frame).

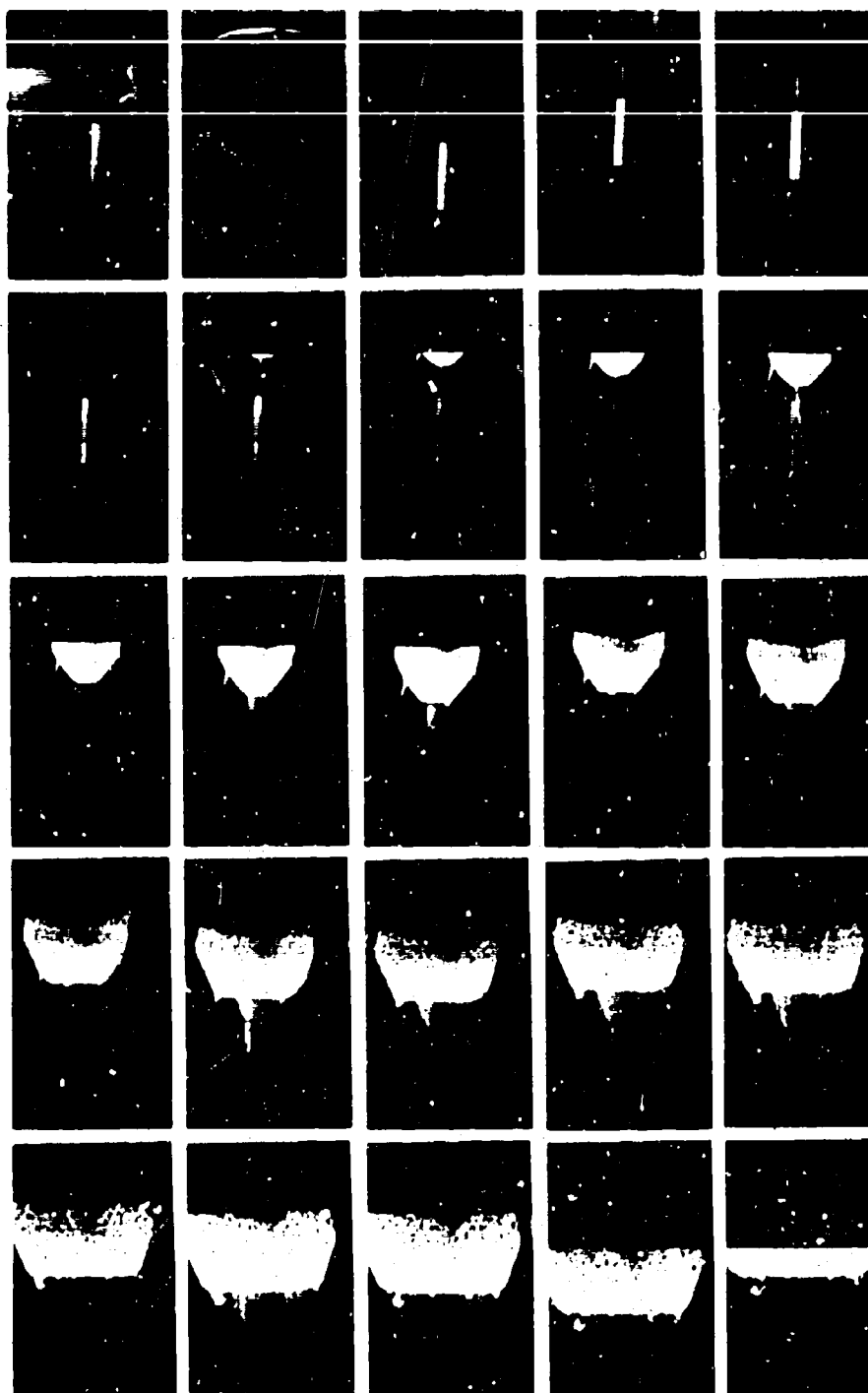


Figure 107. Detonation of RDX-Wax Charge - Test No. B. 1. a. 9
(Time Increment = 1.4 μ sec/frame).

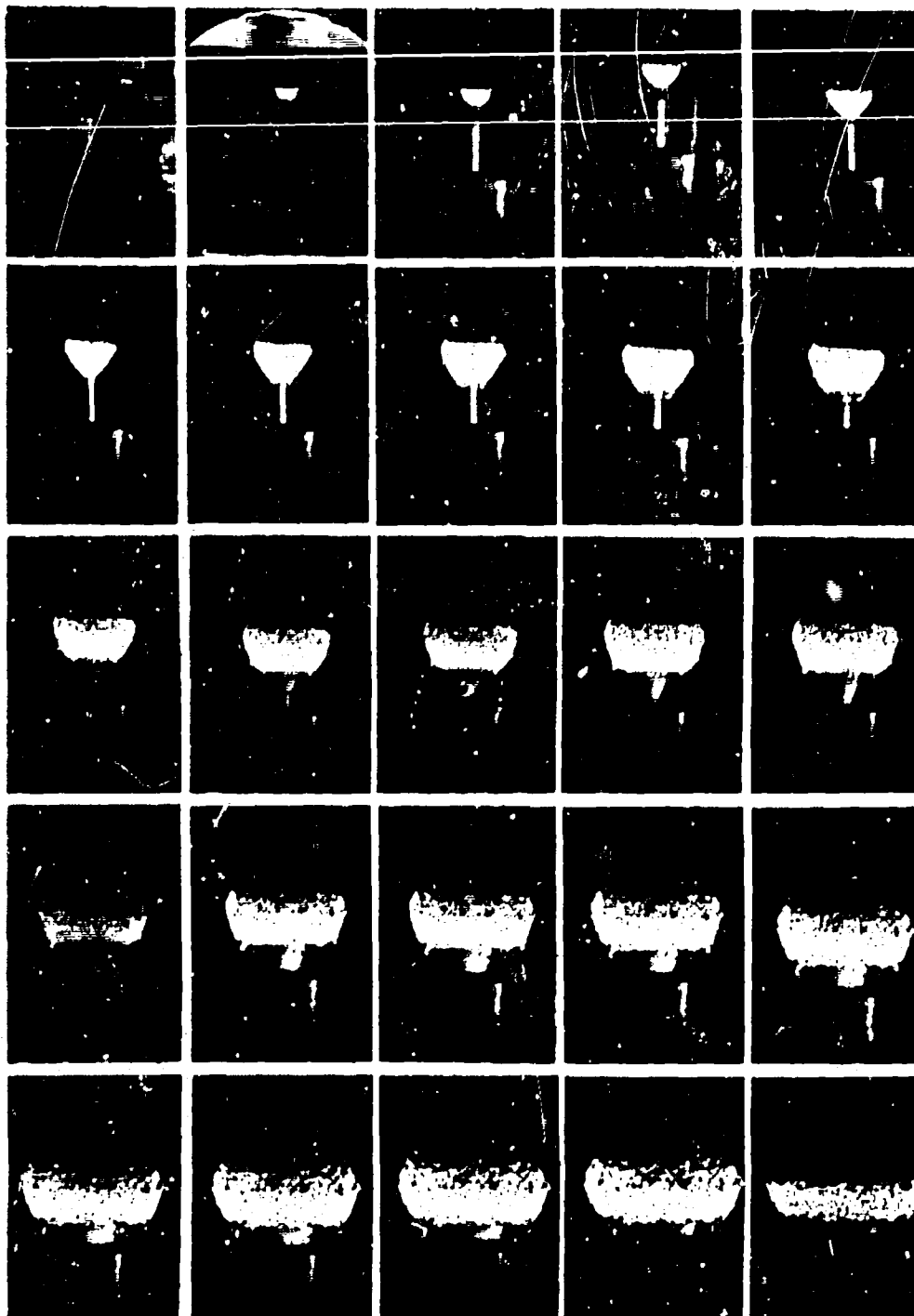


Figure 108. Detonation of RDX-Wax Charge - Test No. B. 1. a. 13
(Time Increment = 1.4 μ sec/frame).

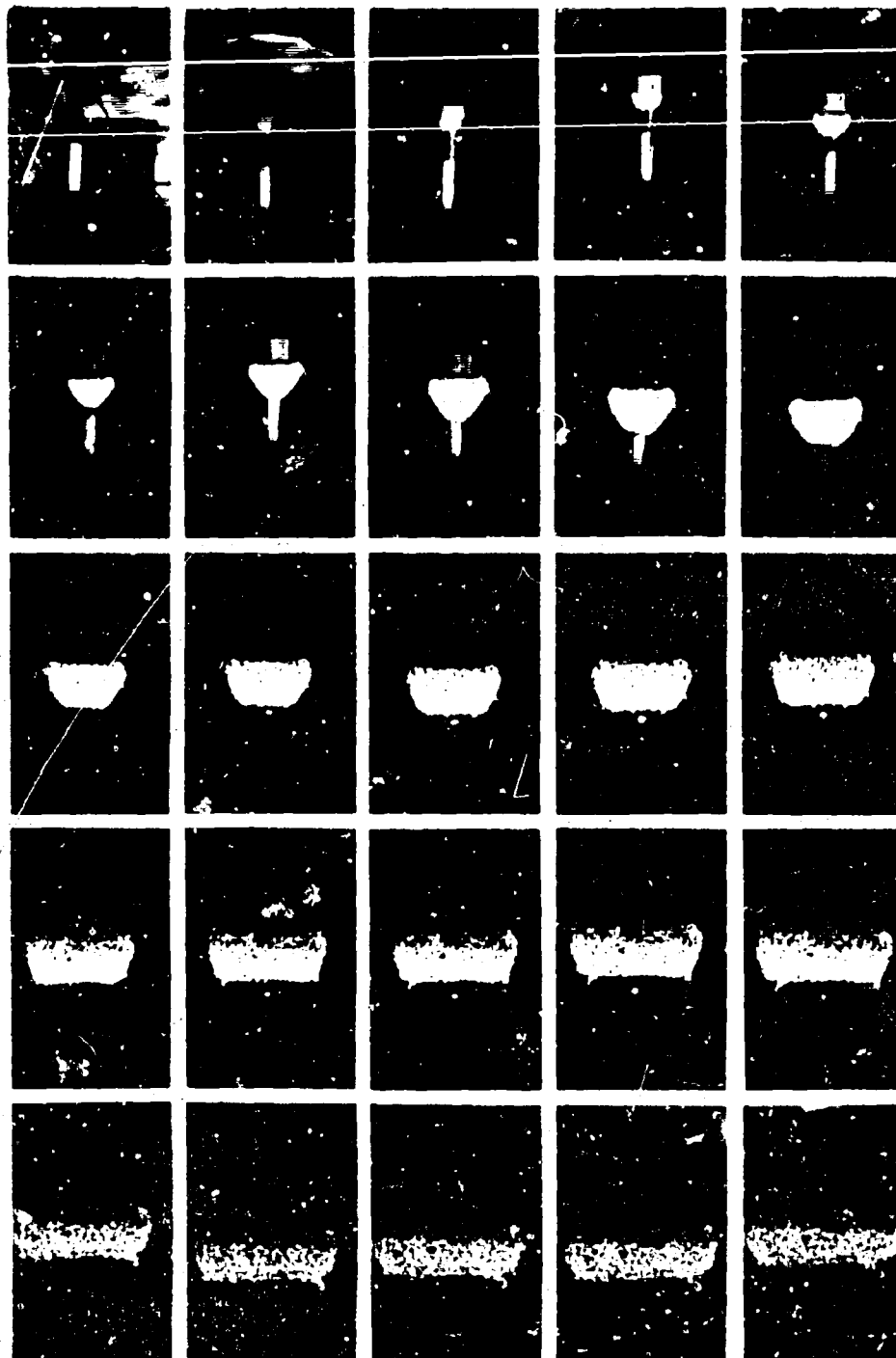


Figure 109. Pure Wax Sample - Test No. B.1.a.12
(Time Increment = 1.4 μ sec/frame).

The presence of steady detonation was, in each case established by frame-to-frame analysis of the advancing detonation front. The best estimates of the detonation velocity values are shown in Table 29. The results of the tests with a pure wax acceptor (see Figure 109) confirmed that the character of the wave in the RDX-wax charges was that of a chemically supported shock wave (i. e., a detonation wave).

5.3.3.1.2 Subtask B.1.b

In Tests B.1.b.1 and B.1.b.2 (see Table 29) the detonation velocity of Composition B was measured simultaneously with a streak camera and a raster-oscillograph pinswitch system. The velocity values (Table 29) show that the average streak camera value is in agreement with the literature within 1/2% while the average pinswitch system result was off by approximately 5%. The two methods differ by approximately 4%.

Because the small separation of the pinswitches can cause error in velocity readings, it was decided that the streak camera should be used on all small-scale tests (less than 3 in.). Further advances in streak camera technique were planned in conjunction with other subtasks but it was determined that camera mirror speeds less than 1500 rps should be used for maximum reading accuracy.

5.3.3.1.3 Subtask B.1.c

In Tests B.1.c.1 through B.1.c.5, the detonation velocity of RDX-wax explosive was measured simultaneously with a streak camera and raster-oscillograph pinswitch system. The results are shown in Table 29. In these tests, it was shown that improved lighting techniques permitted the use of the streak camera to measure the detonation velocity of the RDX-wax charges with sufficient accuracy. Because of the inherent error in the pinswitch data, due to the short sample length, the streak camera results were generally considered more accurate.

5.3.3.1.4 Subtask B.1.d

In Tests B.1.d.1 and B.1.d.2, samples of RDX-wax explosive were detonated against witness plates without other instrumentation. The results are shown in Table 29. The dent data from these tests, together with the applicable data from all previous preliminary tests, are shown in Table 30. From

Table 30. Summary of Dent Data From Preliminary Tests.

Test	Charge Density (gm/cc)	Dent Depth (in.)	Dent Diameter (in.)	Depth/ Diameter	Detonation Velocity (mm/μsec)
B. 1. a. 3	1. 11	~ 0.00	-	-	6. 54
B. 1. a. 4	1. 12	0.063	1.25	0.050	6. 34
B. 1. a. 5	1. 14	0.375	1.63	0.231	6. 73
B. 1. a. 6	1. 13	0.375	1.63	0.231	6. 63
B. 1. a. 7	1. 12	0.250	1.44	0.174	6. 19
B. 1. a. 8	1. 11	0.125	1.19	0.105	6. 67
B. 1. a. 9	1. 12	0.125	1.00	0.125	6. 35
B. 1. a. 10	1. 13	0.170	1.24	0.137	6. 53
B. 1. a. 13	1. 11	0.040	0.75	0.053	5. 53
B. 1. c. 1	1. 13	0.250	1.63	0.154	6. 41
B. 1. c. 2	1. 14	0.250	1.63	0.154	6. 43
B. 1. c. 3	1. 13	0.313	1.31	0.238	6. 29
B. 1. c. 5	1. 11	0.062	1.04	0.060	-
B. 1. d. 1	1. 11	0.250	1.75	0.143	-
B. 1. d. 2	<1.00	0.0	0.0	-	-

these combined results it was found that dent depth did not correlate well with detonation velocity. The effects of batch number and sample density on this correlation were investigated and found to be small although a slight linear increase of dent depth with density (for the range of densities involved) at a given diameter was detected. However, since it was found that dent depth correlates well with charge diameter, irrespective of batch number and density, and detonation velocity should be related to charge diameter, it was concluded that the velocity determinations are not accurate enough for complete evaluation of the witness plate criterion. Examination of the detonation velocity and charge diameter data confirmed this. It was attempted to improve the velocity-dent depth correlation by comparing detonation velocity with the ratio of dent depth to dent diameter (which has some theoretical justification). The correlation did not improve.

Since the foregoing results would be affected by sample quality, and some difficulties were found in this respect, it was decided that witness plate results alone were not sufficient to distinguish between a Go and a No-Go in every case and that streak camera (and/or rasterscillograph) coverage of each test was necessary. However, it was also concluded that the use of witness plates would provide some information in case of failure of the camera (and or rasterscillograph) system and thus should be used (as a backup measurement) on each test.

5.3.3.2 Streak Camera

To eliminate streak distortion caused by misalignment of the camera with the test items, the camera, periscope, and test base plate were carefully aligned. Field-of-view measurements were made to assist in locating charges in such a position that they nearly filled the film width (and thus minimized reading errors). The location of the streak relative to the still, as a function of event-dial setting, was determined by using exploding wires to simulate the events. This calibration was made to prevent overlap of the streak and still for any event at any camera speed. It was found that, for the range of velocities encountered, maximum reading accuracy resulted when camera speeds were between 500 and 1000 rps.

5.3.3.3 Lighting-Method Studies

Because the RDX-wax (and PBAN-RDX) explosive detonation is not inherently luminous, some type of lighting was necessary to permit the camera to record the detonation. Because one-pint argon bombs proved ineffective in preliminary tests, four tests were conducted with one-quart argon bombs to achieve greater illumination of the charge front. Forced development of both Tri-X and Plus-X film did not help appreciably. Location of the camera slit off the axial plane improved light intensity somewhat, but not sufficiently. Because of these difficulties, argon windows were tried instead of the argon bomb. Three window designs were used: (1) a 3/8-in. -diameter butyrate tube placed against the charge front so that the charge axis, tube axis, and camera slit were coplanar; (2) a half-cylinder cut longitudinally and placed against the charge front, to avoid the charge-air-butyrate-argon interfaces of (1); and (3) concentric butyrate tube-explosive charge orientation to reduce distortion caused by deformation of the window surfaces in (1) and (2). Although the quality of the streak-camera records did improve as the window designs improved in (1), (2), and (3), these records were not consistently sharp.

Greatly improved argon bombs were developed from 2:1 cardboard cones. The inside surfaces of the cones were sprayed with silver paint and each cone was loaded with 0.25 lb of C-4 explosive at the apex. The surface of each charge was also sprayed with silver paint. These efforts improved the illumination and sharpness of the streak-camera records so much that this lighting method was used throughout the remainder of the program.

5.3.3.4 Density Measurements

5.3.3.4.1 RDX-Wax Explosive

Because of its direct relation to critical diameter, sample density is an important system parameter. To control the quality of the cast material, the density of each sample was measured (weight-in-air, weight-in-water method) with a Harvard trip balance. The characteristics of this instrument were investigated to assure precision in measuring sample weight under varying load conditions. For loads up to 100 gm, the balance sensitivity is approximately 280 mg/division. But for loads of 1000 gm, the balance sensitivity drops to approximately 400 mg/division. For loads of 2000 gm (maximum for this balance), the sensitivity is between 500 and 600 mg/division. In weight measurements, the null point was determined to

within $\pm 1/10$ division, which is equivalent to ± 0.03 gm at loads up to 100 gm; ± 0.04 gm, at loads of 1000 gm; and ± 0.06 gm at loads of 2000 gm. These measurements represent weighing precisions of 0.03, 0.004, and 0.003%, respectively. Within the range of density variations in a sample, and from sample to sample, these figures represent sufficient precision.

Although precision to three decimal places is possible by the weight-in-air, weight-in-water method of determining density, the inherent accuracy of the system used was not determined and densities have been reported to only two decimal places.

One method of checking the system accuracy is to determine the density of a pure material with this system and then compare the result to the accepted (literature) value. Such a material should have a density in the region of concern; i. e., from 1 to 2 gm/cc. Investigations were made to determine what material might be used for this task. It was found that the densities of readily available materials such as low-density alloys were reported to only two decimal places, while those materials for which accurate densities are known (e. g., Al, 2.699 gm/cc; or Mg, 1.741 gm/cc) are not readily available in the pure state. Because of this, and the fact that the sample density-control was not accurate to three decimal places, all densities for RDX-wax samples were reported to two decimal places only.

5.3.3.4.2 PBAN-RDX Explosive

Because of the importance of sample density as an indicator of sample quality and thus of the variation in critical diameter, this parameter was measured to more decimal places in the PBAN-RDX tests than was done for the RDX-wax explosive. In order to make this improvement, a heavy-duty high-sensitivity Ohaus triple-beam balance with a weighing error of 1 gm was used. An analysis of the error or standard deviation, σ , of density calculations was made. The general rule for determining this error states that, given $W = W(x, y, z, \dots)$ the standard deviation of W , σ_W , is evaluated by:

$$(\sigma_W)^2 = \left(\frac{\partial W}{\partial x}\right)^2 \sigma_x^2 + \left(\frac{\partial W}{\partial y}\right)^2 \sigma_y^2 + \left(\frac{\partial W}{\partial z}\right)^2 \sigma_z^2 + \dots$$

Now when density is determined by the weight-in-air, weight-in-water method,

$$\rho_{\text{sample}} = \rho_{\text{water}} \frac{W_{\text{air}}}{W_{\text{air}} - W_{\text{water}}}$$

where

ρ_{sample} = density of the sample

ρ_{water} = density of the water

W_{air} = sample weight in air

W_{water} = sample weight in water

Therefore, using the above relations, and assuming water density to be a linear function of temperature in the thermal regime encountered, $\sigma_{\rho \text{ sample}} = \pm 2 \times 10^{-4}$ gm/cc for sample sizes of approximately 1200 gm. Obviously $\sigma_{\rho \text{ sample}}$ will be smaller when heavier samples are measured, assuming that the standard deviations of the various parameters remain the same. Because this represents more than third-place accuracy in density determination, all PBAN-RDX samples were reported to three decimal places. It may be seen from Tables 12, 13, 14, 15, 21, and 22 that the maximum range of the density of all samples tested is less than 1%. It was concluded that the sample-to-sample differences in PBAN-RDX explosive are negligible.

5.3.3.5 Central Cavity Jetting

When the central cavity of the circular-core cylinder tests involving the RDX-wax explosive was left empty, a jet was produced that punched the witness plate and obscured the witness-plate test result. When the cavity was filled with soil or dry casting plaster, the jet did not occur but no witness plate damage of any kind was apparent.

From the work of Sultanoff (Reference 7) it was concluded that the jet proceeded faster than any detonation wave produced and, because of the pressures and temperatures involved, initiated reaction on the inside wall of the cavity. This reaction proceeded normal to the "desired" detonation wave and eventually consumed the material in the lower half of the charge. This occurrence is considered possible, whether the central cavity is filled or

not, since the necessary reaction need be initiated only on the inside surface of the cavity. Although the filled cavity might prevent the main body of the jet from damaging the plate, some jetting in the annular space near the fill-charge interface is expected which might initiate reaction in the material. Since this reaction is generally parallel to the witness plate, only minimal witness-plate damage, if any, is expected. For these reasons, it was concluded that even when the central cavity was left empty, the witness plates were not damaged by the detonation reaction. In these cases the damage resulted from the jet only. These conclusions are supported by the test results shown in Table 11.

A careful examination of the streak camera records for these tests showed two general types of behavior. In the one case, the reaction velocity-distance remained steady for from 2 to 2.5 diameters and then suddenly faded to velocities well below the estimated sonic velocity of the material. In the second case the curve simply faded rapidly without any steady portion. This behavior may be explained as follows: If the charge detonated, this wave would proceed down the charge until it was met by the normal wave. At this point, the detonation front would appear to a streak camera to fade rapidly and then disappear. Because of the geometry of this intersection, the velocity would seem to decrease continuously to zero. If the charge did not detonate, the initial wave would attenuate in the usual manner before any intersection with the normal wave occurred. Since the behavior described is precisely that recorded by the streak camera, a short section of constant velocity before the rapid fade was considered sufficient evidence that the charge had detonated. When no such section appeared, it was assumed that no detonation had occurred. This is the manner in which the results in Table 8 were determined.

Because of these difficulties it was suggested that for the PBAN-RDX explosive, the effect might be relieved by (1) drilling a hole in the witness plate to coincide with the charge cavity, as a means of reducing the high pressures associated with the jet; (2) placing a metal rod in the cavity to see whether the jet formation could be prevented without providing surface confinement; and (3) using a solid booster charge and a small amount of Plexiglas attenuator to see whether the jet formation could be delayed sufficiently to obtain better data (i. e., all other tests used a hollow core booster which helps form the jet more quickly). The first suggestion was tried on Test B. 3. 2. 1. 2 where a 1.50-in. hole was cut in the witness plate. Because the 3/8-in. -thick witness plate could not be found after Test B. 3. 2. 1. 2 and a hole was punched in the 2-in. -thick support plate, it was concluded that relief of the jet pressure by this method was not feasible.

Because of the limitation on the number of available samples in Subtasks B. 3. 2. 1 and B. 3. 2. 2 it was decided to carry out the remaining experiments on circular-core Composition B cylinders. Using this material, one charge was tested with and one without a 0.5-in. -diameter steel rod concentric to the cavity. The framing camera results of these tests are shown in Figures 110 and 111, which together with the witness plate results indicate that negligible, if any, delay in the jet formation was accomplished. The motivation for the third suggestion was based on the fact that the reaction velocity-distance data of previous tests had shown an attenuation from the high velocity booster wave ($\sim 7 \text{ mm}/\mu\text{sec}$) to the steady detonation in the propellant ($\sim 4 \text{ mm}/\mu\text{sec}$) and that the shock pressure required for initiation was considerably less than was actually being put into the charge with a direct booster-charge interface. For these reasons it was felt that the use of a solid booster and a small ($\sim 1 \text{ in.}$) thickness of Plexiglas attenuator would cause initiation of the charge with a shock wave closer to the steady detonation velocity of the material. This would promote a quicker attenuation to steady-state and prevent the jet formation in the booster, thus delaying of the formation of the jet in the acceptor. This was found to be highly successful and increased the amount of useful data that could be extracted before the normal wave appeared. Furthermore since it was found that there was evidence that the jet was reflecting off the witness plate and causing retonation of the charge (see Figures 110 and 111) the data available was further increased by cutting a hole in the witness plate (not to relieve the pressure but to allow the jet to pass through without reflection) and digging a hole approximately 1 ft deep in the ground below the charge. With these improvements the results of testing with hollow core charges became more definitive (see Table 15).

5.3.3.6 Side Donor

In order to establish the general character of a detonation initiated by a side donor, a Composition B donor was placed on the side of a cylindrical Composition B sample using the test setup shown in Figure 96. The result is shown in Figure 112 which is a framing camera study of the event. It was noted that the wave front tended to become flat near the bottom of the charge. This result was used as a standard of a Go in Subtasks B. 4. 2. 1. 3 and B. 4. 2. 2. 3.

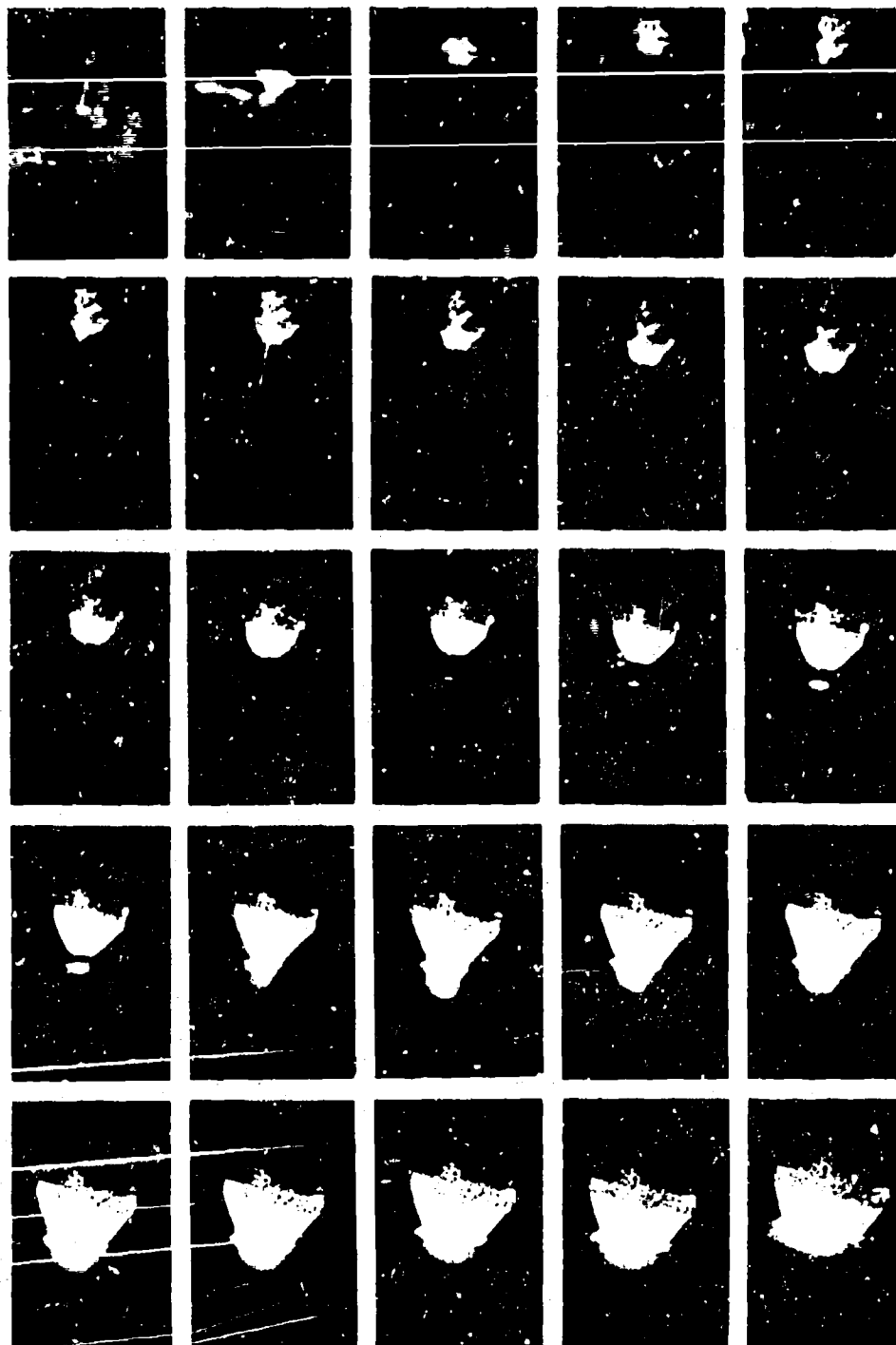


Figure 110. Circular-Core Composition B Booster - Test Without Rod.
(Time Increment = 2.76 μ sec/frame).

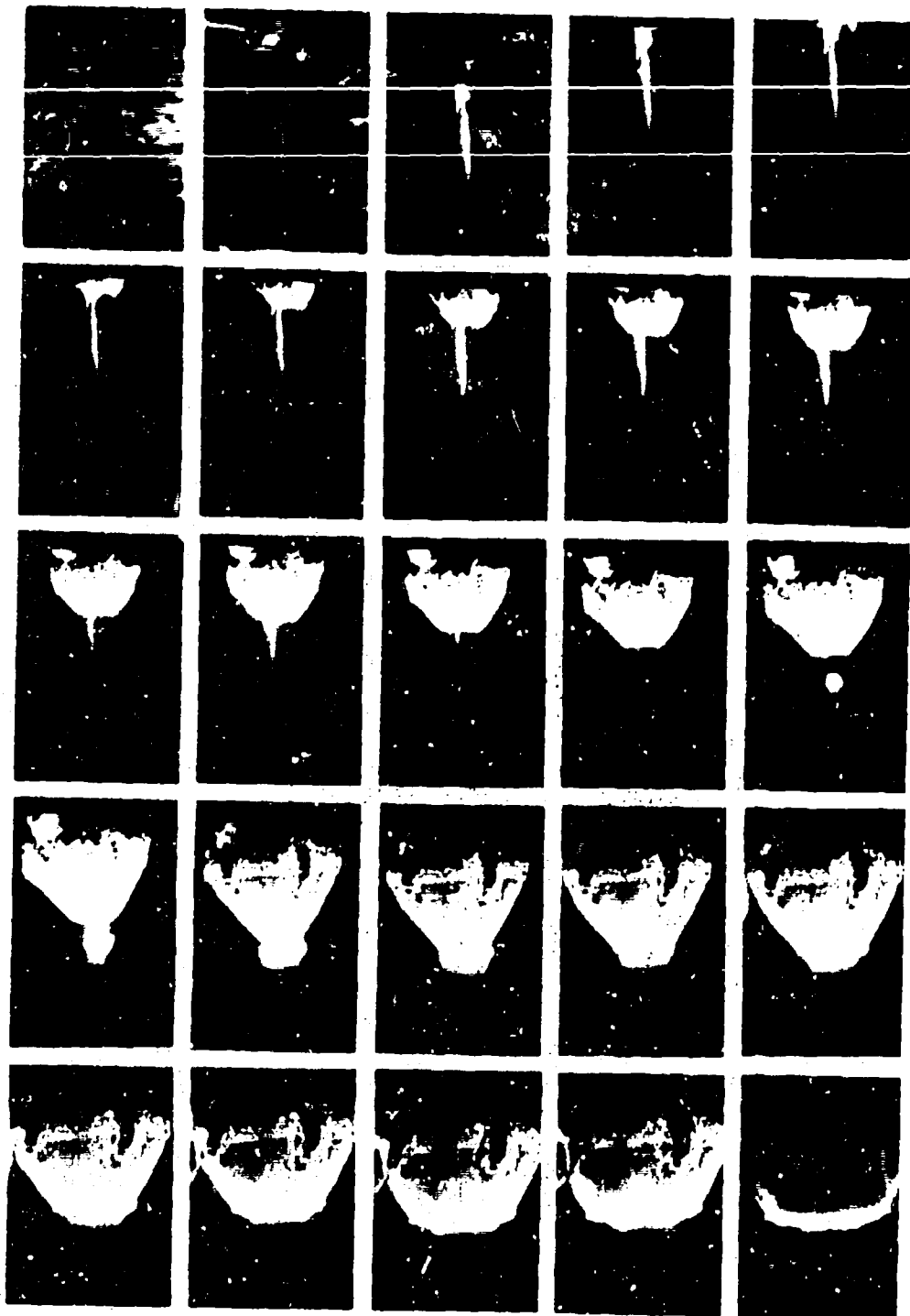


Figure 111. Circular-Core Composition B Booster Test With Rod
(Time Increment = 2.76 μ sec/frame).

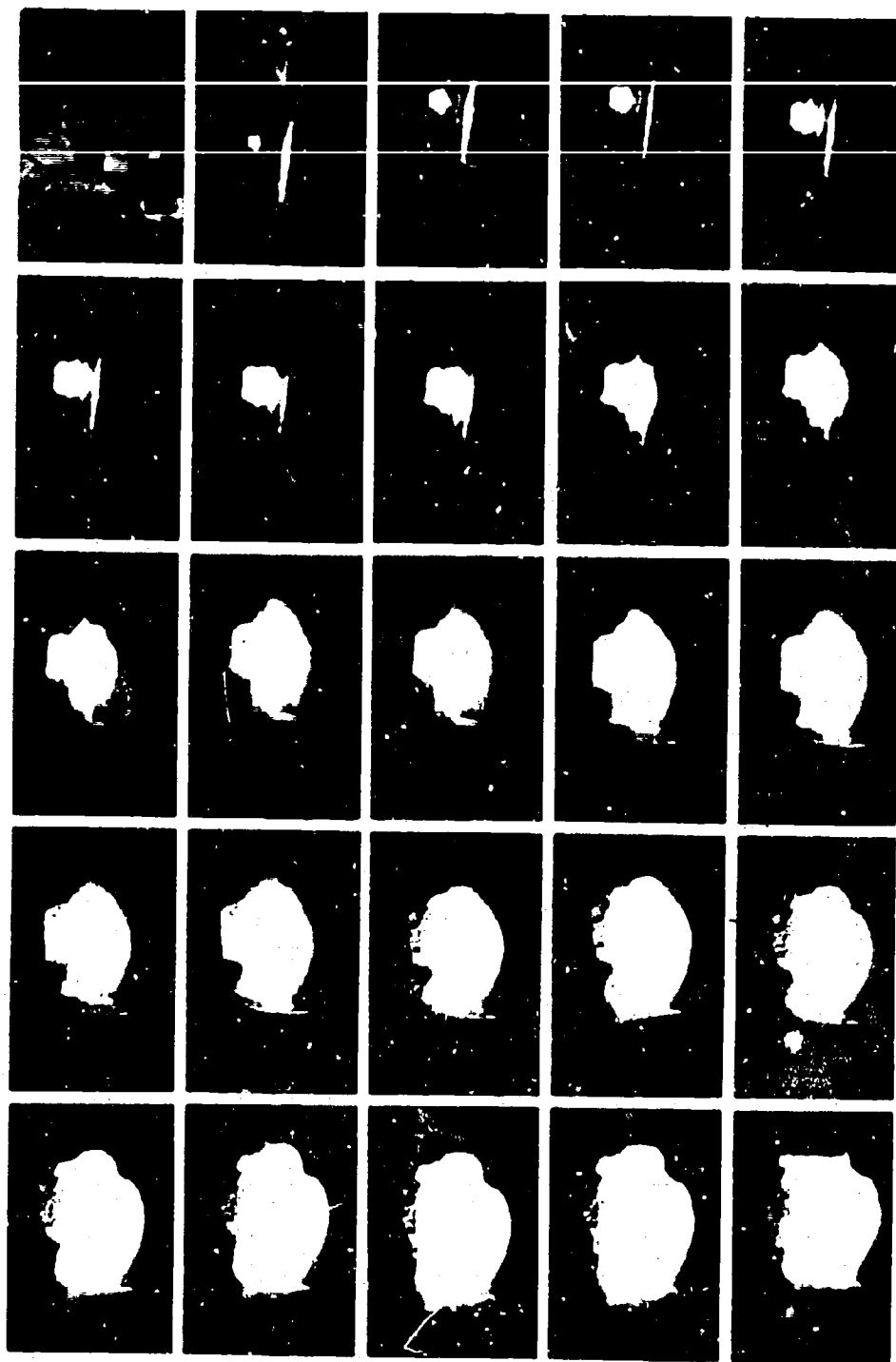


Figure 112. Side Donor Test - Composition B Charge
(Time Increment = 2.76 μ sec/frame).

5.3.4 Data Reduction and Analysis

For conditions far above or far below the critical diameter, it is usually easy to distinguish between a steady detonation and a fading detonation; witness plates usually suffice for this purpose. For conditions at or near the critical diameter, the witness plate result becomes subject to interpretation and is not a clear-cut indicator of steady or fading detonation. For this reason, in any test a measured steady detonation is used as the criterion to distinguish a Go from a No-Go. This was accomplished by recording the detonation wave in each test with a streak camera. The data obtained from each streak camera film was reduced using a 3750 Nikon Measurescope, which reads to 0.0001 in., giving x-y data at the film plane. Multiplication by appropriate time and magnification factors gives the distance-time data. In order to follow the velocity of the wave as it progresses through the test sample, the data were numerically differentiated point-to-point through a simple scheme developed especially for use with streak camera records (Reference 1). This scheme does not obscure local variations in velocity but does allow estimating the error in any given velocity computation. This method was used on all test data obtained.

The velocity-distance data obtained with the numerical differentiation scheme were then plotted on linear paper (detonation velocity vs position on charge) and a judgment made as to whether steady-state had been achieved or not. In most cases, this was very clear since the velocity either attenuated rapidly to sonic velocity for the material (i. e. a fading wave) or it fell to an essentially steady value within one or two diameters from the booster-charge interface. However, in some instances this difference was not so clear and technical judgment was needed. The way in which the detonation velocity varied throughout the test sample was a measure of the properties of the charge, and this information was used in an evaluation of the overall quality of the particular material involved.

A considerable amount of analysis was done in Subtask B.4.2.1.1 in order to obtain the profiles, diameter, area, and average shock pressure of the attenuating waves, but only standard procedures and methods were used and no new developments were necessary. A description of how the data were analyzed is contained in the main body of the text.

5.3.5 Propellant Development and Evaluation

5.3.5.1 RDX-Wax Explosive

In order to obtain RDX-wax explosive samples of reasonable quality, improvements in casting techniques and checks on sample quality were made in all batches cast.

5.3.5.1.1 Previous Work

Experience was gained in a previous experimental program (Reference 11) in preparing a RDX-wax explosive with a given critical diameter. From this study, it was shown that to obtain reasonable reproducibility in the critical dimensions for cylinders, squares, and triangles, it was necessary to control the preparation, mixing, and casting procedures. In the preparation of the explosive, it was found that surface-active agents have an effect on the distribution of RDX in the final material and are necessary to prevent agglomeration, which causes nonhomogeneity. Furthermore, in mixing the explosive, it was found that the order and rate of introducing the hardening agent (in this case, Cab-O-Sil) with respect to the other components also affected the RDX distribution. In casting the explosive into molds, the temperature and cooling rates were critical in preventing the formation of voids.

In addition, the particle-size distribution of RDX had a great effect on critical diameter and had to be carefully controlled.

The best results were obtained with Class E (MIL-R-3980, 95% minimum through 325 mesh) RDX. The study also showed the feasibility of casting into molds into various shapes without any special problems in curing or in releasing the samples.

Detonation tests using this explosive in a card-gap test setup, showed that 30 to 35% by weight RDX is required to obtain a critical diameter from 1-1/2 to 2 in.

5.3.5.1.2 Preliminary Batch

A 15-lb batch of RDX-wax explosive containing 31.5% RDX, was cast for use in the preliminary tests (Subtask B. 1). The samples included six 1-1/4 in. -diameter by 5-in. long cylinders; four 1-1/2-in. -diameter by 6-in. long cylinders; and five 1-3/4 in. -diameter by 7-in. long cylinders. Cylindrical Composition B boosters were cast in the following sizes: four boosters 1-1/4-in. -diameter by 3-3/4-in. long; five boosters 1-1/2-in. -diameter by 4-1/2-in. long, and five boosters 1-3/4-in. -diameter by 5-1/4-in. long.

5.3.5.1.3 Casting

A summary of all the batches cast is shown in Table 31 where the changes in operating procedures, composition, size, and density are indicated.

Vacuum melt procedures were introduced in Batch 5 and the resultant samples, although of higher density than before, showed about the same variability in density. However, when the batch size was increased in Batches 6 and 7, this variability increased by a factor of two to three while the density decreased slightly. Investigations of the records showed that the large increase in batch size in Batches 6 and 7 (with respect to Batch 5) resulted in a 3-hr increase in the melting and mixing period during casting. Based on the results of the previous program (Reference 11) it is believed that this extra time results in a "wetting time phenomenon" wherein the Cab-O-Sil structure deteriorates with time and decreases the mix viscosity. Such a decrease was noted during the preparation of Batches 6 and 7. A decrease in mix viscosity will allow the RDX to settle during the pouring operation (which would account for sample-to-sample density variations) and the cooling and hardening period in the molds (which would account for RDX and density variations within a sample). An investigation of this "wetting time phenomenon" and means of avoiding it was made.

As noted in Table 31, the standard deviation of the density data for Batch 7 was not excessive and compared favorably with the much smaller Batch 5. Since certain charges were recast, because of poor density or poor dimensional symmetry, the final standard deviation was somewhat less than that indicated. However, the separation of clear melt in the molds (Table 31) indicated that settling of the RDX was taking place.

Table 31. Development of Propellant Casting.

Batch	RDX (%)	Total Weight (lb)	Cast Density (gm/cc)*	Remarks
1	31.5	10	1.121 ± 0.010	- - -
2	31.5	10	1.119 ± 0.009	Cab-O-Sil percentage increased slightly, and mineral oil percentage decreased with respect to Batch 1.
3	30.75	10	1.059 ± 0.005	Cab-O-Sil percentage increased further, while mineral oil decreased. More paraffin and less RDX than in Batches 1 and 2 to increase the critical diameter.
4	30.75	25	1.059 ± 0.005	Composition the same as in Batch 3. Mixing procedures improved to obtain more uniform sample appearance than previously obtained.
5	30.75	10	1.093 ± 0.007	First attempt to vacuum melting before casting. A vacuum of 15-in. Hg was applied for 1 hr.
6	30.75	50	1.087 ± 0.019	Large variations found in sample-to-sample densities. Less efficient mixing noted in larger casting kettle. Vacuum melt procedures used.
7	30.75	250	1.081 ± 0.010	Separation of clear melt observed in molds to depth of about 1/4 in. RDX composition gradients suspected. Vacuum melt procedures used.

*The figure after the average density of the batch is the standard deviation of the densities of all samples cast.

5.3.5.1.4 Density and RDX Composition Variations Within a Sample

In order to determine a measure of the uniformity of the RDX-wax explosive, a number of cast samples were cut up and analyzed for density and RDX content. The results of these analyses and the implications on the quality of the test material are described in detail in Appendix C.

5.3.5.1.5 RDX Particle-Size Analysis

In order to assure sample uniformity with respect to the subdivision of RDX in a test sample, two samples of RDX were withdrawn from the storage container, divided into two subsamples, and analyzed for particle distribution. The first sample was removed on 29 June 1964; the other on 13 September 1964. Since the first sample was used in preparing Batches 1 to 4, it was not replaced in the storage container and the latter sample was distinct. The results of this analysis are shown in Figures 1 and 2. These figures are frequency charts of percent of total RDX vs particle-size range. The two subsamples of the first sample (Figure 1) show the highest percentage of particles (~40%) between 10 and 20 μ , and are very similar. The two subsamples of the second sample (Figure 2) show the highest percentage of particles (~50 to 60%) between 5 and 20 μ , but appear to be only slightly different. From these results it was concluded that the RDX particle size distribution was effectively constant from sample to sample.

5.3.5.2 PBAN-RDX Explosive

In order to be assured that the PBAN-RDX explosive samples were in the right range of critical diameter and of high quality, checks were made on all batches cast.

5.3.5.2.1 Preliminary Batches

To bracket the correct percentage of RDX and give a critical diameter of approximately 3 in., four small batches of PBAN-RDX explosive were ordered from Aerojet Solid Rocket Operations, Sacramento. Of these, two were cast, and 14 critical-diameter tests were performed in conjunction with the critical diameter program.

To estimate the correct percentage of RDX to provide a critical diameter of approximately 3 in., all critical-diameter data (at that date) were plotted as shown in Figure 113. In the region of interest, smooth curves were then drawn through the data to represent the maximum and minimum estimates of the actual curves of critical diameter and RDX content. By drawing a horizontal line at a diameter of 3 in., the expected maximum range of RDX content to give a critical diameter of 3 in. was found to be from 9.00 to 9.40 wt % (Figure 113). The value of 9.20 wt % was chosen as a best estimate. The critical diameter should have been greater than 2.80 in. and less than 3.25 in. for this value as shown in Figure 113.

Since the actual critical diameter of PBAN-RDX propellant containing 9.20 wt % RDX was found to be about 2.71 in. and the prepared casting molds were based on a critical diameter of 3 in. most of the charges received in Batches 1, 2, and 3 were supercritical. Therefore many samples had to be machined to smaller sizes to enable testing to take place.

5.3.5.2.2 Sample Quality

Because most of the charges in Batch 1 of the PBAN-RDX explosive had many small depressions on the surface (Figure 114, upper left), most of them were X-rayed to determine if internal voids existed. Typical results are shown in Figure 115, where 1/2-in. voids are seen. Since most of the voids appeared at the periphery of the charges, one was ground down on a lathe and the observation confirmed (Figure 114). This result supports the conjecture that improper temperature-control of the molds during the casting operation caused the voids. However, since the critical diameter of this material is somewhat smaller than anticipated, it was possible to effectively eliminate the voids by turning down most of the charges to diameters below which voids were present (Figure 116). Most of the tests using Batch 1 material were conducted with essentially voidless material.

Samples were sent to Aerojet's Solid Rocket Operations, Sacramento, for microtoming and photomicroscopic examination to ensure against the possibility that a large amount of porosity might be associated with the voids found in this material. The results are shown in Figure 117. The voids were caused by the microtome blade, as evidenced by their lack of sphericity and the lack of a fuel-rich fringe around the holes. This information, which does not indicate any void content in the samples analyzed, gives some assurance that the samples are not of unusual porosity.

No evidence of voids or porosity was found in Batches 2 and 3 of this material and no X-ray or photomicroscopic examinations of this material were made.

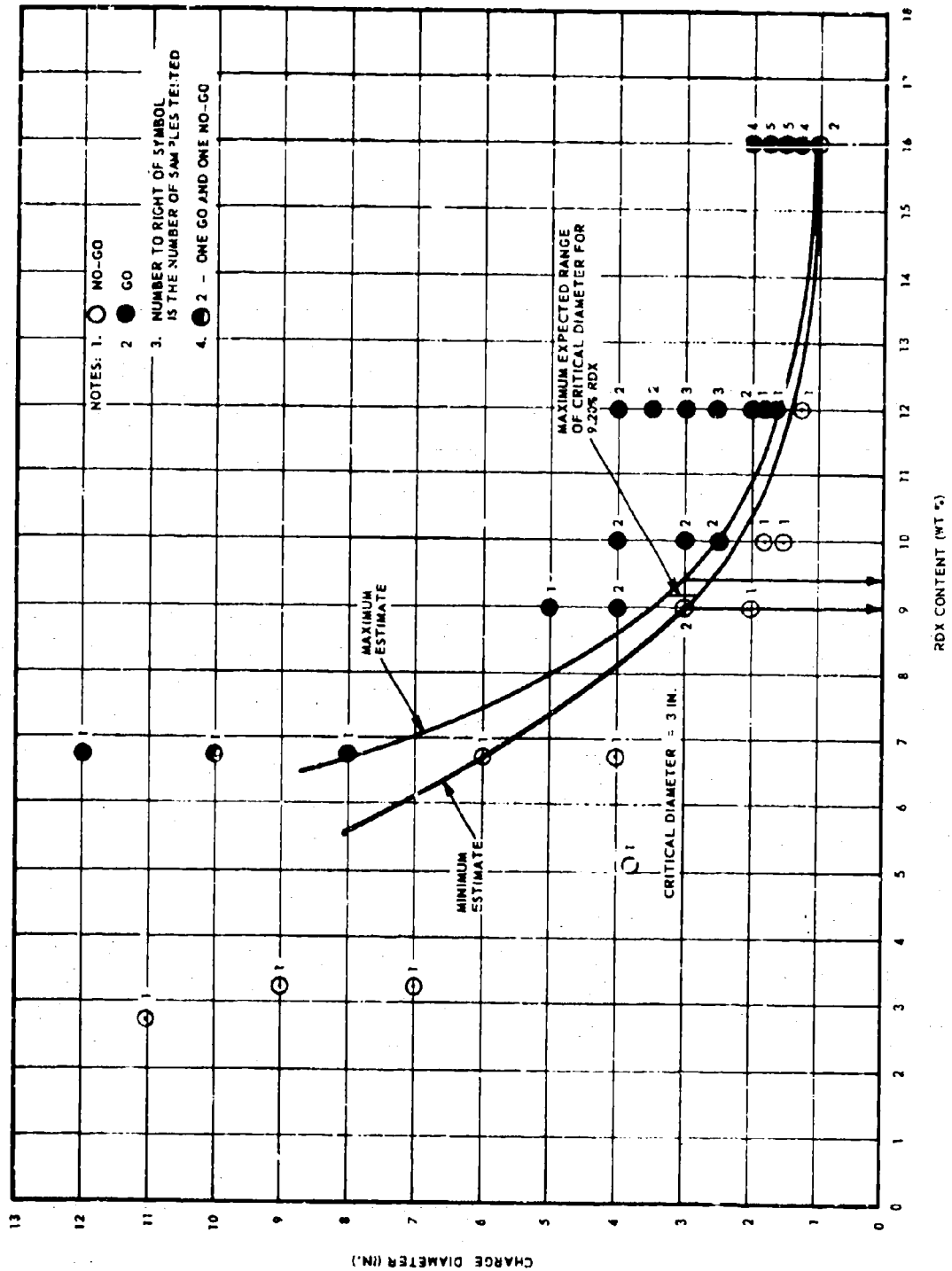
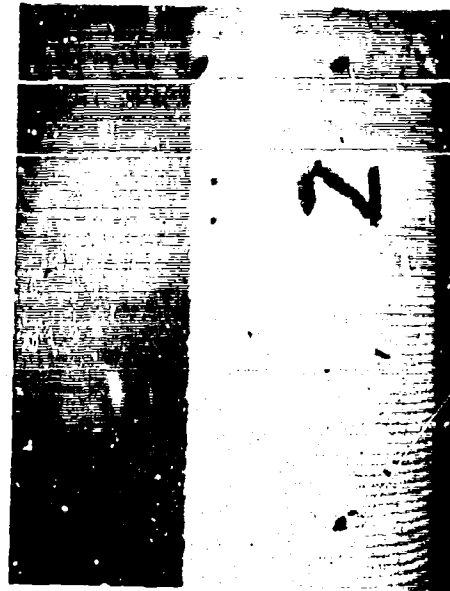


Figure 113. Estimation of Correct RDX Content to Give a Critical Diameter of 3 in.



EXTERIOR VIEW



VOIDS, 1/8 IN. BELOW SURFACE



VOIDS, 1/4 IN. BELOW SURFACE



VOIDS, 1/4 IN. BELOW SURFACE

Figure 114. Voids in PBAN-RDX Batch 1.

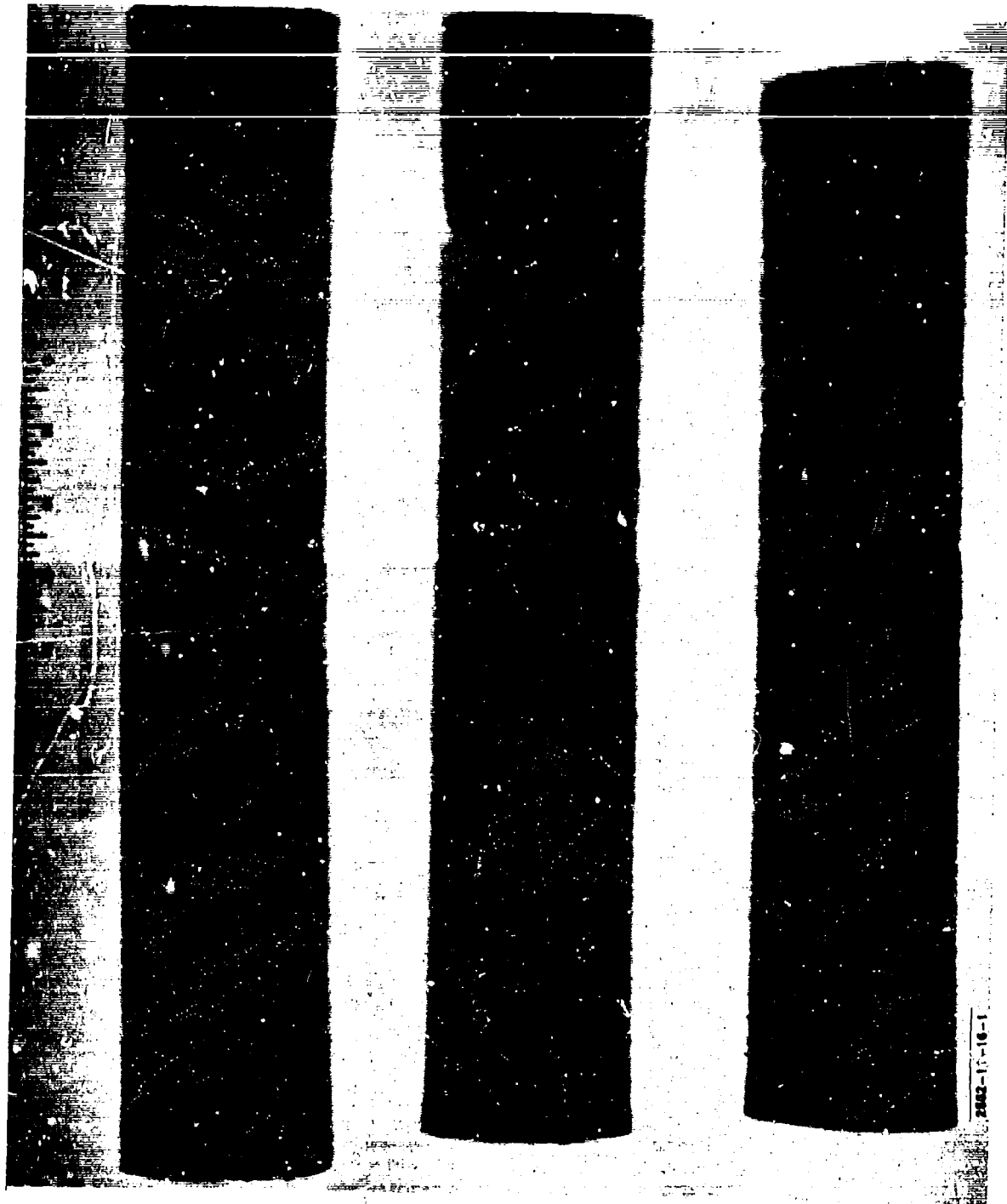


Figure 115. Typical X-Rays of Samples from PBAN-RDX Batch 1.

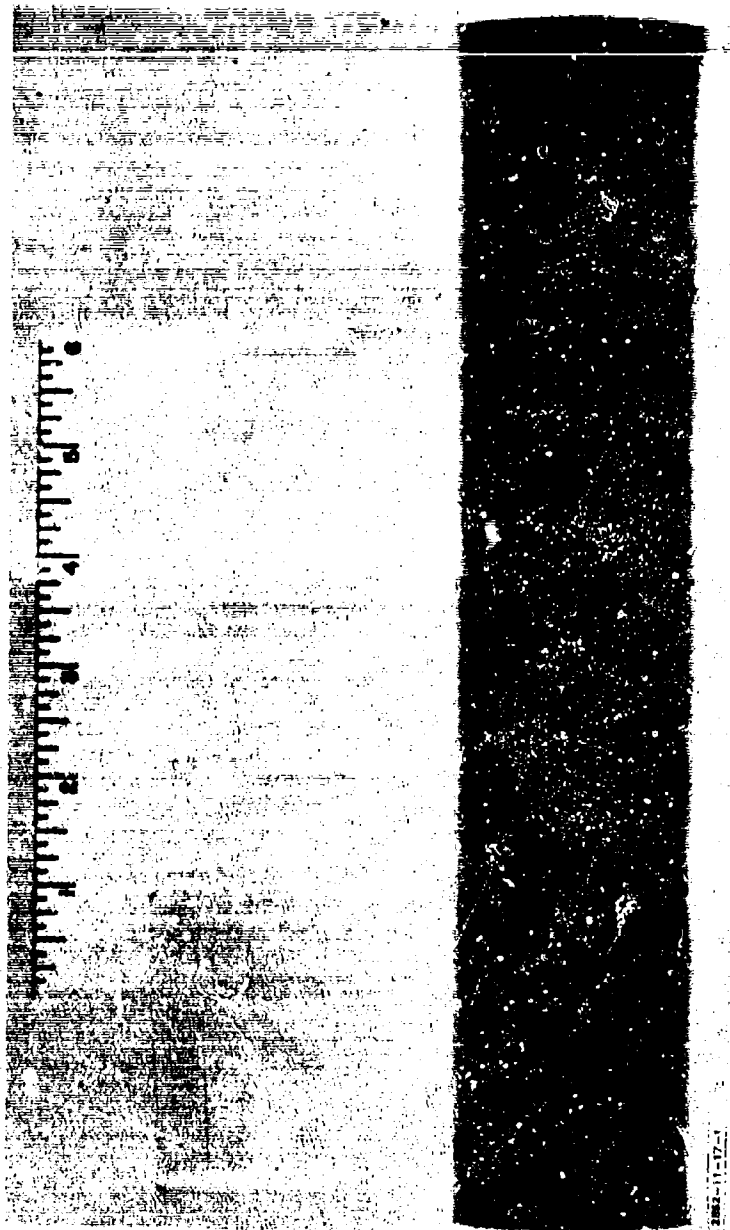


Figure 116. X-Ray of Turned Down Sample from PBAN-PDX Batch 1.

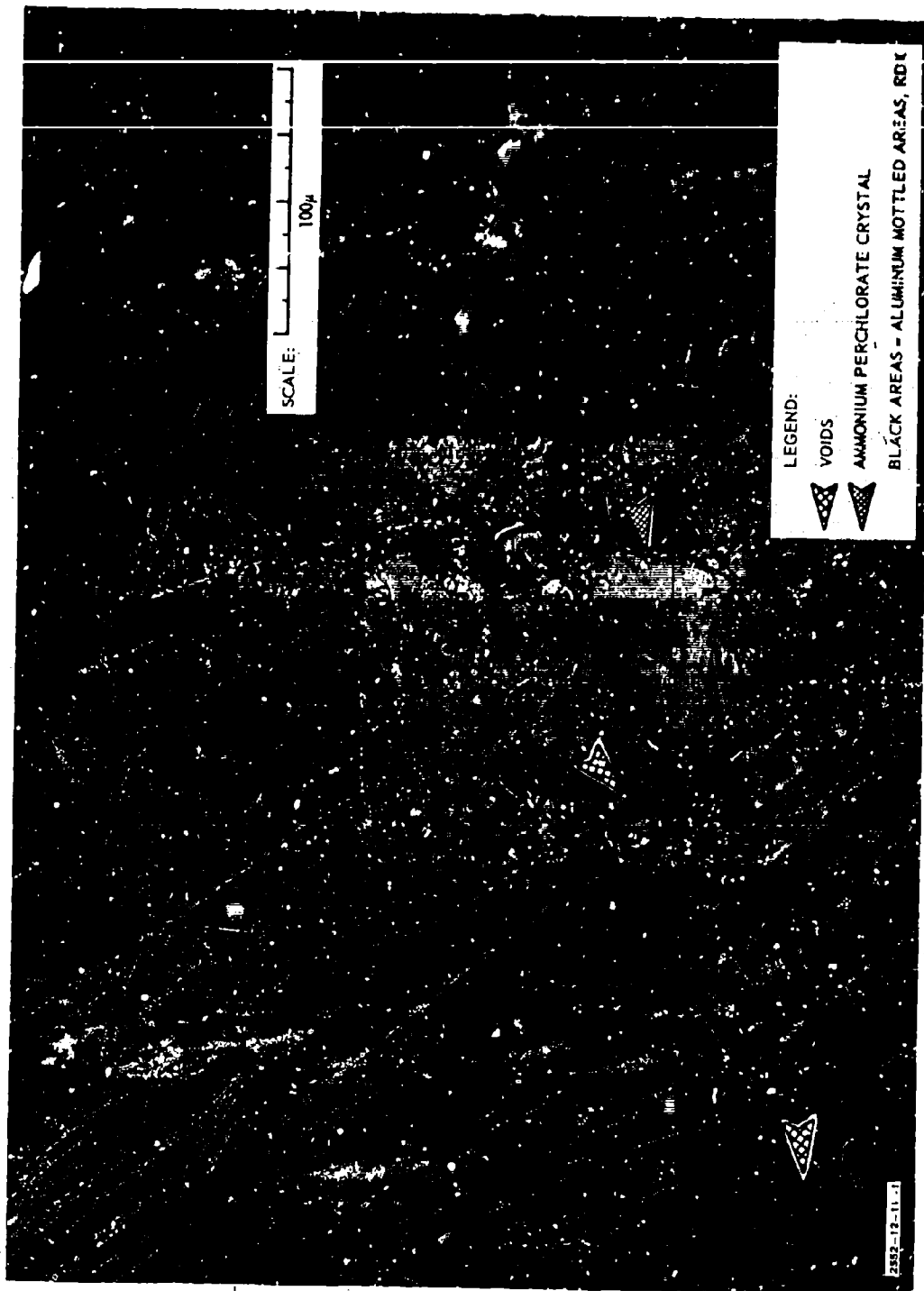


Figure 117: Photomicrograph of PBAN-RDX Sample Containing 9.2% RDX.

ACKNOWLEDGEMENTS

The following Aerojet-General Corporation personnel made important contributions to the success of this program:

Robert Elwell	Research Chemist	Coordinated testing for critical geometry studies
Roy Coley	Research Engineer	Test conductor for the critical diameter studies
Bruce Cooper	Test Engineer	Coordinated ordnance activities for critical diameter studies
David Frutchey	Associate Engineer	Performed data analysis for critical diameter and critical geometry studies
Aubrey Hammond	Development Chemist	Coordinated propellant development activities
Dr. Paul Longwell	Senior Staff Scientist	Served as technical consultant to Program Manager
Dr. Charles Strickler	Specialist in Physics & Polymer Chemistry	Technical guidance of propellant development activities
Arthur VanRyckeghen	Electronic Engineer	Coordinated instrumentation design and application

We also gratefully acknowledge the invaluable assistance given by the Air Force Rocket Propulsion Laboratory, Edwards, California, in the form of suggestions, review and editing assistance. AFRPL personnel who made major contributions include, Messers C. R. Cooke and D. H. Wian, Major B. E. Giesler and Captain N. H. Valor.

REFERENCES

1. A Simple Method of Finding Numerical Derivatives, Technical Memo to D. V. Paulson from P. K. Salzman, 10 May 1961 (Unclassified).
2. Andersen, W. H., O. R. Irwin, and P. K. Salzman, "Theoretical Detonability Behavior of Solid-Composite Propellants," (U), Bulletin of the 20th Interagency Solid Propulsion Meeting, Philadelphia, Pennsylvania, July 1964 (Confidential).
3. Andersen, W. H., and R. F. Chaiken, "Detonability of Solid-Composite Propellants," ARS Journal, 31, 1379-1387 (1961).
4. Jones, M., Proc. Roy. Soc., A189, 415-46 (1947).
5. Andersen, W. H., and R. B. Farlin, "New Approaches to the Determination of the Thermodynamic-Hydrodynamic Properties of Detonation Processes," Institute for the Study of Rate Processes, University of Utah Technical Report No. 28, October 1953.
6. Miller, R. O., "Estimating Caloric State Behavior in Condensed Phase Detonations," Progress in Astronautics and Aeronautics, Vol 6, Edited by S. S. Penner and F. A. Williams, Academic Press, N. Y., 65-74 (1962).
7. Sultanoff, M., "Detonation and Shock in a Hollow Explosive Cylinder," Fourth Symposium (International) on Combustion, 494-7. The Williams and Wilkins Company, Baltimore, Md. 1953.
8. Analysis of Shock Attenuation for 0.5- and 2.0-in. Diameter Card-Gap Sensitivity Tests, Aerojet-General Corporation Report No. SRP 289 (Special), January 1962.
9. Al'tshuler, L. V., Krupnikov, K. K., and Brazhnik, M. I., "Dynamic Compressibility of Metals under Pressures from 400,000 to 4,000,000 Atmospheres," Soviet Physics JETP, Vol. 34 (7), No. 1 614-19, October 1958.
10. Sensitivity of High Explosives: Projectile and Gap Tests, E.R.D.E. Report No. 6/R/59, May 1959 (Confidential).
11. Study of the Effect of Geometry on Detonation Characteristics, Aerojet-General Corporation Final Report, Independent Research and Development, Work Authorization 8706-01, December 1964.

APPENDIX A

THE THEORY OF CRITICAL GEOMETRY

APPENDIX A - THE THEORY OF CRITICAL GEOMETRY

A.1 INTRODUCTION

In evaluating the blast, fire, and fragmentation effects to be anticipated from the detonation of large solid-propellant motors, it is first necessary to determine the conditions under which such a detonation can take place.

Because almost all propellant grains of current interest are not right-solid cylinders but contain some form of hollow core (e.g., internal star perforation), it is clear that the critical diameter concept alone is not sufficient to evaluate the detonability of such systems. This concept is further limited in that it cannot evaluate the effects of variations in donor intensity, configuration, and location on even right-solid cylindrical systems.

Thus, to account for variations, both in grain configuration and in donor intensity, configuration, and location, a new concept, the "Theory of Critical Geometry," was recently developed. This theory determines the detonability of a given system by answering the two questions:

- a. Is the given solid-propellant configuration capable of supporting detonation?
- b. If the configuration is capable of supporting detonation, are sufficient forces available to initiate detonation?

The first question is answered by determining the dimensions of a noncylindrical charge that will allow sustainment of detonation (i.e., the "critical geometry") as a function of the critical diameter of a cylindrical charge of the same material. The second question is answered by determining an initiation criterion (a property of the given material) that must be met by the stimulus from a given donor.

A-2 THEORY

The theory of critical geometry is developed by evaluating the two parts of the problem of detonability (i. e., sustainment and initiation) separately. Consider a long uniform propellant charge of any constant, cross-sectional shape*.

First, it is assumed that regardless of grain shape, there are certain grain geometries that will support a unique steady-state detonation to infinite length. Further, for those geometries capable of supporting detonation, there is, at some distance from the point of initiation, a point at which the detonation characteristics will be independent of the mode of initiation (although this initiation must be strong enough to start detonation in the first place). For such geometries, the ability to support detonation becomes purely a property of the acceptor material without regard to the donor, and for a given acceptor material, it becomes purely a property of acceptor geometry. Therefore, sustainment can be studied as a function of acceptor geometry only. It is then possible to define and categorize acceptor geometries as (1) subcritical - those that will not sustain detonation; (2) critical - those that just support detonation; and (3) supercritical - those that amply support detonation.

Second, for those configurations found to be supercritical with respect to sustained detonation, the intensity, configuration, and location of a donor may be studied to determine if detonation can be established. Since such a study of initiation requirements contains four variables (donor intensity, configuration, and location, and a supercritical acceptor shape), which can vary over wide ranges, the simplest case (symmetrically end-initiated right-solid cylinders) will be considered in detail. Following this, the analysis of more complex systems can be made by allowing a gradual step-by-step deviation from simplicity.

*The following definitions are used when discussing the acceptor:

Shape = form of the cross-section (e. g., square, rectangular, cylindrical, etc.)

Geometry = the size or magnitude of a given shape.

A-2.1 Sustainment of Detonation

A-2.1.1 General

The critical diameter of a particular material is known to depend on the relative energy gains and losses in the region of the detonation reaction zone. The energy gains depend upon the reaction zone length, which is a function of both the kinetics of the detonation reaction for the material involved and the velocity of the detonation wave, while energy losses depend solely on the rarefaction waves moving in from the lateral portions of the charge.

Therefore, in the case of a right-solid cylinder, the two factors affecting the distribution of energy gains and losses are: (1) detonation reaction zone length (i. e., kinetics and wave velocity), and (2) charge diameter (i. e., rarefaction waves).

In the general case, the critical dimensions of a given shape will also be dependent on the relative energy gains and losses in the region of the detonation reaction zone. Again the gains will depend on the reaction zone length, and thus, on the kinetics and wave velocity. Energy losses will be dependent solely on the lateral rarefaction waves, and thus, on charge geometry.

Therefore, in the general case, the two factors that affect the distribution of energy gains and losses are (1) detonation reaction zone length, and (2) charge geometry.

Since the kinetics in the reaction zone are dependent only on the material properties and wave velocity, they will be the same for any geometry at the same velocity. Thus, energy gains will be affected by charge geometry only insofar as the detonation velocity is affected. If it is then assumed that the detonation velocity is approximately the same for any shape at the critical dimensions of the shape, the detonation reaction zone length will be the same for every shape of the same material. Therefore, for different shapes, energy gains will be the same, and the only factor affecting the energy balance (and thus the critical dimensions) will be charge geometry.

The theory of critical geometry, when based on an extension of the critical diameter concept, may then be developed on a purely geometrical basis, since the kinetics and wave velocity of the system are

already accounted for in the critical diameter evaluation. Also, since charge composition, particle size, density, and temperature affect the reaction zone length (but not the rarefaction waves) the effect of changes in these quantities on critical geometry will be accounted for by the effect of these changes on critical diameter.

The effect of confinement on the critical geometry concept is more complex, since it affects both the reaction zone length (by affecting the wave velocity) and the rarefaction waves. However, if current theories of the effect of confinement on critical diameter can be used to define an equivalent confinement for noncylindrical shapes, the critical geometry concept will apply without change.

A-2.1.2 Critical Geometry Concept

Based on the reasoning just discussed, a simple theory of critical geometry is developed for a given material (i. e., unconfined, fixed composition, density, particle size, etc.) by finding a function, based on the parameters that describe the charge geometry, that can be made the critical criterion.

It is assumed that: (1) there is one critical criterion for any given shape, and (2) this same critical criterion holds for all shapes. Therefore, for criticality in any case, the parameters used must combine in such a way as to give the critical diameter d_c , for a solid cylinder, since criticality for the cylindrical case is specified in terms of only one parameter, namely the charge diameter.

In terms of energy gains and losses, the important features of charge geometry for any shape would be:

- a. Reactive volume (proportional to total energy output, and thus, to energy gains).
- b. Surface area of reactive volume (proportional to losses by rarefaction waves).

For long, uniform charges of constant cross-section

$$\text{Reactive volume} \propto \text{Cross-Sectional Area} \times \text{Reaction Zone Length} \quad (1)$$

and

$$\text{Surface area} \propto \text{Cross-Sectional Perimeter} \times \text{Reaction Zone Length} \quad (2)$$

Since it has been assumed that the reaction zone length is approximately constant for any shape, the pertinent parameters of charge geometry are simply cross-sectional area and cross-sectional perimeter. If these are the important features in determining the critical condition for detonation of any shape, they also must be applicable to cylinders. In addition, since it is known that for cylinders only one geometrical parameter (i.e., charge diameter) is necessary to do this; in the cylindrical case, these features must combine to give charge diameter, d . Thus for a cylinder the cross-sectional area, A is

$$A = \frac{\pi d^2}{4} \quad (3)$$

and cross-sectional perimeter, P is

$$P = d \quad (4)$$

The proper combination must be $(4 A/P)$ since

$$\frac{4A}{P} = \frac{4 \left[\frac{\pi d^2}{4} \right]}{\pi d} = d \quad (5)$$

Therefore, the critical condition for the cylinder becomes

$$\left[\frac{4A}{P} \right]_c = d_c \quad (6)$$

as expected. Because the proper combination of geometrical features has been found in the particular case, Equation 6 may be generalized, using Assumption (1), page A-5, to define the critical criterion in the

general case, as

$$\left[\frac{4A}{P} \right]_c = \sigma \quad (7)$$

where

σ = the "critical geometry"

Based on Assumption (2), page A-5, this may be further generalized by observing that, if d_c is the critical geometry for the cylindrical case (Equation 6), it must also be the critical geometry for all shapes. Thus,

$$\sigma = d_c \quad (8)$$

and Equation 6 can be assumed to be applicable to all shapes.

To use this equation for determining the critical values of the parameters that describe a given shape, the area and perimeter of that shape are written in terms of these parameters, and $(4A/P)$ is found. Criticality results when this becomes equal to d_c . Solving this equation for the parameters gives their critical values in terms of d_c . This has been done for a variety of nonperforated cross-sectional shapes and the results are shown in Figure A-1. Of particular interest is the result for a rectangle of infinite (large) width. In this case the theory predicts criticality when the thickness is one-half the critical diameter of a cylinder.

Although the same theory may be applied to various perforated shapes as shown in Figure A-2 (the perimeter used is the sum of the outside and inside perimeters), it should be noted that the lateral expansion waves in the perforated sections may affect one another (i. e., interact) in such a way as to delay rarefaction waves, and thus, to reduce the loss of energy. Accordingly, the results in Figure A-2 may be considered conservative in that the critical dimensions may be smaller than those indicated. In any instance, it is of interest to note the result for a circular core, wherein, for criticality the web thickness need only be one-half the critical diameter of a cylinder.

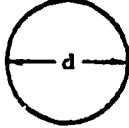
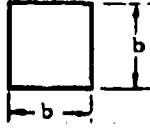
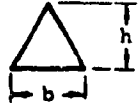
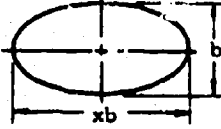
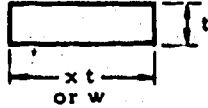
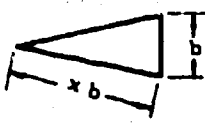
SHAPE AND CHARACTERIZING DIMENSIONS	CRITICAL VALUE OF CHARACTERIZING DIMENSIONS
<p>CIRCLE</p> 	$d_c = d_c$
<p>SQUARE</p> 	$b_c = d_c$
<p>EQUILATERAL TRIANGLE</p> 	$b_c = (\sqrt{3}) d_c \text{ or } h_c = \left(\frac{3}{2}\right) d_c$
<p>ELLIPSE</p> <p>WHERE: $x > 1$</p> 	$b_c = \left[\frac{\int_0^{\pi/2} \sqrt{1 - \frac{x^2 - 1}{x^2} \sin^2 \phi} d\phi}{\pi} \right]$ $b_{c\infty} = \lim_{x \rightarrow \infty} b_c = \frac{d_c}{\pi}$
<p>REC/ANGLE</p> <p>WHERE: $x > 1$</p> 	$t_c = \left(\frac{x+1}{2x} \right) d_c$ $t_{c\infty} = \lim_{x \rightarrow \infty} t_c = \frac{d_c}{2}$ <p>or if w is fixed</p> $t_c = \frac{w d_c}{2w - d_c}$
<p>ISOSCELES TRIANGLE</p> <p>WHERE: $x > 1$</p> 	$b_c = \sqrt{\frac{2x+1}{2x-1}} d_c$ $b_{c\infty} = \lim_{x \rightarrow \infty} b_c = d_c$

Figure A-1. Critical Dimensions of Various Shapes
Nonperforated Grains.

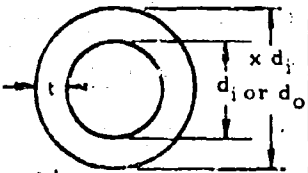
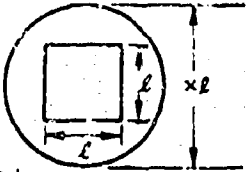
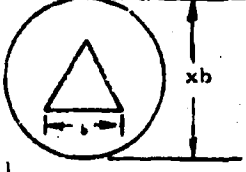
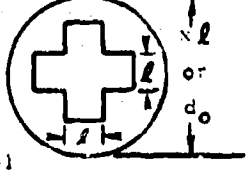
SHAPE AND CHARACTERIZING DIMENSIONS	CRITICAL VALUE OF CHARACTERIZING DIMENSIONS
<p>CIRCULAR CORE</p>  <p>WHERE: $x > 1$</p>	$d_{1c} = \left(\frac{1}{x-1} \right) d_c \quad \text{or} \quad t_c = \frac{d_c}{2}$ <p>or if d_i is fixed</p> $d_{oc} = d_i + d_c$
<p>SQUARE CORE</p>  <p>WHERE: $x > 1$</p>	$l_c = \left(\frac{\pi x + 4}{\pi x^2 - 4} \right) d_c$
<p>EQUILATERAL TRIANGLE CORE</p>  <p>WHERE: $x > 1$</p>	$b_c = \left(\frac{\pi x + 3}{\pi x^2 - \sqrt{3}} \right) d_c$
<p>CROSS CORE</p>  <p>WHERE: $x > 1$</p>	$l_c = \left(\frac{\pi x + 12}{\pi x^2 - 20} \right) d_c$ <p>or if l is fixed</p> $d_{oc} = \frac{d_c}{2} \left[1 + \sqrt{1 + \frac{16l}{\pi d_c} \left(5 \frac{l}{d_c} + 3 \right)} \right]$

Figure A-2. Critical Dimensions of Various Shapes
Perforated Grains.

A-2.2 Initiation of Detonation

A-2.2.1 General

The fact that a material will sustain detonation does not indicate the ease or difficulty in initiating the detonation. To investigate the initiation of supercritical configurations, the effects of intensity, configuration, and location of the donor must be determined. Intensity is important since for any explosive (acceptor) there is a critical shock pressure below which no detonation will occur regardless of the size or shape of the acceptor or of the duration of the shock pressure*. Also, different acceptor geometries may require different intensities for detonation. Donor configuration and location are important, since the spatial distribution of the shock produced determines if initiation will lead to sustainment.

Because these variables can take on many values, the concept of initiation is discussed for the symmetrically end-initiated right-solid cylinder first, and then extended to more complex systems.

A-2.2.2 Initiation Concept

Shock Sensitivity:

Because shock pressure is considered the most important parameter in causing shock-initiated detonation, the sensitivity (i.e., ease of initiation) of a given material may be evaluated in terms of the minimum shock pressure required to initiate detonation. From this, a sensitivity (initiation) criterion can be determined as a property of the given material itself and independent of its shape. Based on this criterion, it is possible to determine whether a given donor will or will not cause initiation of detonation by determining if the stimulus imparted to the acceptor has met the criterion. The shock pressure transmitted to an acceptor will depend on the properties of the donor. Initiation of detonation will occur if, at any time in its propagation through the acceptor, the shockwave parameters are such that the sensitivity criterion is met.

Because the criterion is independent of grain shape, it is most easily determined by reference to the simplest case; symmetrically end-initiated right-solid cylinders.

*Shock-pressure duration is also important and is discussed further on page A-23, Pressure Pulse Duration.

Cylindrical Systems - Initiation Criterion:

It has been well established that detonation velocity for right-solid cylinders increases with charge diameter from a minimum at the critical diameter to an asymptotic maximum at the ideal diameter.

From this it is proposed that the minimum shock pressure, P^+ , ("P-cross") required to initiate detonation varies with diameter. Since below d_c it is impossible for the explosive to sustain detonation, it can be assumed that P^+ at d_c is a maximum. As diameter increases, it is expected that P^+ decreases and flattens out in the "ideal" region. Figure A-3 is a representation of such a plot. The asymptote is P^* ("P-star"), the shock pressure required to initiate detonation in the "ideal" region. This plot of Figure A-3 indicates a spatial-intensity relationship that is necessary for initiation, i.e., the initiation criterion. Any pressure-diameter condition above the line ("Go" region) will give initiation; conditions below ("No-Go" region) will not. Therefore, the initiation criterion is seen to contain two parameters A^+ and h , as shown in Figure A-22, and presented on Page A-23, the criterion contains at least three parameters, the following arguments are not impaired. This sensitivity curve was experimentally established recently for a detonable propellant. The results are shown in Figure A-4. This was established by determining the minimum shock pressure necessary to cause initiation using various diameter card-gap tests, and applying the Hugoniot method to the results.

Since this criterion is applicable only to cylindrical systems, it must be extended so that it is also applicable to noncylindrical systems, and thus be a property of the material used. Before extending this criterion to noncylindrical systems, it would be desirable to see how the criterion in the cylindrical case can be used to determine if initiation will occur with a given donor.

Cylindrical Systems - Shock Pressure Initiation:

Consider a cylindrical donor placed symmetrically at the end of a cylindrical acceptor as shown in Figure A-5. The cylindrical initiation criterion can then be combined with donor geometry consideration to see if initiation occurs, i.e., if the "Go" region in Figure A-3 will be reached.

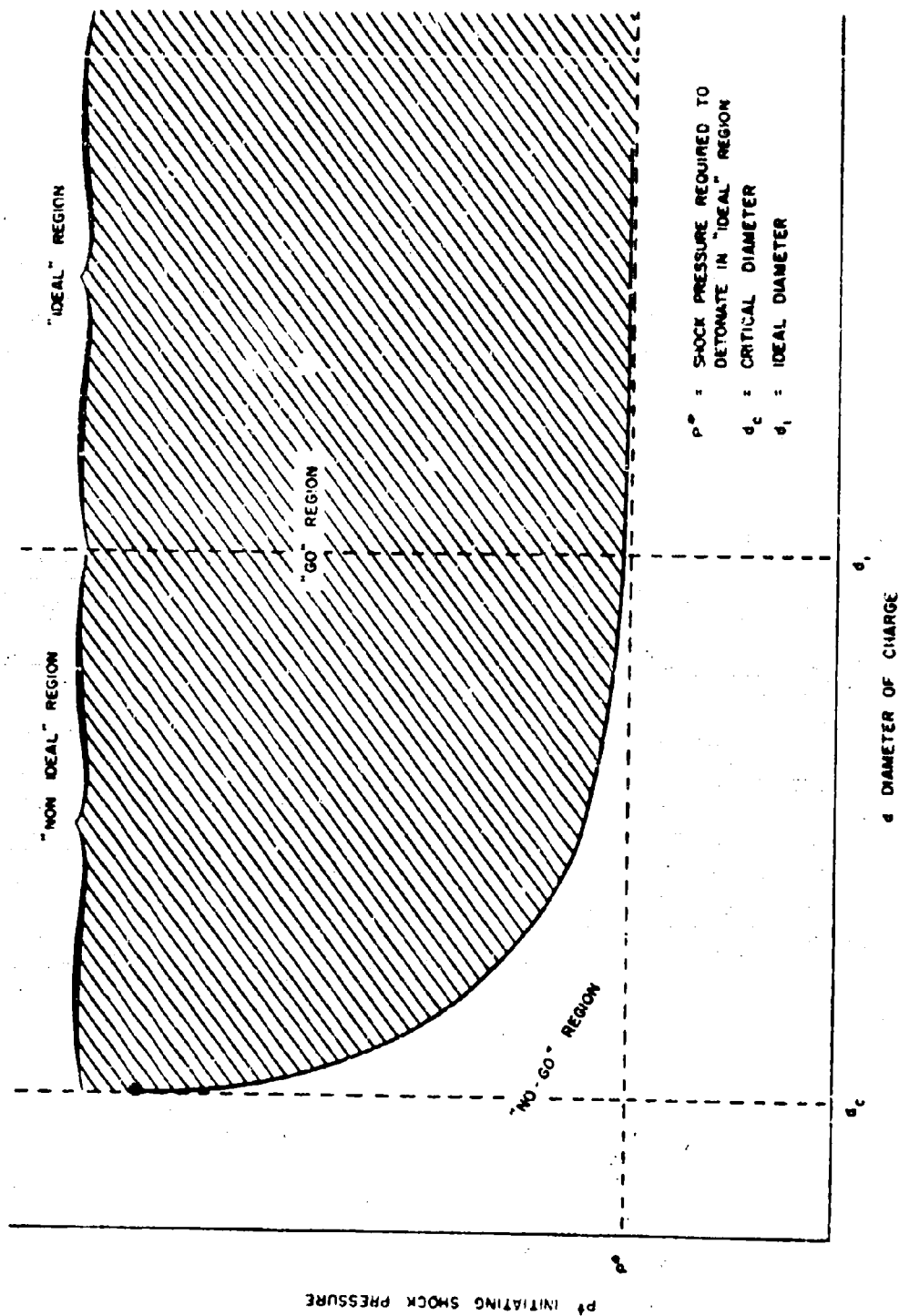


Figure A-3. Shock Pressure Required to Initiate Detonation Versus Diameter of Charge - Initiation Criterion.

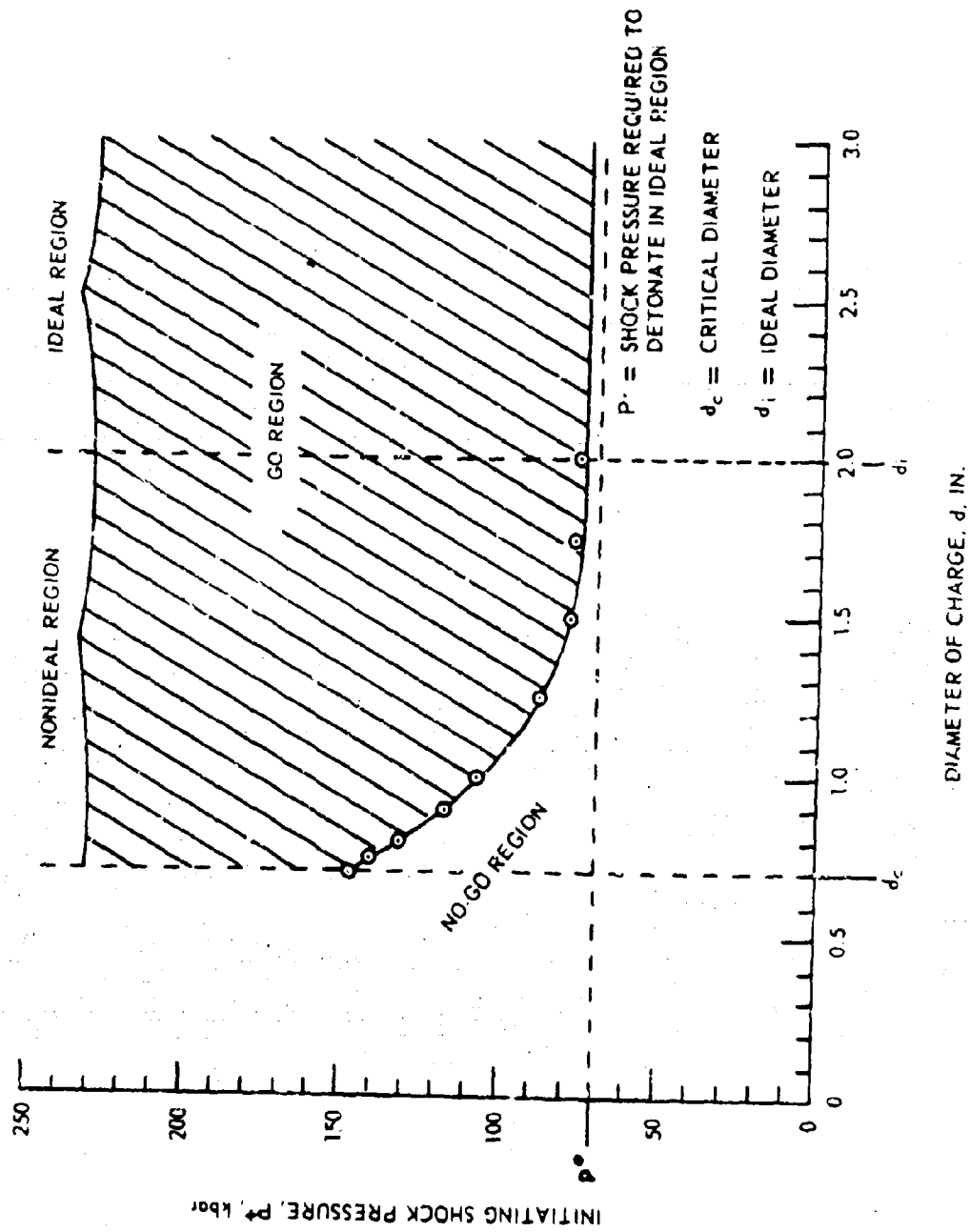


Figure A-4. Shock Pressure Required for a Detonable Propellant.

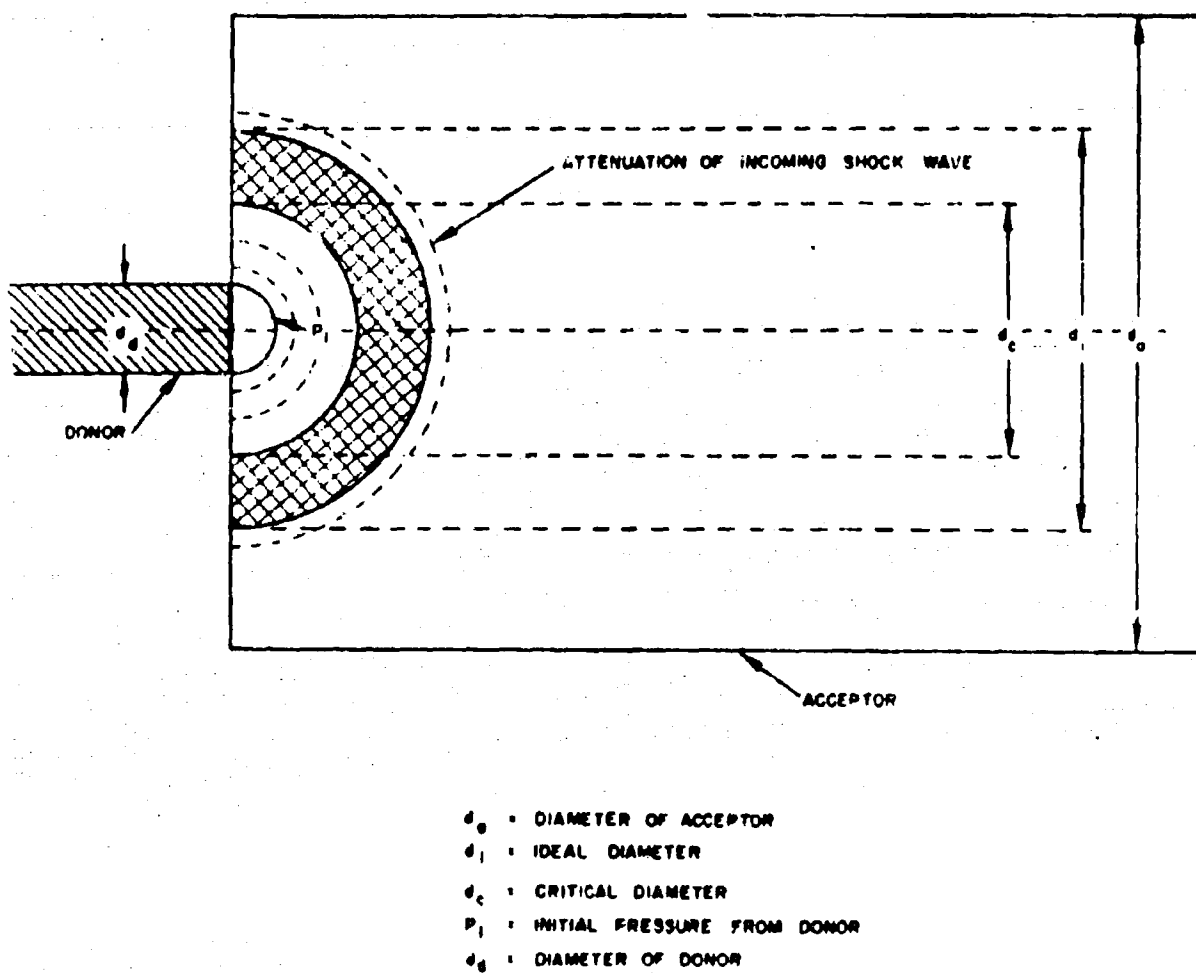


Figure A-5. Attenuation of Incoming Shockwave in Acceptor.

After the donor detonates*, a shockwave enters the acceptor and immediately begins to attenuate as depicted by the concentric semi-circles in Figure A-5.

Knowledge of how this wave attenuates in a given case gives the relation between pressure and the maximum diameter of the wave, d , in the acceptor. If the donor gives an initial shock pressure (P_i , Figure A-5), in the acceptor such that $P_i < P^*$ (Figure A-3), no initiation will occur for any donor (or acceptor) shape. In the case where $P_i > P^*$, three possible conditions exist:

Case 1: $d_{\text{donor}} < d_c$

Case 2: $d_c \leq d_{\text{donor}} \leq d_i$

Case 3: $d_{\text{donor}} > d_i$

In Case 1, the shockwave will start at a diameter smaller than the critical diameter of the acceptor but at an intensity greater than P^* . In this case, d can be treated as a variable. Two possible types of attenuation that vary with d may be considered. These attenuation curves, superimposed on Figure A-3, are illustrated in Figure A-6. For Curve 1, the transmitted pressure P_i is greater than P^* and will thus cause local reaction as it begins to attenuate. However, these local reactions will not cause sustained detonation. Since this curve, as drawn, always stays below the "Go" region, no sustained detonation can occur and the local reactions will die out when the pressure has attenuated below P^* .

For Curve 2, local reaction only will take place until the curve has entered the "Go" region at d^+ (d -cross). At this point, detonation will begin at a rate commensurate with d^+ as read from the D vs d plot (Figure A-6). Wave attenuation has no meaning after detonation begins (dotted line). The velocity will increase to D_i as the detonation front expands to the full diameter of the charge (Figure A-6). Since Curve 2 may cross into "Go" region at any point on the P^+ vs d curve, d^+ may be anywhere between d_c and d_i , and the corresponding initial velocity will be known from the D vs d plot. It is clear that for Case 1, even though the donor diameter is smaller than the critical diameter of the

* The donor diameter may be considered to be above its own ideal diameter in all cases.

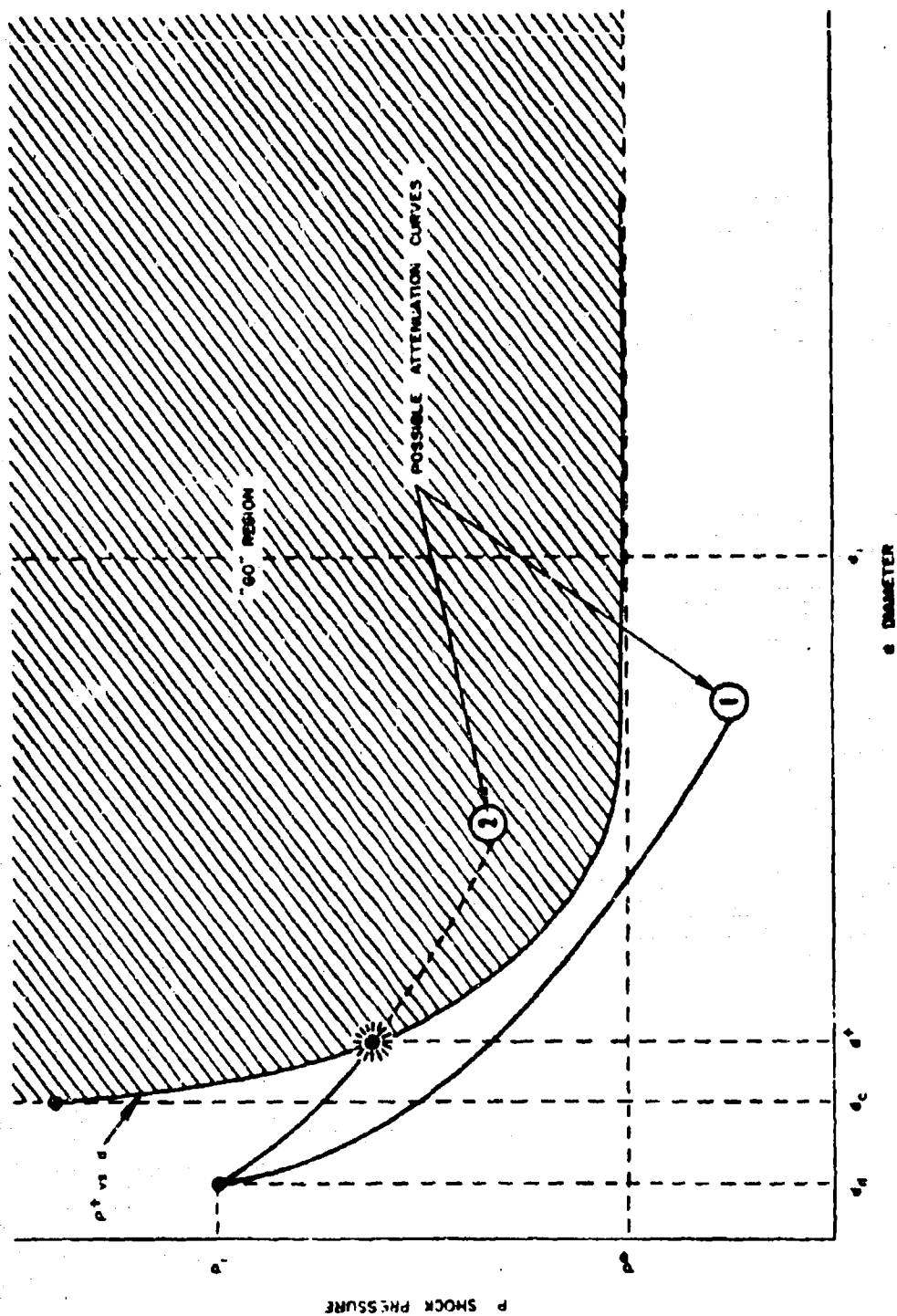


Figure A-6. Effect of Different Shock Attenuation Curves on Initiation of Detonation (Case 1. $d_{\text{donor}} < d_c$).

acceptor, detonation can occur. Whether detonation occurs or not depends on d_{donor} , P_i , P^+ vs d , and the rate of attenuation of P_i .

Case 2 may be visualized in much the same way as Case 1 except that three possibilities exist. These are illustrated by Curves 1, 2, and 3, Figure A-7. If P_{i1} is greater than P^+ for the particular diameter (i.e., d_{donor}), then detonation will begin immediately (Curve 1). This detonation will start at some velocity higher than given in the D vs d plot (i.e., overboosting) and the velocity will reduce in some complex manner to D_i . This will be complex since the detonation wave is increasing in size from d_{donor} to d_{ideal} , which tends to increase its velocity, while overboosting leads to a reduction in velocity toward the unique steady-state condition shown in the D vs d plot. Once the detonation velocity has reached D_i it will continue at this velocity indefinitely as long as d_{acceptor} is greater than d_i .

It is also possible for P_{i2} to be less than P^+ for a given d_{donor} . In this case, the attenuation may proceed along either of two curves (Curves 2 and 3, Figure A-7). For Curve 2, only local reaction is expected until P_{i2} has attenuated to P^* . Curve 3 is identical to Curve 2 in Figure A-6 in that local reaction will occur until the curve enters the "Go" region (which can be at any point along the P^+ vs d curve). At that point, detonation will begin at a velocity commensurate with d^+ . Again, wave attenuation is meaningless after detonation begins. From these possibilities, detonation may or may not occur even where d_{donor} is greater than the critical diameter but less than the ideal diameter.

For Case 3 ($d_{\text{donor}} > d_i$), the detonation will begin immediately. Again, overboosting (i.e., $P_i > P^*$ in the "Go" region) will cause the initial velocity to be greater than D_i . However, the velocity will decrease to D_i in a simple manner since there are no diameter effects.

As indicated, the way in which the incoming wave attenuates will determine whether, in a given case, the "Go" region will or will not be reached. Thus, the dotted concentric semi-circles in Figure A-5 which represent pure spherical attenuation, are only schematic in that attenuation (especially with local reaction) takes place in a more complex manner.

From this discussion, symmetrical right-solid cylindrical systems can be evaluated for initiation of detonation by establishing a sensitivity criterion previously stated and determining if this criterion is met. This was done for the propellant previously mentioned.

for hypervelocity pellet impact (i.e., the donor). The method was used to predict if a pellet of a given velocity and size would or would not initiate detonation in the propellant. The agreement with the experimental data was excellent.

Noncylindrical Systems - Initiation Criterion:

From the analysis of the cylindrical system, it is possible to develop a more general initiation criterion for any shape. This can be accomplished by noting in Figure A-3 that the "Go" region is bounded by a shock pressure-diameter condition. Based on kinetics and heat transfer considerations, it is likely that the bounding curve is a shock pressure-area condition. That is, initiation will take place when a given shockwave in the acceptor has a sufficient shock pressure covering a sufficient area. In this case, Figure A-3 would be replotted as in Figure A-8, where A_c is the critical area of the material corresponding to the critical diameter and A_i is the ideal area corresponding to the ideal diameter. Figure A-9 shows the same transformation for the data in Figure A-4. Because a shock pressure-area condition does not depend on the shape of the charge, the initiation criterion becomes independent of the cylindrical system (although it is most easily found in the cylindrical system) and is applicable to any shape. The initiation criterion therefore becomes a property of the given material only.

Noncylindrical Systems - Shock Pressure Initiation:

Using this new criterion it is possible to determine if initiation will take place with a given donor (of any configuration and location) through an analysis similar to that described in a previous section. That is, will the "Go" region (Figure A-8) be reached by the input shock stimulus.

Since there are no restrictions on the acceptor shape, or on the donor configuration or location, the way in which the input shockwave attenuates (i.e., how shock pressure and area of the wave vary) can be complex. It is possible for the wave to move in and out of the "Go" region because of the acceptor geometry (e.g., side initiation of a hollow-core cylinder). However, it is anticipated that for any given shape, and donor configuration and location, the shock pressure area history of the input shock may be followed by solid geometry considerations (e.g., the area of the intersection of a spherical donor wave and a hollow-core cylindrical acceptor) and hydrodynamic theories of attenuation. Such an analysis will probably require the use of high-speed computer techniques.

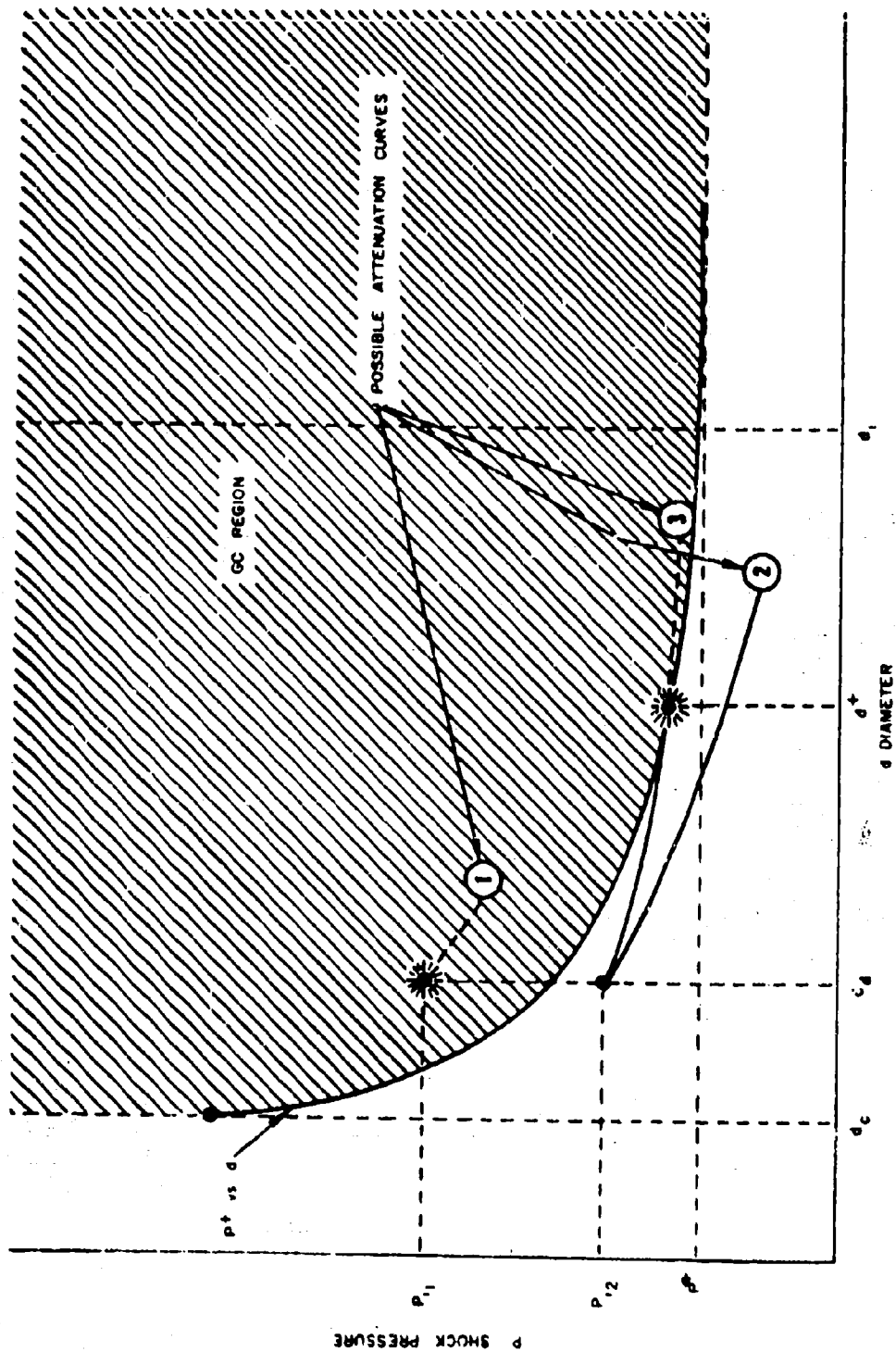


Figure A-7. Effect of Different Shock Attenuation Curves on Initiation of Detonation (Case 2, $d_c \leq d_{\text{donor}} \leq d_1$).

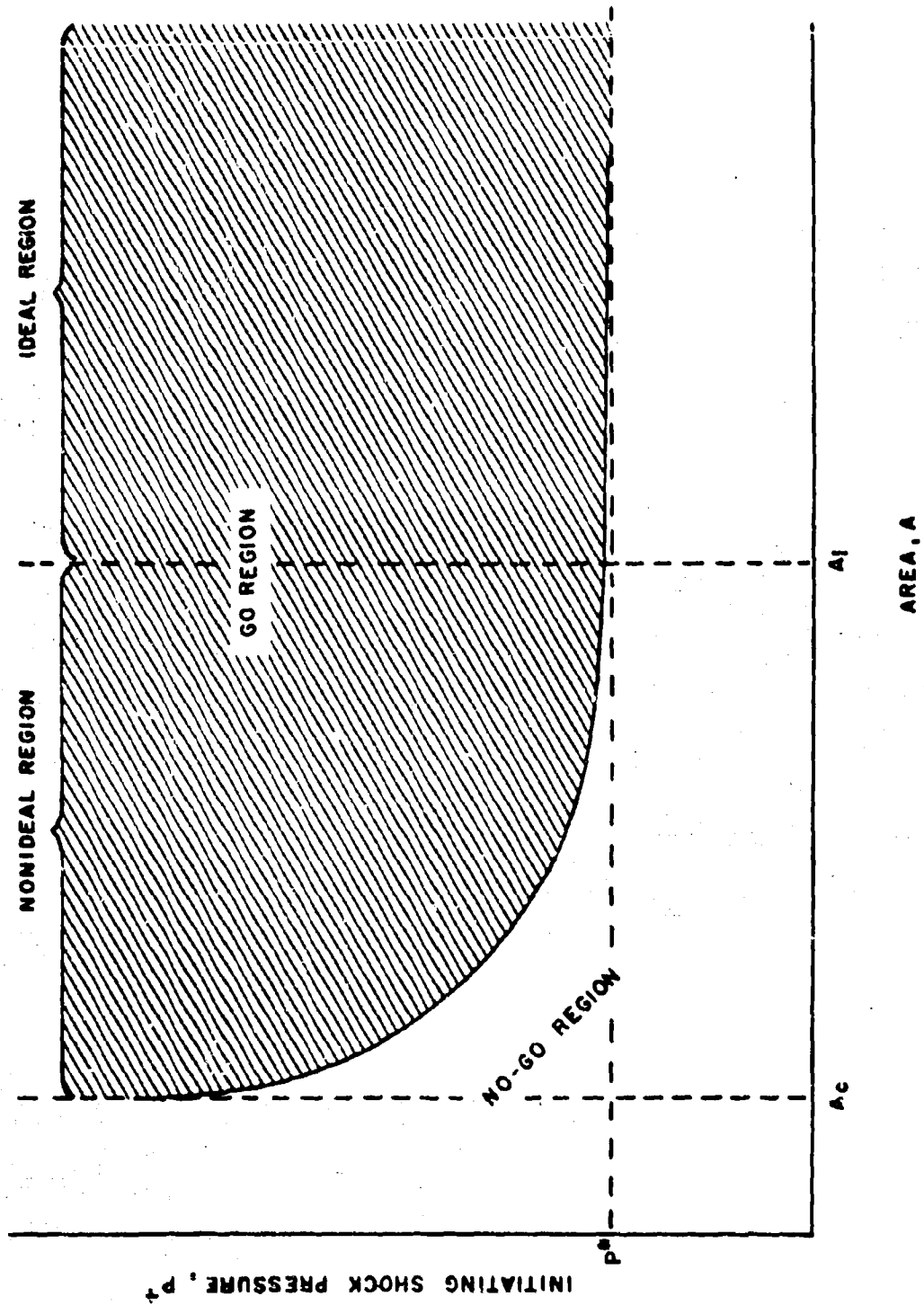


Figure A-8. Shock Pressure Required to Initiate Detonation Versus Area of Wave-Initiation Criterion.

2418-8-1

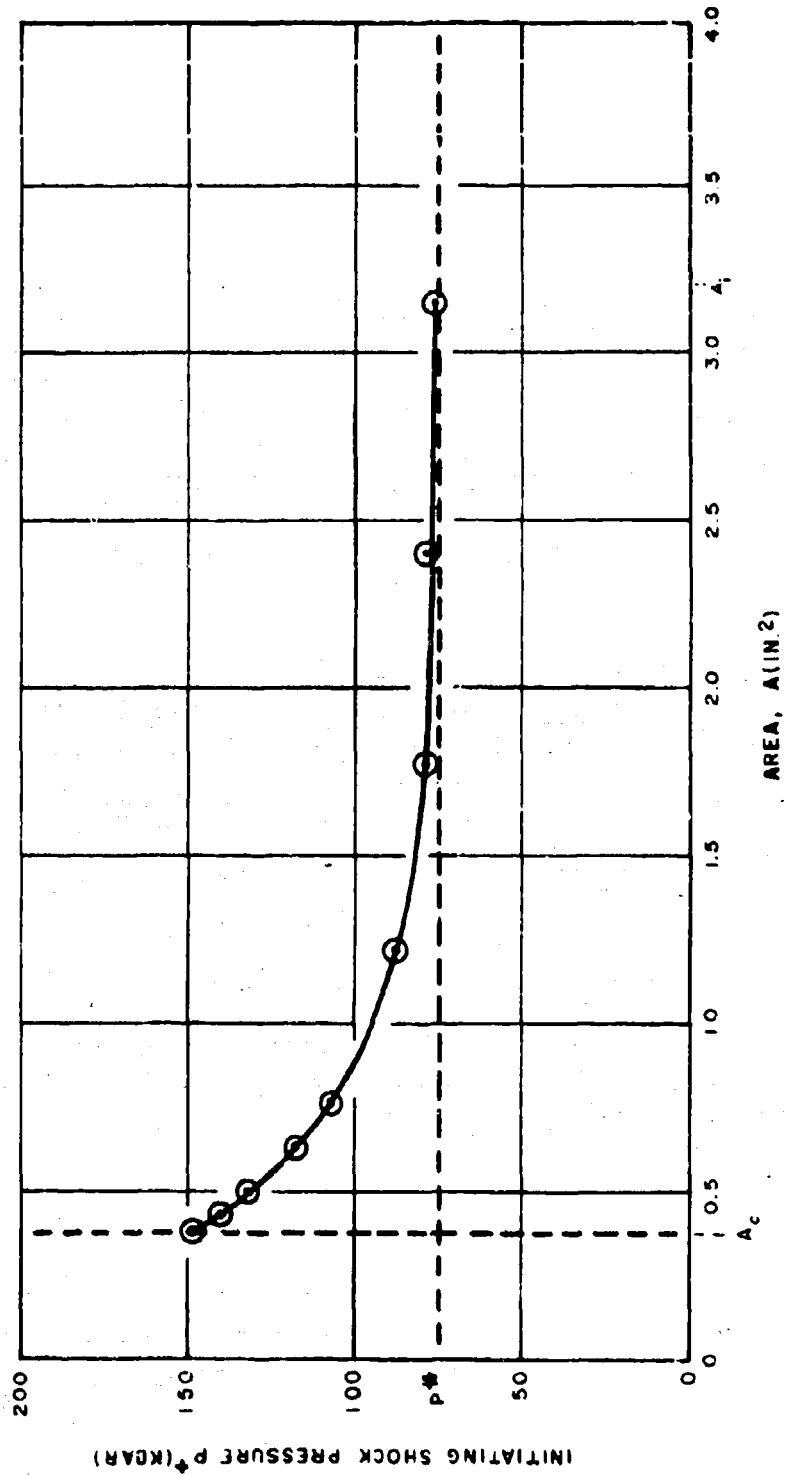


Figure A-9. Shock Pressure Required to Initiate Detonation Versus Area of Wave for a Detonable Propellant-Initiation Criterion.

2418-1

Further Considerations:

a. Pressure Pulse Duration

As indicated in a previous section, the initiation criterion contains three parameters instead of the two; shock pressure, and area. This aspect of the problem, which has not yet been considered, is the effect that the time duration of the pressure pulse in the acceptor has upon initiation. From arguments similar to those previously presented, one would predict the existence of curves of initiating shock pressure, P^+ , vs pulse width, w , at a given area over which the shockwave is applied, similar to the P^+ vs A plot, Figure A-8. A three-dimensional plot of P^+ , A , and w (pulse width) would then form a surface separating the "Go" from the "No-Go" regions. By analogy with Figure A-8, a "Go" would result whenever a shock attenuation curve touches or penetrates this surface.

This situation may be visualized in Figure A-10 which is a plot of shock pressure, P , vs area, A , and pulse width, w . The shaded surface represents a plot of P^+ vs A and w . This surface is bounded on the front by the plane of critical area, below which no value of pressure or pulse width can cause initiation. On this plane, there are finite values of pressure that will cause detonation depending on the pulse width.

The "Go" surface is asymptotically bounded on the left by a plane of critical pulse width, w_c , below which initiation cannot occur for any pressure or area. On this plane, the pressure required to initiate is infinite, for any area. This plane must exist since as the pulse width becomes smaller the time allowed for the initiation reaction becomes shorter. A point is reached where the chemical reaction cannot get started because the shock pressure, no matter how high, is not applied long enough.

For large values of w , and for any value of A , the surface asymptotically approaches a plane. This is called the plane of P^* , and represents the minimum pressure below which initiation cannot occur even for infinite pulse width and area. In Figure A-8, the indicated value of P^* represents a minimum value of the required initiating pressure for a given pulse width and large values of A . In Figure A-10, the individual minimum values for a given pulse width (P vs A curves) become lower as the pulse width increases and, as w approaches infinity, there is a lower limit of the individual minimums. That is, for infinite pulse width, there is still a pressure below which initiation will not occur. In Figure A-8, the same minimum pressure is approached as A increases in the "ideal" region (P vs w curves in Figure A-10). This new minimum pressure becomes a redefinition of P^* (as described in a previous section) and is represented by a plane in Figure A-10 that bounds the surface on the bottom for large values of w .

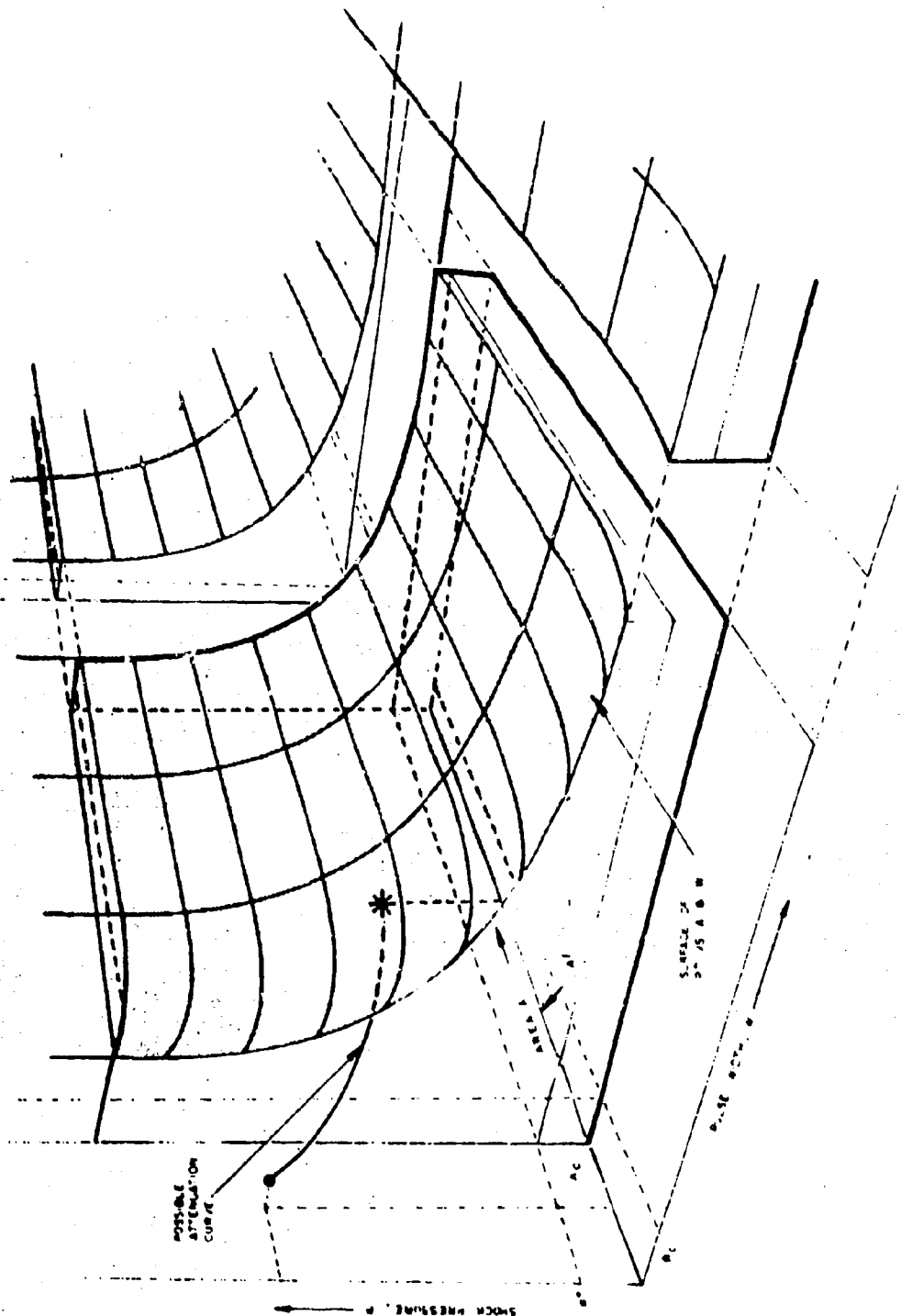


Figure A-10. Shock Pressure (P) Versus Area (A) and Pulse Width (w).

By analogy with Figure A-5, any condition lying above this surface and inside the bounds described, represents the "Go" region; any condition below this surface, or outside these bounds, represents the "No-Go" region. In Figure A-10, a shock attenuation curve intercepts this surface, indicating initiation of detonation at that point. As is previously described, this detonation will begin with a velocity commensurate with d^+ (found from A^+) as read from the D vs d plot.

Other types of attenuation curves may be similarly evaluated to see if they will or will not enter the "Go" region and initiate detonation.

The P^+ vs w and A surface shown in Figure A-10 represents the initiation properties of the acceptor material and is independent of the shape of the material in the same way as the P^+ vs A curve of Figure A-8 represented a property of the acceptor material. It should also be noted that, in this case, the initiation takes place when a given shock-wave in the acceptor has a sufficient shock pressure covering a sufficient volume. This concept of initiation is in agreement with current theory.

Although the initiation criterion, as pictured in Figure A-10, is more complete, it complicates analysis since the input wave in a given case must be analyzed for pulse width as well as for shock pressure and area.

b. Pressure Pulse Shape

Another important aspect of the problem of initiation which was not considered in the discussion is the effect of the shape of the pressure pulse. This shape would affect the kinetics of the initiation reaction and thus alter the initiation criterion as depicted in Figure A-10. For a given pressure, pulse width, and area, a variation in the pulse shape might shift a particular condition from the "Go" to the "No-Go" region, or vice versa.

c. Distribution of Parameters-Integrated Properties

In a real shockwave, the pressure, pulse width, and wave shape will be different in different parts of the wave. Therefore, a distribution of these parameters in space is to be expected and the concept of a simple initiation criterion, and the requirements for meeting this criterion, might become vague. To avoid the many-dimensional nature of this problem, and to provide a simple method of analysis, it may be possible to use area and the integrated value of pressure over the pulse width

(thus including the shape) and the entire wave, as the initiation criterion. Thus, Figure A-8 would become a plot of Q vs A where Q is given by:

$$Q = \iiint P \, dx \, dy \, dz,$$

and x, y, z are the three space coordinates. In this case, the Q and area of an input shockwave would be followed as it attenuates and initiation would occur if the Q -area value reached the "Go" region.

This approach is considered tentative in that it may or may not be necessary. The initiation criterion previously described may prove satisfactory in practice.

0866-01(01)FP

APPENDIX B

**APPLICATION OF TWO DIMENSIONAL COMPUTATIONS
TO THE STUDY OF SUB-CRITICAL INITIATION AND
FADEOUT IN A HOMOGENEOUS EXPLOSIVE**

APPLICATION OF
TWO DIMENSIONAL COMPUTATIONS TO THE STUDY OF
SUB-CRITICAL INITIATION AND FADEOUT
IN A HOMOGENEOUS EXPLOSIVE

L. Zernow
E. A. Tkachenko
Nancy B. Brooks
R. L. Lansdale
G. E. Lewis

JULY 1965

SUMMARY REPORT

Submitted To
Aerojet-General Corporation
On Sub-Contract D-454840-OPD

BY

SHOCK HYDRODYNAMICS, INC.
15010 VENTURA BOULEVARD
SHERMAN OAKS, CALIFORNIA

TABLE OF CONTENTS

	Page
1. INTRODUCTION	1
2. NATURE OF THE PROBLEM	1
3. GENERAL DESCRIPTION OF THE SHEP PROGRAM	2
3.1 GENERAL	2
3.2 FORMULATION	2
3.3 FUNDAMENTAL EQUATIONS	3
4. SOLUTION OF ONE- AND TWO- DIMENSIONAL DETONATION PROBLEMS BY MEANS OF THE SHEP PROGRAM	7
4.1 GENERAL	7
4.2 EQUATION OF STATE FOR NITROMETHANE	7
4.3 RATE OF CHEMICAL ENERGY RELEASE	10
4.4 INDUCTION TIME	11
4.5 COMPUTATIONAL TECHNIQUE OF COMBINING HYDRODYNAMIC AND CHEMICAL KINETIC INTEGRATION	12
5. OVERALL COMPUTATIONAL PLAN	14
6. RESULTS OF COMPUTATIONS	15
6.1 INERT CYLINDER - 2D	15
6.2 1st REACTIVE CASE - 1D CONSTRAINED	15
6.3 2D - REACTIVE CASES	16
7. ANALYSIS OF 2D COMPUTATIONS	16
7.1 CONSTRUCTION OF THE CURVED DETONATION FRONT	17
7.2 PRESSURE-TIME HISTORY AS AFFECTED BY DIAMETER	17
8. COMPUTATION OF PARTIAL YIELDS FOR SUB-CRITICAL CASES	17
9. LOCATION OF THE REACTIVE-TO-UNREACTIVE SHOCK TRANSITION	18

TABLE OF CONTENTS (Cont'd)

	Page
10. INHOMOGENEOUS MODEL - 1D STUDIES	19
10.1 BASIS FOR THE MODEL	19
10.2 CHARACTERISTICS OF INHOMOGENEOUS SYSTEMS	20
10.3 RESULTS OF COMPUTATIONS	20
11. COMPARISON OF COMPUTED AND LITERATURE VALUES OF DETONATION CHARACTERISTICS OF NITROMETHANE	22
11.1 CRITICAL DIAMETER (UNCONFINED)	22
11.2 INDUCTION TIMES	22
11.3 DETONATION VELOCITIES	23
12. CONCLUSIONS	24
REFERENCES	

1. INTRODUCTION

The critical diameters of composite non-porous propellant systems have¹, in the past, been estimated to range from 10' - 50'. The enormous cost of the experimental effort required to reliably determine the critical diameter has long been apparent. These potential costs provide a very strong incentive for the generation of a realistic theoretical model capable of providing estimates of the critical diameter based upon the physical and chemical nature of the propellant and the nature of the initiating pulse. Such a model would be particularly valuable if it could provide the highly desirable information concerning the transient behavior and partial yields in the sub-critical region.

2. NATURE OF THE PROBLEM

It is quite evident that the analysis of the two dimensional flow with the boundary conditions involved in critical diameter analysis, can only be handled rigorously by means of machine computational techniques. Previous analytical approximations including the Jones model² and the Eyring model³ are severely limited because the essentially one-dimensional approximations involved eliminate important elements of realism. They are also essentially steady state analyses, although the Eyring theory has been extended to the non-steady state regime.

Previously reported numerical studies of the transient initiation problem have either been one-dimensional or have involved the analyses of the two-dimensional flow around a single imperfection.

The major goals of the research program described here and its guiding philosophy are as follows:

(1) The major goal has been the determination of the feasibility of attainment of a capability to compute the two-dimensional combined hydrodynamic and chemical kinetic aspects of the transient initiation problem for a simple circular cylinder initiated at one end.

(2) If this capability could be attained, it was to be followed by the application of such computations to the sub-critical transient regime of a cylindrical homogeneous reactive system, where choice of nitromethane as the particular homogeneous reactive system, was based primarily upon the ready availability of a good equation of state and reliable chemical kinetic data. This would minimize the effort required in connection with acquisition of input data, and maximize the effort in establishing feasibility of the technique.

The specific approach used in this research program and the results obtained are described in this report.

3. GENERAL DESCRIPTION OF THE SHEP PROGRAM

3.1 GENERAL

The SHEP program, written in FORTRAN II language, represents a computational procedure which is capable of treating one- and two-dimensional time dependent hydrodynamic-chemical kinetic, elastic, and elastic-plastic phenomena in compressible homogeneous isotropic media. As applied to detonation phenomena, the SHEP program makes possible the simultaneous numerical solution of the fundamental equations which include

- (a) Equation of motion,
- (b) Equation of continuity,
- (c) Energy equation,
- (d) Chemical reaction rate equation, and
- (e) Equation of state

for a cylindrically symmetrical charge, yielding details of the process of shock initiation of detonation, or of the failure of detonation. A brief discussion of the general computational approach is as follows.

3.2 FORMULATION

The SHEP program is based on a Lagrangian formulation employing a convective coordinate system which moves and distorts with the material. For cases in which the material undergoes severe distortion, an "overlay" process provides a means for redefining a deformed grid system into a new, undeformed grid system. The integration of the partial differential equations describing the hydrodynamic-chemical kinetic processes is performed by a numerical procedure which is based on finite difference techniques in both the space and time variables. For problems in which shock and detonation waves develop, an "artificial viscosity" term, which is part of the computational formulation, provides stability of the numerical procedure in the vicinity of the shock or detonation wave.

Initial conditions for a particular computation consist of dividing the plane of symmetry passing through the longitudinal axis of the cylindrical body of given dimensions into small rectangular areas or "cells," and specifying initial conditions of stress, strain, velocity, density, and internal energy for these cells. After initiation of the computational process, initially rectangular cells may deform into non-rectangular quadrilaterals depending on the hydrodynamic and chemical-kinetic conditions and the material properties existing in the various cells.

In order to carry out computations on detonation behavior one must supply the following input specifications to the SHEP program.

- (1) an equation of state for each of the materials involved (the equation of state must relate pressure, relative density and specific internal energy),
- (2) a chemical kinetic rate expression for reactive materials (the form of the rate expression as well as the values of any parameters appearing in the rate expression must be provided),
- (3) if elastic behavior is to be considered the shear modulus and Young's modulus must be furnished, and
- (4) if plastic flow is expected a value of the yield strength must be specified.

3.3 FUNDAMENTAL EQUATIONS

Expressing the basic equations of the SHEP program in cylindrical coordinates one obtains:

- (1) Equation of Motion:

$$\rho \ddot{z} = \frac{\partial \Sigma_{zz}}{\partial z} + \frac{\partial T_{zr}}{\partial r} + \frac{T_{zr}}{r}, \quad (1)$$

$$\rho \ddot{r} = \frac{\partial T_{zr}}{\partial z} + \frac{\partial \Sigma_{rr}}{\partial r} + \frac{\Sigma_{rr} - \Sigma_{\theta\theta}}{r},$$

where

$$\Sigma_{zz} = S_{zz} - (P + q),$$

$$\Sigma_{rr} = S_{rr} - (P + q),$$

$$\Sigma_{\theta\theta} = S_{\theta\theta} - (P + q)$$

- (2) Equation of Continuity:

$$\frac{\dot{V}}{V} = \frac{\partial \dot{z}}{\partial z} + \frac{\partial \dot{r}}{r} + \frac{\dot{r}}{r}, \quad (2)$$

- (3) Energy Equation:

$$\dot{E} = -(P + q) \dot{V} + V(S_{zz} \dot{\epsilon}_{zz} + S_{rr} \dot{\epsilon}_{rr} + S_{\theta\theta} \dot{\epsilon}_{\theta\theta} + T_{zr} \dot{\epsilon}_{zr}) + Q\dot{f}, \quad (3)$$

(4) Chemical Reaction Rate Expression:

$$\frac{\partial f}{\partial t} = A(1-f)^N e^{-\frac{E_0}{RT}} \quad (4)$$

(5) Equation of State:

(a) Elastic behavior:

$$\begin{aligned} \dot{s}_{zz} &= 2\mu \left(\dot{\epsilon}_{zz} - \frac{1}{3} \frac{\dot{V}}{V} \right) + \delta_{zz} \quad , \\ \dot{s}_{rr} &= 2\mu \left(\dot{\epsilon}_{rr} - \frac{1}{3} \frac{\dot{V}}{V} \right) + \delta_{rr} \quad , \\ \dot{s}_{\theta\theta} &= 2\mu \left(\dot{\epsilon}_{\theta\theta} - \frac{1}{3} \frac{\dot{V}}{V} \right) \quad , \\ \dot{s}_{zr} &= \mu (\dot{\epsilon}_{zr}) + \delta_{zr} \quad , \end{aligned} \quad (5)$$

where

$$\begin{aligned} \dot{\epsilon}_{zz} &= \frac{\partial \dot{z}}{\partial z}; \quad \dot{\epsilon}_{\theta\theta} = \frac{\dot{r}}{r} \\ \dot{\epsilon}_{rr} &= \frac{\partial \dot{r}}{\partial r}; \quad \dot{\epsilon}_{zr} = \frac{\partial \dot{r}}{\partial z} + \frac{\partial \dot{z}}{\partial r} \quad , \end{aligned}$$

(b) Hydrostatic behavior:

Any of the following five forms of the equations of state may be specified presently in the SHEP program

(i) Los Alamos Metal Fit

$$P = (A + B\epsilon + C\epsilon^2)(\epsilon_0 + \epsilon)^{-1} \quad (6)$$

where

$$\epsilon = \rho_0 \rho$$

and where $\rho_0, a_1, a_2, b_0, b_1, b_2, C_0, C_1$ are empirical constants

$$\mu = \eta - 1$$

$$A = \mu (a_1 + a_2 |\mu|)$$

$$B = b_0 + b_1 \mu + b_2 \mu^2$$

$$C = C_0 + C_1 \mu$$

(iii) Brode Tuff Equation of State Fit

$$P = \eta \{ a_1(e)^{1/2} + (a_2 + a_3(\eta))^{1/2}e + a_4e^2(a_5 + e)^{-1} \} \quad (7)$$

where a_1, a_2, a_3, a_4 and a_5 are constants

(III) Tabular Fit

Double linear interpolation on $\log \eta, \log e'$ is employed in a table of

$$P(\log \eta, \log e') \quad (8)$$

where $e' = e + e_0$

and where the table is uniform in $\log e'$, but not in $\log \eta$

(iv) Wilkins' Analytic Fit

$$P = A + B\epsilon, \quad (9)$$

where

$$\epsilon = \rho_0 e$$

$$A = a_0 + a_1\mu + a_2\mu\mu' + a_3\mu^3$$

$$B = b_0 + b_1\mu + b_2\mu^2 + b_3\mu^3$$

$$\mu = \eta - 1, \text{ and } \mu' = |\mu| \text{ if } C_\mu < 0$$

$$\mu' = \mu \text{ if } C_\mu \geq 0$$

where $\rho_0, a_1, a_2, a_3, b_0, b_1, b_2, b_3$, and C_μ are constants

(v) Gamma Law Gas

$$P = (\gamma - 1)\rho e, \quad (10)$$

(c) Plastic Behavior:

Von Mises Yield Condition:

$$(S_1^2 + S_2^2 + S_3^2) - (2/3)(Y^0)^2 \leq 0, \quad (11)$$

where Y^0 = material strength

and S_1 , S_2 , and S_3 are the principal stress deviators.

The notation in equations (1) through (11) is as follows:

z, r, θ	cylindrical coordinates
z	velocity in z direction
r	velocity in r direction
$\Sigma_{zz}, \Sigma_{rr}, \Sigma_{\theta\theta}$	total stresses
T_{zr}	shear stress
$S_{zz}, S_{rr}, S_{\theta\theta}$	stress deviators
$\epsilon_{zz}, \epsilon_{rr}, \epsilon_{\theta\theta}, \epsilon_{zr}$	strains
P	hydrostatic pressure
q	"artificial viscosity"
V	specific volume
E, e	specific internal energy
ρ	density
Q	heat of reaction
f	burn fraction
A	frequency factor
N	order of reaction
E_0	activation energy
R	ideal gas constant
T	temperature
η	compression = ρ / ρ_0

μ shear modulus in Eqn. (5), otherwise $\mu = 1 - \eta$

γ ratio of specific heats.

A detailed discussion of the finite difference equations for Equation (1), (2), (3), and (5) is presented in Reference (4). Equation (4) is solved by means of the Runge Kutta method considering the burn fraction and the specific internal energy which is related to temperature by $E = E_0 + C_V(T - T_0)$ as functions of time within a hydrodynamic finite difference time step.

4. SOLUTION OF ONE- AND TWO-DIMENSIONAL DETONATION PROBLEMS BY MEANS OF THE SHEP PROGRAM

4.1 GENERAL

Prior to discussing in some detail the computational results obtained by the SHEP program as applied to a homogeneous explosive, a brief statement of previous work in this field will be helpful. The first published results of the numerical integration of the one-dimensional time-dependent hydrodynamic equations including chemical energy release as related to the initiation of detonation appeared in 1959⁵. This work, as well as an investigation published shortly afterward⁶ achieved only qualitative agreement with experiment. Subsequently, one dimensional studies carried out for homogeneous explosives⁷⁻¹⁰ have shown much better agreement with experimental results.¹¹⁻¹² In addition, there have been two-dimensional studies of shock interactions with a single imperfection.¹³ However, no published results exist in the literature on the two-dimensional computation of initiation and failure of detonation in a homogeneous or inhomogeneous explosive charge as functions of charge radius. In order to be able to estimate the critical diameter, detonation velocity, detonation front curvature, detonation pressure, and the transient, sub-critical fadeout process, one must employ appropriate expressions for the equation of state and chemical reaction rate and also permit 2D boundary effects to influence the reaction. It is desirable first to apply the computational method to a homogeneous explosive before proceeding to the quite complex problem of treating the inhomogeneous case. For this reason a careful computational study of shock propagation, shock initiation of detonation and failure of detonation in nitromethane was undertaken, especially since quite reliable equation of state, chemical reaction rate and experimental data on detonation behavior for nitromethane are available. A discussion of the equation of state and chemical reaction rate expression for nitromethane employed in this study will be followed by a discussion of computational techniques of combining efficiently the numerical solution of the hydrodynamic and chemical kinetic differential equations, and by a discussion of computational results.

4.2 EQUATION OF STATE FOR NITROMETHANE

We believe the best recently developed equation of state for nitromethane to be

the one presented in Reference 14. This equation of state has been derived on the basis of work described in Reference 15 and can be stated as follows:

$$\begin{aligned}
 V - V_0 + \mu(\alpha) \left[1 + \frac{(P - \alpha) \left(\beta + \frac{\alpha}{2} \right)}{(P + \beta) (\alpha + \beta) \ln \left(1 + \frac{\alpha}{\beta} \right)} \right] &= 0 \\
 E - E_0 + P(V - V_0) + \mu(\alpha) \left(P - \frac{1}{2} \alpha \right) - \mu(\alpha) \frac{\left(\beta + \frac{1}{2} \alpha \right)}{(\alpha + \beta) \ln \left(1 + \frac{\alpha}{\beta} \right)} (\alpha - P) \\
 + (\alpha + \beta) \ln \left(\frac{P + \beta}{\alpha + \beta} \right) &= 0, \quad (12)
 \end{aligned}$$

where

$$\mu(\alpha) = \frac{1}{\alpha} \left[V_0 + \frac{(C_0')^2}{2\alpha\alpha} - \left[\left(V_0 - \frac{(C_0')^2}{2\alpha\alpha} \right)^2 - V_0^2 \right]^{\frac{1}{2}} \right],$$

where V specific volume

V_0 $0.8861 \text{ cm}^3 \text{ g}^{-1}$

P pressure

α 1.637

C_0' $1.647 \text{ km sec}^{-1}$

β 15.8 Kbar

along the Hugoniot curve

$$E_H = E_0 + \frac{1}{2} P_H \mu(P_H), \quad (13)$$

and

$$V_H = V_0 - \mu(P_H) \quad (14)$$

In Reference 14 a derivation of the thermal equation of state, $T = T(P, V)$, is given and calculated values of $C_V(T)$ and $C_V(V)$ for families of isobars and isentropes are given in graphical form. As shown by Equations (6) through (10), the SHEP program requires either a pressure explicit equation of state, or a tabulation of the P-V-E relationship such that $P(\log E, \log \eta)$, where $\log E$ varies by equal increments ($\Delta \log E$).

Evidently, it is not possible to solve for P explicitly (in terms of E and V) from Eqns. (12), so that a separate FORTRAN program was written to generate the required tabular values for use in the SHEP program. In order to facilitate the application of Newton's iterative method to Eqns. (12) to obtain the desired sets of P_i ($\log E_i$, $\log \eta_i$), the relationship of the parameter α to E at various constant V 's was calculated for the purpose of obtaining reasonably good estimates of α , thus reducing considerably the number of iterations.

namely, a contribution to the temperature due to the heat liberated by the decomposition, so that

$$T = T_0 + \frac{E - E_0}{\bar{C}_V} + \frac{Qf}{\bar{C}_V} \quad (20)$$

resulting in the final burn fraction rate expression:

$$\frac{\partial f}{\partial t} = A(1-f) \cdot \frac{\frac{-E_0}{\bar{C}_V} + \frac{R}{\bar{C}_V} (T_0 \bar{C}_V + E - E_0 + Qf)}{\quad} \quad (21)$$

For convenience one may let $E_0 = 0$. The values

$$\bar{C}_V = 0.41 \text{ cal g}^{-1} \text{ } ^\circ\text{K}^{-1}$$

$$Q = 1.28 \text{ K cal g}^{-1},$$

were employed in all calculations for nitromethane.

4.4 INDUCTION TIME

A good approximation of the induction time, which is that portion of the reaction time during which $f \approx 0$, may be obtained from Eqn. (21) as follows. Writing Eqn. (21)

$$\frac{\partial f}{\partial t} = A(1-f) \cdot \frac{\frac{-\epsilon/E_t}{1 + Qf/E_t}}{\quad}, \quad (22)$$

where $\epsilon = E_0 \bar{C}_V R^{-1}$,

$$E_t = T_0 \bar{C}_V + E,$$

and employing the approximation

$$\left(1 + \frac{Qf}{E_t}\right)^{-1} \approx 1 - \frac{Qf}{E_t},$$

4.3 RATE OF CHEMICAL ENERGY RELEASE

(I) Chemical Kinetic Rate Expression for Nitromethane

The rate expression for the thermal decomposition of nitromethane as presented in Reference 16 was chosen as the basis of Eqn. (4). It should be stated that this rate expression is the result of a study of the thermal decomposition of nitromethane by a static method over the range 653-703°K and at pressures ranging from 200 to 400 mm. Nitromethane decomposition was shown to be first order and homogeneous with a rate constant given by

$$k = A e^{-E_a/RT} \quad (15)$$

$$\text{where } A = 10^{14.6} \text{ sec}^{-1}$$

$$E_a = 5.36 \times 10^4 \text{ cal mole}^{-1}$$

Under the above experimental conditions, the main products of the decomposition are nitric oxide, methane, carbon monoxide and water with relatively small quantities of carbon dioxide, ethane, ethylene and nitrous oxide.

(II) Burn Fraction Expression

As shown by Eqn. (3), the rate of chemical energy release is expressed in terms of the burn fraction, which is defined as the fraction of mass reacted in a "cell" at a given time. Accepting that nitromethane decomposition is a first order reaction, from Equations (4) and (15) one obtains

$$\frac{df}{dt} = A(1-f)e^{-E_a/RT} \text{ sec}^{-1} \quad (16)$$

Since the SHEP program does not contain temperature as a variable, but specific internal energy, T in Eqn. (16) must be related to E . Employing the definition

$$\left(\frac{\partial E}{\partial T}\right)_V = C_V \quad (17)$$

$$\text{one obtains } E = E_0 + \bar{C}_V(T-T_0) \quad (18)$$

$$\text{or } T = T_0 + \frac{E-E_0}{\bar{C}_V} \quad (19)$$

where \bar{C}_V is an effective, or average specific heat value. Introduction of the specific internal energy into the burn fraction expression necessitates a further modification,

one obtains

$$t = A^{-1} \cdot \frac{\epsilon}{E_f} \int_0^f \frac{-\epsilon Qf}{E_f^2} df = -A^{-1} \cdot \frac{\epsilon}{E_f} \frac{E_f^2}{\epsilon Q} \left[\frac{-\epsilon Qf}{E_f^2} - 1 \right], \quad (23)$$

but $\frac{-\epsilon Qf}{E_f^2} \approx 0$,

therefore $t_{ind} = \frac{E_f^2}{A\epsilon Q} \cdot \frac{\epsilon}{E_f} \quad (24)$

In applying the burn fraction rate expression, Eqn. (21), and the relationship (24) for induction time one must bear in mind that the relatively large pressure changes taking place in shock initiation of detonation may influence the decomposition mechanism and therefore the rate, and the values of the thermodynamic quantities such as C_v , and Q , which are temperature dependent, in addition. The inclusion of such pressure and temperature effects is however considered to be an unwarranted refinement at this stage in the computation.

4.5 COMPUTATIONAL TECHNIQUE OF COMBINING HYDRODYNAMIC AND CHEMICAL KINETIC INTEGRATION

Several problems appear in the numerical solution of the coupled burn fraction differential equation and the conservation of energy equation. First, due to the von Neumann "q" method for describing a shock wave, the pressure (P) versus position (z) relationship at a given time shows no discontinuity in $\partial P / \partial z$, but a gradual transition occupying approximately three zone widths, or grid spaces regardless of their size (see Figure 1). This "smearing" of the shock position, or of the time of arrival of the pressure peak at a given position complicates computational initiation of the chemical reaction process. In addition, the nature of the burn fraction-time relationship is such that quite small time steps (relative to the time steps in the hydrodynamic integration) should be used in the numerical solution of Eqn. (21) requiring much computing time. Finally, small computational oscillations yielding small, but significant values of specific internal energy prior to the arrival of the desired pressure peak may initiate integration of the burn fraction differential equation. A brief description of how these problems were handled is given below.

In order to avoid premature release of chemical energy because of the "unreared" shape of the shock front, and because of numerical oscillations, and in order to conserve computing time, the following computational criteria were included in the SHEP program:

(a) Integration of the burn fraction differential equation in a cell is begun only when the conditions

$$\frac{\Delta P}{\Delta t} < 0, \text{ and} \quad (25)$$

$$P > 0.01 \text{ Mbar} \quad (25a)$$

are satisfied. Physically, these criteria mean that the cell must have been compressed, and that a pressure decrease in the cell must have taken place sometime after the cell had experienced a pressure above a specified level.

(b) For the purpose of saving computing time, variable time steps for the integration of the burn fraction equation are chosen on the basis that when

$$\frac{\Delta E}{\Delta t} < 0.03E_{\text{Shock}}, \text{ Use: } \Delta t_{\text{Chem. Kin.}} = \Delta t_{\text{Hydro.}}, \quad (26)$$

and when

$$\frac{\Delta E}{\Delta t} > 0.03E_{\text{Shock}}, \text{ Use: } \Delta t_{\text{Chem. Kin.}} = 0.005 \mu\text{sec}$$

Writing Equation (21) simply as

$$\frac{\partial f}{\partial t} = A(1-f) e^{\frac{-B}{E(t)+C}} \quad (27)$$

where A, B, and C are constants, it is clear that

$$E(t) = E_H(t) + E_C(t). \quad (28)$$

Here E_H signifies the hydrodynamic specific internal energy, and E_C the specific energy contribution due to chemical reaction. E_C is obtained from

$$\frac{dE_C}{dt} = Q \frac{df}{dt} \quad (29)$$

For $E_C(0) = 0$ one obtains

$$E_C = Qf$$

The hydrodynamic energy, E_H , is governed by

$$\frac{dE_H}{dt} = -(P + q) \frac{dV}{dt} + \frac{dE_d}{dt} \quad (31)$$

where the term $\frac{dE_d}{dt}$ describes the rate of change of the distortional energy.

The simultaneous numerical integration (Runge-Kutta) of Equations (3) and (21) proceeds as follows:

In general, the initial conditions are for $t = 0$,

$$f = f_0, (E_H)_0 = E_0 - (E_C)_0, (E_C)_0 = Qf_0 \quad (32)$$

For one hydrodynamic integration step $\frac{dV}{dt}$ and $\frac{dE_d}{dt}$ (from the previous integration step) are assumed to be constant. For each E value resulting from an integration step, the corresponding new value of P is obtained from the equation of state, $P(E, V)$.

5. OVERALL COMPUTATIONAL PLAN

The computations were planned to permit the following logical sequence:

- a. Shocking of cylinder of inert homogeneous nitromethane - 2D
- b. Shocking of cylinder of reactive homogeneous nitromethane - 1D
- c. Shocking of cylinder of reactive homogeneous nitromethane - 2D
Various cylinder diameters.
- d. Examination of simplest inhomogeneous models - 1D.

6. RESULTS OF COMPUTATIONS

6.1 INERT CYLINDER - 2D

This computation was carried out with the initial conditions prescribed to provide an 87.5 kilobar shock of 1.1 μsec duration at one end of the cylinder as shown in Figure 2. The proper number of cells at the shocked end of the cylinder were therefore loaded to the prescribed pressure and energy content determined from the equation of state. The appropriate particle velocity, determined from the shock Hugoniot was also imparted to the material in each of the loaded cells. Chemical reaction was ignored since this was to be an inert calculation. The results obtained from this computation are shown in Figures 3, 4, 5 and 6 which indicate the decaying shock velocity as well as the development of shock curvature. The latter is of particular importance since it has a very significant effect upon the behavior of either a detonation wave, or a transient reaction wave.

6.2 1st REACTIVE CASE - 1D CONSTRAINED

In carrying out the first reactive calculations, it was found to be easiest to utilize an impacting aluminum plate as the source of the initiating shock. The plate thickness and impact velocity selection permitted control of the duration and pressure amplitude, since the equation of state and shock Hugoniot for aluminum are well known.

Two cases were run. In the first case the initiating peak pressure was set at 88 kilobars and in the second case, at 70 kb. The shock duration was controlled to approximately 1.1 μsec by using the aluminum plate thickness corresponding to 1.1 μsec double transit time at 88 kilobars. This turned out to be .35 cms of aluminum. The velocity of impact of aluminum on nitromethane which was required to give 88 kilobars peak pressure was found to be 0.226 cm/ μsec while for 70 kilobars, 0.182 cm/ μsec was required. Since the shock velocity at 70 kb is less than at 88 kb, the duration of the 70 kb shock was actually longer than 1.1 μsec .

The results of these two calculations are summarized in Figures 7 and 8 which indicate that at 88 kb, the initiation grew to a detonation and then proceeded to steady state, whereas at 70 kilobars the reaction faded, despite the longer duration of the 70 kb shock. Figure 9 shows the displacement time history for the piston, the shock and the detonation front for the 88 kb case. This figure illustrates the establishment of the detonation front at the piston-nitromethane interface and the overtaking of the shock front by the initial detonation, followed by merger into a steady state detonation front. While such 1D results have previously been reported¹⁰ they serve as a useful check on the operation of the program, the criteria discussed in Section 4.5 and the physical processes involved.

6.3 2D - REACTIVE CASES

Following the successful outcome of the 1D constrained computations, sufficient confidence could be felt in the operation of the program to warrant the computation of the much more expensive 2D reactive cases.

The computations were carried out for 5, 10, 12, 15, 20, 25, and 30 mm diameter cylinders initiated by aluminum plate impact at one end. The initial impact conditions, in all cases, were specified to provide an 88 kb shock of 1.1 μ sec duration exactly as it was done for the 1D reactive cases.

7. ANALYSIS OF 2D COMPUTATIONS

With the exception of the 30 mm diameter, all diameters were found to be sub-critical with an initial pressure buildup followed by a pressure decay, leading to a subsequent quenching of the chemical reaction. In some cases, once the downward trend of decaying pressure was satisfactorily confirmed, the computations were terminated even though the shock was still reactive. This permitted examining many more cases. The pressure buildup in the case of the 30 mm diameter was such as to lead to the conclusion that, as closely as one could afford to check it, this case was very close to the critical diameter.

Figures 10 through 14 indicate the portion of the cylinder that has reacted for the 5, 10, 12, 20 and 30 mm diameters. Figures 11a, b and c illustrate the time sequence in fade out of the detonation for the 10 mm sub-critical case. Comparison of Figures 10 thru 14 shows the effect of diameter upon the fraction of the cylinder which has reacted. Note that Figure 14 has been truncated parallel to the Z axis to keep it on one page.

Figures 15 and 16 illustrate the computed data points and the estimated smoothed pressure time history for the 10 mm diameters. The location of the smoothed curve is based upon previous experience with this type of program and comparisons which have been made between computed solutions and corresponding analytical solutions, which indicate that the computed results oscillate about the analytical value. A finer mesh size would have reduced these oscillations drastically, but the available computing time did not permit further reduction in the mesh size.

Figures 17, 18 and 19 illustrate the development of the detonation front curvature for the 10 mm diameter. These show the pressure-distance profiles at various radial distances from the axis along J lines. J lines define the Lagrangian mesh boundaries which are parallel to the cylinder axis prior to deformation. In this particular case, J = 1 is on the axis and J = 11 is the outside cylinder boundary. The pressure-distance profiles shown are plotted at 1.43 μ sec, 1.92 μ sec and 2.93 μ sec respectively to illustrate the changing curvature.

Figure 20 illustrates the pressure-distance profiles along the cylinder axis ($J=1$) as a function of time, for the 15 mm sub-critical diameter. The initiation of detonation behind the shock, the overtaking of the initiating shock by the detonation, and the subsequent rise and decay of the peak pressure in this sub-critical case are clearly apparent. The general similarity of the 1D results in Figure 7 and the 2D results in Figure 20 is clearly evident. The very important difference, however, should be carefully noted. The 1D case went to steady state detonation while the 2D case faded.

7.1 CONSTRUCTION OF THE CURVED DETONATION FRONT

From Figures 17, 18 and 19 it is possible to construct the time dependent development of the curved detonation fronts. These are shown in Figure 21 for the 10 mm diameter charge. The location of the detonation front is defined for this purpose as the location of the pressure peak along any J lines.

The curved detonation front for the 30 mm charge at $t = 2.18 \mu\text{sec}$ is determined from Figure 22 and shown in Figure 23. It is evident from the comparison that as the charge diameter increases, a larger fraction of the detonation front remains essentially plane.

7.2 PRESSURE-TIME HISTORY AS AFFECTED BY DIAMETER

The pressure profiles along the axis ($J=1$) were examined as a function of time as shown in Figures 15 and 16 and smoothed for purposes of comparison.

Figure 24 shows the effect of charge diameter upon the computed pressure-time history.

Two important aspects are evident. The pressure rises to higher peak levels as the diameter becomes progressively closer to the critical diameter. In addition, the pressure decay occurs progressively later as the diameter approaches critical. At the critical diameter, the pressure is of course maintained indefinitely without decay, by definition.

8. COMPUTATION OF PARTIAL YIELDS FOR SUB-CRITICAL CASES

From Figures 11a, 11b and 11c one can estimate the fraction of material which has reacted when the shock has progressed to various axial positions. We will define the yield percent as the percent of total material which has reacted 100%. Furthermore, we will neglect yields in any cell less than 10%. This truncation is quite reasonable since most cells adjacent to a fully reacted cell, have reacted only about 1%. The 10 mm diameter case is ideally suited to this analysis because the reactive shock has decayed to an unreactive pressure level during the interval of the computation.

It is clear that in such sub-critical cases, in which the decay to a non-reactive shock always occurs, the effective yield will depend on the amount of material originally available which is used as the basis for 100% yield. Figure 25 illustrates the computation for the 10 mm case for which $D = .33 D_C$ based on $D_C = 30$ mm. The 5 mm diameter for which $D = .17 D_C$ is also shown. Since even for 30 mm, it is evident that for the unconfined case which we are examining, the curvature of the shock front near the edges results in undetonated material. The yield is therefore not 100% even in the case $D = D_C$. Extrapolation of these results would indicate that as D became greater than D_C , the undetonated belt would become a progressively smaller fraction of the total mass and hence the yield would approach 100% for $D \gg D_C$.

A very common misconception which exists, associates a specific yield with a specific propellant composition in the sub-critical regime. It should be very evident from Figure 25 that such a correlation is incorrect unless the charge geometry is specified as well as the initiating pulse conditions.

9. LOCATION OF THE REACTIVE-TO-UNREACTIVE SHOCK TRANSITION

In those cases in which it was possible to follow the full progress of the decaying reactive shock, it is found that the shock pressure at which the shock becomes less than 10% reactive, does not vary very much. One can find plausible arguments that the shock transition pressure probably approaches a constant. The axial distance at which this transition occurs however, increases as the charge diameter D increases, that is as the ratio D/D_C approaches 1. Thus at 10 mm dia., $D/D_C = .33$ and the transition shock pressure is found to be about 43 kilobars. The shock peak is at 1.27 cm. At 5 mm dia., $D/D_C = .17$ and the transition shock pressure is found to be about 48 kilobars. In this case, the shock peak is at .31 cm. The respective elapsed times at which these situations occur are 2.75 μ sec for the 10 mm charge and .73 μ sec for the 5 mm charge. It was not possible because of computing cost limits, to follow the larger diameters all the way out to the final fadeout, but it is roughly estimated by extrapolation of the decaying pressure time curve, that it takes more than 4 microseconds for the axial pressure to decay to 45 kilobars when $D = 1.5$ cm, $D/D_C = .50$, and more than 5 μ secs in the case $D = 2.0$ mm; $D/D_C = .67$. The corresponding estimated lower limits of the distances for the locations of the transition for the 1.5 cm and the 2.0 cm diameters are respectively > 1.8 cm and > 2.4 cm. Figure 26a shows a plot of D/D_C vs transition time and transition distance. In Figure 26b, the reciprocal times and distances are plotted as a function of D/D_C . The first two data points are computed and the last two are the estimated lower limits. It is clear that the transition time and distance must both approach infinity as $D/D_C \rightarrow 1$.

The significant aspect of this portion of the effort lies in the fact that the computations have been shown to provide an output which permits the quantitative comparison of the fading characteristics as a function of D/D_C , and hence a means for estimating D_C from fading measurements made at $D < D_C$ for the homogeneous system.

10. INHOMOGENEOUS MODEL - 1D STUDIES

10.1 BASIS FOR THE MODEL

The simplest kind of Inhomogeneous model, defining the next level of model complexity, is represented by a homogeneous system containing non-reactive imperfections, such as porosity of inert particles.

Porosity in real propellant systems is described by a pore size distribution and a geometrical distribution. However, for purposes of a 1D model, it is necessary to simplify this description in such a way that each macro cell is characterized in a manner which averages the contributions from both the pore size and the geometrical distribution. This is equivalent to the restriction that any macro cell contains essentially the same pore size distribution and geometrical distribution of pores as any other macro cell. Basically, this requires that the propellant be macroscopically uniform. This is a goal that propellant manufacturers strive for and therefore represents a desirable situation. In any case, before analyzing the more complex case of a propellant which has large random imperfection variations in the macro cell it is logical to analyze the case of low (or zero) random imperfection variations in the macro cell.

The porosity, defined as the volume % of voids, is a special case of the more general definition of the imperfection content, which can be defined as the volume % of imperfections.

The imperfections have been shown¹³ to have the effect of generating hydrodynamic hot spots as a result of the flow processes which accompany the passage of a shock. Since the volume which is heated hydrodynamically is roughly equal to the volume of the original imperfection, and the energy density in the hot spot region is approximately twice that in the normally shocked homogeneous material, one has here the elementary basis for a simple inhomogeneous model. Specifically, this model requires that one examine the effects of varying the term in the reaction rate expression which is affected by the changes in shock energy deposition arising from the imperfection content. A convenient way to treat this in the computations is to vary the activation energy. The shock energy deposition is of course, related to the average imperfection content. Alternatively, one may view shock initiation of detonation for inhomogeneous substances from a chemical-catalytic standpoint. It is known from experiment that it is possible to initiate detonation in inhomogeneous substances by means of lower shock pressures than are required for initiation of the same substance in the homogeneous state. In contrast to the homogeneous case, in which lower shock pressure results in lower shock specific energy, or lower shock temperature, and therefore lower chemical reaction rate, one may reason that in the inhomogeneous case the overall chemical reaction rate can remain relatively high even at the lower temperatures due to catalytic effects at the interfaces formed by the inhomogeneities. To simulate inhomogeneous behavior computationally on this basis would also involve examination of the effects of decreasing the activation energy. In fact, the rates of several inhomogeneous gas reactions¹⁷ are explained in terms of decreased values of

the activation energy. Thus, without any final commitment as to whether the specific initiating mechanism is catalytic or originates in hydrodynamic hot spots or is a combination of both, the initial study of initiation behavior for an effectively inhomogeneous explosive substance can be usefully carried out by finding the influence of varying the activation energy upon the development of detonation.

10.2 CHARACTERISTICS OF INHOMOGENEOUS SYSTEMS

There are two major differences in the initiation behavior of inhomogeneous systems as compared to homogeneous systems.

- (1) Inhomogeneous systems are initiated by lower shock pressures.
- (2) The transition from initiation to detonation is characterized by a shock displacement time relationship as shown in Figure 27 rather than the typical relationship shown in Figure 9 for the homogeneous case.

10.3 RESULTS OF COMPUTATIONS

One dimensional inhomogeneous model computations were carried out with the remaining available computing time, aimed at examining the effects of varying the activation energy E_a .

Activation energies of $1/4$ and $3/4 E_{a(0)}$ were examined where $E_{a(0)}$ is now defined as the full activation energy for nitromethane. The initiating pressure was reduced to 70 kilobars, which had previously been used for the 1D homogeneous case (see Fig. 8) and had failed in that case to initiate steady state detonation. This therefore provided a potential point of comparison with respect to the question of reduced initiation shock amplitudes necessary for inhomogeneous initiation.

In addition, the nature of the transition phenomenon was examined for each of the activation energies.

The first interesting result of these computations, was the observation that 70 kb, which was previously found to be insufficient to initiate the homogeneous system did initiate the model inhomogeneous systems for which E_a was $1/4$ and $3/4$ of $E_{a(0)}$.

The induction times for first burn were found to decrease with decreasing values of the activation energy.

The form of the transition from shocking to detonation was found to have changed in a manner which, at least superficially, resembled the experimentally observed transition depicted in Figure 27.

The computed results for $E_a = 1/4 E_{a(0)}$ and $3/4 E_{a(0)}$, are shown in Figure 28. It is noted that the transitions for $1/4$ and $3/4 E_{a(0)}$ are characterized by an essentially linear portion, representing the initial shock trajectory and a curvilinear intermediate transition region which connects the initial shock trajectory to the final, linear, steady state detonation trajectory.

One cannot easily visualize in simple terms why a change in the activation energy should change the transition region in the manner found. However, the effect of the activation energy change is quite complex and can be felt in many ways, including the change in induction time. This can have a secondary effect upon the pressure-time history and therefore also the velocity-time history for the overtaking detonation wave.

This portion of the effort represents a very brief examination of a more complex model. The completion of the program prevents further examination of the problem at this time. However, it is encouraging to note the trend toward realism both in the reduced initiation pressure and in the transition process derived from the computations.

Despite these initially encouraging results in the 1D inhomogeneous case, it is felt that ultimately, the most useful inhomogeneous models will not be found among these effectively inhomogeneous models, but rather among the class of models which consider the imperfections and their interaction with each other and the shock in greater detail.

11. COMPARISON OF COMPUTED AND LITERATURE VALUES OF DETONATION CHARACTERISTICS OF NITROMETHANE

A useful evaluation of the computations can be made by the comparison of computed and literature reported observations of the detonation characteristics of nitromethane.

Three useful comparison bases are

- (a) Critical diameter
- (b) Induction Times
- (c) Detonation Velocities (Steady State)

11.1 CRITICAL DIAMETER (UNCONFINED)

11.1.1 Present Computation \approx 30 mm with zero confinement.

11.1.2 Experimental^(a) 26.5 mm < D_C < 29 mm (in paper confinement)

Source (a) Ref. G. Nachmani and Y. Manheimer, J. Chem. Phys. 24 1074 (1956).

The apparent close agreement is perhaps better than one should expect, but nevertheless is very encouraging.

11.2 INDUCTION TIMES

11.2.1 Present Computation @ 88 kb $t_{ind} \approx .5 \mu\text{sec}$ @ 300° K
27° C

11.2.2 <u>Experimental</u> ^(c)	@ 82 kb	0.70 μsec	Initial
	85 kb	0.81 μsec	Temperature not
	84 kb	1.94 μsec	clearly specified
	92 kb	3.14 μsec	in Reference, but
	84 kb	0.71 μsec	is inferred to be
	87 kb	1.08 μsec	300° K
Average (13 shots)	86.6 kb	1.71 μsec	(p 505)

Source (c), Ref. 11, Campbell, Davis, Travis (P 503)

The computed induction time of 0.5 μsec compares favorably with induction times estimated in references 11 and 14, but is appreciably smaller than the experimentally observed average induction time of 1.71 μsec at 86.6 kb (Ref. 11) even when the induction time is further reduced by about 20% to correct it to 88 kb.

There is indicated in the source reference a variability in the nitromethane. The measurements are very difficult. There is a high sensitivity of the induction time to the initial temperature (which was not clearly specified in the source reference from which the experimental data came). In fact, the reference shows experimental data indicating a 300% change in experimentally observed induction time for a 30°K change in temperature.

For these reasons the agreement between computed and experimental induction times is considered to be fair. Disagreement by an order of magnitude or more has not been uncommon in earlier calculations.

11.3 DETONATION VELOCITIES

The experimental values of detonation velocity depend upon the degree of confinement and the diameter. The present computations consider the unconfined case only and should therefore be compared with the lightest confinement data. The experimental data also varies with the source.

11.3.1 Present Computation ID .63 cm/μsec
2D .63 - .65 cm/μsec

11.3.2 Experimental Values

V _D (cm/μsec)	Confinement			Source
	Mat'l.	ID	OD	
.6280	Paper	44 mm	Not Given	d
.6260	Paper	34 mm	Not Given	d
.6150	Paper	29 mm	Not Given	d
.660 ± .0132	Glass Steel	30 mm	Not Given	e
.6320	Iron	40 mm	44 mm	f
.6280	Iron	25 mm	42 mm	f
.6275	Steel	27 mm	Not Given	f
.6285	Alum.	27 mm	Not Given	f
.6263 - $\frac{8.85 \times 10^{-4}}{\text{dia.}}$	Glass	NOT GIVEN		c

Source (d) G. Nachmani and Y. Manheimer - J. Chem. Phys. 24 1074 (1956).

Source (e) L. Medard, Mem. Poudres 33 125 (1951).

Source (f) R. W. Van Dolah et al., Comp. Rend. XXXI Congres Intern. Chim. Industr., Liege, 1958.

Source (c) Campbell, Davis and Travis, see Ref. (11).

The agreement of this aspect of the computation with the literature data is considered to be fairly good.

12. CONCLUSIONS

1. It has been found feasible to apply a 2D computational procedure to the study of the sub-critical transient initiation process.

2. The procedure has been applied to the case of a homogeneous reactive system, namely nitromethane.

3. It has been shown that a reactive-to-non reactive shock transition can be observed and followed by means of this procedure.

4. Computation of successively larger diameters of charge have led to the conclusion that the critical diameter of unconfined nitromethane is near 30 mm. This is in reasonable agreement with experimental data in the literature which cites paper confined charges as having a critical diameter between 26.5 and 29 mm.

5. Smaller diameters have shown characteristic fadeout behavior which changes systematically as D/D_C is varied.

6. Development of shock front and detonation front curvature has been demonstrated and its effect upon the detonation shown.

7. The fadeout behavior has been translated into the form of partial yield estimates for these sub-critical transient cases. The dependence of the numerical value of the partial yield upon the original charge geometry has been pointed out.

8. Initial examination of the next level of model complexity, i.e. an inhomogeneous system with a macroscopically uniform distribution of imperfections has been studied briefly in 1D.

9. The inhomogeneous 1D model shows some encouraging elements of realism specifically with respect to reduced initiation pressure requirements, and the nature of the transition from shock to steady state detonation.

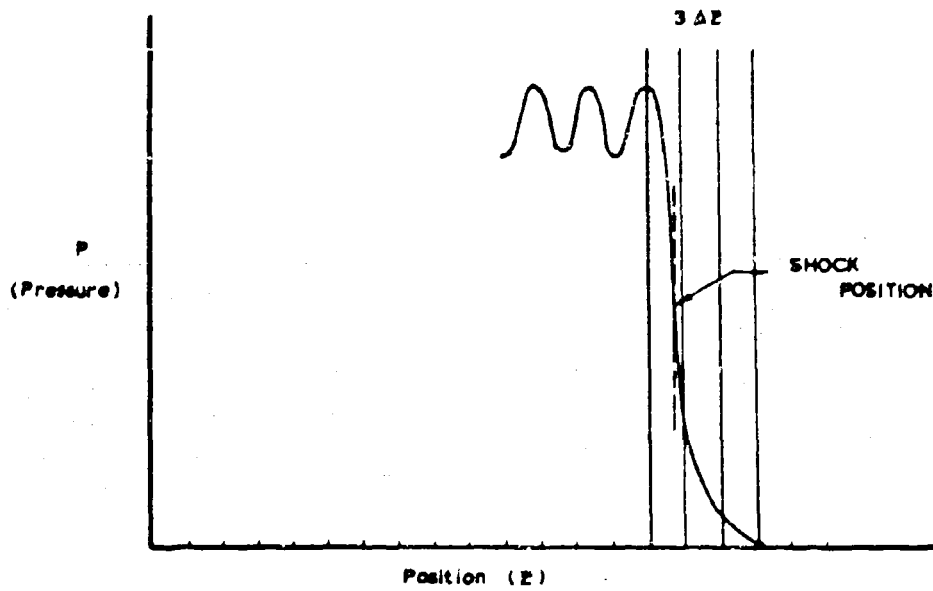


Figure 1a. SHOCK DESCRIPTION WITH VON NEUMANN q

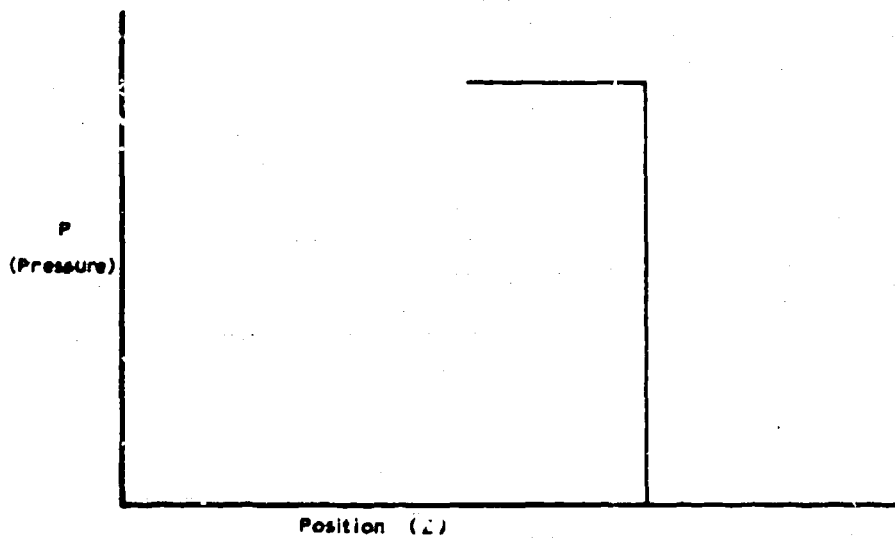


Figure 1b. EXACT SHOCK DESCRIPTION

RELATIVE DIMENSIONS OF SHOCKED NITROETHANE CYLINDER AT $t = 0$

Shock Intensity = 0.0875 megabar
Shock Duration = 1.1 μ sec
Initial Particle Velocity = 0.172 cm/ μ sec

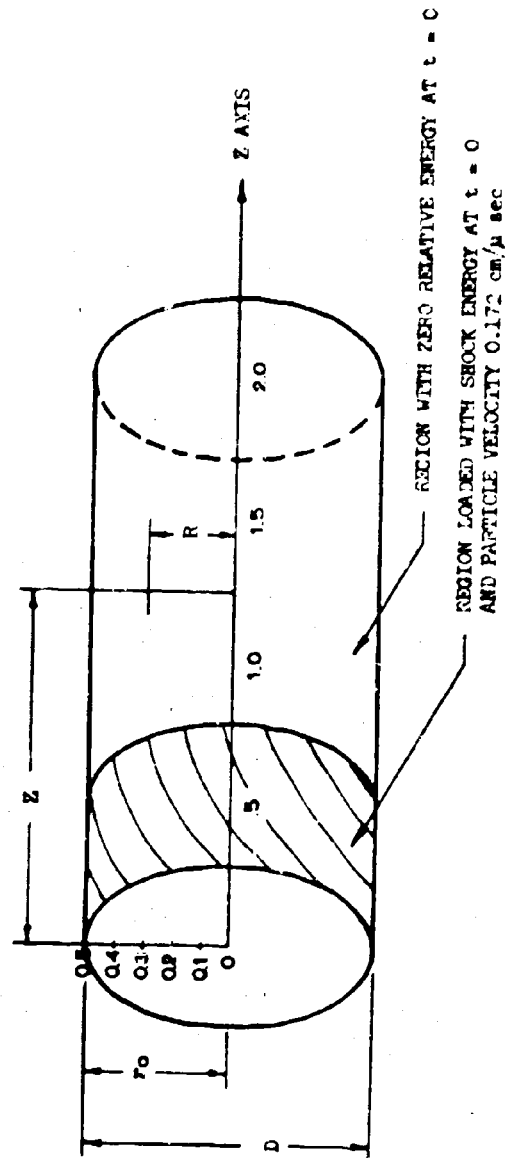


Figure 2.

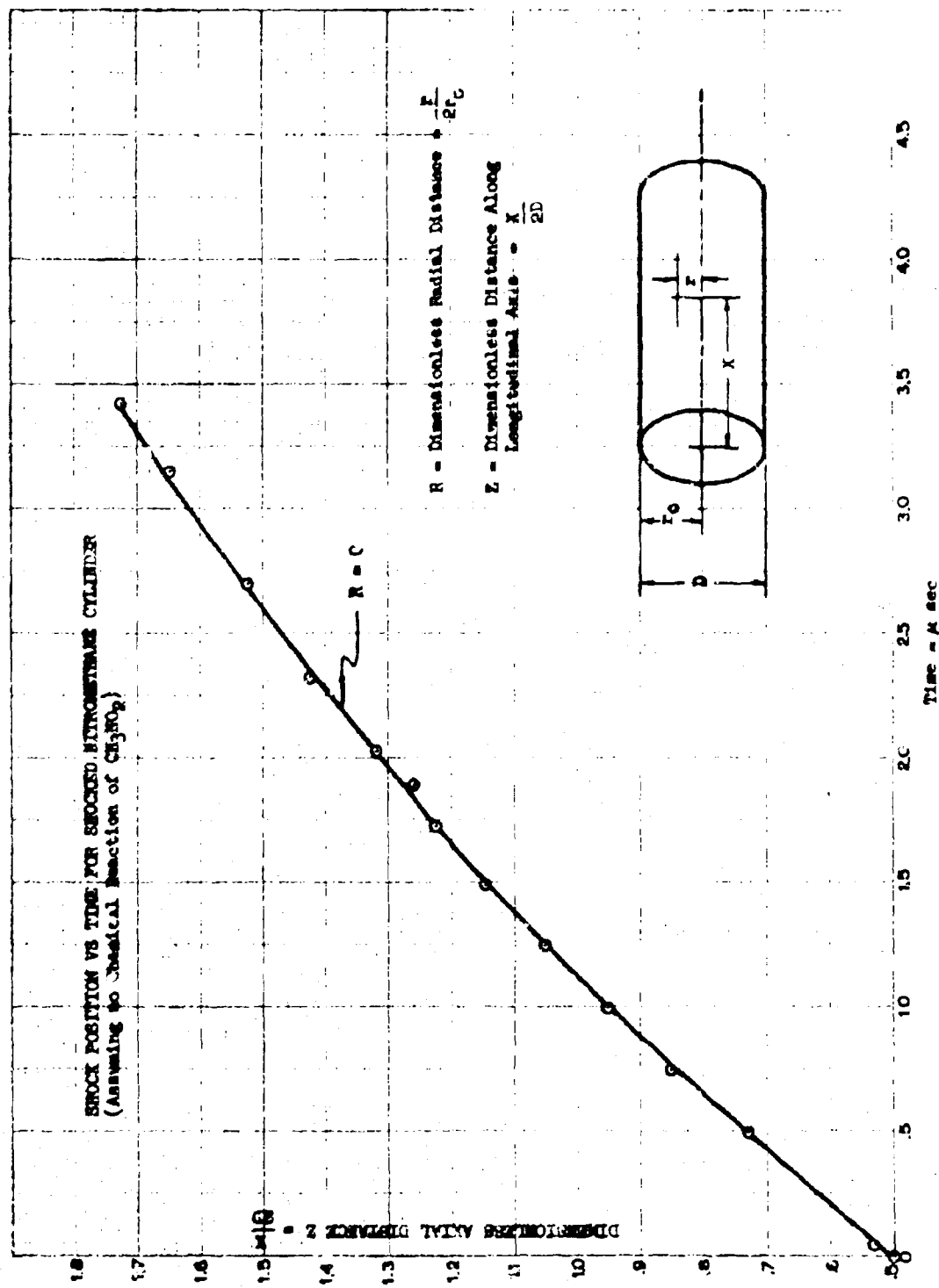


Figure 3.

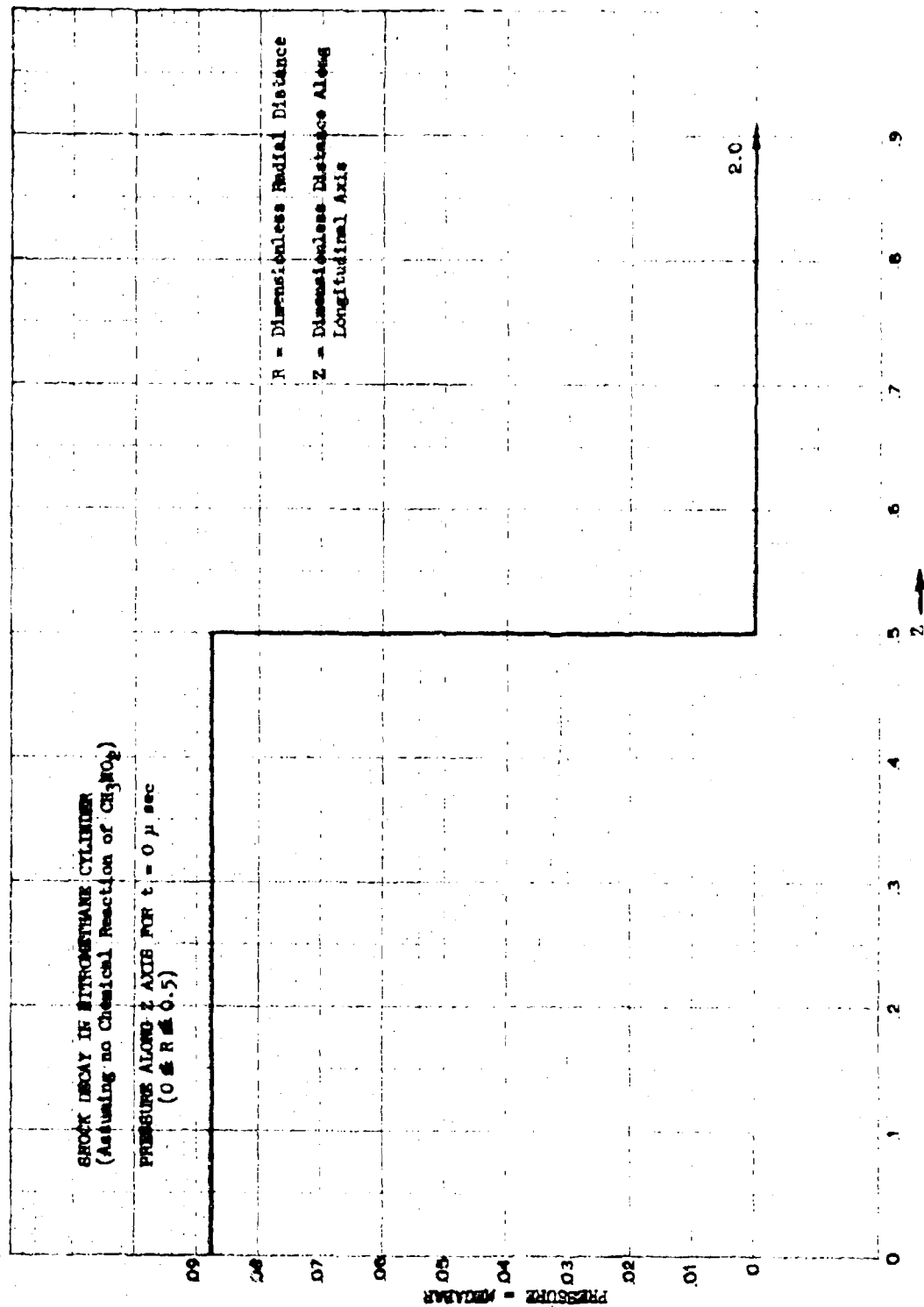


Figure 4.

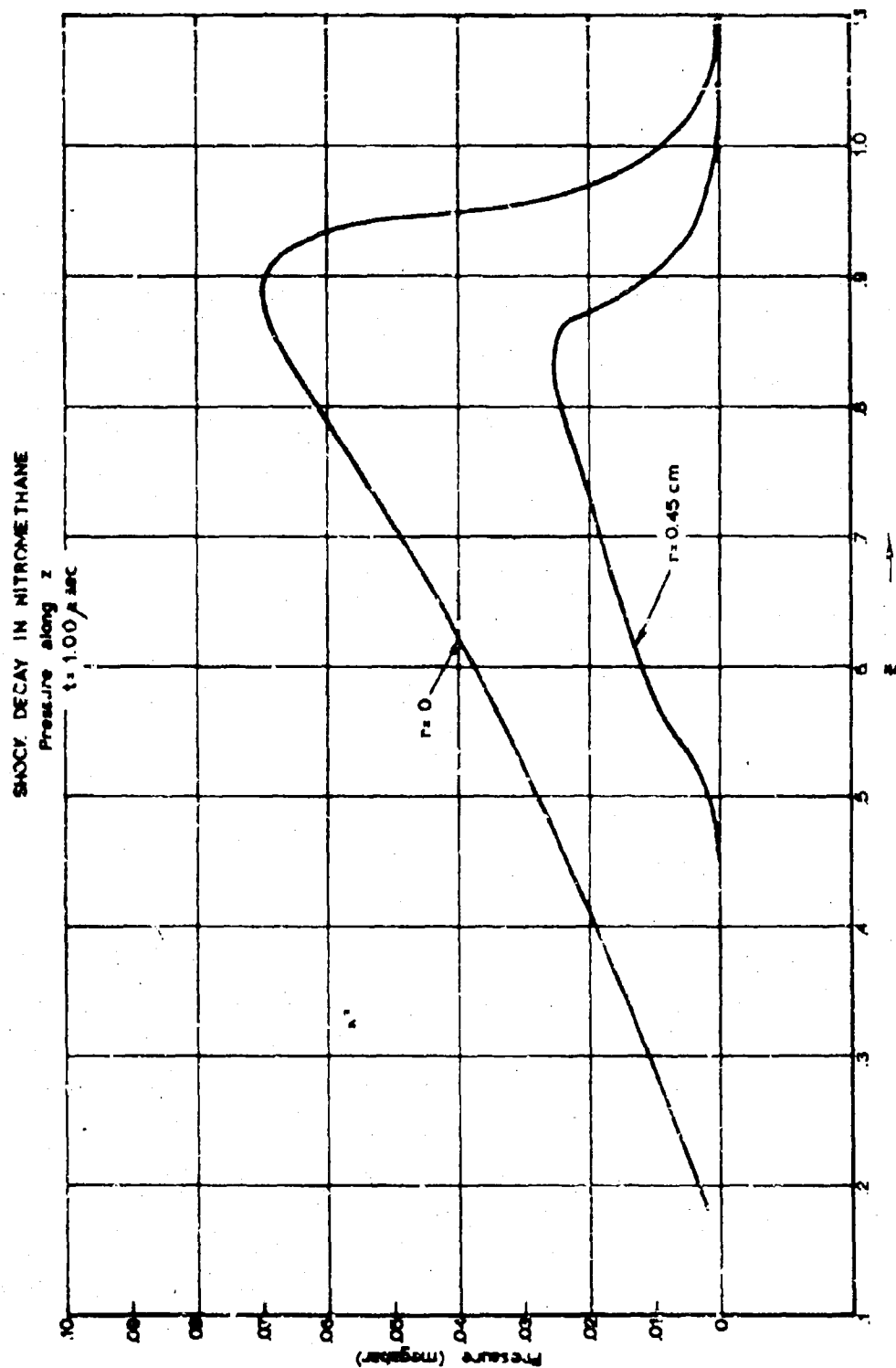


Figure 5.

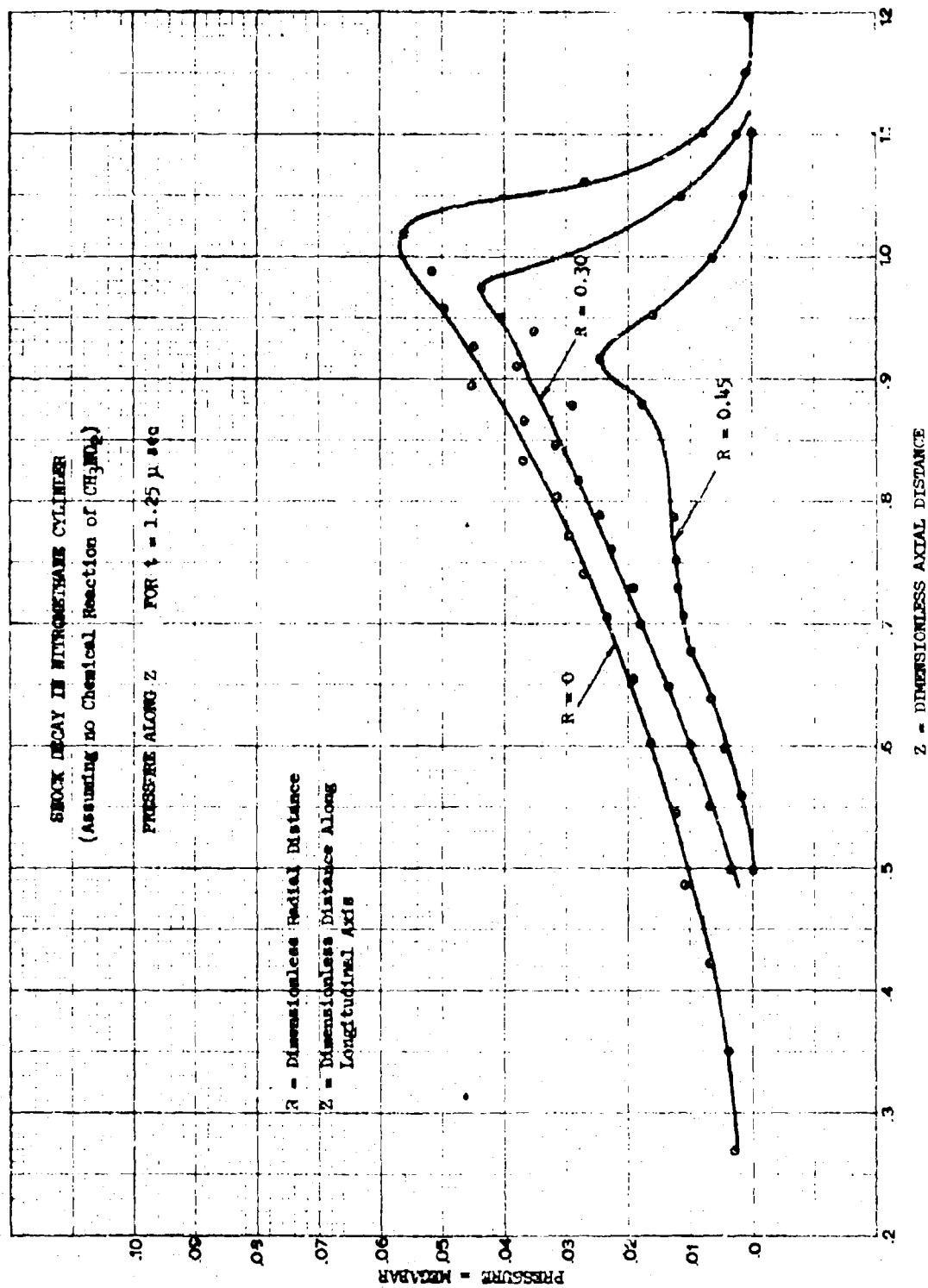


Figure 6.

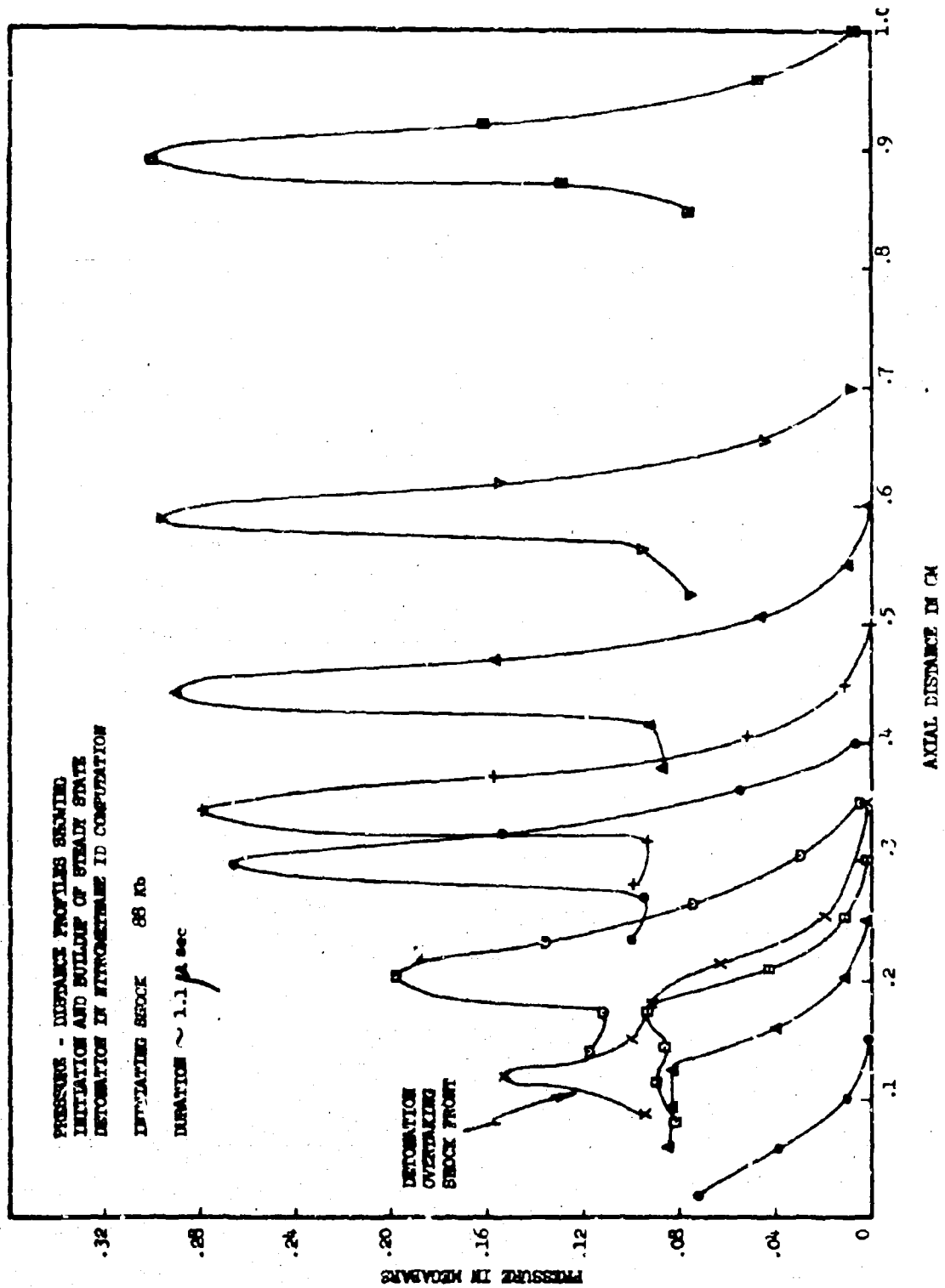


Figure 7.

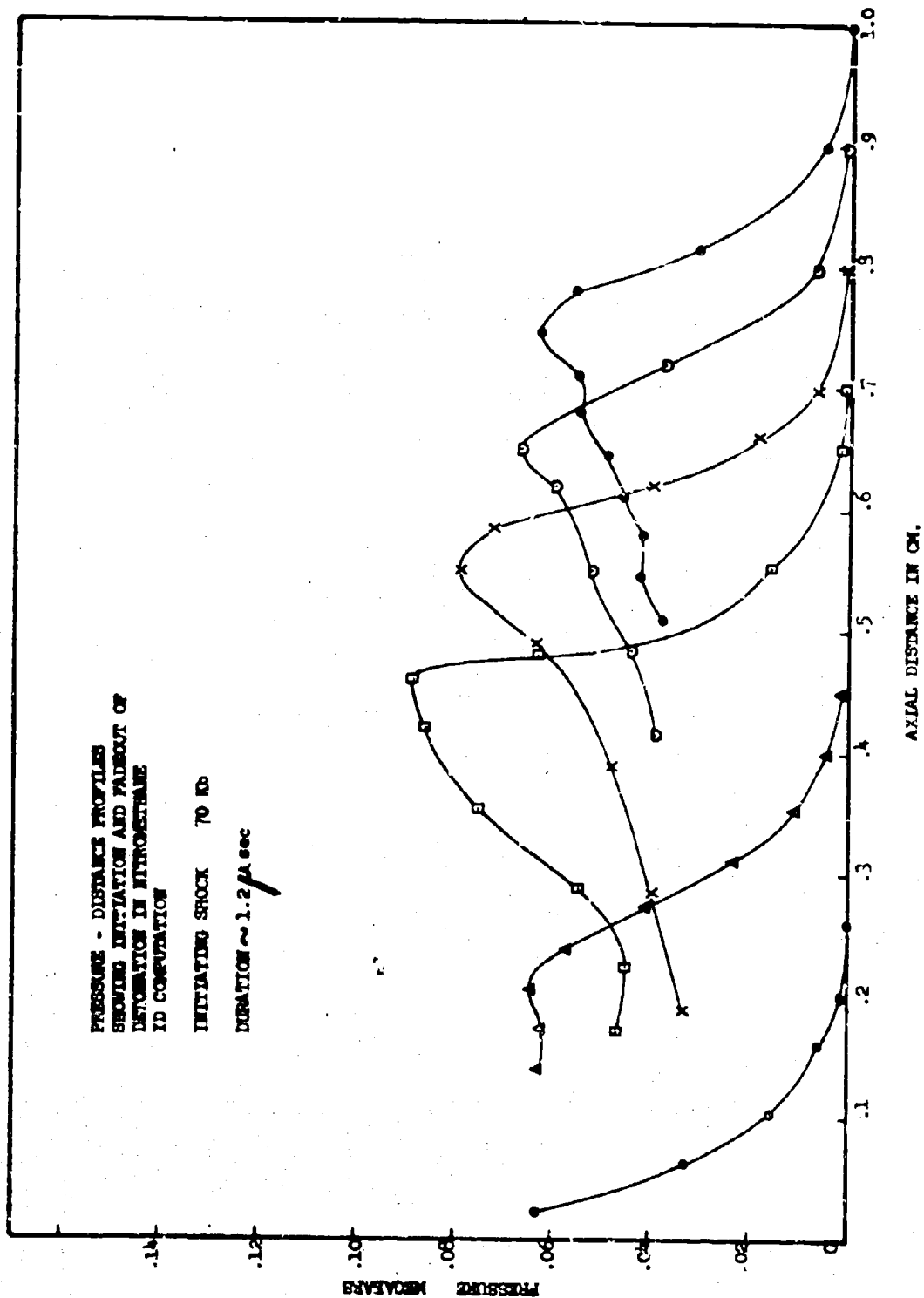


Figure 8.

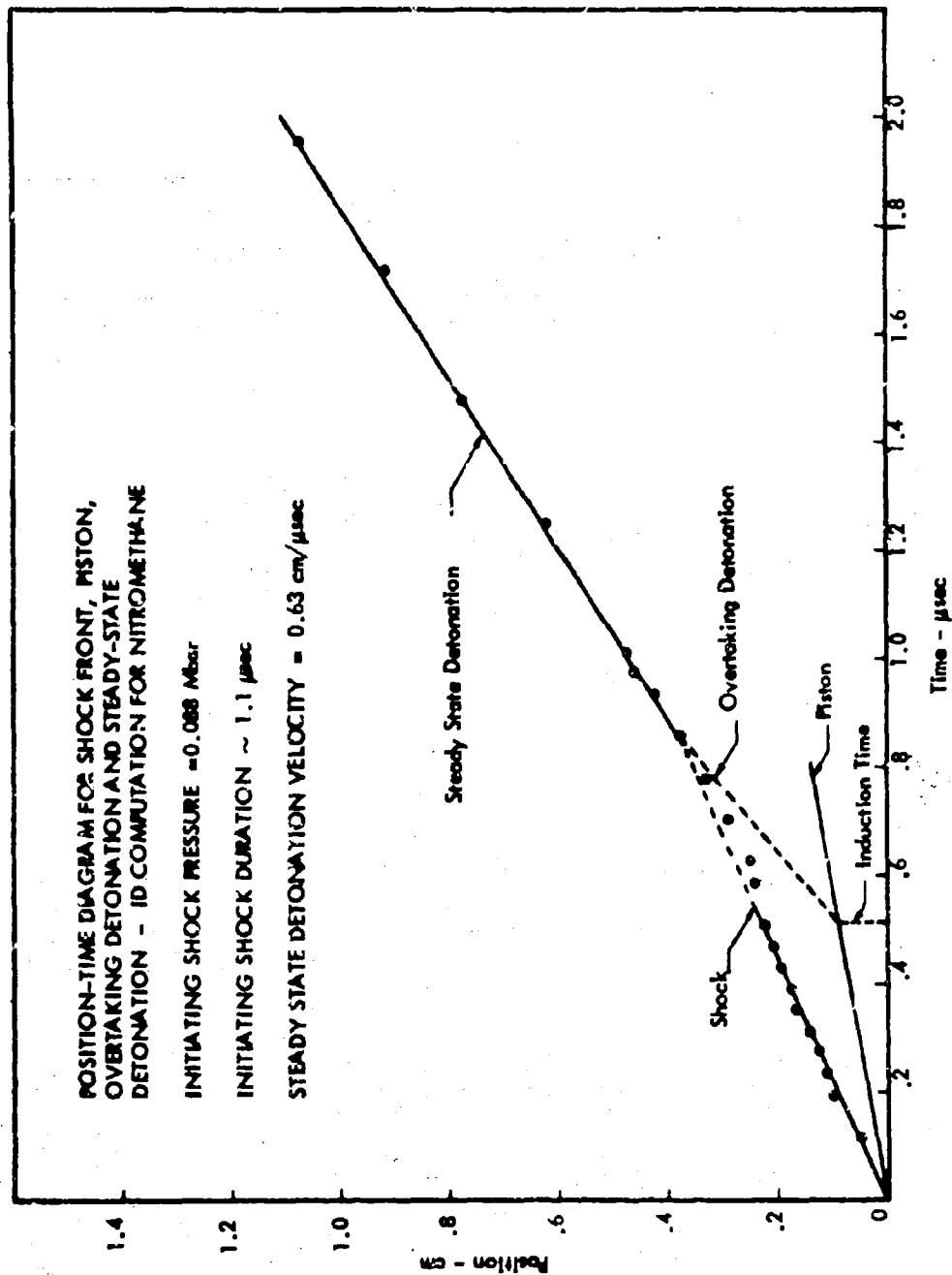


Figure 9.

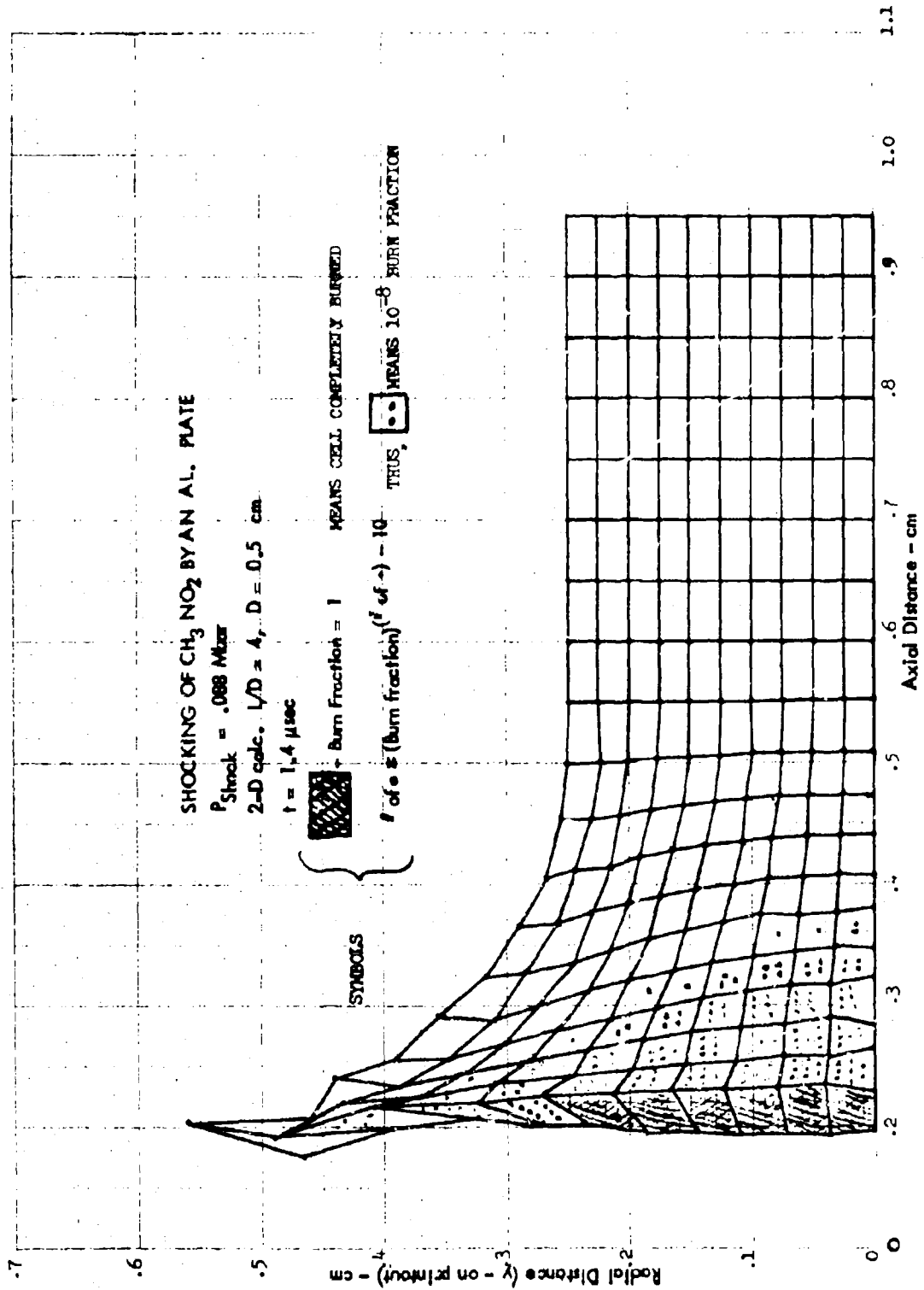


Figure 10.

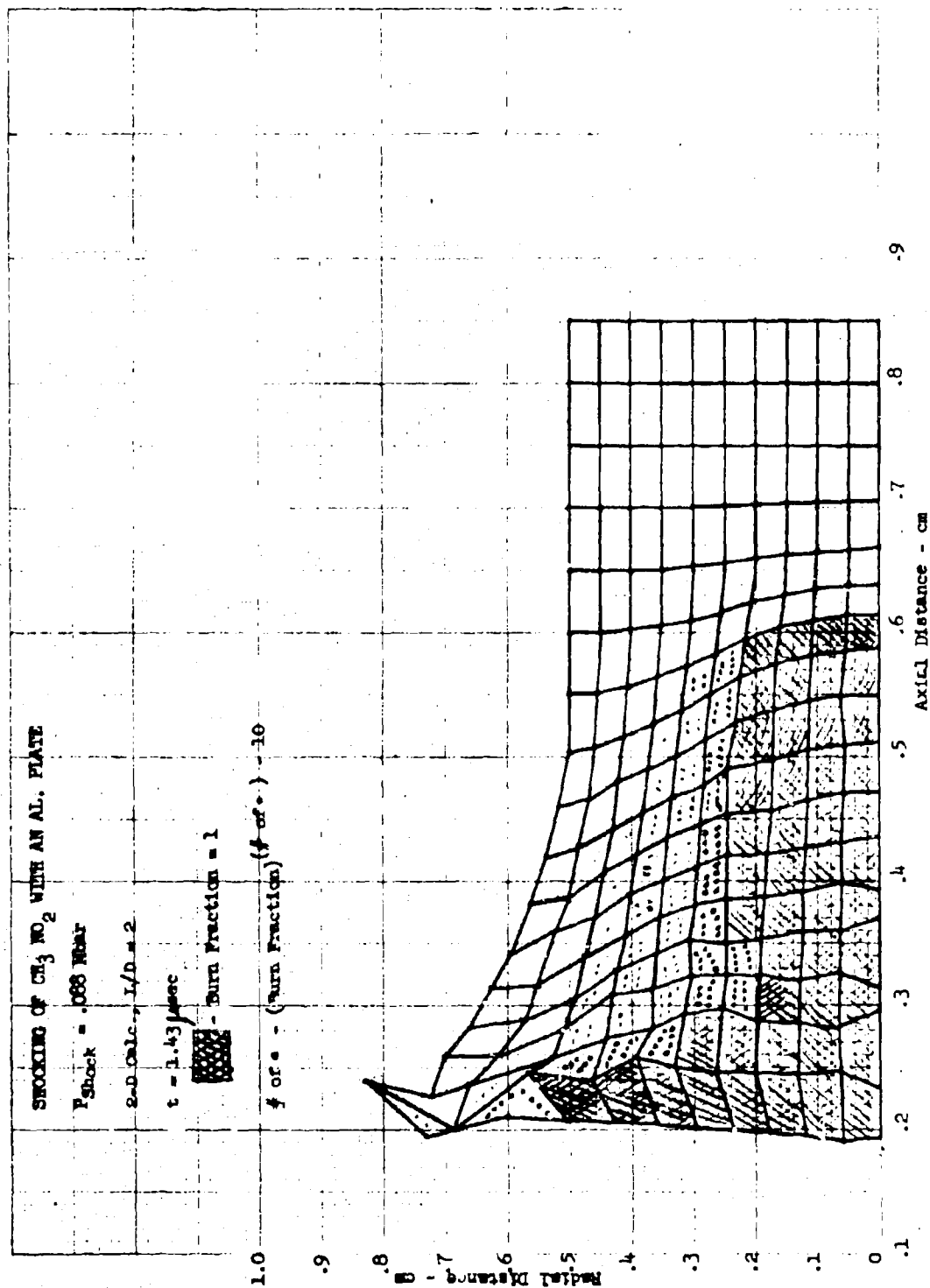


Figure 11a.

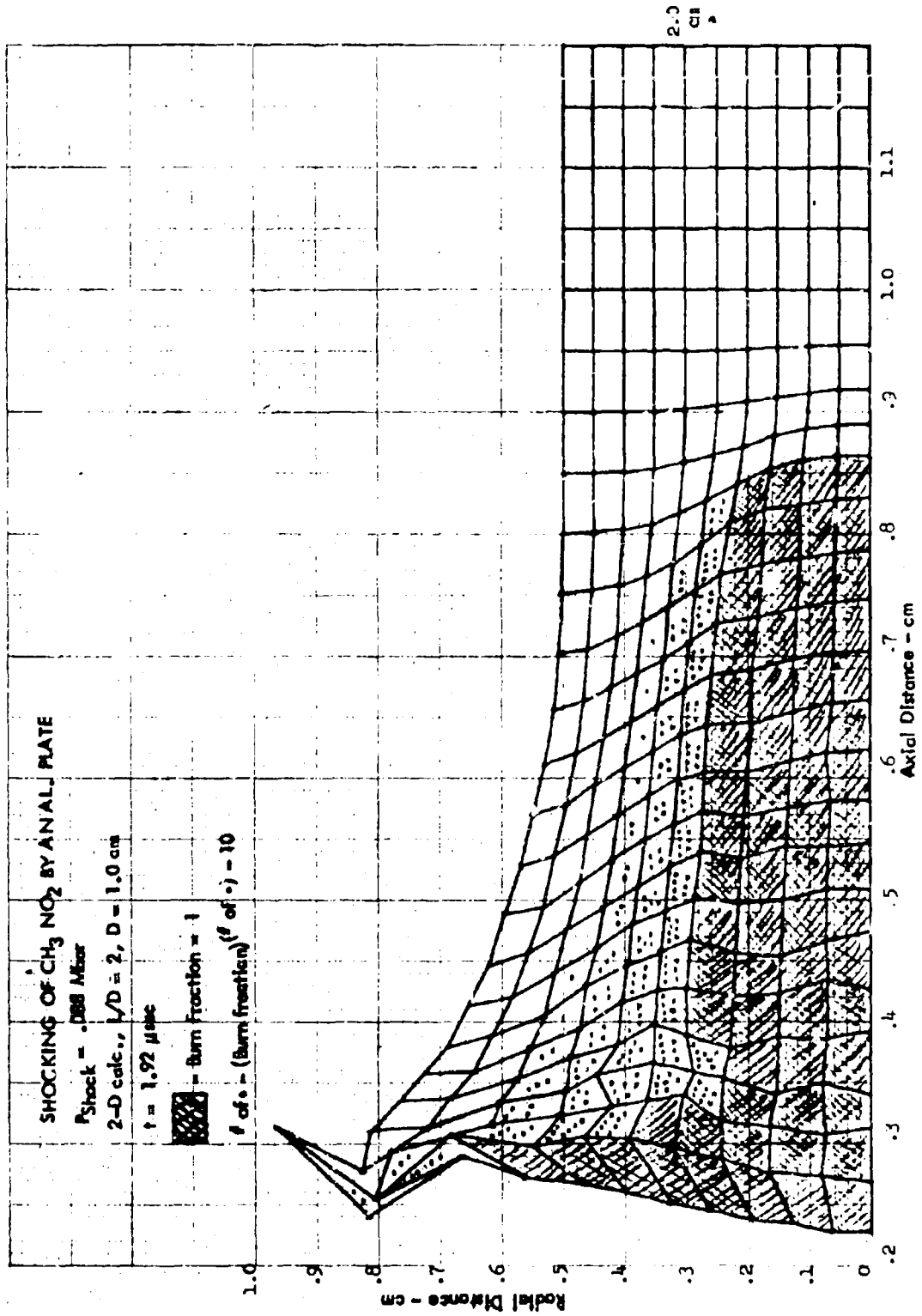


Figure 11b.

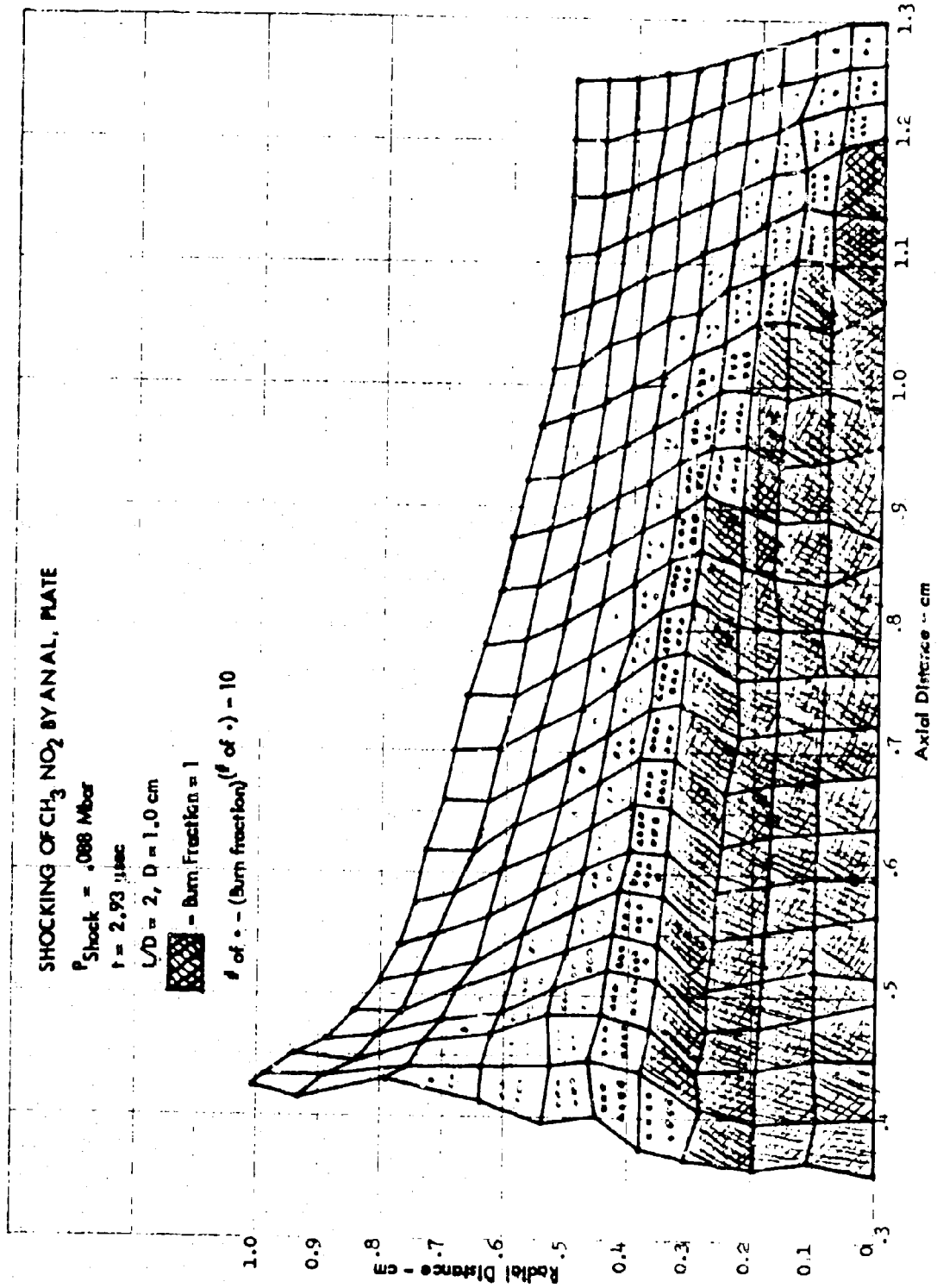


Figure 116.

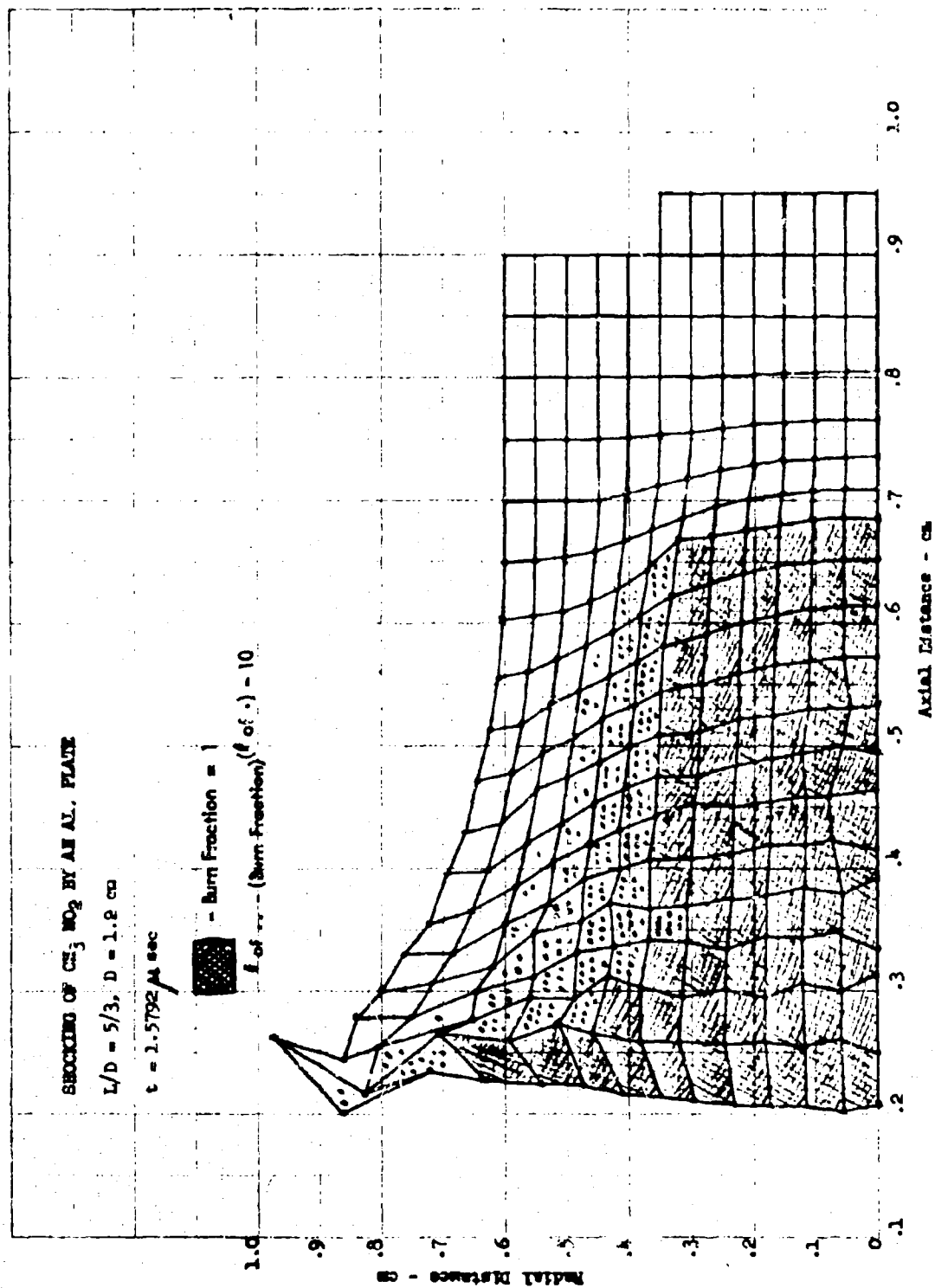


Figure # 12.

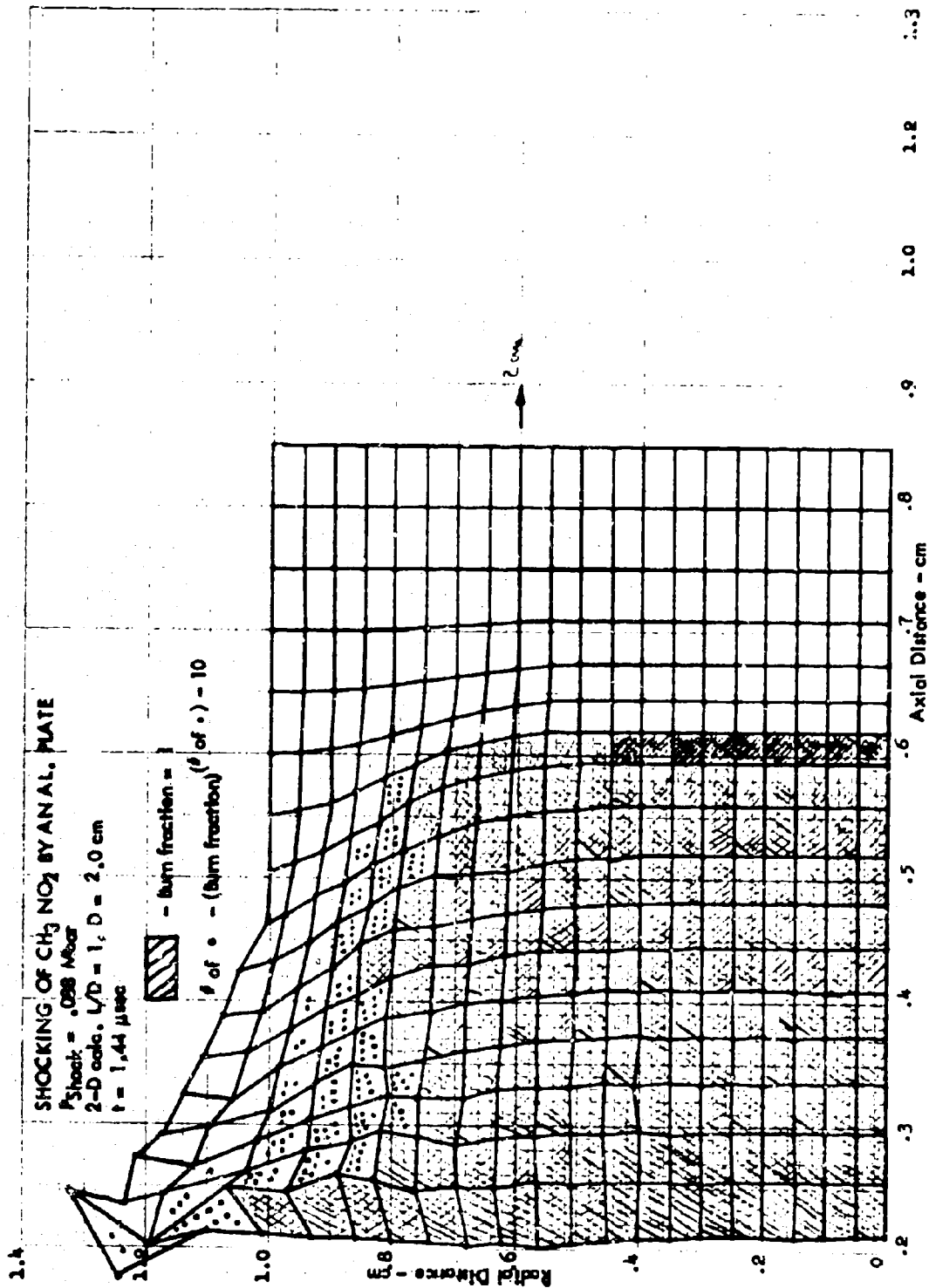


Figure - 13.

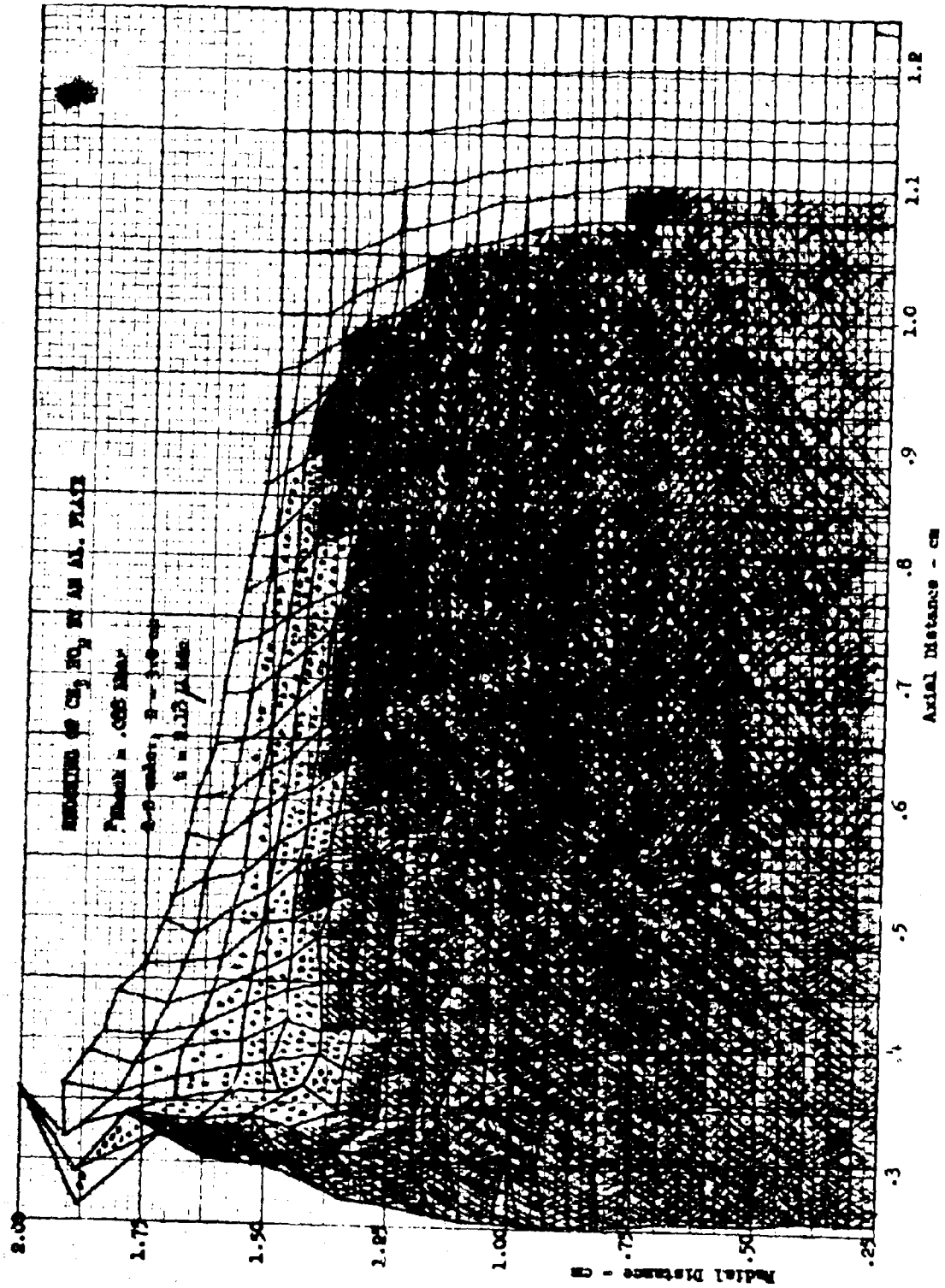


Figure 14.

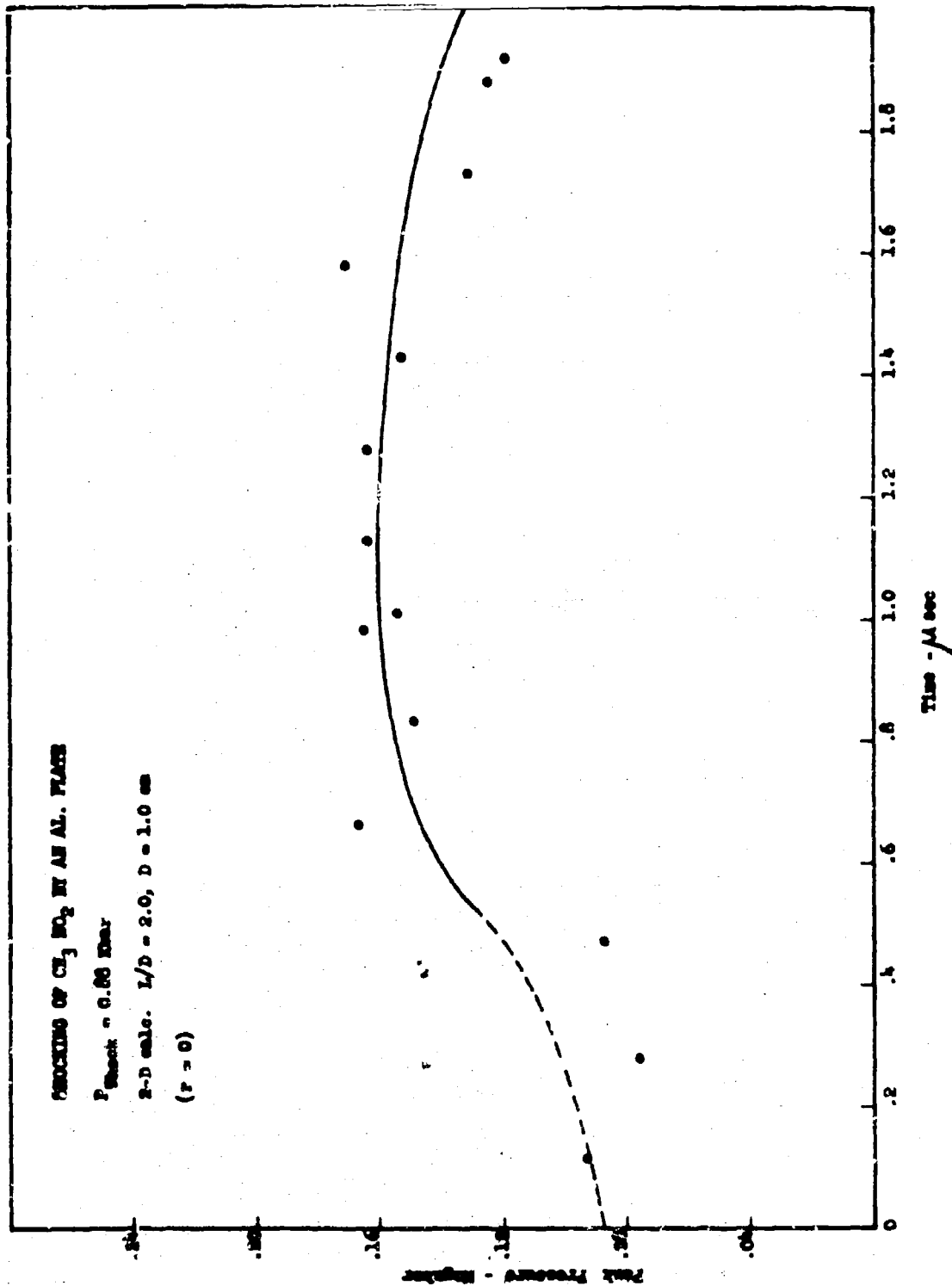


Figure 15.

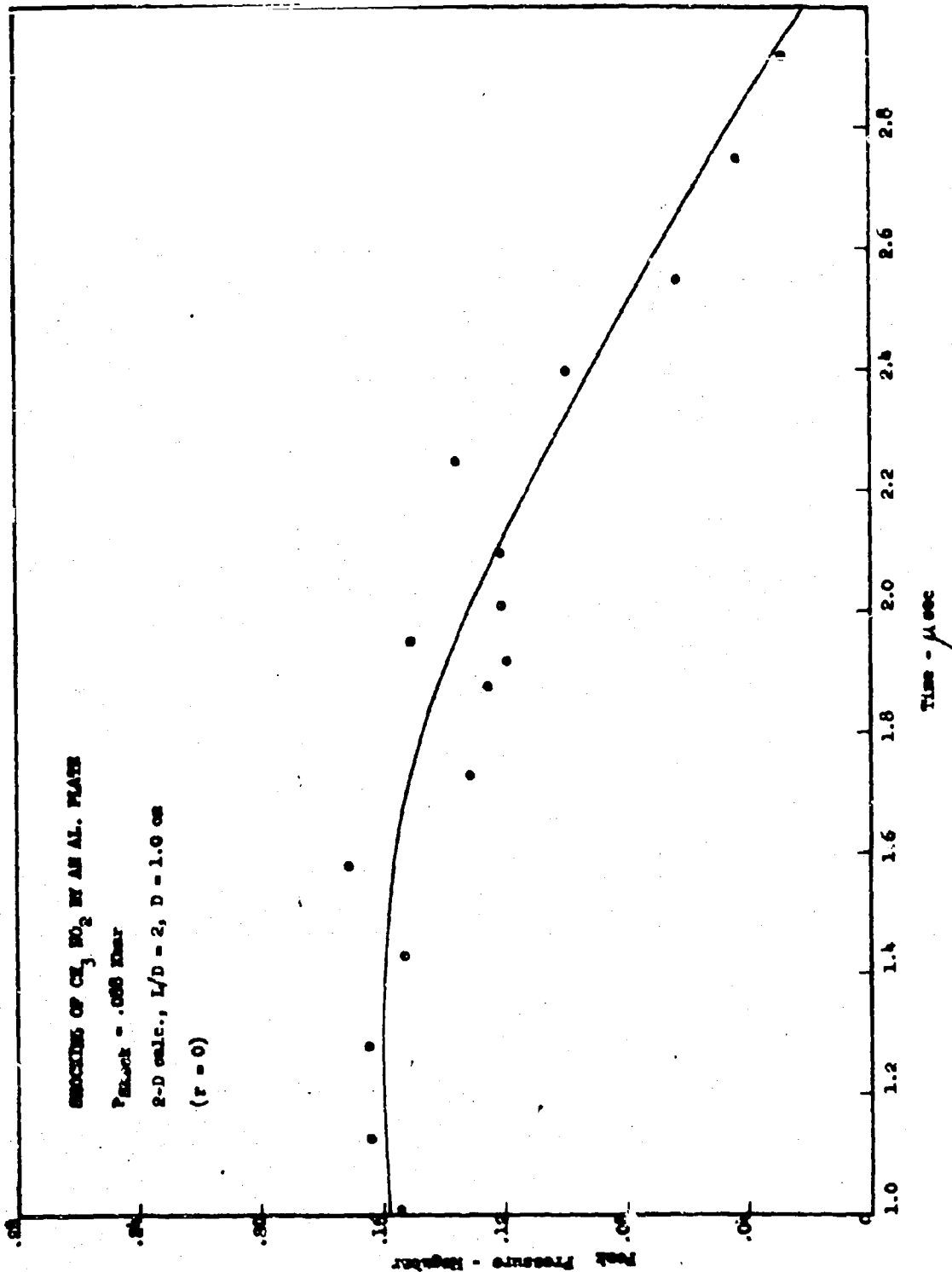


Figure 16.

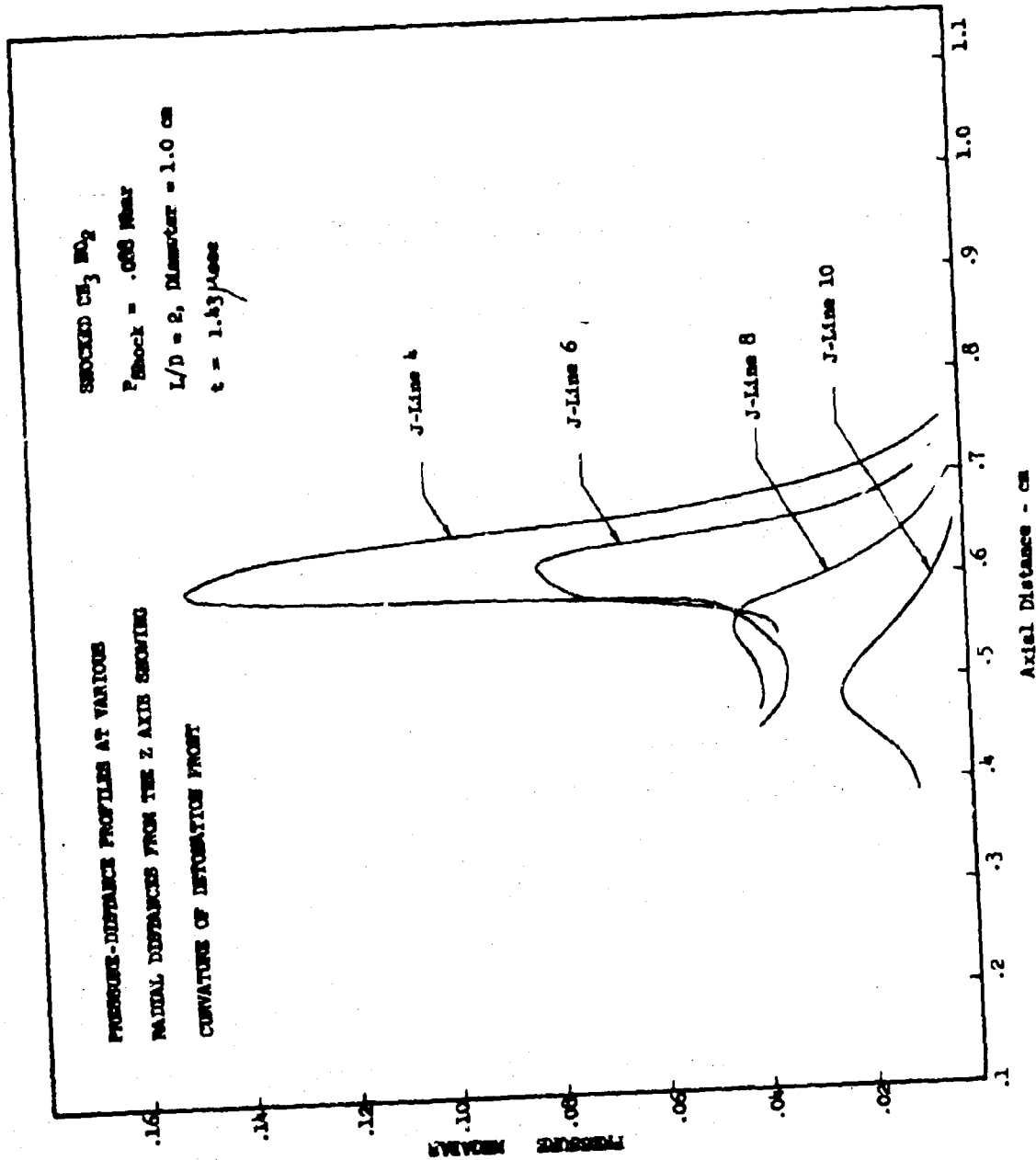


Figure 17.

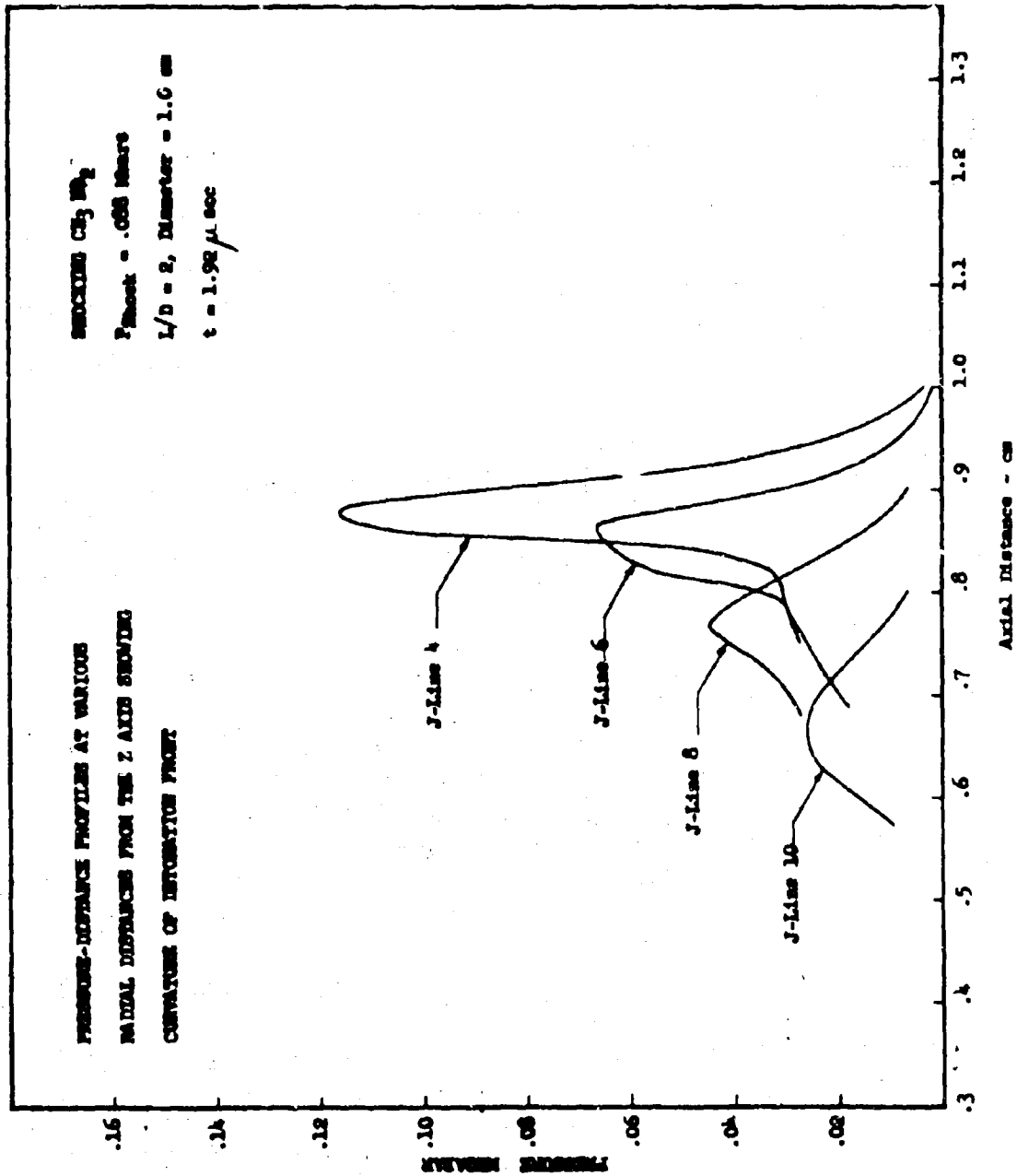


Figure 18.

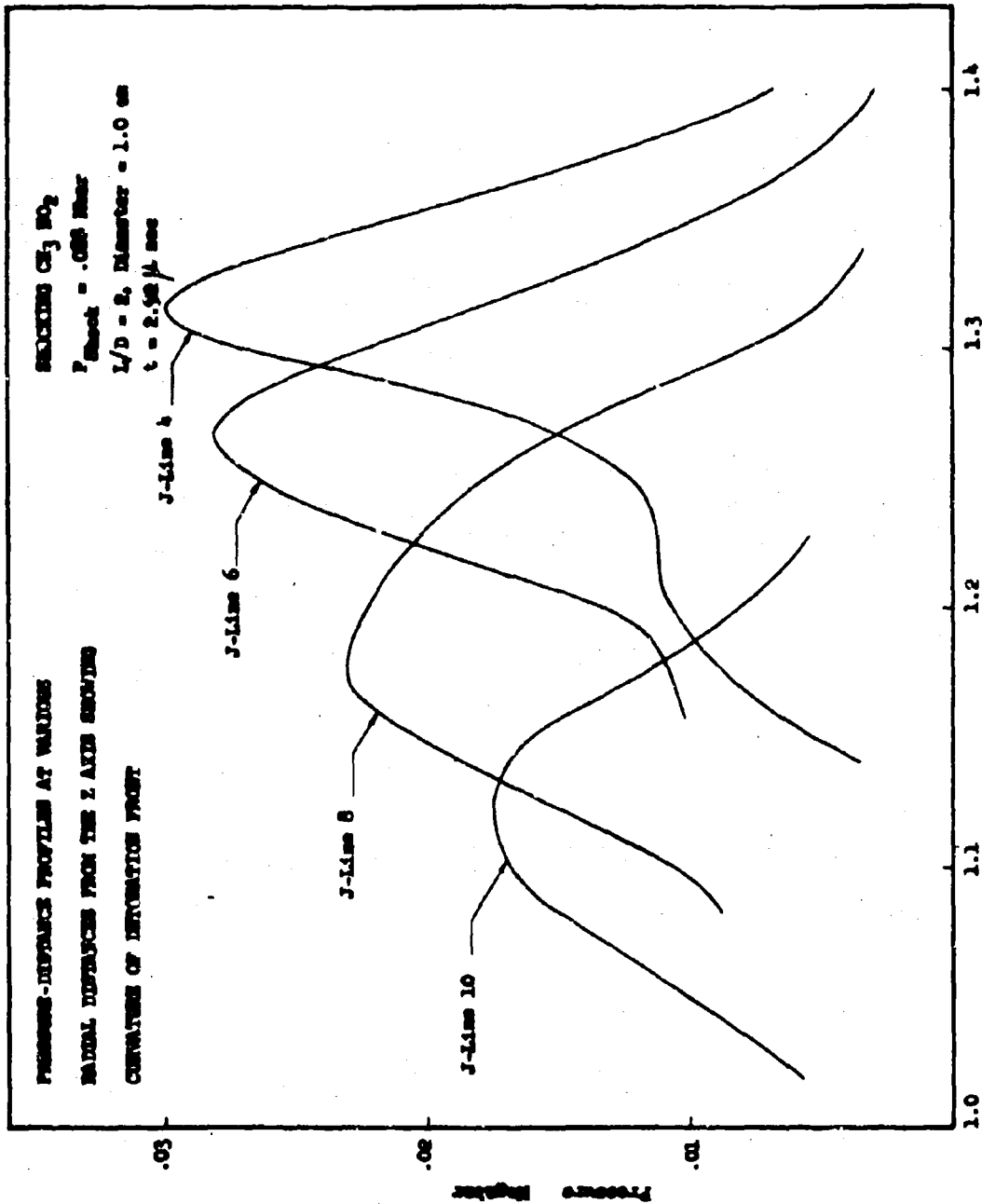


Figure 19.

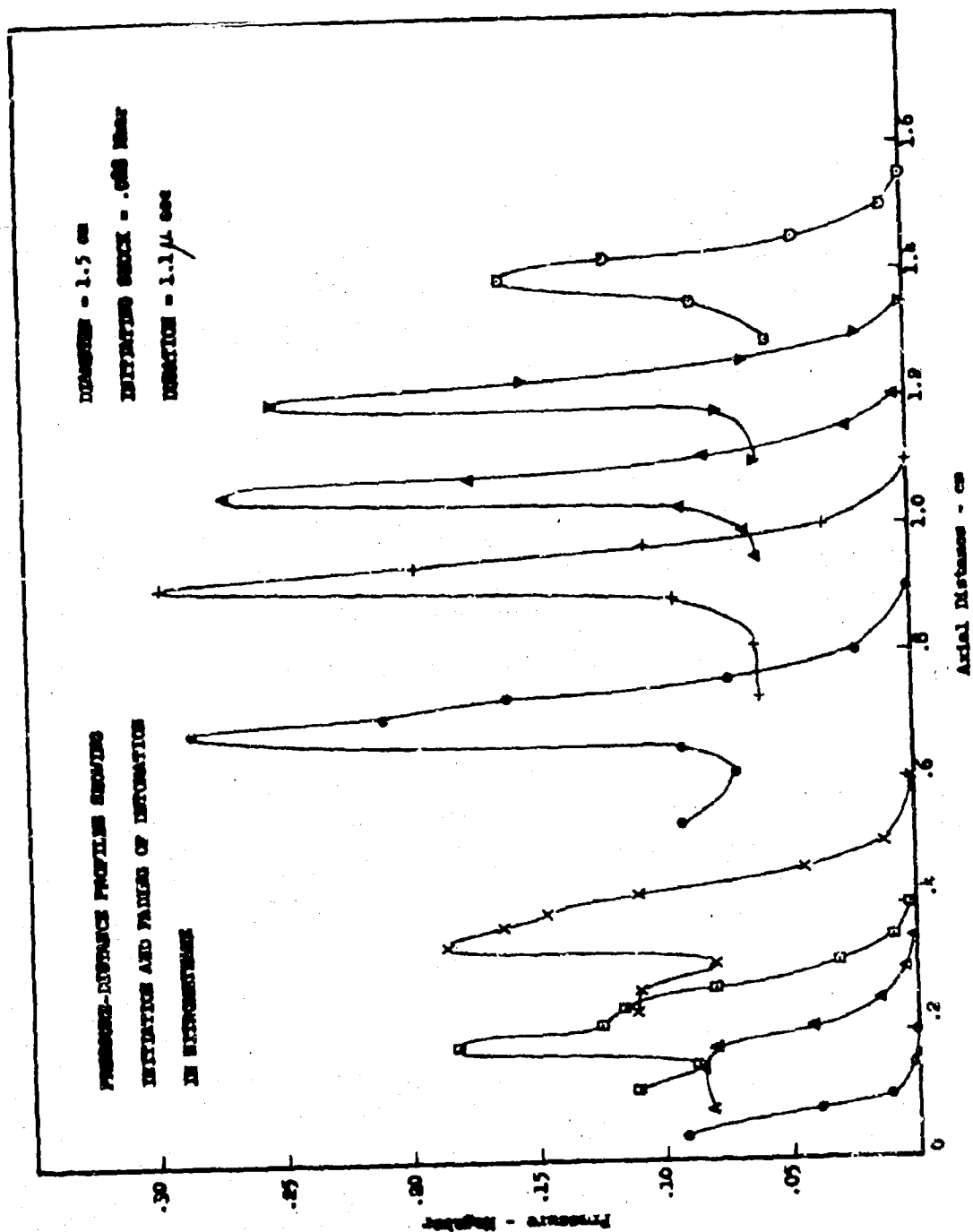


Figure 20.

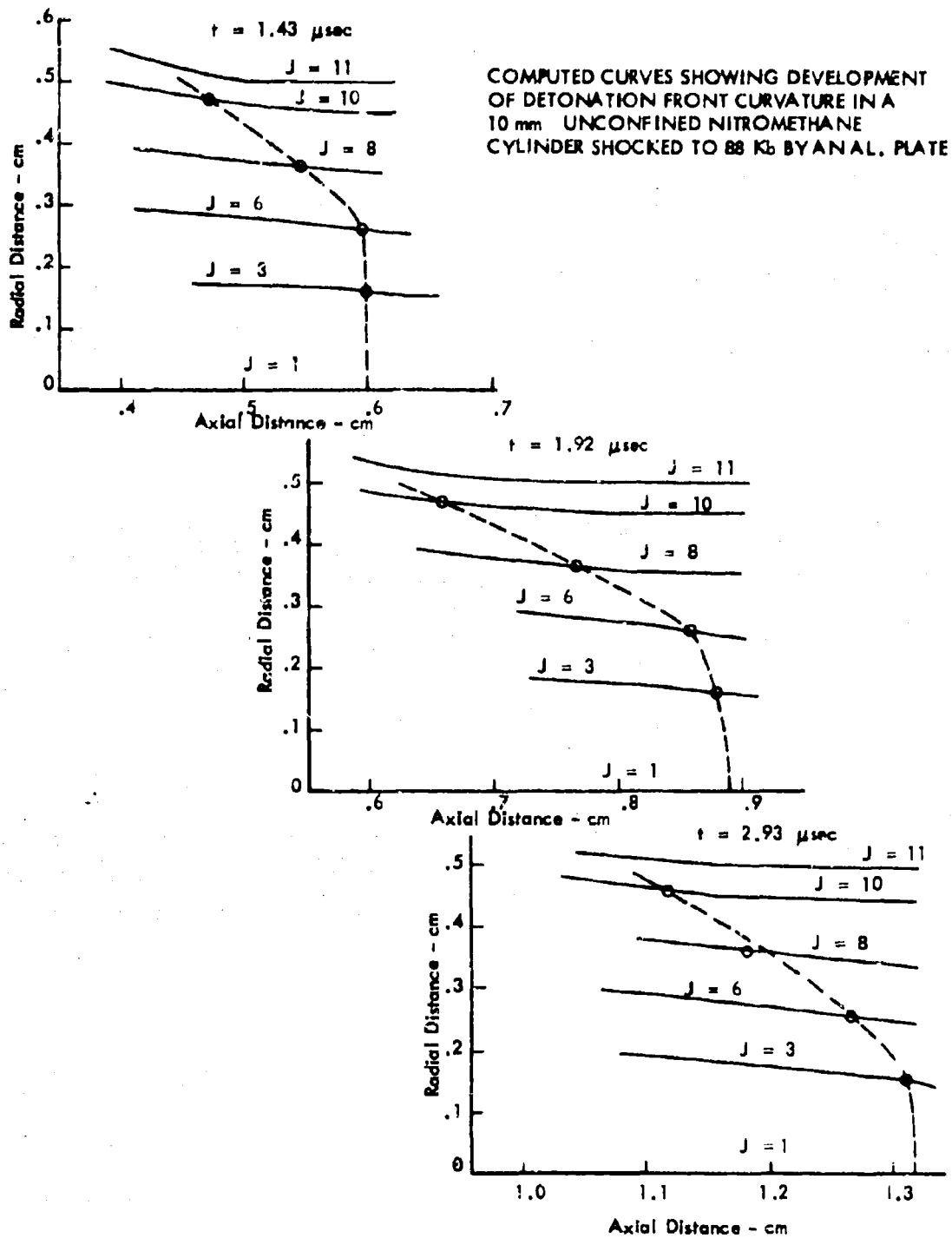


Figure 21.

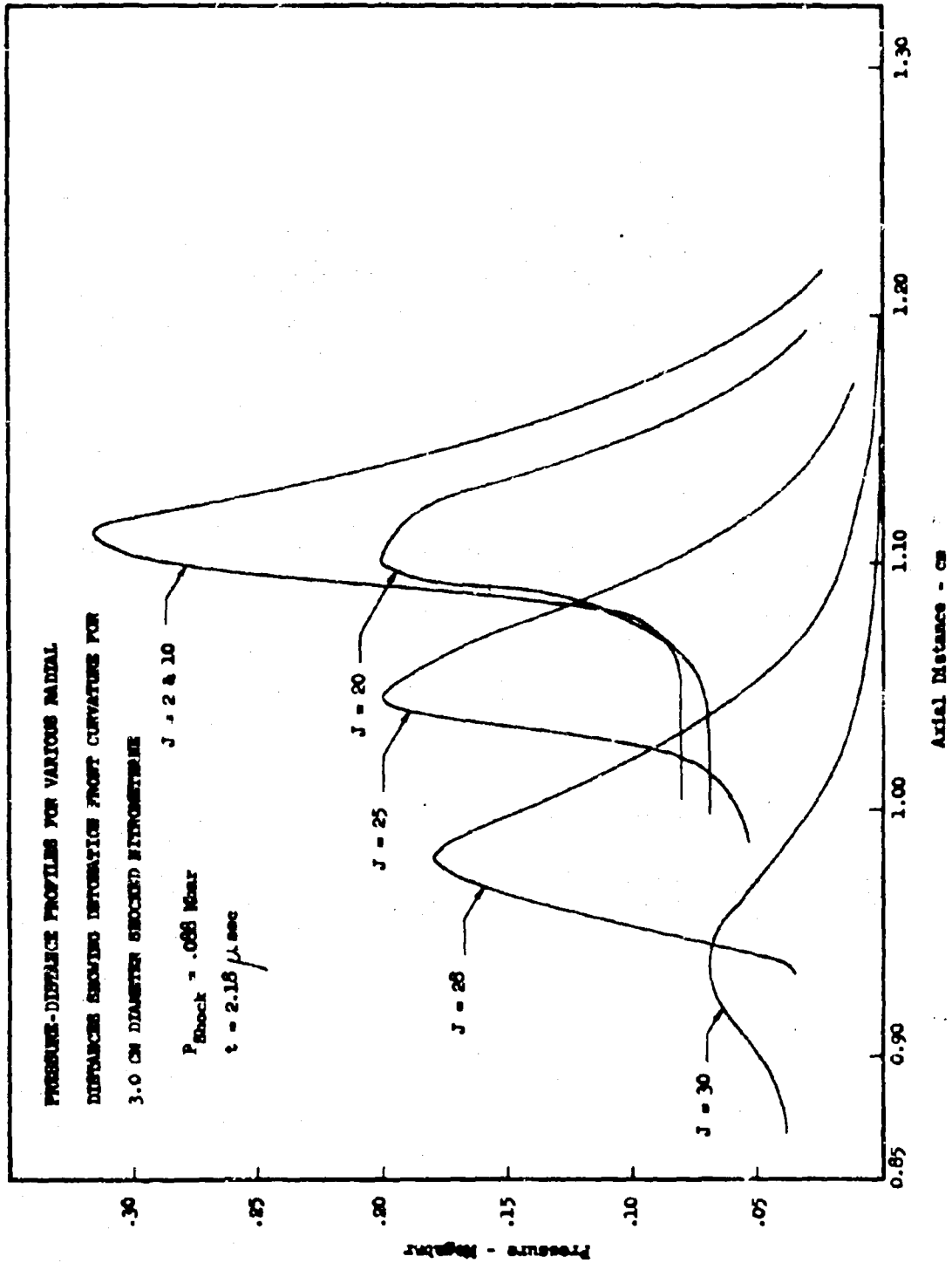


Figure 22.

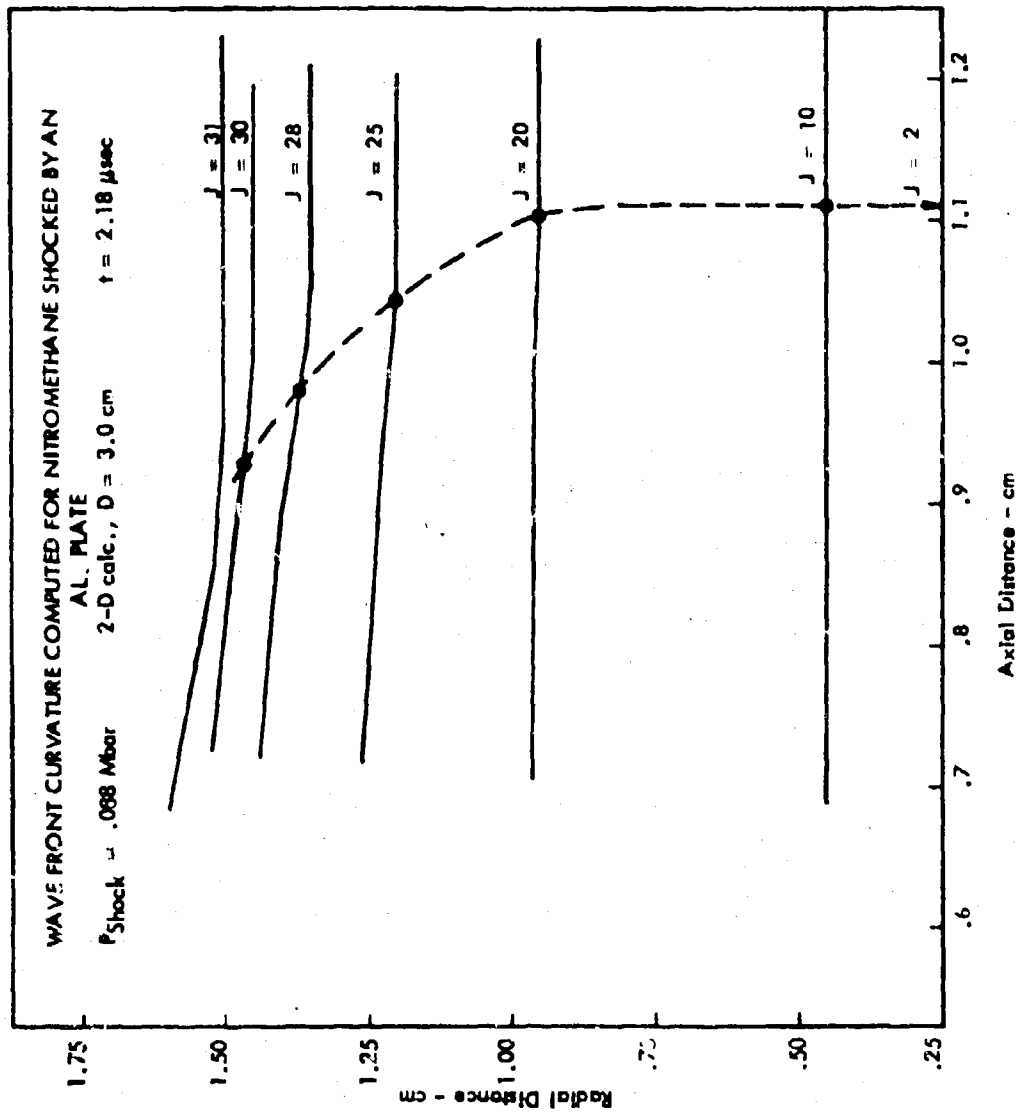


Figure 23.

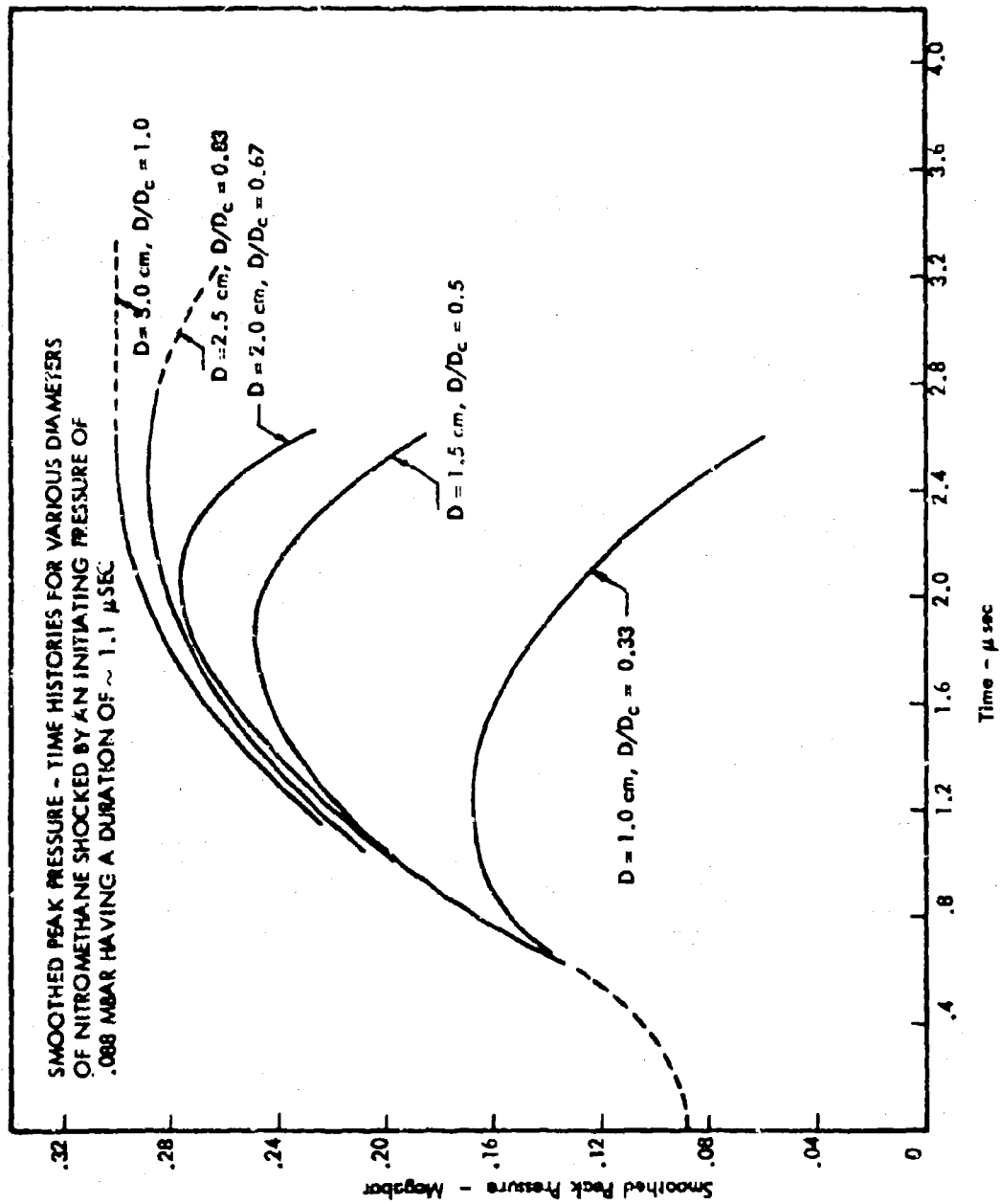


Figure 24.

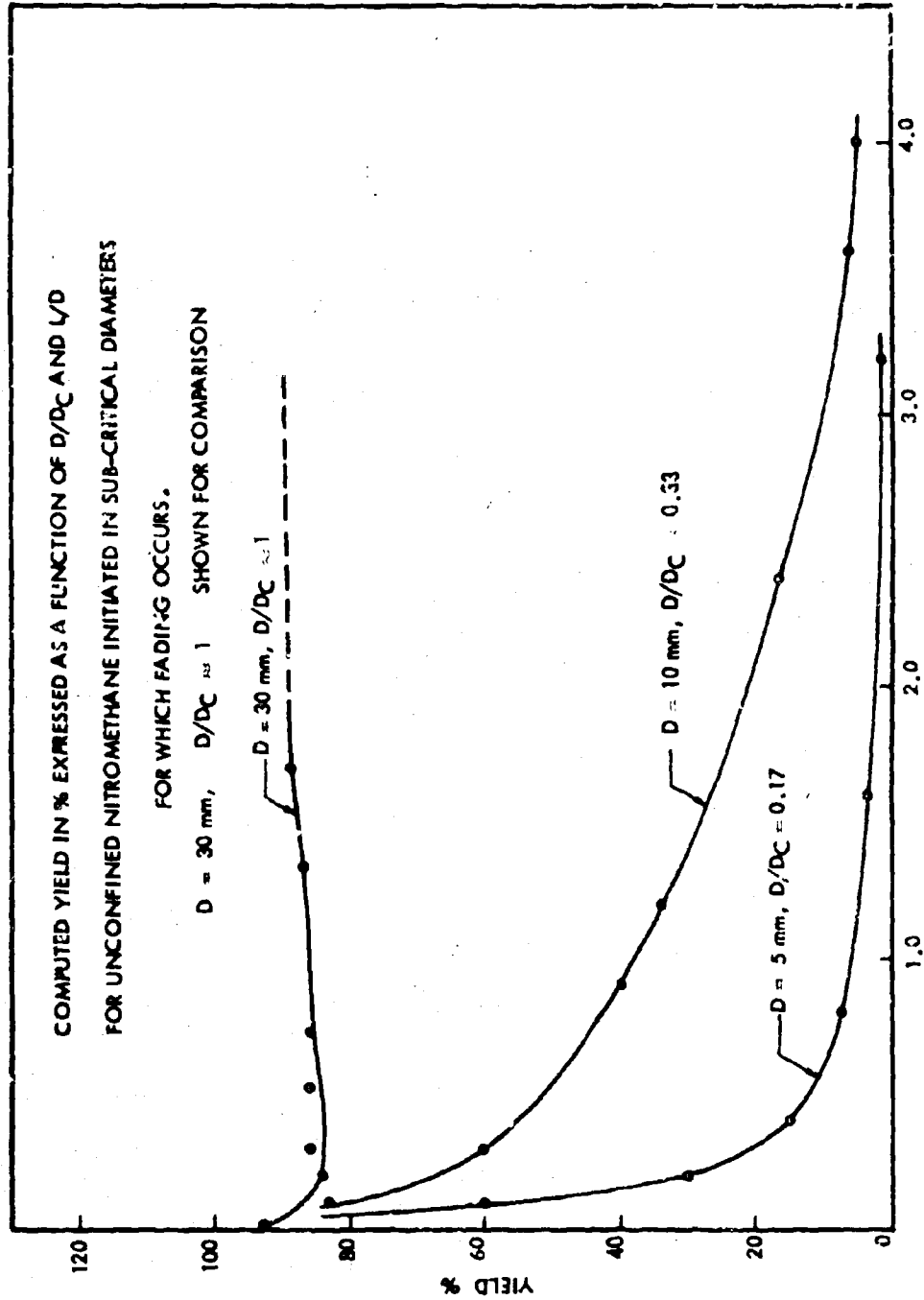


Figure 25.

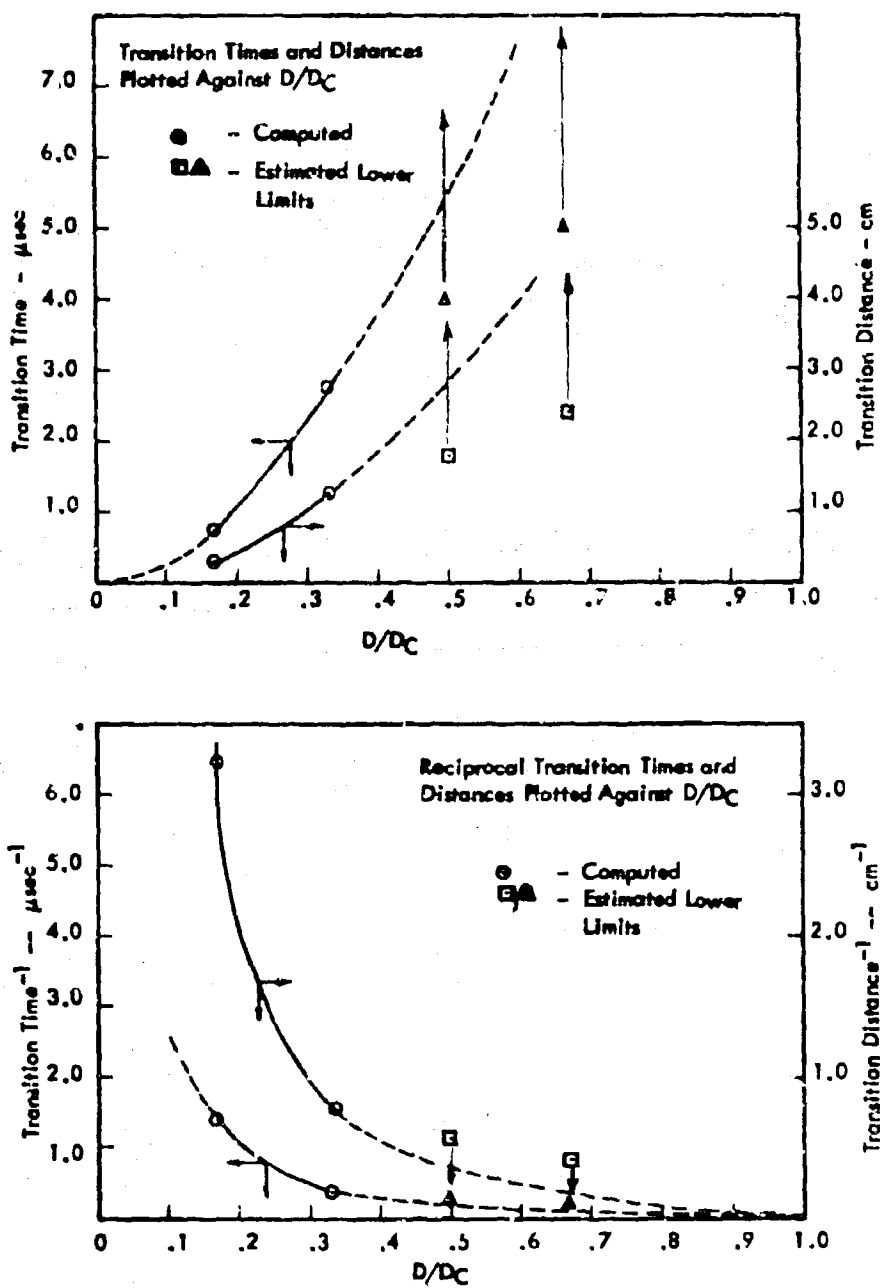


Figure 26.

SCHEMATIC CHARACTERISTIC SHOCK DISPLACEMENT-
TIME HISTORY FOR INITIATION OF AN INHOMOGENEOUS
EXPLOSIVE

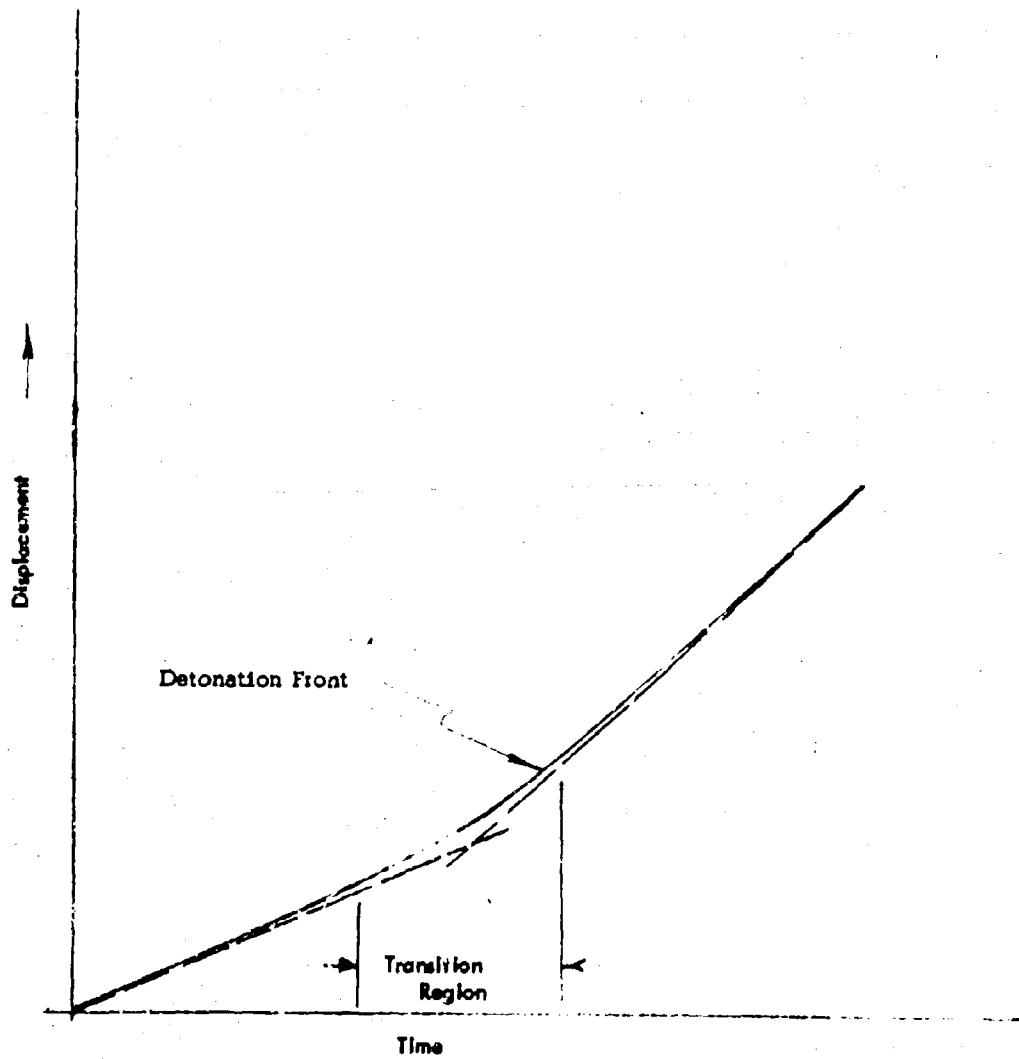


Figure 27.

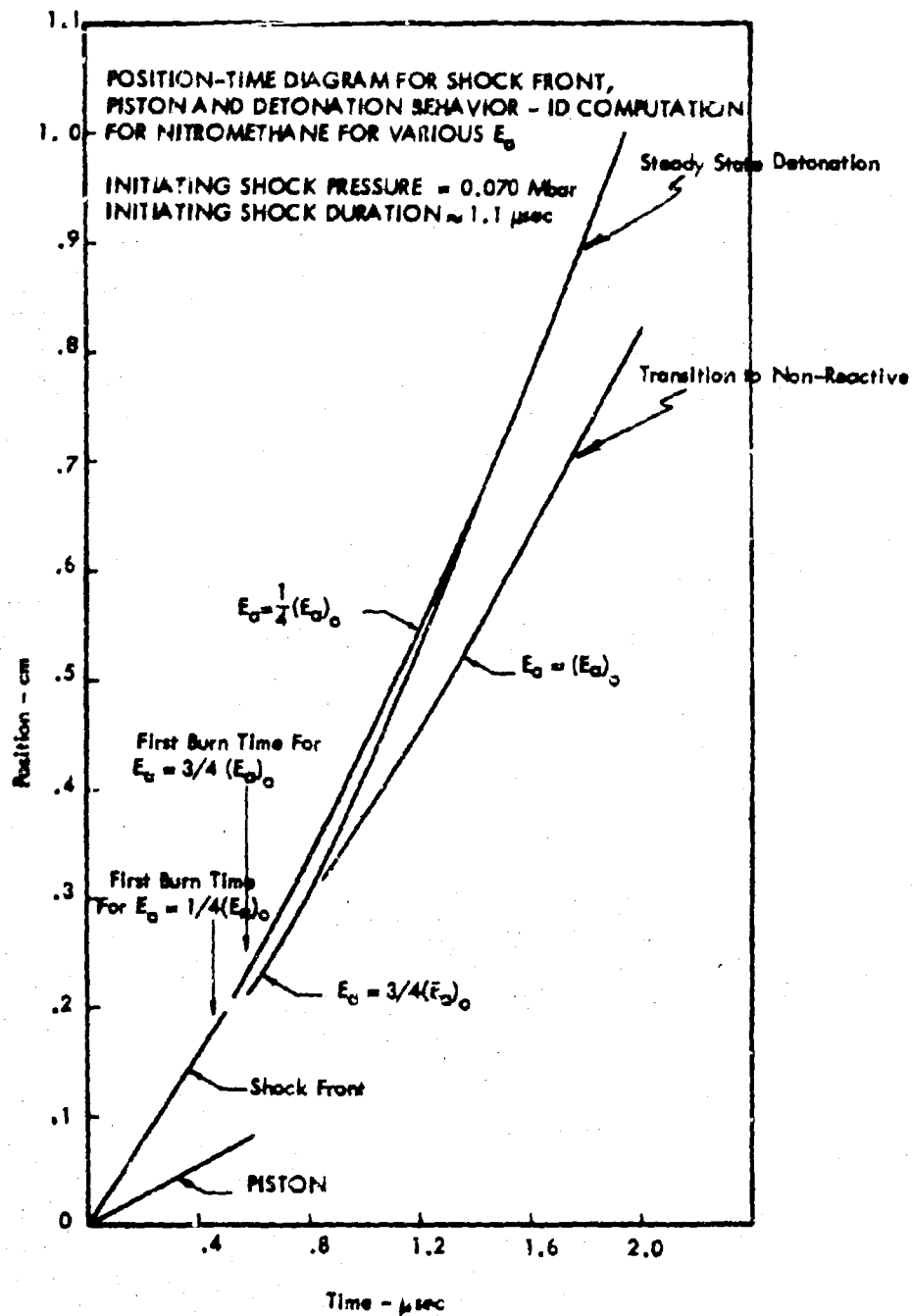


Figure 28.

REFERENCES

1. W. H. Andersen, et al., *Int'l Conf. on Sensitivity & Hazards of Expl.*, London (1963).
2. H. Jones, *Proc. Roy. Soc. (London)* A189, 415 (1947).
3. H. Eyring, et al., *Chem. Rev.* 45, 69 (1949).
4. M. L. Wilkins, *Report UCRL-7322 Physics, UC-34, TID-4500 (22nd Ed.,)* 1963.
5. H. W. Hubbard and M. H. Johnson, *J. Appl. Phys.* 30, 675 (1959).
6. J. W. Enig, *Third Symposium on Detonation, Office of Naval Research Report ACR-52* (1960).
7. Martha E. Evans, F. H. Harlow and B. D. Meixner, *Phys. Fluids* 5, 651 (1962).
8. J. Zinn, *J. Chem. Phys.* 36, 1949 (1962).
9. C. L. Mader, *Los Alamos Scientific Laboratory Report LA-2703*, 1962.
10. C. L. Mader, *Phys. Fluids* 6, 375 (1963).
11. A. W. Campbell, W. C. Davis and J. R. Travis, *Phys. Fluids* 4, 498 (1961).
12. A. W. Campbell, W. C. Davis, J. B. Ramsey and J. R. Travis, *Phys. Fluids* 4, 511 (1961).
13. C. L. Mader, *Los Alamos Scientific Laboratory Report LA-3077*, 1964.
14. J. W. Enig and F. J. Petrone, *Manuscript on "An equation of state and Derived Shock Initiation Criticality Conditions for Liquid Explosives,"* 1964, U. S. Naval Ordnance Laboratory, Silver Spring, Md.
15. J. M. Walsh and R. H. Christian, *Phys. Rev.* 97, 1544 (1955).
16. T. M. Cottrell, T. E. Graham and T. Y. Reid, *Trans. Faraday Soc.* 47, 584 (1951).
17. S. Glasstone, K. J. Laidler, and H. Eyring, *The Theory of Rate Processes*, McGraw Hill Book Co., Inc., 1941.

APPENDIX C

DENSITY AND RDX COMPOSITION VARIATIONS
WITHIN A SAMPLE

A cylindrical RDX-wax explosive charge from Batch 3 was cut into 28 slices and analyzed for density and percent RDX. The percentage variation in density was found to be less than 1.5%, which is in agreement with sample-to-sample variations, and is not considered excessive. There was no indication of a density trend from the top to the bottom of the sample. Although the percentage variation in RDX content (1%) was greater than expected, it was relatively small and no trends from top to bottom were indicated from the data.

To determine if significant variations in RDX content (and density) existed within a sample of Batch 6 material, a rectangular charge was cut into 33 slices and analyzed for density and percent RDX. It was found that the average density for the samples (1.062 gm/cc) was greater than that for the batch as a whole (see Table C-1, Batch 6). This implied a high RDX content and supported the idea that the RDX was settling during the pouring period; i.e., if this sample had been cast late in the pouring period, relatively high concentrations of RDX would have remained in the kettle. The variability in the density was somewhat higher than that for the batch as a whole although such an increase was expected when smaller size samples were taken. The variation of RDX content within a sample was not reflected in this figure since the density samples were taken in a horizontal plane only and the RDX settles vertically. Although the average percent RDX was higher than that for the batch as a whole (33.9% vs 30.75%), indicating settling of the RDX during the pouring period, the variation in this figure (1.23%) was less than expected. However, with regard to the other evidence discussed in this and other sections, it is expected that these concentration variations did exist in Batch 6 explosive.

To determine whether significant variations in RDX content and density did exist within a sample from Batch 7, a cylindrical charge was cut into 20 slices and analyzed for density and percent RDX. The average density for the samples (1.054 gm/cc) was found to be less than that for the batch as a whole (Table C-1). Although this implied a low RDX content, the average percentage of RDX was slightly higher than that for the batch as a whole (30.82% vs 30.75%). However, since the standard deviation in both cases was relatively high (the average density could be as high as 1.071 gm/cc and the average percentage of RDX as low as 28.31%), the conjecture that the RDX was settling during the pouring period was not contradicted. If this sample had been cast early in the pouring period, relatively low concentrations of RDX would have existed in the first liquid cast. It is interesting to note that the variability of the density was found to be somewhat larger than that for the batch as a whole, although such an increase was expected when smaller numbers of samples are taken.

Table C-1. Summary of Density and RDX-Composition Variation Data for
Samples from Batches 3, 6, 7, 7B, and 7C.

Batch	Shape	Dimensions (in.)	Number of Samples	Maximum RDX Content (%)		Minimum RDX Content (%)		Average RDX Content (%)		Standard Deviation in RDX Content (%)		Maximum Density (gm/cc)		Minimum Density (gm/cc)		Average Density (gm/cc)		Standard Deviation in Avg. Density (gm/cc)		Remarks
				(%)	(%)	(%)	(%)	(%)	(%)	(%)	(%)	(gm/cc)	(gm/cc)	(gm/cc)	(gm/cc)	(gm/cc)	(gm/cc)	(gm/cc)	(gm/cc)	
3	Cylinder	1-3/4 x 7	28	31.81		29.16		30.90		0.93		1.085		1.026		1.062		0.019		
6	Rectangle	1-1/4 x 2-3/4 x 11	33	37.0		29.9		33.87		1.23		1.170		1.065		1.120		0.028		
7	Cylinder	1-1/4 x 5	20	33.83		27.24		30.82		2.51		1.073		1.016		1.054		0.017		
Recast 7	Cylinder	1 x 8	8 4	31.21** 28.86		26.05 28.32		28.42 28.64		1.37 0.23		1.077 1.073		1.044 1.065		1.063 1.068		0.010 0.003		Normal (L/D=4) Charge
7B	Cylinder	1-3/4 x 11-1/2	9									1.142		1.011		1.073		0.046		
7C	Cylinder	1-3/4 x 11-1/2	10	38.17		19.16		31.62		4.23***		1.122		1.022		1.087		0.023***		Not all samples cut to same thickness
7C	Square	1-3/8 x 7-1/2	6	33.51		31.33		32.52		0.76		1.100		1.085		1.091		0.007		Normal (L/D=4) Charge
7C	Cylinder	1 x 1 x 4	4									1.088		1.069		1.079		0.007		Normal (L/D=4) Charge
7C	Cylinder	1-1/2 x 6	4									1.108		1.056		1.096		0.008		Normal (L/D=4) Charge

*Obtained by difference.
**Uncertain

***Data weighted according to the thickness of the sample

To establish direct evidence of gradients within the sample, the data in this case were plotted against the known vertical position on the charge where the sample was taken. These results showed that there is a definitely increasing trend (probably related) in both density and RDX content toward the bottom of the charge. This is evidenced by the fact that the top section had about 27.5% RDX and a density of about 1.04 gm/cc, while the bottom section had about 32.4% RDX and a density of about 1.07 gm/cc.

After consultation with the Advisory Group, it was concluded that RDX settling had taken place and that the problem had arisen because of the peculiarities imposed by the large batch size. The peculiarities were: (1) the prolonged soaking time of Cab-O-Sil in mineral oil during the extended period required to melt 100 lb of wax, which might have caused a lower melt viscosity (the "wetting-time phenomenon"); and (2) the increased "working of the melt," which might have caused further break-up of the Cab-O-Sil structure and thus a lowering of the melt viscosity.

Three plans were suggested to remedy the problem: (1) save Batch 7 by remelting and recasting it at a lower kettle temperature, (2) slightly modify the batch by remelting, adding Cab-O-Sil, and then casting at a lower temperature, and (3) start over with a new batch and include a considerably reduced soak time and lower cast temperature during the casting procedure.

The first plan was evaluated by recasting (from excess Batch 7 sheet-cast material) a cylindrical sample at a kettle temperature of approximately 140°F, as opposed to the previous standard temperature of from 212 to 215°F. This sample was analyzed for density and RDX content. The results of these analyses showed that the average density of all the slices was less than that for the batch as a whole. Since the average RDX content of the slices was also lower than that for the batch as a whole, this data is consistent with the concept of RDX settling in the original melt, as discussed previously.

Because the variability in density (which is the same as that of the original batch, taken as a whole) and in RDX content, was almost halved with respect to the prior sample, it was concluded that the low kettle temperature reduced the amount of RDX settling. However, to help determine whether gradients existed in the sample, the data was plotted against vertical position and a definite increasing trend toward the bottom of the charge was evident. This is clear from the fact that the top section had about 26.5% RDX and a density of about 1.04 gm/cc.

while the bottom section had about 31.2% RDX and a density of about 1.08 gm/cc. Although a trend was established, the magnitude of the changes was smaller than in the previous case. If the top 3 in. and bottom 1 in. of the charge were cut off (as would normally be the case when the cast charges are trimmed to give a length-to-diameter ratio of 4) the average density and percentage of RDX would be considerably decreased. This represents an improvement in variability because the significant parts of the density and RDX-content trends were effectively eliminated.

Because of this improvement, the charges from Batch 7 were remelted and recast (as Batch 7B) at a kettle temperature of 140°F. A cylindrical sample was cut into nine slices and each slice was analyzed for density. Again, the average density was less than that for the batch as a whole, and further RDX settling during the recasting operation is indicated. Furthermore, because the large variability of these results (more than four times the previous result) strong gradients were suspected. This was borne out when the data was plotted against vertical position. It was assumed that the trend in RDX content was similar.

It was noted that the viscosity of the melt in this case (at 140°F) was about the same as, or lower than, the viscosity in the previous case (when original Batch 7 sheet-cast material was melted), therefore it was concluded that the wetting-time phenomenon was still operating and that each reheating and remixing of the original Batch 7 material would further break down the Cab-O-Sil structure.

In a further effort to overcome this problem and to determine whether the first plan for saving Batch 7 was feasible, the batch was then recast as Batch 7C, at the lowest kettle temperature possible (110°F) and a cylindrical sample was submitted for analysis.

The averages and standard deviations of the data were computed for all the slices and for those that would remain after the charge had been trimmed for testing. It was noted that the average density of all the samples (1.087 gm/cc) was very close to that of the entire batch (Table C-1). Since the RDX content of the samples (31.62%) was also close to that of the batches as a whole (30.75%), this data was consistent with the concept that there was a direct correlation between density and RDX content; i.e., density changes are directly indicative of changes in RDX percentage. Because the variability in both density and RDX content was higher than that for the original Batch 7 material it was concluded that, as before, the RDX was settling, probably in the molds. When the trimmed charge is considered, the average density and RDX content are higher than for the

overall sample, and for the batch as a whole. Since the trimmed portion is taken from the lower portion of the charge, this result is expected if RDX settling is taking place. However, it was noted that the variability in both density and RDX content is considerably reduced and is within acceptable limits.

To determine the nature of the suspected gradients in the sample, these data were again plotted against vertical position on the charge. The trends were obvious. The top section had about 19.2% RDX and a density of 1.03 gm/cc, while the bottom section had about 38.2% RDX and a density of about 1.12 gm/cc. It is noteworthy that, when the trimmed charge is considered, there are gradients in density and RDX content, even though the variability of the data is considerably reduced. The viscosity of the melt in this case (110°F) was about the same or less than the viscosity in the previous case (Batch 7B). It was again concluded that the wetting-time phenomenon was causing a breakdown in the Cab-O-Sil structure.

In order to verify this result, a square charge and a cylindrical charge (both trimmed) were cut into four slices for analysis. Because of the correlation already established between density and RDX content, each piece was analyzed for density only.

For the square charge, the average density and standard deviation for the samples (1.079 and 0.007 gm/cc) were close to the corresponding values for the batch as a whole (1.081 and 0.010 gm/cc) and were within acceptable limits. Since this sample had been trimmed before the analysis, this low variability in density, despite settling of the RDX, might be explained by the same reasoning discussed previously. The fact that the average density is close to that of the batch as a whole might be accounted for by assuming that this sample was cast at about the middle of the pouring period, when the concentration of RDX (and thus density) was about the same as that for the batch as a whole.

To establish information on gradients within the sample, the data were plotted against the known vertical position on the charge where each sample was taken. An increasing trend was indicated and evidenced by the fact that the top section had a density of about 1.07 gm/cc whereas the bottom section had a density of about 1.08 gm/cc. However, because this difference is relatively small, it was concluded that, for this sample, RDX-concentration gradients were minor.

For the cylindrical sample, the average density of the samples was greater than that for the batch as a whole. This is indicative of RDX settling if this sample were cast late in the pouring period when relatively high concentrations of RDX would have existed in the remaining melt. Again, the variability in density was close to that of the batch as a whole and was within acceptable limits. Since the charge had been trimmed before analysis this might be explained by the same reasoning considered for the square sample.

To determine whether gradients within the sample could be detected, the data were plotted against vertical position as before. In this case the trend was clear. However, since the top section had a density of about 1.09 gm/cc and the bottom section had a density of about 1.11 gm/cc the difference is small and it may be concluded that the RDX-concentration gradients were minor.

From these data it was concluded that although trimmed charges from Batch 7C might have an acceptably low variability in density (and therefore in RDX content) and an acceptably small (or zero) gradient in RDX content, sample-to-sample variations in average density (i. e., in average RDX content) indicated RDX settling, at least in the original melt.

A summary of all the data obtained concerning density and RDX composition variations within a sample is shown in Table C-1. Examination of the data for Batch 7 material shows that, with one exception, the charges considered are unacceptable, either because of excessive variability in average density and RDX content or variation in average density and average RDX content from the overall batch average (Table C-1). Therefore, it was concluded that the attempt to rectify Batch 7 by the first plan was not feasible.

It was noted in the density and RDX content vs vertical position curves, when traversing the charge from top to bottom, there is a steep rise in both curves, a relatively flat portion, and finally another steep rise. This behavior, as opposed to a continuously rising curve, may be explained as follows: if the RDX particles were of the same size they would, according to Stokes' law, settle at the same terminal velocity. In this case, a certain thickness (depending on the time interval) at the top of the charge would be devoid of RDX. However, below this thickness the concentration of RDX would be normal down the charge except near the bottom where the sinking RDX is collecting. This is so since any RDX particle in the central portion of the charge that settles from its initial

position will be replaced (on the average) by one that was initially above it. Thus, a plot of RDX content vs position would include a steeply rising (relatively large) section, a perfectly flat section (with normal properties), and another steeply rising (relatively thin) section. The flat section would represent an acceptable sample for testing. The data do not follow this idealized behavior (i.e., the central section is not flat but gently sloping), because all the RDX particles are not of the same diameter. In this instance, larger particles settle faster than smaller ones and the naturally resulting "classification" of particles results in gradients at every point in the charge. The amount of classification, and thus gradient, depends on the relative sizes and number of the different RDX particles. Thus, it may be concluded that, since the available RDX has a definite and substantial range of particle sizes (see Section 4.3.1.1.2), definite gradients will exist in the central section, and recovery of Batch 7 using this section is not feasible.

As discussed previously, the second plan to remedy the problem of RDX settling was to slightly modify the batch by remelting it, adding Cab-O-Sil, and then casting it at a lower temperature. However, because of the uncertainties involved with further operations on the existing material, it was decided not to pursue this plan.

The third plan to remedy the problem of RDX settling was to start over with a new batch and include a considerably reduced soak time and a lower cast temperature during the casting procedure. This was considered to have more merit than the second plan and materials were ordered and received for making a new 250-lb batch of RDX-wax explosive (Batch 8). The planned casting procedure was modified to include reduction of the Cab-O-Sil/mineral-oil premix soak time, melting of the wax separately to reduce the initial heating time, and casting at a temperature just above the melting point of the mix. However, because the quantitative nature of the wetting-time phenomenon (which causes the settling of the RDX) is not known, there was no technical assurance that the modified casting procedure would be successful. Therefore, it was decided neither to cast Batch 8 nor to continue studies with the RDX-wax explosive.

DOCUMENT CONTROL DATA - RED		
(Security classification of title, body of abstract and if found annotation must be entered when the overall report is classified)		
1. ORIGINATING ACTIVITY (Corporate author)		2a. REPORT SECURITY CLASSIFICATION
Aerojet-General Corporation Downey, California		Unclassified
		2b. GROUP
		-
3. REPORT TITLE		
Large Solid-Propellant Boosters Explosive Hazards Study Program (Project SOPHY)		
4. DESCRIPTIVE NOTES (Type of report and inclusive dates)		
Final Report, 24 November 1965		
5. AUTHOR(S) (Last name, first name, initial)		
Irwin, O. R. Roark, G. L. Salsman, P. K.		
6. REPORT DATE	7a. TOTAL NO. OF PAGES	7b. NO. OF REFS
24 November 1965	330	11
8a. CONTRACT OR GRANT NO.	9a. ORIGINATOR'S REPORT NUMBER(S)	
AF 04(611)-9945 PROJECT NO 6000	0866-01(01)FP	
c	9b. OTHER REPORT NO(S) (Any other numbers that may be assigned this report)	
d	-	
10. AVAILABILITY/LIMITATION NOTICES		
11. SUPPLEMENTARY NOTES		12. SPONSORING MILITARY ACTIVITY
		AF RPL, Hazards Analysis Branch AF Systems Command Edwards, AFB, California
13. ABSTRACT		
<p>Experimental and theoretical studies aimed at evaluating the detonation characteristics of solid-composite propellant rocket motor grains are described. A combined experimental-theoretical program was conducted to determine the effect of RDX adulterant concentration on the critical diameter of a typical Class II (AP-PBAN type) propellant. The resulting detonation model indicated that the critical diameter of AP-PBAN type propellant is about 75 in. Experiments were conducted to test the validity of a previously developed theory of critical geometry that (1) relates the critical diameter to the minimum size of shapes other than solid right cylinders that will sustain detonation and (2) consider the effect of donor intensity, configuration, and location on initiation of detonation in an acceptor. The experimentally determined critical dimensions for detonation of the various shapes tested were in reasonable agreement with predictions of the theory. The initiation criteria proposed by the critical geometry theory was measured and found to correctly predict the initiation of detonation in a supercritical acceptor charge by an axial, end donor. Supercritical charges could be initiated to detonation by an axial, end donor whose diameter was only about 40% of the critical diameter of the acceptor.</p>		

KEY WORDS	LINK A		LINK B		LINK C	
	ROLE	WT	ROLE	WT	ROLE	WT

INSTRUCTIONS

1. ORIGINATING ACTIVITY: Enter the name and address of the contractor, subcontractor, grantee, Department of Defense activity or other organization (corporate author) issuing the report.

2a. REPORT SECURITY CLASSIFICATION: Enter the overall security classification of the report. Indicate whether "Restricted Data" is included. Marking is to be in accordance with appropriate security regulations.

2b. GROUP: Automatic downgrading is specified in DoD Directive 5200.10 and Armed Forces Industrial Manual. Enter the group number. Also, when applicable, show that optional markings have been used for Group 3 and Group 4 as authorized.

3. REPORT TITLE: Enter the complete report title in all capital letters. Titles in all cases should be unclassified. If a meaningful title cannot be selected without classification, show title classification in all capitals in parenthesis immediately following the title.

4. DESCRIPTIVE NOTES: If appropriate, enter the type of report, e.g., interim, progress, summary, annual, or final. Give the inclusive dates when a specific reporting period is covered.

5. AUTHOR(S): Enter the name(s) of author(s) as shown on or in the report. Enter last name, first name, middle initial. If military, show rank and branch of service. The name of the principal author is an absolute minimum requirement.

6. REPORT DATE: Enter the date of the report as day, month, year, or month, year. If more than one date appears on the report, use date of publication.

7a. TOTAL NUMBER OF PAGES: The total page count should follow normal pagination procedures, i.e., enter the number of pages containing information.

7b. NUMBER OF REFERENCES: Enter the total number of references cited in the report.

8a. CONTRACT OR GRANT NUMBER: If appropriate, enter the applicable number of the contract or grant under which the report was written.

8b, c, & d. PROJECT NUMBER: Enter the appropriate military department identification, such as project number, subproject number, system numbers, task number, etc.

9a. ORIGINATOR'S REPORT NUMBER(S): Enter the official report number by which the document will be identified and controlled by the originating activity. This number must be unique to this report.

9b. OTHER REPORT NUMBER(S): If the report has been assigned any other report numbers (either by the originator or by the sponsor), also enter this number(s).

10. AVAILABILITY/LIMITATION NOTICES: Enter any limitations on further dissemination of the report, other than those imposed by security classification, using standard statements such as:

- (1) "Qualified requesters may obtain copies of this report from DDC."
- (2) "Foreign announcement and dissemination of this report by DDC is not authorized."
- (3) "U. S. Government agencies may obtain copies of this report directly from DDC. Other qualified DDC users shall request through _____."
- (4) "U. S. military agencies may obtain copies of this report directly from DDC. Other qualified users shall request through _____."
- (5) "All distribution of this report is controlled. Qualified DDC users shall request through _____."

If the report has been furnished to the Office of Technical Services, Department of Commerce, for sale to the public, indicate this fact and enter the price, if known.

11. SUPPLEMENTARY NOTES: Use for additional explanatory notes.

12. SPONSORING MILITARY ACTIVITY: Enter the name of the departmental project office or laboratory sponsoring (paying for) the research and development. Include address.

13. ABSTRACT: Enter an abstract giving a brief and factual summary of the document indicative of the report, even though it may also appear elsewhere in the body of the technical report. If additional space is required, a continuation sheet shall be attached.

It is highly desirable that the abstract of classified reports be unclassified. Each paragraph of the abstract shall end with an indication of the military security classification of the information in the paragraph, represented as (TS), (S), (C), or (U).

There is no limitation on the length of the abstract. However, the suggested length is from 150 to 225 words.

14. KEY WORDS: Key words are technically meaningful terms or short phrases that characterize a report and may be used as index entries for cataloging the report. Key words must be selected so that no security classification is required. Identifiers, such as equipment model designation, trade name, military project code name, geographic location, may be used as key words but will be followed by an indication of technical context. The assignment of links, roles, and weights is optional.